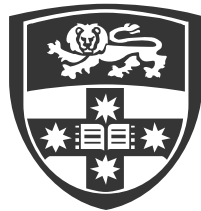


Microbiological modulation of suspended particulate matter dynamics

A study of biological flocculation in nutrient-enriched waters

Fiona H.M. TANG



THE UNIVERSITY OF
SYDNEY

School of Civil Engineering
Faculty of Engineering & Information Technologies
The University of Sydney

January 2017

A thesis submitted in fulfilment of
the requirements for the degree of
Doctor of Philosophy

Supervisor: Dr. Federico Maggi
Auxiliary Supervisor: A/prof Abbas El-Zein

ISBN 978-0-646-96701-1

Copyright ©2017, Fiona H.M. Tang

All rights reserved. No part of this publication may be reproduced in any form, by print, or photo print, microfilm or any other means, without written permission by the author.

Abstract

The study of suspended particulate matter (SPM) dynamics has conventionally focused on physical and hydrodynamical interactions, with little attention paid on exploring the role of SPM as a micro-ecosystem that sustains a wide diversity of microbial colonies. This thesis puts forth a new paradigm of SPM dynamics that integrates mineral, chemical, and biological components into one framework to emphasize the role of microorganisms in altering the chemistry and structure of SPM, which further affect its transport and deposition. Microbiological modulation of SPM dynamics was investigated in this thesis by coupling experiments with numerical models.

Experiments were conducted in a settling column that allows generation of isotropic and homogenous turbulence, continuous measurement of water quality parameters, and automated acquisition of micro-photographs of SPM. Three SPM types (nutrient- and biomass-free NFBF, nutrient-affected and biomass-free NABF, and nutrient- and biomass-affected NABA) were tested in various combinations at five turbulence shear rates, three nutrient concentrations, and three mineral concentrations. Micro-photographs were then used to analyse the physical characteristics of SPM, in terms of size, internal architecture and settling velocity. To quantify the internal architecture and the space-filling capacity of SPM, a semi-analytical method that reconstructs its three-dimensional capacity (fractal) dimension from light intensity spectra of its two-dimensional micro-photographs was developed. Experimental results revealed that the size of NABA aggregates was approximately 60% larger and the capacity dimension was 2% lower as compared to NFBF aggregates. In contrast, the average settling velocity was observed to be nearly invariant for all SPM types.

Experimentally acquired SPM showed high irregularity in shape, especially those of NABA; this motivates the investigation of the extent to which SPM shape can control the interparticle collision and aggregation dynamics. Investigations were carried out using spheropolygon theory to approximate the shape of SPM. The generated spheropolygons were then used within a particle-based model to assess SPM collision and aggregation dynamics under the action of gravitational, viscous, contact, electrostatic, and van der Waals forces. Simulation results showed that the probability for SPM to aggregate was highly dependent on SPM shape and surface asperity, suggesting that microorganisms can alter SPM collision and aggregation kinematics through their role in modifying SPM structure and shape.

To assess the interactions between minerals, chemicals, and microorganisms living attached to SPM, a biogeochemical model was developed to describe biotic and abiotic processes in the sedimentary ecosystem, including chemical adsorption on SPM, aqueous complexation, gas dissolution, microbial metabolic reactions, and necromass dynamics. The model considered explicitly five microbial functional groups and involved eight microbial metabolic pathways to create an ecological feedback loop with competition and facilitation interrelationships. Simulation results showed that interactions between microbial functional groups are highly non-linear and highly sensitive to changes in nutrient concentrations. This analysis emphasizes the feedback interactions between minerals, chemicals, and microorganisms. It shows how changes in sediment and water qualities can have impacts on microorganisms that in turn modify SPM characteristics and result in further alteration of sediment and water qualities.

This thesis provides an insight into the role played by microorganisms in engineering the architecture and altering the chemistry of SPM, with experimental evidence and simulation results put forth to emphasize that the contributions of nutrients and microorganisms cannot be neglected in modelling and predicting SPM dynamics.

Statement of Originality

This is to certify that to the best of my knowledge, the content of this thesis is my own work. This thesis has not been submitted for any degree or other purposes.

I certify that the intellectual content of this thesis is the product of my own work and that all the assistance received in preparing this thesis and sources have been acknowledged.

Name: Fiona H.M. Tang

Signature: 

Date: 27 | 08 | 2016

Authorship Attribution Statement

Chapter 3 of this thesis was published in technical report¹, and manuscripts^{2,3} detailed below. The experimental facility presented in this chapter was designed by myself and the co-author (F. Maggi) of the manuscripts, while the publications were prepared by myself.

Chapter 4 of this thesis was published as a research article⁴ in *Soft Matter*. I contributed in developing the method, analysing the data, and writing the manuscript.

Chapter 5 of this thesis was published as a research article³ in *Water Research*. I designed and conducted the experiments, analysed the data, and wrote the manuscript.

Chapter 6 of this thesis was published as a research article⁵ in *Water Research*. I conducted the numerical simulation, analysed the data, and wrote the manuscript. The source code of the spheropolygon and particle-based model used to conduct the simulation was developed by the co-author (F. Alonso-Marroquin).

Chapter 7 of this thesis was submitted as a research article⁶ to *Ecosystems*. I contributed in designing the reaction network, conducting the simulation, analysing the data, and writing the manuscript. The source code of the BRTSim-v2 solver used to conduct the simulation was developed by the co-author (F. Maggi).

List of publications:

¹Tang F.H.M. and Maggi F. (2015). A laboratory facility for flocculation related experiments. Report No. R952, The University of Sydney.

²Tang F.H.M. and Maggi F. (2015). Anthropogenic nutrient leaching alters the size distribution of suspended particle matter. *In Proceedings of the 36th IAHR World Congress*, The Hague, The Netherlands.

³Tang F.H.M., and Maggi F. (2016). A mesocosm experiment of suspended particulate matter dynamics in nutrient- and biomass-affected waters, *Water Research*, 89, 76-86.

⁴Tang F.H.M., and Maggi F. (2015). Reconstructing the fractal dimension of granular aggregates from light intensity spectra, *Soft Matter*, 11(47), 9150-9159.

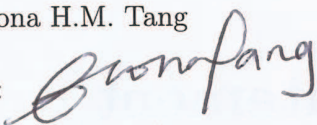
⁵Tang F.H.M., Alonso-Marroquin F., and Maggi F. (2014). Stochastic collision and aggregation analysis of kaolinite in water through experiments and the spheropolygon theory, *Water Research*, 53, 180-190.

⁶Tang F.H.M., and Maggi F. (2016). Nitrogen-modulated dynamics of microbial colonies living on suspended sediment, submitted to *Ecosystems*, Manuscript ID: ECO-16-0150.

Hereby, I (F. Tang) confirm that I am the first and the corresponding author of the publications listed above.

Name: Fiona H.M. Tang

Signature:



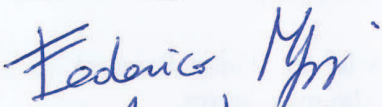
Date:

27/08/2016

As supervisor for the candidature upon which this thesis is based, I can confirm that the authorship attribution statements above are correct.

Name: Dr. Federico Maggi

Signature:



Date:

27 August 2016

Contents

Abstract	1
Statement of Originality	2
Authorship Attribution Statement	3
List of Figures	8
List of Tables	12
1 Introduction	14
1.1 Background and motivation	14
1.2 Aim and objectives	15
1.3 Outline	16
2 A review of SPM dynamics	17
2.1 Composition of SPM	17
2.2 SPM as a micro-ecosystem	18
2.2.1 Adsorption of chemicals on mineral surfaces	18
2.2.2 Chemicals as nutrients to sustain biological growth	20
2.2.3 Microorganisms as ecosystem engineers	21
2.3 SPM dynamics	24
2.3.1 Flocculation of SPM	24
2.3.2 Irregularity of SPM	25
2.3.3 Settling of SPM	26
2.4 Bridging the gap	27
3 Experimental facility and procedures	29
3.1 Introduction	29
3.2 Design criteria	29
3.3 Settling column	30
3.4 Turbulence generating system	32
3.4.1 Grid geometry	32
3.4.2 Oscillation control	33
3.4.3 Determination of turbulence shear rate	33
3.4.4 Discussion	34
3.5 Water quality measuring system	34
3.6 μ PIV system	35

3.6.1	Imaging system	35
3.6.2	Illumination system	36
3.7	Micro-controlling system	38
3.8	Sample preparation	38
3.9	Experimental protocols	40
3.10	Image processing	40
3.11	Summary	40
4	Reconstructing SPM capacity dimension from light intensity spectra	41
4.1	Introduction	41
4.2	Methods	42
4.2.1	Earlier approach	42
4.2.2	Perimeter-based fractal dimension spectrum	42
4.2.3	Analytical description of the spectrum	43
4.2.4	The optimal perimeter-based fractal dimension	45
4.2.5	Control set of test aggregates	45
4.2.6	Statistical estimators	47
4.3	Results	47
4.3.1	Projection-based and analytical spectra $d_{P,I}$ of numerical aggregates	47
4.3.2	Empirical derivation of the function $f(\ell)$	47
4.3.3	Validation against numerically-generated aggregates	49
4.3.4	Validation against stereolithographically-fabricated aggregates	50
4.3.5	Application to experimentally-acquired SPM	51
4.4	Recommendations	53
4.5	Summary	53
5	Characteristics of SPM in nutrient- and biomass-affected waters	54
5.1	Introduction	54
5.2	Data analyses	54
5.2.1	Analyses of size, capacity dimension, and settling velocity	54
5.2.2	Statistical quantification	55
5.2.3	Background of statistical entropy	55
5.3	Results	57
5.3.1	SPM size distribution	57
5.3.2	SPM capacity dimension distribution	59
5.3.3	Capacity dimension and size of SPM	60
5.3.4	SPM settling velocity distribution	61
5.3.5	Settling velocity and size of SPM	62
5.3.6	Entropy of size and capacity dimension	62
5.4	Summary	65
6	Stochastic collision and aggregation analysis of SPM	66
6.1	Introduction	66
6.2	Methods	67
6.2.1	Experiments	67
6.2.2	Definition of spheropolygon	67
6.2.3	Spheropolygon optimization	67
6.2.4	Spheropolyfloc interaction forces	68

6.2.5	Ortho-axial and peri-axial collisions	70
6.3	Results	70
6.3.1	Experimental size distribution	70
6.3.2	Optimal spheropolyflocs	71
6.3.3	Collision probability in the double layer	72
6.3.4	Aggregation probability	72
6.3.5	Relative trajectory of spheropolyflocs	73
6.4	Discussion	75
6.5	Summary	77
7	Dynamics of microbial colonies living on SPM	78
7.1	Introduction	78
7.2	Methods	78
7.2.1	Reaction network	78
7.2.2	Biogeochemical modelling	81
7.2.3	Model calibration and validation	84
7.2.4	Analyses of nitrogen leaching	84
7.3	Results	85
7.3.1	Calibrated model parameters	85
7.3.2	Goodness-of-fit analyses	88
7.3.3	Effect of N leaching on microbial dynamics	88
7.3.4	Effect of N leaching on aqueous NH_4^+ and NO_3^-	89
7.3.5	Effect of N leaching on total N phase partitioning	89
7.3.6	N leaching and N mass flow through reactions	91
7.4	Discussion	92
7.5	Summary	94
8	Conclusions and perspectives	95
8.1	Conclusions	95
8.2	Perspectives	96
	Appendix A Photographs of the facility	98
	Appendix B Algorithms for reconstructing SPM capacity dimension	101
	B.1 Matlab function	101
	Appendix C SPM size, capacity dimension, and settling velocity distributions	104
	Appendix D Derivations of microbial metabolic reactions	117
	Bibliography	121
	List of Symbols	134
	Acknowledgements	136

List of Figures

2.1	Composition of SPM.	18
2.2	Classification of aquatic microorganisms according to metabolic requirements (after Kelly, 1971; Van Kessel, 1977; Gottschalk, 1986; Rittmann and McCarty, 2001; Dworkin et al., 2006; Raven, 2009; Chariton et al., 2010). Note that, e^a and e^d refer to electron acceptor and electron donor, respectively.	23
2.3	Biotic and abiotic interactions in SPM micro-ecosystem. Note that, EPS and TEP refer to extracellular polymeric substances and transparent exopolymer particles, respectively.	28
3.1	Photograph of the experimental facility.	30
3.2	Schematic drawings of (a) the settling column, (b) the flocculation section, (c) the diaphragm, and (d) the measuring section.	31
3.3	(a) the plan view and the cross-sectional view of a grid element, and (b) schematic drawing of the grid oscillation system.	32
3.4	Schematic drawing of the CCD camera and the high magnification lens mounted on the height-adjustable camera stand.	36
3.5	Schematic drawing of the optical box for holding Cree LED and optical fibers.	37
3.6	Schematic drawings of (a) the optical fibers holder, and (b) the positioning stand for holding the optical fibers holder.	37
3.7	The interface built in Matlab2011b environment used for monitoring and controlling all components of the facility.	38
4.1	Conceptual perimeter-based fractal dimension spectra $d_{P,I}$ of S_2 projections of SPM aggregate A with high capacity dimension $d_0(S_3)$ and SPM aggregate B with low capacity dimension $d_0(S_3)$	43
4.2	(a) example grayscale reconstructed projections of diffusion-limited (DLA), cluster-cluster (CCA), and self-correlated (SCA) aggregates in the three principle directions (first three columns) and experimental images of natural SPM (fourth column). (b) example images of stereolithographically-fabricated SCA aggregates (top row) as compared to their grayscale reconstructed projections (bottom row).	48
4.3	Example projection-based and analytical spectra $d_{P,I}(\ell)$ of diffusion-limited (DLA), cluster-cluster (CCA), and self-correlated (SCA) numerical aggregates for dimensionless aggregate size: (a) $\ell = 2^6$; (b) $\ell = 2^8$; and (c) $\ell = 2^{13}$. (d) NRMSE and R of analytical spectra $d_{P,I}(\ell)$ against projection-based spectra for all 36 numerical aggregates at different ℓ	49
4.4	(a) least square fitting of $f(\ell)$ using calibration coordinates $(\hat{I}(\ell), d_{P,I}(\ell))$ sets. (b) fitting parameters $\beta_1(\ell)$, $\beta_2(\ell)$, and $\beta_3(\ell)$ of the $f(\ell)$ function in Eq. (4.18) for dimensionless aggregate size $\ell = 2^m$, with $m \in [6, 13]$	49
4.5	Percent error PE, normalized root mean square error (residuals) NRMSE and correlation coefficient R of estimated $d_0(S_3)$ for numerical aggregates obtained by using the methods in Maggi and Winterwerp (2004) (M&W (2004)) and in this chapter.	50
4.6	Estimated $d_0(S_3)$ using the methods in Maggi and Winterwerp (2004) (M&W (2004)) and in this chapter against actual $d_0(S_3)$ for dimensionless aggregate size $\ell = 2^m$ with $m \in [6, 13]$	51

4.7	Projection-based and analytical spectra $d_{P,I}$ of stereolithographic self-correlated (SCA) aggregates for dimensionless aggregate size: (a) $\ell = 2048$; (b) $\ell = 4096$; and (c) $\ell = 8192$. (d) percent error PE, normalized root mean square error (residuals) NRMSE, and correlation coefficient R of estimated $d_0(S_3)$ for stereolithographic aggregates obtained by using the methods in Maggi and Winterwerp (2004) (M&W (2004)) and in this chapter.	51
4.8	Projection-based and analytical spectra $d_{P,I}$ of (a) organic and (b) mineral SPM for dimensionless aggregate size $\ell = 256$; relationship between aggregate density ρ_s and capacity dimension $d_0(S_3)$ according to force balance equation for (c) organic and (d) mineral SPM.	52
5.1	Average \bar{L} against median \tilde{L} (first row), standard deviation σ_L against size range ($L_{max} - L_{min}$) (second row), and excess kurtosis $\gamma_{2,L}$ against skewness $\gamma_{1,L}$ (third row) of SPM size distributions for nutrient- and biomass-free (NFBF), nutrient-affected and biomass-free (NABF) and, nutrient- and biomass-affected (NABA) suspension types with $[\text{NH}_4\text{NO}_3] = \{0, 1.5, 3.0, 6.0\}$ mM, $G = \{32, 48, 64, 80, 96\}$ s ⁻¹ (first to fifth column), and $C_K = \{0.1, 0.2, 0.4\}$ g/L (corresponding to small, medium, and large markers, respectively), while, n_A is the number of aggregates analysed in an experimental set.	58
5.2	Correlation of \bar{L} (first column), \bar{d}_0 (second column), and \bar{v} (third column) with NH_4NO_3 concentration $[\text{NH}_4\text{NO}_3]$ (first row) and kaolinite concentration C_K (second row) for nutrient- and biomass-free (NFBF), nutrient-affected and biomass-free (NABF), and nutrient- and biomass-affected (NABA) suspension types, and for G ranging between 32 s ⁻¹ and 96 s ⁻¹ . CK0.1, CK0.2, and CK0.4 denote $C_K = 0.1$ g/L, $C_K = 0.2$ g/L, and $C_K = 0.4$ g/L, respectively. N1.5, N3.0, and N6.0 denote $[\text{NH}_4\text{NO}_3] = 1.5$ mM, $[\text{NH}_4\text{NO}_3] = 3.0$ mM and $[\text{NH}_4\text{NO}_3] = 6.0$ mM, respectively. '+' and '-' indicate positive and negative correlation, respectively.	59
5.3	Average \bar{d}_0 against median \tilde{d}_0 (first row), standard deviation σ_{d_0} against capacity dimension range ($d_{0,max} - d_{0,min}$) (second row), and excess kurtosis γ_{2,d_0} against skewness γ_{1,d_0} (third row) of SPM capacity dimension distributions for nutrient- and biomass-free (NFBF), nutrient-affected and biomass-free (NABF) and, nutrient- and biomass-affected (NABA) suspension types with $[\text{NH}_4\text{NO}_3] = \{0, 1.5, 3.0, 6.0\}$ mM, $G = \{32, 48, 64, 80, 96\}$ s ⁻¹ (first to fifth column), and $C_K = \{0.1, 0.2, 0.4\}$ g/L (corresponding to small, medium, and large markers, respectively), while, n_A is the number of aggregates analysed in an experimental set.	61
5.4	Bin-averaged capacity dimension d_0 against aggregate size L for experiments of nutrient- and biomass-free (NFBF, green), nutrient-affected and biomass-free (NABF, blue) and nutrient- and biomass-affected (NABA, red) with $G = \{32, 48, 64, 80, 96\}$ s ⁻¹ (left to right). The correlation coefficient R represents the goodness of fit of Eq. (5.4) against experiments.	61
5.5	Average \bar{v} against median \tilde{v} (first row), standard deviation σ_v against settling velocity range ($v_{max} - v_{min}$) (second row), and excess kurtosis $\gamma_{2,v}$ against skewness $\gamma_{1,v}$ (third row) of SPM settling velocity distributions for nutrient- and biomass-free (NFBF), nutrient-affected and biomass-free (NABF) and, nutrient- and biomass-affected (NABA) suspension types with $[\text{NH}_4\text{NO}_3] = \{0, 1.5, 3.0, 6.0\}$ mM, $G = \{32, 48, 64, 80, 96\}$ s ⁻¹ (first to fifth column), and $C_K = \{0.1, 0.2, 0.4\}$ g/L (corresponding to small, medium, and large markers, respectively), while, n_A is the number of aggregates analysed in an experimental set.	63
5.6	Bin-averaged settling velocity v against aggregate size L for experiments of nutrient- and biomass-free (NFBF, green), nutrient-affected and biomass-free (NABF, blue) and nutrient- and biomass-affected (NABA, red) with $G = \{32, 48, 64, 80, 96\}$ s ⁻¹ (left to right).	64

5.7	Entropy of SPM capacity dimension distribution $E[Q(d_0) P(d_0)]$ against entropy of SPM size distribution $E[Q(L) P(L)]$ for nutrient- and biomass-free (NFBF), nutrient-affected and biomass-free (NABF), and nutrient- and biomass-affected (NABA) suspensions with $[\text{NH}_4\text{NO}_3] = \{0, 1.5, 3.0, 6.0\}$ mM, mineral concentration $C_K = \{0.1, 0.2, 0.4\}$ g/L (corresponding to small, medium, and large markers, respectively), and turbulence shear rate $G = \{32, 48, 64, 80, 96\}$ s ⁻¹ (first to fifth column).	64
6.1	Polygon P_s with $N_v = 16$ (solid line) and disk Q_s with $r = 4 \mu\text{m}$ (circles) are shown with the spheropolygon $P_s \oplus Q_s$ drawn (dashed line).	67
6.2	Equivalent radius r_{eq} histogram of experimental SPM aggregates.	70
6.3	Average and standard deviation of the relative error percent PE(%) of generated spheropolyflocs in size class $r_{eq} \leq 5 \mu\text{m}$ (5 samples) and $r_{eq} > 5 \mu\text{m}$ (5 samples) as a function of number of vertices N_v and for spheroradius (a) $r = 1 \mu\text{m}$, (b) $r = 2 \mu\text{m}$ and (c) $r = 4 \mu\text{m}$, with dashed lines representing the average PE(%) of equivalent spheres (i.e., $N_v = 1$ and $r = r_{eq}$).	71
6.4	Probability of collision within the attraction zone $p_r[C(D_c < D_a)]$ for (a) Type I, (b) Type II, and (c) Type III collisions, with δ_s ranging from 0 to δ_{smax} . The number of vertices N_v on the x-axis refers to the approaching spheropolyfloc in each collision type.	73
6.5	Conditional probability of aggregation after collision within the attraction zone $p_r[A C(D_c < D_a)]$ for (a) Type I, (b) Type II, and (c) Type III collisions, with δ_s ranging from 0 to δ_{smax} . The number of vertices N_v on the x-axis refers to the approaching spheropolyfloc in each collision type.	74
6.6	Conditional probability of aggregation after collision outside the attraction zone $p_r[A C(D_c \geq D_a)]$ for (a) Type I, (b) Type II, and (c) Type III collisions, with δ_s ranging from 0 to δ_{smax} . The number of vertices N_v on the x-axis refers to the approaching spheropolyfloc in each collision type.	74
6.7	Trajectories of spheropolyflocs with $N_v = 64$ and $r = 1 \mu\text{m}$ in Type I ortho-axial collision ($\delta_s = 0$) for the cases where the collision occurred (a) within D_a and resulted in aggregation (Trajectory A), (b) within D_a and did not lead to aggregation (Trajectory B), (c) beyond D_a and led to aggregation (Trajectory C) and (d) beyond D_a with no aggregation observed (Trajectory D).	75
6.8	Probability of four different types of trajectory (A, B, C and D) in 5000 stochastic replicates with δ_s ranging from 0 to δ_{smax} for (a) Type I, (b) Type II, and (c) Type III collisions. The number of vertices N_v on the x-axis refers to the approaching spheropolyfloc in each collision type.	76
7.1	Biogeochemical reaction network of SPM micro-ecosystem described in the model. Pathways shaded in grey were not included in the model.	79
7.2	Comparison between experimental measurements and modelled results for (a) $[\text{NH}_4^+]$, (b) $[\text{NO}_3^-]$, (c) pH, (d) the net oxygen consumption $[\text{O}_2(\text{aq})]_C$, (e) $[\text{C}_6\text{H}_{12}\text{O}_6]$, and biomass concentrations for (f) phototrophic bacteria B_{PHOTO} , (g) heterotrophic bacteria B_{HET} , (h) nitrifying bacteria B_{NIT} , (i) denitrifying bacteria B_{DEN} , (j) dissimilatory nitrate reducing bacteria B_{DNR} , and (k) necromass NEC .	86
7.3	Goodness-of-fit analyses of the modelled against experimental $[\text{NH}_4^+]$, $[\text{NO}_3^-]$, pH, and the net oxygen consumption $[\text{O}_2(\text{aq})]_C$ using (a) correlation coefficient R, (b) normalized root mean square error NRMSE, (c) Nash-Sutcliffe efficiency NSE, (d) index of agreement IA, and (e) percent bias PBIAS. The red asterisk indicates calibration set and the green dot represents validation tests that passed the good-of-fit benchmark analyses. '+' and '-' signs indicate positive and negative values in R and PBIAS tests, respectively. Note that kaolinite concentration C_K and $[\text{NH}_4\text{NO}_3]$ plotted corresponded to the initial concentrations in incubation.	88

7.4	(a) Concentrations of total living biomass B_{TOT} and biomass fraction relative to B_{TOT} for (b) phototrophic bacteria B_{PHOTO} , (c) heterotrophic bacteria B_{HET} , (d) nitrifying bacteria B_{NIT} , (e) denitrifying bacteria B_{DEN} , and (f) dissimilatory nitrate reducing bacteria B_{DNR} at steady-state (end of 50-year simulation period) and for leaching rates $R_{NH_4^+}$ and $R_{NO_3^-}$ ranging between 8.64×10^{-9} and 8.64×10^{-3} mol L ⁻¹ day ⁻¹ . NB indicates no trace of living biomass detected.	90
7.5	Concentrations of (a) NH_4^+ and (b) NO_3^- in the aqueous phase at steady-state (end of 50-year simulation period) for leaching rates $R_{NH_4^+}$ and $R_{NO_3^-}$ ranging between 8.64×10^{-9} and 8.64×10^{-3} mol L ⁻¹ day ⁻¹	90
7.6	Partitioning of total N (N_{total}) into (a) protected (p), (b) aqueous (aq), (c) gaseous (g), and (d) biological (b) phases at steady-state (end of 50-year simulation period) for leaching rates $R_{NH_4^+}$ and $R_{NO_3^-}$ ranging between 8.64×10^{-9} and 8.64×10^{-3} mol L ⁻¹ day ⁻¹	91
7.7	Mass flow of total N N_{total} through microbial metabolic reaction R1 to R8 at steady-state (end of 50-year simulation period) for leaching rates $R_{NH_4^+}$ and $R_{NO_3^-}$ ranging between 8.64×10^{-9} and 8.64×10^{-3} mol L ⁻¹ day ⁻¹ , and for $R_{NH_4^+}/R_{NO_3^-} = 1$	92
8.1	Feedback loop describing the interactions between SPM, nutrients, and microorganisms.	96
A.1	Components of the settling column including the flocculation section, the measuring section, and the diaphragm.	98
A.2	The multi-parameter water quality meter (TOA-DKK, WQC-24) equipped with Standard and Ion modules.	98
A.3	Photographs of (a) a grid element, (b) evenly spaced grid elements connected through a stainless steel bar, and (c) the grid oscillation system.	99
A.4	Photograph of the CCD camera and the high magnification lens mounted on the height-adjustable camera stand.	99
A.5	Photographs of (a) a Cree LED, (b) the optical box, and (c) the optical fibers holder fixed on the positioning stand.	100
A.6	Photographs of (a) the <i>Arduino Uno</i> board, (b) the motor shield, and (c) the screw shield used in the micro-controlling system.	100

List of Tables

3.1	Table of parameters measured by the water quality meter (TOA-DKK, WQC-24) equipped with the Standard and Ion modules. Table adapted from “Hand-held Water Quality Meter WQC-24 Instruction Manual” provided by the manufacturer.	35
3.2	Characteristics of SPM samples during the incubation in 500 mL beaker and the testing in settling column. The total liquid volumes contained in the flocculation section of the settling column and the beaker were 15 L and 0.5 L, respectively. ^a Nutrient- and biomass free SPM prepared using only kaolinite mineral; ^b nutrient-affected and biomass-free SPM prepared using kaolinite mineral and ammonium nitrate; and ^c nutrient- and biomass-affected SPM prepared using kaolinite mineral, ammonium nitrate and glucose with inoculation of sedimentary microbial communities. *Note that NFBF and NABF samples were only mixed in beaker for 30 minutes and were not incubated. C_K and $[\text{NH}_4\text{NO}_3]$ denote the concentrations of kaolinite and ammonium nitrate, respectively.	39
4.1	Characteristics of DLA, CCA and SCA numerical aggregates.	46
5.1	Results of one-way analysis of variance (ANOVA) and multiple comparison <i>post hoc</i> test for the null hypothesis that nutrient- and biomass-free (NFBF), nutrient-affected and biomass-free (NABF) and nutrient- and biomass-affected (NABA) aggregates are equal in size L , capacity dimension d_0 , and settling velocity v . Significance $p < 0.01$ indicates that the null hypothesis is rejected.	59
6.1	Values of parameters used in Eq. (6.5) - Eq. (6.8) for each spheropolyfloc collision type (I, II and III). ^(a) Values of λ_n depended on the effective mass of spheropolyflocs and were calculated as described in Chapter 6.2.4.	69
7.1	Summary of microbial metabolic reactions, Langmuir adsorption kinetic reactions, and equilibrium aqueous complexation and gas dissolution reactions included in the reaction network. Note that R1 to R8 were written in the form used to code in the BRTSim-v2 solver. ^a Parameter assumed after Servais et al. (1985) and Billen et al. (1990). ^b Parameters calibrated based on NABF experiments. ^c Parameters from EQ3/6 at 25°C (Wolery, 1992). ^d Interpolated parameters at 21°C.	83
7.2	Summary of calibrated parameters for microbial metabolic reactions R1 to R8. ^a Values of μ_s relative to reactions R1 to R8 written as in Table 7.1. Note that, the value of μ_s changes depending on the stoichiometry represented in the reactions. ^b Competition term was included in R1 and R2 to account for competitive substrate consumption between NH_4^+ and NO_3^- . ^c Competition term was included in R3 and R4 to account for competitive substrate consumption between NH_4^+ and NO_3^- . ^d Competition term was included in R3 and R4 to account for competitive substrate consumption of $\text{C}_6\text{H}_{12}\text{O}_6$	87

C.1	Cumulative frequency of SPM size L distribution for nutrient- and biomass-free (NFBF), nutrient-affected and biomass-free (NABF), and nutrient- and biomass-affected (NABA) experiments and for different ammonium nitrate concentrate $[\text{NH}_4\text{NO}_3]$, kaolinite concentration C_K and turbulence shear rate G	105
C.2	Cumulative frequency of SPM capacity dimension d_0 distribution for nutrient- and biomass-free (NFBF), nutrient-affected and biomass-free (NABF), and nutrient- and biomass-affected (NABA) experiments and for different ammonium nitrate concentrate $[\text{NH}_4\text{NO}_3]$, kaolinite concentration C_K and turbulence shear rate G	109
C.3	Cumulative frequency of SPM settling velocity v distribution for nutrient- and biomass-free (NFBF), nutrient-affected and biomass-free (NABF), and nutrient- and biomass-affected (NABA) experiments and for different ammonium nitrate concentrate $[\text{NH}_4\text{NO}_3]$, kaolinite concentration C_K and turbulence shear rate G	113

Chapter 1

Introduction

1.1 Background and motivation

The growing global human population and the increasing power of technology call for the expansion of human activities in both the scale and the intensity, especially in agriculture and industry. Human activities modify substantially the use of land and water, the structure and functioning of ecosystems, global climate, and biogeochemical cycles (e.g., Vitousek et al., 1997a,b; Galloway, 1998; Paerl and Huisman, 2009). As much as terrestrial ecosystems, our natural waters suffer from these pervasive anthropogenic modifications; traces of hazardous substances (e.g., heavy metals and organochlorine compounds) are often observed in many open water systems (e.g., McCready et al., 2006; Ize-Iyamu et al., 2007), and the frequency, intensity, and duration of algal blooms are observed to increase globally in both fresh and marine waters (e.g., Parsons and Dortch, 2002; Verschuren et al., 2002; Heisler et al., 2008; Leliaert et al., 2009). While extensive research has been conducted in recent decades to develop an understanding of anthropogenic impacts on water quality, ecological functioning, and aquatic biodiversity, there is a much less explored aspect of research, that is, the impact of altered ecological equilibria on the dynamics of suspended particulate matter (SPM).

SPM is an important aspect of aquatic ecosystems because it can transform the geomorphology of coastal areas, estuaries, river banks, waterways and harbours (e.g., Toffolon, 2002; Siviglia and Crosato, 2016), and it can alter the quality of water and deposits (e.g., Golterman et al., 1983; McCready et al., 2006) as well as biogeochemical cycles (e.g., Klump and Martens, 1981; Middelburg and Levin, 2009). The transport and deposition of SPM are governed by hydrodynamic processes (e.g., waves, currents, turbulence, and differential settling, Kranck, 1973; McCave, 1984; Fredsøe and Deigaard, 1992; Elfrink and Baldock, 2002) and water properties (e.g., fluid viscosity and density, Rubey, 1933), as well as the characteristics of SPM itself (e.g., size, composition, density, shape, internal architecture, Maggi, 2013, 2015b), which affect the buoyancy, inertia, viscous, and gravitational forces acting on it. These factors have been extensively studied in the past decades, with a focus on sediment-water interactions (e.g., Einstein and Krone, 1962; Gibbs, 1985; Van Leussen, 1988; Mehta, 1989; Stone and Krishnappan, 2003; Maggi, 2005; Kumar et al., 2010). Although a solid framework on physical interactions has been established and contributed to the development of sediment transport prediction (e.g., Ariathurai and Krone, 1976; Wilcock and Crowe, 2003; Hu et al., 2009; James et al., 2010), the microbiological contributions in altering SPM dynamics are still relatively under-explored, and are often not accounted for in sediment transport models.

SPM by itself is a micro-ecosystem that sustains a wide diversity of microbial strains living in a facilitative, competitive, or symbiotic interrelationship with one another (e.g., Groffman and Bohlen, 1999; Horner-Devine et al., 2004). Fine minerals of SPM provide surfaces for chemical

adsorption (e.g., Hedges, 1977; Ongley et al., 1981), creating a protected and nutrient-rich habitat for microbial colonization (e.g., Kjørboe et al., 2002; Grossart et al., 2006). Analogous to how human has modified the Earth's ecosystem, microorganisms engineer their habitat by modifying the chemistry and structure of SPM (e.g., Meadows and Tufail, 1986; Meadows et al., 2012). Microorganisms uptake nutrients, degrade organic compounds and transform ions from one form to another (e.g., nitrify NH_4^+ to NO_3^-), thus, changing the chemical properties of SPM, such as, pH and dissolved oxygen content (e.g., Meadows and Tufail, 1986; Hedges and Keil, 1995; Rittmann and McCarty, 2001). Microbial metabolism produces extracellular polymeric substances (EPS) and transparent exopolymer particles (TEP) as metabolites, which act as biological glue to facilitate aggregation and modify the internal architecture of SPM (e.g., Jackson, 1995; Passow et al., 2001). SPM colonized by microorganisms generally develops extensive web-like networks, with larger size and lower fractal dimension as compared to SPM free from microbial colonization (e.g., Paerl, 1975; Azetsu-Scott and Passow, 2004; Tan et al., 2012). EPS and TEP were also found to facilitate the binding of chemicals and contaminants (e.g., Headley et al., 1998; Bhaskar and Bhosle, 2006), thus modifying further the chemistry and causing an alteration to the ecological balance of the sediment habitat. Offset of ecological balance may cause variations in microbial communities and may result in changes to the secretions and properties of EPS and TEP (e.g., Meadows and Tufail, 1986; Bruckner et al., 2011); hence, this may result in a different form or a different extent of modification to the structure of SPM. All these physical, chemical, and biological processes are interconnected and their interrelationships are complex and largely undiscovered.

With increasing rates, scales, and types of anthropogenic forcing imposed onto our natural waters, the ecological functioning and microbial diversity of the micro-ecosystem on SPM are continuously being altered. It is becoming questionable if studies focusing only on sediment-water interactions and neglecting contributions from microbial interactions are enough to fully-elucidate the dynamics of SPM. This thesis addresses the need to shift from the conventional paradigm that only emphasizes physical interactions to a new paradigm of SPM dynamics that explores the interrelationships between minerals, chemicals, and microorganisms.

1.2 Aim and objectives

While acknowledging all possible anthropogenic stresses experienced by natural aquatic ecosystems, this thesis focuses on a narrower scope, and in particular, it aims at understanding how increased dissolved inorganic nitrogen (NH_4^+ and NO_3^-) can affect ecological functions and dynamics of microbial communities living on SPM, and the extent to which microbial activity together with nutrient enrichment can modulate SPM dynamics.

The first objective of this thesis is to experimentally quantify physical characteristics of SPM in terms of size, fractal characteristic, and settling velocity. This objective was achieved by testing SPM samples in a settling column equipped with a turbulence generating system, a water quality measuring system, and a μPIV imaging system to acquire micro-photographs of SPM. A semi-analytical approach was also developed to retrieve the three-dimensional capacity (fractal) dimension of SPM from its two-dimensional micro-photographs.

The second objective is to investigate how microorganisms change the characteristics of SPM and how these changes respond to different turbulence intensities, mineral concentrations, and nutrient (NH_4^+ and NO_3^-) concentrations. Experiments were conducted with three different suspension types in nutrient- and biomass-free (NFBF), nutrient-affected and biomass-free (NABF), and nutrient- and biomass-affected (NABA) conditions. Five turbulence shear rates, three NH_4NO_3 concentrations,

and three mineral concentrations were tested for each suspension type.

The third objective is to understand how modification to SPM characteristics can alter its collision and aggregation dynamics. This was achieved by using spheropolygons to approximate the shape of experimentally-acquired SPM and using the generated spheropolygons within a particle-based model to assess their collision and aggregation dynamics.

The fourth objective is to understand how nutrients and microorganisms feedback on one another. This is achieved by coupling experimentally-acquired water quality measurements with a biogeochemical model that describes various biotic and abiotic processes in a sedimentary habitat.

1.3 Outline

A literature review on SPM dynamics is presented in Chapter 2 with a focus on the interrelationships between minerals, chemicals, and microorganisms living on it. Chapter 3 describes the experimental facility used to quantify physical characteristics of SPM and to monitor the ambient water quality for experiments conducted in different chemical and environmental conditions. The protocols used to conduct each set of experiments are also presented in Chapter 3. Chapter 4 describes a semi-analytical approach used to improve quantification of three-dimensional capacity dimension of SPM. The analyses of experimentally-acquired SPM size, capacity dimension, and settling velocity distributions are presented in Chapter 5. The effect of shape and surface asperity on SPM collision and aggregation dynamics were explored in Chapter 6 using the spheropolygon theory. Lastly, a biogeochemical reaction network involving both biotic and abiotic processes in a sedimentary ecosystem is presented in Chapter 7 to investigate the effect of increased inorganic nitrogen concentrations on the dynamics of microbial communities living on SPM. A summary of major achievements of this doctoral thesis and future perspectives of this research are outlined in Chapter 8.

Chapter 2

A review of SPM dynamics

This chapter reviews the properties and characteristics of suspended particulate matter (SPM) in aquatic ecosystems with particular attention paid on exploring the interrelationships between mineral, chemical, and microbiological components of SPM.

2.1 Composition of SPM

Suspended particulate matter (SPM) refers to particles with sizes ranging from nanometers to centimeters, suspended in the water column of aquatic ecosystems such as streams, rivers, lakes, estuaries, and oceans. SPM is commonly classified into organic and inorganic fractions (e.g., Ongley et al., 1981; Eisma, 1986; Droppo and Ongley, 1992; Maggi, 2005). Droppo (2001) proposed a detailed model for floc classification, which divided a floc into four components: inorganic, bioorganic, water and pores. This conventional classification is debatable because researchers commonly refer to inorganic flocs as aggregates made of sand, silt and clay minerals, whereas, the inorganic fraction can also include substances such as metal ions (e.g., Al^{3+} , K^+ , Fe^{2+}) and nutrients (e.g., NO_3^- , NH_4^+ , PO_4^{3-}) in either absorbed or dissolved form (e.g., Hart, 1982; Jain and Ram, 1997). The organic fraction is widely referred to as organic matter attached and adsorbed on SPM, while organic fraction also consists of living cells such as phytoplankton and bacteria (e.g., Hedges, 1977; Kiørboe et al., 2002; Grossart et al., 2006). In order to have a better understanding of the interrelationships between nutrient enrichment, biological growth, and minerals, a new SPM classification model is proposed here (Figure 2.1), where SPM is divided into three main components: biological, mineral, and chemical.

The biological component consists of both living and non-living cells. SPM was found to be colonized by living microorganisms such as microalgae, phytoplankton, diatoms, bacteria, zooplankton, and others (e.g., Kiørboe et al., 1990; Passow et al., 2001; Droppo, 2001; Grossart et al., 2003a). The non-living component, on the other hand, consists of the residuals of living cells (e.g., metabolic products, polysaccharide, necromass, fecal pellets and dead cells, Riebesell, 1991; Simon et al., 2002; Grossart et al., 2003b), which can also be used as a carbon source for cell respiration. The mineral component is subdivided into cohesive (e.g., kaolinite, illite, smectite, montmorillonite) and non-cohesive minerals (e.g., sand, quartz, silicate, calcite) (e.g., Van Leussen, 1994; Bibby and Webster-Brown, 2005). The chemical component consists of either adsorbed or dissolved ions and both organic and inorganic molecules (e.g., NH_4^+ , NO_3^- , organochlorines and other contaminants, Mee, 1992; Jain and Ram, 1997; McCready et al., 2006).

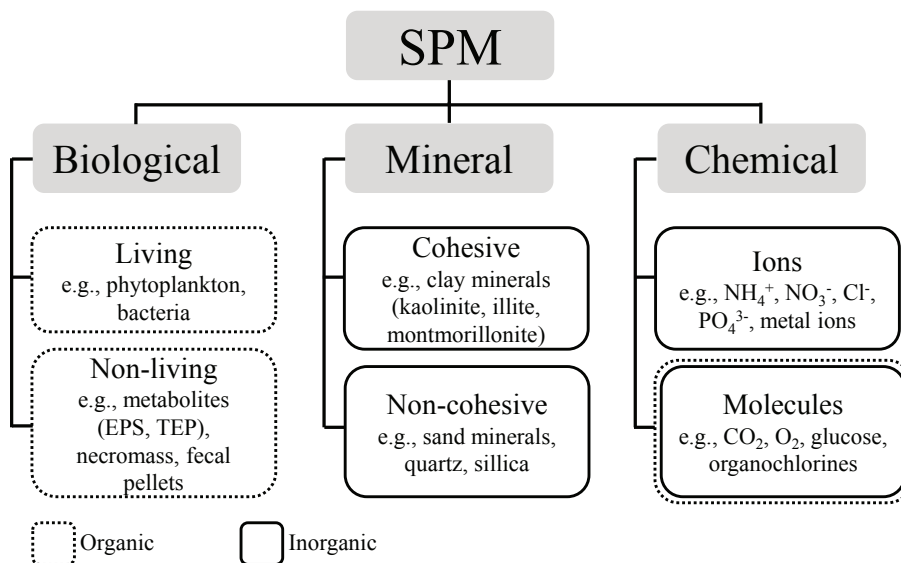


Figure 2.1: Composition of SPM.

2.2 SPM as a micro-ecosystem

SPM, as an important part of an aquatic ecosystem, is itself a micro-ecosystem that sustains multiple biotic and abiotic processes. The three major components (biological, mineral, and chemical) described above are closely correlated and their interrelationships are complex and highly non-linear. This section presents the state-of-the-art knowledge of the interactions between each of the three components.

2.2.1 Adsorption of chemicals on mineral surfaces

Traces of nutrients (e.g., NH_4^+ , NO_3^- , PO_4^{3-} , Shanks and Trent, 1979; Kumar et al., 2011), metals (e.g., Fe, Al, Ag, Hg, Ongley et al., 1981; Hart, 1982; McCready et al., 2006), and contaminants (e.g., aromatic hydrocarbons, organochlorines, DDT, dioxins, Karickhoff et al., 1979; McCready et al., 2006) have been observed on SPM sampled in many different aquatic ecosystems (e.g., lakes, rivers, estuaries, and oceans) and across different continents. These observations stress the importance of SPM as the carrier of nutrients and contaminants in natural waters and this link between mineral and chemical components is well documented and is, historically, the main research interest of water quality chemists, who focus on the transport and removal of nutrients and contaminants in aquatic ecosystems.

Research in this area mainly focusses on adsorption characteristics of chemicals on SPM, especially clay minerals (e.g., Henrichs and Sugai, 1993; Wang and Lee, 1993; Zamparas et al., 2013). Studies suggest that the mineralogy of SPM is one of the main factors that influence its adsorptive capacity (e.g., Ongley et al., 1981; Hedges, 1977; Dashman and Stotzky, 1982; Hedges and Hare, 1987). The difference in the layering structure of clay minerals (e.g., kaolinite is two-layered while montmorillonite is three-layered) determines the surface area available for chemical adsorption and cation-exchange capacities, hence, influencing the adsorption affinity of clay minerals for particular types of chemical (e.g., Ongley et al., 1981; Dashman and Stotzky, 1982; Hedges and Hare, 1987). Hedges (1977) reported that the surface area and cation-exchange capacity of montmorillonite were approximately 10 and 25 times higher than those of kaolinite, respectively. As a result

of highly negatively-charged surface, montmorillonite was observed to have higher uptake of cationic (positively-charged) chemicals (e.g., Theng, 1974; Hedges and Hare, 1987) and lower affinity for anionic (negatively-charged) chemicals as compared to kaolinite (Hedges and Hare, 1987). Fine SPM clay minerals generally have selective sorption characteristics, with a higher affinity for polar than non-polar molecules (e.g., Ensminger and Gieseking, 1939; Hedges and Hare, 1987). An increased concentration of ionic and polar nutrients (e.g., NH_4^+ , NO_3^- , glutamic acid, lysine) in natural waters could therefore lead to desorption of neutral molecules (e.g., monosaccharides, alanine), hence, altering the nutrient cycle and biological processes in SPM.

Mathematical models have been developed to describe chemical adsorption onto solid surfaces, which can also be applied to SPM. A chemical X(aq) in aqueous phase is assumed to be in a dynamic equilibrium with X(ad) adsorbed onto mineral surfaces, where the mass of X(ad) being adsorbed per unit mass depends on the concentration of X(aq) and the ambient temperature (Atkins and De Paula, 2005). The simplest and most commonly used form of adsorption isotherm is the linear function (e.g., Hedges, 1977; Cantrell et al., 2002)

$$X(\text{ad}) = K_{\text{linear}}X(\text{aq}), \quad (2.1)$$

where K_{linear} is the adsorption distribution coefficient. Because Eq. (2.1) assumes linear relationship between X(aq) and X(ad), K_{linear} can only approximate the adsorption in a narrow range of X(aq) concentrations. Non-linear equations such as Freundlich and Langmuir were developed to provide better prediction of chemical adsorption. Freundlich adsorption isotherm is one of the oldest non-linear adsorption models as (Freundlich, 1906)

$$X(\text{ad}) = K_{Fr}X(\text{aq})^{n_{Fr}}, \quad (2.2)$$

where K_{Fr} and n_{Fr} are the Freundlich adsorption coefficients. The Freundlich equation does not approach Henry's Law of dilute solutions and is commonly found to not fit well to experimental data at low X(aq) concentrations and it does not reach an asymptote at high X(aq) concentrations (e.g., Kinniburgh, 1986; Robens et al., 1999; Ng et al., 2002). Langmuir adsorption isotherm, on the other hand, was derived based on the kinetics of adsorption and desorption processes under three main assumptions: (1) monolayer adsorption on a surface; (2) surface is uniform and perfectly flat; and (3) the adsorption of a molecule to a given site is independent of the neighbouring sites (e.g., Langmuir, 1918; Atkins and De Paula, 2005). The kinetics of Langmuir adsorption is written as (Atkins and De Paula, 2005)

$$\frac{dX(\text{ad})}{dt} = k_aX(\text{aq})(q_m - X(\text{ad})) - k_dX(\text{ad}), \quad (2.3)$$

where k_a and k_d are the adsorption and desorption rate constants, respectively, and q_m is the maximum adsorption per unit mass. At equilibrium $dX(\text{ad})/dt = 0$, Langmuir equation can be written as (Langmuir, 1918)

$$X(\text{ad}) = \frac{q_m K_L X(\text{aq})}{1 + K_L X(\text{aq})}, \quad (2.4)$$

where $K_L = k_a/k_d$ is the Langmuir adsorption constant. The fitting of experimental data is specific in each system, where, one may fit well to Freundlich model while the other may fit better to Langmuir equation (Gessner and Hasan, 1987).

Adsorption processes have been applied widely in developing technology for the removal of nutrients and contaminants in natural waters (e.g., Ramesh et al., 2007; Vymazal, 2007; Wendling et al.,

2012). However, studies on the extent to which nutrients and contaminants adsorbed on mineral surfaces can alter the physical attributes of SPM are relatively scarce. Adsorbed chemicals could potentially alter the surface charges of SPM and modify the thickness of the electrochemical double layer around clay minerals; this may affect its collision efficiency, i.e., the probability for a collision between two particles to result in an aggregation (e.g., Van Leussen, 1994; Sobeck and Higgins, 2002; Mietta et al., 2009).

2.2.2 Chemicals as nutrients to sustain biological growth

Microorganisms present in abundance and in wide diversity in all natural water bodies, either free living or attached to surfaces such as sediment and other living organisms (e.g., Crump et al., 1999; Groffman and Bohlen, 1999; Wilson et al., 2010; Schluter et al., 2015). Microorganisms can vary greatly across species with differences in size, shape, niche, and metabolism (e.g., Rittmann and McCarty, 2001; Green et al., 2008; Stanca et al., 2013). In this thesis, microorganisms are grouped according to their metabolism (as in Figure 2.2, redrawn after Kelly (1971); Van Kessel (1977); Gottschalk (1986); Rittmann and McCarty (2001); Dworkin et al. (2006); Raven (2009); Chariton et al. (2010)), where a microbial functional group is used here to refer to a group of microorganisms that possess the same metabolic requirements. Each microbial functional group has its own ecological functions and the interactions between different functional groups (e.g., facilitative, competitive, and symbiotic relationships) are non-linear.

Microorganisms from different functional groups utilize nutrients in different ways (Figure 2.2); for example, photolithoautotrophs (e.g., cyanobacteria) use light energy to fix CO_2 into their biomass (e.g., Gottschalk, 1986; Dworkin et al., 2006; Raven, 2009), chemolithoautotrophs (e.g., nitrifiers, sulfide oxidizer, sulfate reducer) use chemical compounds such as NH_4^+ , NO_3^- , and H_2S to produce energy for carbon fixation (e.g., Van Kessel, 1977; Gottschalk, 1986; Raven, 2009), while, heterotrophs (e.g., denitrifiers, fermenters) in general consume organic matter as carbon source (e.g., Gottschalk, 1986; Rittmann and McCarty, 2001). The coexistence of different functional groups within an ecosystem allows nutrient cycling between oxidized and reduced states, maintaining an ecological balance that ultimately sustains growth of organisms at higher trophic levels. For example, phototrophic microorganisms (e.g., phytoplankton, diatoms) are the primary producers in the ecosystem, and provide nutrients to heterotrophs (Duarte and Cebrian, 1996; Brönmark and Hansson, 2005) and oxygen to aerobic microorganisms that may enhance, for example, mineralization of organic matter and nitrification (e.g., Rizzo, 1990; Pind et al., 1997; Wilson, 2006), which result in positive feedback on phototrophs.

The dependency of biological growth on nutrient availability is well documented and there is a general consensus that the growth rate of microorganisms increases with increasing nutrient availability (e.g., C, N, P, K), provided that other parameters influencing growth rate (e.g., O_2 , coenzymes, cofactors) are not limiting (e.g., Wheeler and Kirchman, 1986; Vitousek et al., 1997a; Cloern, 2001). Experiments conducted in Wheeler and Kirchman (1986) supported this statement by demonstrating that bacterial growth rate was the highest in samples containing both glucose and ammonium, while samples that contained only either carbon or nitrogen compound did not show any significant growth. However, the response of microorganisms towards chemicals and the impacts of chemical concentrations on the microbial community are not intuitive. For example, microorganisms have to compete for survival when substrate concentrations are low, and those that can out-compete the others would become the dominating functional groups in the ecosystem. This has been observed in many studies; as for instance, growth of nitrifying bacteria was experimentally observed to be suppressed by phototrophic and heterotrophic microorganisms (e.g., Verhagen and Laanbroek, 1991;

Risgaard-Petersen et al., 2004). In addition, introducing alien chemicals in an ecosystem can off-set its ecological equilibrium by selecting only those functional groups or species that can adapt well to the alien chemicals. For example, studies have shown that glyphosate inhibited the growth of microalgae (e.g., Tsui and Chu, 2003; Magbanua et al., 2013), while, some microbial functional groups can utilize glyphosate as nutrient and transform it into molecules with less toxicity (e.g., Hallas et al., 1988; Zaranyika and Nyandoro, 1993). The response and resilience of an ecosystem towards anthropogenic alteration of the chemical properties of the environment are indeed complex.

2.2.3 Microorganisms as ecosystem engineers

Microorganisms have been found, in many *in-situ* and laboratory studies, to live attached on SPM at a few orders of magnitude higher concentration than those living freely in ambient water (e.g., Paerl, 1975; Shanks and Trent, 1979; Caron et al., 1986; Kiørboe et al., 1990; Droppo and Ongley, 1992; Grossart and Simon, 1993; Turley and Mackie, 1994; Droppo, 2001; Simon et al., 2002). Kiørboe (2001) discussed the possible colonization mechanisms of microorganisms, which can either be active or passive, and can vary with different types of microorganisms. Active colonization involves the ability of microorganisms to detect the aggregates chemically and being attracted and swimming towards the aggregates, whereas, passive colonization involves the random collision of free-living bacteria either by its own movement or by the aid of hydrodynamic effects (Kiørboe, 2001). The attachment of microorganisms on surfaces is a reversible process; microorganisms form colonies to strengthen their grip when conditions are favourable, and they detach from surfaces if conditions are not suitable for their growth (O’Toole et al., 2000).

Nutrients adsorbed on mineral surfaces create a protected, nutrient-rich habitat that makes SPM an optimal site for microbial colonization (Grossart et al., 2006). Microorganisms living attached to SPM were observed to have higher enzymatic activity and reaction rate as compared to free-living microorganisms (e.g., Goulder, 1977; Grossart et al., 2007). Logan and Alldredge (1989) suggested that aggregate-attached microorganisms, which experienced gravitational settling, could uptake nutrients at a rate of approximately 2 times higher as compared to non-attached microorganisms that were in suspension. This agrees with the observation from previous studies that the growth rate of aggregate-attached microorganisms was at least about one order of magnitude higher than that of free-living microorganisms (e.g., Riebesell, 1991; Simon et al., 2002).

The concept of ecosystem engineers was introduced by Jones et al. (1994) to describe the role of organisms in modifying, creating, and maintaining the habitat. Analogously, SPM-attached microorganisms play the role of ecosystem engineers by altering the chemistry and structure of SPM (e.g., Meadows and Tufail, 1986; Meadows et al., 2012). Microbial secretions (e.g., extracellular polymeric substances (EPS) and transparent exopolymer particles (TEP)) have been observed to attach on SPM (e.g., Jackson, 1995; Passow et al., 2001) and modify its properties and internal architecture (e.g., size, surface irregularity, compactness, shear strength, permeability, stability, and sedimentation rate, Meadows and Tufail, 1986; Yallop et al., 2000; Lubarsky et al., 2010; Maggi and Tang, 2015). EPS and TEP are a high-molecular-weight matrix of polymers, consisting of polysaccharides, proteins, nucleic acids, phospholipids and glycoproteins (e.g., Tsuneda et al., 2003; McSwain et al., 2005; Sheng et al., 2010). These metabolic products of microorganisms have a sticky fibrillar nature that provides adhesion, strength and pseudoplasticity to SPM, acting as “biological glue” that promotes SPM flocculation (e.g., Kiørboe et al., 1990; Alldredge et al., 1993; Jackson, 1995; Logan et al., 1995; Droppo, 2001; Passow et al., 2001; Grossart et al., 2006). SPM colonized by microorganisms tends to acquire an extensive web-like network of slime material with larger size commonly associated with lower density and settling velocity as compared to mineral aggregates (e.g., Paerl, 1975; Droppo,

2001; Azetsu-Scott and Passow, 2004; Tan et al., 2012). Kiørboe et al. (1990) also observed that the cohesiveness of SPM in nutrient- and biomass-affected waters increased by approximately 2 orders of magnitude. The role of EPS and TEP in flocculation dynamics of biological aggregates has also been studied in the wastewater treatment sector, with a focus on chemical properties, such as mass transfer, adsorption capacity, and flocculation stability for application in nutrient and contaminant removal (e.g., Pavoni et al., 1972; More et al., 2012; Métivier et al., 2013).

The presence of EPS and TEP in SPM does not only promote the binding of SPM, but also provides large surface area and sites for the adsorption of nutrients and contaminants (e.g., Headley et al., 1998; Späth et al., 1998; Bhaskar and Bhosle, 2006; Sheng et al., 2010). Studies have observed that EPS and TEP had very high binding capacity to both organic and inorganic chemicals, with their adsorption rate obeying the Langmuir and Freundlich equations (e.g., Späth et al., 1998; Zhang et al., 2006). In addition, microbial secretions were also found to facilitate the adhesion of microorganisms to SPM (e.g., Timmerman et al., 1991; Romero et al., 2010; Absalon et al., 2011). These, therefore, further promote chemical and biological processes in SPM and increase process interconnectedness.

SPM-attached microorganisms grow on chemicals adsorbed on mineral surfaces and play an important role in the solubilisation and remineralisation of these chemicals (e.g., Shanks and Trent, 1979; Ongley et al., 1981). They transform molecules from one form to the other, hence, altering the chemical properties of SPM. Opposed to the general consensus that growth was enhanced with adhesion of microorganisms to SPM (e.g., Goulder, 1977; Riebesell, 1991; Simon et al., 2002; Grossart et al., 2007), some studies argue that flocculation might trap microorganisms and nutrients within the mixed matrix of mineral and microbial secretions, hence, limiting the supply of nutrients to the trapped microorganisms and resulting in decreasing growth rate (Brandt et al., 2000). However, microorganisms growing within the matrix are able to exploit their adhesion capability to access nutrients, expand their colonies, and eventually out-compete less adhesive microorganisms (Schluter et al., 2015).

Apart from their roles in promoting flocculation, some studies argue that microorganisms are also responsible for the breakup of aggregates. The grazing of microorganisms on other attached bacteria and matter could potentially weaken the bonds and could eventually cause SPM to break apart (e.g., Alldredge and Silver, 1988; Kiørboe, 2001). The fragile structure of EPS and TEP may also decrease the ability of SPM to withstand turbulence shear. Studies advocate that solubilisation and remineralisation of chemicals as a result of microbial activity could fragment and degrade SPM stability, hence, causing aggregate breakup (e.g., Cho and Azam, 1988; Kiørboe, 2001). Kiørboe (2001) suggested that the solubilisation rate on SPM generally exceeds the remineralisation rate, hence, resulting in the leaking of dissolved chemicals (both organic and inorganic) out of the aggregates. This leaking of nutrients, however, would then paint a trail in the wake during the sinking of SPM and potentially increase active colonization of microorganisms (Kiørboe, 2001). Hence, with all the interconnectedness between all physical, biological, and chemical processes, the outcome on how microorganisms can modulate the dynamics of SPM is very unlikely to be predictable to its entirety.

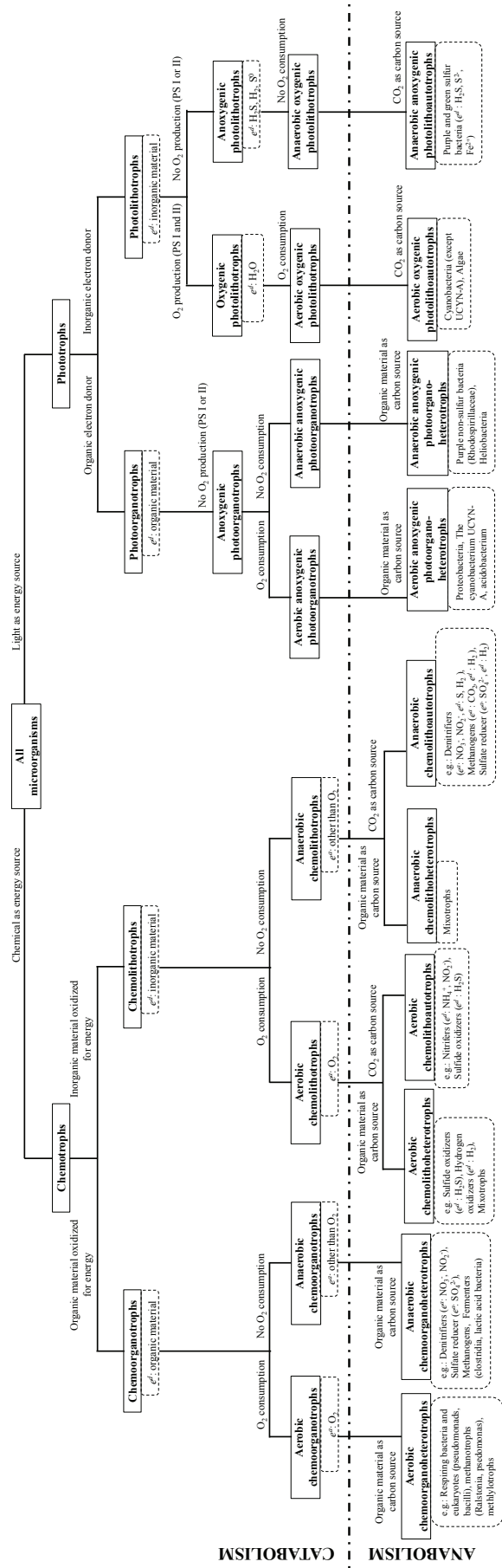


Figure 2.2: Classification of aquatic microorganisms according to metabolic requirements (after Kelly, 1971; Van Kessel, 1977; Gottschalk, 1986; Rittmann and McCarty, 2001; Dworkin et al., 2006; Raven, 2009; Chariton et al., 2010). Note that, e^o and e^d refer to electron acceptor and electron donor, respectively.

2.3 SPM dynamics

In-situ observations of SPM in various aquatic ecosystems have led to a general recognition that SPM does not only undergo transport in the form of individual particles, but very commonly as aggregates, which are widely known as flocs (e.g., Sheldon, 1968; Kranck, 1973; Zabawa, 1978; Gibbs, 1985; Bale and Morris, 1987; Droppo and Ongley, 1992; Lartiges et al., 2001; Stone and Krishnappan, 2003; Bainbridge et al., 2012). This section describes the flocculation dynamics of SPM under control of various biotic and abiotic processes and how the aggregation and breakup processes can affect SPM characteristics in terms of size, geometry, space-filling capacity, and settling velocity.

2.3.1 Flocculation of SPM

Flocculation is a process involving both aggregation and breakup mechanisms, by which individual colloids are clumped into larger aggregates. In general, aggregation of suspended particles is governed by two-stage processes: in the first stage, particles are moved to get in contact with each other; and in the second stage, particles are kept together through “glueing” processes.

Mechanically, suspended particles are brought together to collide with each other by the aid of hydrodynamic processes, such as, differential settling and turbulence shear (e.g., McCave, 1984; Eisma, 1986). Brownian motion plays a less significant role in flocculation dynamics as it influences only the interparticle collision of particles with size smaller than $1\ \mu\text{m}$ (e.g., Krone, 1972; Kranck, 1975; Van Leussen, 1994); hence, its effect is neglected in most studies. The collision frequency, i.e., the probability for two particles to collide, depends also on the shape and size difference between the two colliding particles (e.g., Stolzenbach and Elimelech, 1994; Li and Logan, 1997). Biologically, active colonization of microorganisms (i.e., the process of swimming microorganisms trailing a nutrient adsorbed onto aggregates) may increase the rate of contact between SPM and, hence, promotes flocculation (Kiørboe, 2001).

The “stickiness” of aggregates is often considered as a parameter that determines the flocculation rate of SPM. It is well documented that the diffusive double layer of cohesive minerals and intermolecular forces (e.g., van der Waals attractive and electrostatic repulsive forces) tend to act as “physical glue”. During a collision, the in-contact particles would have to overcome the repulsive force and stay sufficiently close to each other for the attractive force to keep them attached (e.g., Einstein and Krone, 1962; Eisma, 1986). The likelihood of two approaching particles to adhere after a collision is known as collision efficiency, which depends also on the size and surface morphology of the two approaching particles (e.g., Overbeek, 1952; Hogg et al., 1966). In addition, the presence of long-chained polysaccharide (e.g., EPS and TEP) on SPM, as discussed in above section, was observed in various studies to act as “biological glue” and potentially provides adhesion to SPM (e.g., Kiørboe et al., 1990; Droppo, 2001).

If SPM undergoes only an aggregation process, all suspended particles will eventually lump into one massive aggregate. However, this is unlikely to be observed in natural aquatic systems because aggregation of SPM is counterbalanced by breakup processes. Aggregates that are not able to withstand hydrodynamical forcing or collision impact will undergo breakup. The breakup frequency of SPM generally increases with increasing turbulence shear, aggregate size, and SPM concentration (e.g., Spicer and Pratsinis, 1996; Serra and Casamitjana, 1998). Flocculation is a stochastic process where the aggregation and breakup processes are not fully reversible. For example, if two particles with the same size and mass collided to form an aggregate, the breakup of this aggregate is unlikely to result in two daughter particles with exactly the same size and mass; instead, the breakup may result in smaller aggregates of different sizes following a Gaussian distribution (Higashitani and Iimura,

1998).

Flocculation alters the characteristics of SPM, resulting in SPM with different sizes, shapes, and settling velocities. Many studies have investigated the effect of flocculation on SPM characteristics in various environmental conditions such as pH, salinity, turbulence intensity, and temperature (e.g., McCave, 1984; Gibbs, 1985; Chen and Eisma, 1995; Van Leussen, 1994; Stone and Krishnappan, 2003; Maggi, 2005; Kumar et al., 2010; Markussen and Andersen, 2014). Among many, turbulence has been identified as one of the parameters that has the greatest effect on SPM flocculation dynamics (e.g., Van Leussen, 1994; Mikkelsen et al., 2007). Low values of turbulence shear increase SPM collision frequency and promote aggregation, whereas, high turbulence tends to break the bondings between individual particles and tear apart the aggregates. In addition to physical mechanisms, turbulence can increase the adhesion of EPS (Wågberg and Lindström, 1987) and, hence, may increase the “biological stickiness” of SPM. Some studies also stress the role of turbulence in shifting the diversity of phytoplankton communities and its effect in governing the ecological equilibria of a microbial community (e.g., Huisman et al., 2004; Lévy et al., 2014; Grošelj et al., 2015). Apart from turbulence, salinity is also one of the factors that can modify the physical characteristics of SPM; saline water tends to act as electrolyte that suppresses the repulsive force around clay minerals and, hence, it promotes flocculation (Eisma, 1986; Van Leussen, 1994).

2.3.2 Irregularity of SPM

Neither SPM aggregates nor primary particles exist as perfectly smooth and solid spheres in natural waters; rather, they are irregularly-shaped bodies with their shape depending on their composition and flocculation mechanisms. For example, SPM with higher sphericity has been commonly found in estuaries associated with high turbulence shear (Van Leussen, 1994), whereas, SPM with web-like structure has been commonly observed in aquatic ecosystems rich in organic matter (Paerl, 1975). Several parameter studies have addressed the significance of SPM shape in affecting its dynamics (e.g., Clift et al., 2005; Dietrich, 1982; Vainshtein et al., 2004) by expressing particle shape using complex empirical equations such as Corey shape factor (Corey, 1963), dynamic shape factor (Briggs et al., 1962), and Janke shape factor (Janke, 1966). These parametric quantities, however, have limited effectiveness in describing particle shape and contact dynamics in an explicit way.

In numerical modelling, SPM aggregates are often assumed as spherical and non-porous particles as in the Stokes regime (Stokes, 1851) to provide analytical simplicity in describing particle-particle interactions (Wacholder and Sather, 1974), settling (e.g., Rubey, 1933; Clift et al., 2005; Krishnappan, 1990; Han and Lawler, 1991), collision rate (e.g., Abrahamson, 1975; Valioulis and List, 1984), and aggregation and breakup probability (e.g., Saffman and Turner, 1956; Han and Lawler, 1991). SPM transport models were improved when porous spherical particles were adopted (e.g., Kusters et al., 1997; Wu and Lee, 2001). Among many, Stolzenbach (1993) observed very distinct collision kinetics between porous and non-porous particles, and was able to achieve a better estimation of collision and aggregation probability using porous spheres. SPM models were further improved by fractal scaling laws, that is, higher-order aggregates were assumed to be made by (statistically) self-similar assemblies of lower-order aggregates (e.g., Krone, 1962; Meakin, 1991; Kranenburg, 1994; Maggi, 2007).

SPM as a fractal architecture can be characterized in many aspects by means of the generalized fractal dimensionality d_q (Hentschel and Procaccia, 1983; Stanley and Meakin, 1988; Chhabra and Jensen, 1989), which includes the capacity ($q = 0$), correlation ($q = 1$) and information ($q = 2$) dimensions as well as an infinite number of other fractal dimensions (for other moments q). Among these, the capacity dimension d_0 is one of the most important because it describes the space-filling

capability and relates closely to the mass, density and porosity (e.g., Maggi, 2005; Khelifa and Hill, 2006; Maggi, 2007). By assuming that the fractal dimension is invariant in a real system, d_0 was scaled with many geometrical and physical properties of SPM (Kranenburg, 1994). For example, the SPM mass m_A was scaled as a power of its dimensionless size ℓ , such that, $m_A \propto \ell^{d_0}$, with the exponent as the capacity dimension d_0 (Logan and Kilps, 1995). A better fractal description was then developed by expressing d_0 as a scale-dependent quantity as $d_0 = \delta \ell^\gamma$, where δ is the d_0 of primary particle and γ is the characteristic rate of change in d_0 over ℓ (e.g., Maggi, 2005; Khelifa and Hill, 2006; Maggi, 2007). Since then, fractal scaling laws have been successfully used to describe settling velocity (e.g., Vahedi and Gorczyca, 2011; Maggi, 2013), flocculation rate (e.g., Li and Logan, 1997; Serra and Casamitjana, 1998; Serra and Logan, 1999; Kim and Stolzenbach, 2004) and sediment fluxes (e.g., Kranenburg, 1994; Stone and Krishnappan, 2003).

The direct measurement of d_0 in either *in-situ* or laboratory-based experiments remains challenging, even though it may be possible with techniques such as electron microscope tomography (e.g., Skoglund and Daneshmandi, 1986; Midgley and Weyland, 2003), X-ray computed tomography (Kalender, 2006), and magnetic resonance interferometry (e.g., Cline et al., 1987; Clarke et al., 1995). However, these techniques are either capital intensive or hamper measurements when they require the transferring of samples, operation that can affect SPM structures. The measurements of d_0 without physical perturbation of samples have been made possible in experiments with methods that relate the three-dimensional (3D) capacity dimension of SPM to its two-dimensional (2D) fractal properties assessed from planar images (projections).

The capacity dimension $d_0(S_2)$ of a 2D image S_2 from a 3D SPM S_3 with capacity dimension $d_0(S_3)$ is widely accepted to follow the expression (Vicsek, 1989)

$$d_0(S_2) = \min\{2, d_0(S_3)\}. \quad (2.5)$$

Inverting Eq. (2.5) allows to calculate $d_0(S_3) = d_0(S_2)$ when $d_0(S_2) < 2$, while $d_0(S_3)$ is undetermined otherwise. Note that Eq. (2.5) is an approximation; Hunt and Kaloshin (1997) has given evidence that a projection only preserves information of the dimensionality d_q for the moments $1 < q \leq 2$, thus excluding the capacity dimension d_0 at $q = 0$. In addition, Eq. (2.5) is valid for indefinitely extended fractal sets, while it fails to describe the relation between $d_0(S_2)$ and $d_0(S_3)$ for compact sets (e.g., Maggi and Winterwerp, 2004; Sánchez et al., 2005; Maggi, 2008). As an alternative to Eq. (2.5), Maggi and Winterwerp (2004) proposed a mathematical expression that estimates $d_0(S_3)$ from the perimeter-based fractal dimension $d_P(S_2)$, which measures the segmentation of the external boundary of S_2 . The advantage of using $d_P(S_2)$ is that it is not included in d_q and, therefore, is not subject to any of the above limitations. Application of this equation to numerically-generated diffusion-limited (DLA) and cluster-cluster (CCA) aggregates (Maggi, 2008), interstellar medium (Sánchez et al., 2005), paramagnetic particles (Domínguez-García and Rubio, 2010) and lime softening flocs (Vahedi and Gorczyca, 2011) showed a significant improvement in retrieving $d_0(S_3)$ as compared to Eq. (2.5), but it was found to lead to 3 to 10% underestimation of the actual $d_0(S_3)$ for small aggregates with high fractal dimension (e.g., Maggi, 2008; Vahedi and Gorczyca, 2011).

2.3.3 Settling of SPM

The settling of SPM is important in both engineering and environmental contexts because SPM deposition can alter the geomorphology of river banks, coastal, and harbours (e.g., Toffolon, 2002; Siviglia and Crosato, 2016), control the fluxes of organic matter sinking into deep oceans (e.g., Martin et al., 1987; Christian et al., 1997), and affect water quality (McCready et al., 2006). The settling velocity of SPM is governed by many factors, including the properties of ambient fluids (e.g.,

fluid density and viscosity Rubey, 1933), the environmental conditions (e.g., waves, turbulence, temperature McCave, 1984; Elfrink and Baldock, 2002), and the physical characteristics of SPM itself (e.g., size, composition, shape, porosity, density Maggi, 2013, 2015b).

There is a general consensus that the settling velocity of SPM in low turbulence or standing water commonly increases with increasing SPM size (e.g., Dietrich, 1982; Lick et al., 1993; Hill et al., 1998; Milligan and Hill, 1998; Curran et al., 2007). However, some studies observed the settling velocity to increase to a maximum value beyond which an increase in SPM size led to a decrease in settling velocity (e.g., Shanks and Trent, 1980; Asper, 1987; Wu and Lee, 2001). This may be explained by the fact that the capacity dimension of SPM is negatively correlated to its size, i.e., an increasing SPM size is associated with a decrease in capacity dimension; hence, resulting in decreasing settling velocity (e.g., Maggi, 2005; Khelifa and Hill, 2006; Maggi, 2007).

All processes governing SPM settling velocity are interconnected, making it a complex system to predict. For example, the effect of organic matter content on SPM settling velocity is still an ongoing debate. Studies observed that the presence of organic matter is commonly associated with an increase in SPM size and mass (Alldredge and Silver, 1988), therefore, suggesting an increase in its settling velocity. However, SPM affected by organic matter generally has higher irregularity in shape and lower capacity dimension as compared to mineral aggregates; in addition, organic matter generally has low density. In fact, some recent studies observed invariant settling velocity with increasing organic matter content; this is because the increase in SPM mass is counterbalanced by the decrease in its density and capacity dimension (e.g., Hill et al., 2013; Maggi and Tang, 2015).

2.4 Bridging the gap

Historically, in the eye of sedimentologists, the fraction of SPM that plays the most important role in flocculation and sediment transport has been the mineral sediment itself. With a focus on mineral-water interactions, a solid physical framework of SPM flocculation dynamics has been well established and contributes substantially to the modelling and prediction of sediment transport.

SPM, however, is a heterogeneous mixture of different minerals (e.g., kaolinite, montmorillonite), chemicals (e.g., NH_4^+ , NO_3^-), and biological matter (e.g., various microbial colonies, microbial metabolites); all these components interact with one another and also, with the surroundings (e.g., fluid motion, water temperature, pH) to form a feedback loop (Figure 2.3). For example, chemicals, especially ions and polar molecules, can alter SPM collision efficiency by modifying the thickness of diffusive double layer of clay mineral and changing the balance between van der Waals attractive and electrostatic repulsive forces. In addition, chemicals are nutrients that sustain growth of microorganisms living either attached on SPM or freely in ambient water. Microbial growth produces metabolites that increase the stickiness of SPM, increase SPM aggregation, and further promote the binding of chemicals. All biotic and abiotic processes in natural aquatic ecosystems affect SPM dynamics simultaneously with high interconnectedness.

Anthropogenic forcing exerted on aquatic ecosystems may introduce another layer of complexity to SPM dynamics that is already rather complex by itself. For example, increased chemical concentrations as a result of anthropogenic leaching of nutrients and contaminants can modify not only the electro-chemical characteristics of SPM, but it can also offset the ecological equilibrium of microbial communities living on SPM. Properties of EPS and TEP secreted by different microbial communities may be different and this may result in a different modification to SPM aggregation dynamics. The increase of sediment loads may potentially increase the collision frequency, and it also increases the surface areas for chemical adsorption and microbial colonization. With non-linear

connections between all processes, it is not straightforward to determine the dominating mechanisms and to predict the outcome of SPM dynamics.

Studies of these processes were, however, commonly conducted independently in a “labour-splitting” system. For example, sedimentologists and physicists focused on mineral and hydrodynamic interactions; chemists mainly focused on adsorption characteristics of minerals; chemical engineers studied the application of biological flocculation in the removal of contaminants; whereas, microbiologists and ecologists paid greater attention to exploring anthropogenic impacts on microbial growth and diversity. The combined effects of interactions between each individual process are expected to alter SPM dynamics as a whole. Hence, the prediction of natural SPM fluxes would not be representative of nature if the role played by any one of either mineral, chemical or biological components were not considered, leaving a gap that requires future investigations.

This thesis acknowledges the need to integrate the interactions between minerals, chemicals, and microorganisms into one system and puts forward a different perspective of SPM flocculation dynamics.

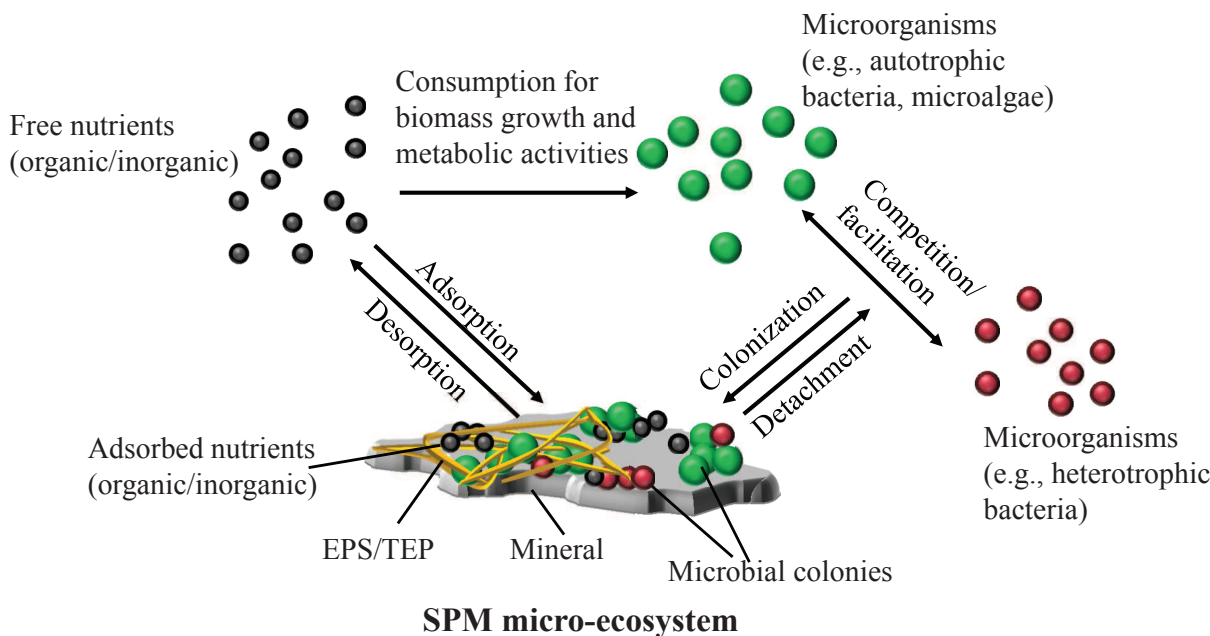


Figure 2.3: Biotic and abiotic interactions in SPM micro-ecosystem. Note that, EPS and TEP refer to extracellular polymeric substances and transparent exopolymer particles, respectively.

Chapter 3

Experimental facility and procedures

Contents of this chapter were published in Tang and Maggi (2015a)¹, Tang and Maggi (2015b)², and Tang and Maggi (2016a)³ during PhD candidature of the author.

3.1 Introduction

This chapter presents a small-scale settling column that is able to control the most relevant physical, chemical and biological processes governing SPM dynamics in natural aqueous ecosystem. The settling column was designed to be equipped with a mechanical system that creates an isotropic and homogenous turbulence field at any desirable shear rate; and a water quality measuring system that tracks water quality parameters in the settling column, which can then be used to infer chemical and biological interactions. The characteristics and dynamics of SPM can be analysed based on imaging data acquired using an automated μ PIV system. This facility also enables experiments to be carried out automatically at any arbitrary scheduling. This facility was designed and manufactured at the School of Civil Engineering, The University of Sydney, and is one of the major contributions of this doctoral thesis. The protocols for SPM sample preparation and testing in the settling column, together with the algorithms used to process SPM images, are also presented in this chapter.

3.2 Design criteria

This experimental facility was designed to fulfil the following criteria:

1. replicate the hydrodynamic (turbulence), sediment and nutrient characteristics found in natural water bodies.
2. allow for the monitoring of chemical and biological processes in the control volume.
3. capture and fully preserve the detailed information of settling SPM (e.g., size, shape, morphology, fractal characteristics, settling motion, etc.).

¹Tang F.H.M. and Maggi F. (2015). Anthropogenic nutrient leaching alters the size distribution of suspended particle matter. In Proceedings of the 36th IAHR World Congress, The Hague, The Netherlands.

²Tang F.H.M. and Maggi F. (2015). A laboratory facility for flocculation related experiments. Report No. R952, The University of Sydney.

³Tang F.H.M., and Maggi F. (2016). A mesocosm experiment of suspended particulate matter dynamics in nutrient- and biomass-affected waters, *Water Research*, 89, 76-86.

- allow for instantaneous, simultaneous and automatic monitoring and control of all parameters and measurements, including turbulence shear rate, sediment concentration, chemical concentration, SPM image acquisition and water quality measuring.

To satisfy the design criteria, this experimental facility (Figure 3.1) was designed to consist of five major components: the settling column, the turbulence generating system, the water quality measuring system, the μ PIV system, and the micro-controlling system. The design of each of the above components is described in details in following sections.

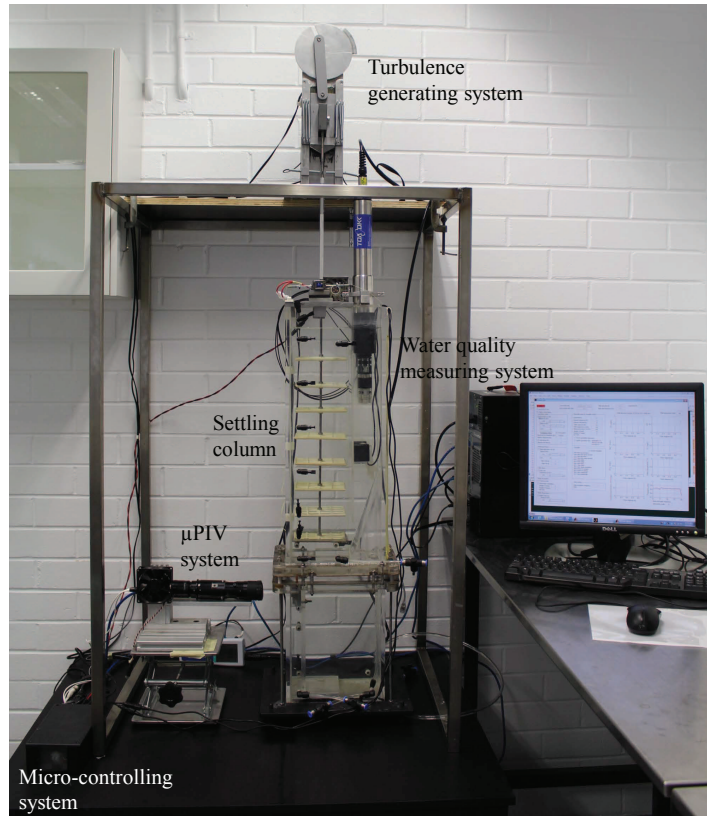


Figure 3.1: Photograph of the experimental facility.

3.3 Settling column

The settling column (Figure 3.2a), made of Perspex, consists of three main components: a flocculation section with a total capacity of approximately 16 L (210 mm \times 140 mm \times 600 mm, Figure 3.2b), which is the control volume where SPM was tested; a measuring section (210 mm \times 140 mm \times 270 mm, Figure 3.2d); and a diaphragm (Figure 3.2c) that separates the flocculation and the measuring sections. Both the flocculation and measuring sections are filled with water and the three components are fastened together with screw connections, while gaskets are used in between the connections to provide water proof seal.

The flocculation section (Figure 3.2b) is partitioned into a compartment equipped with a turbulence generating system (140 mm \times 140 mm cross-section), and a compartment that hosts a water quality meter inserted vertically from the top of the flocculation section (70 mm \times 140 mm cross-section). A triangular slope was placed at the bottom of the water quality meter compartment to

drive the deposited SPM into the compartment with turbulent mixing. Several holes equipped with elbow valves were made along the flocculation section to control overflow, allow sampling of SPM at various depths, drain and clean the column and provide flexibility if insertion of other equipments is needed in future.

SPM in the flocculation section is allowed to flow into the measuring section through a 5 mm sediment sampling hole located on the diaphragm during time at which image measurements are taken. Five sediment sampling holes were made on the diaphragm to provide flexibility in choosing the position for SPM image acquisition. However, only one sampling hole is used at once and those not in use are temporarily sealed. The opening and closing of the sampling hole are controlled using a slider connected to a two shaft 3 V DC motor through two fishing lines that run inside the flocculation section up to the top. To ensure the movement of the slider is not hindered by deposited SPM, a cleaning system, consisting of two immersible water pumps with pump outlets directed onto the slider, is used to remove deposited SPM from the slider.

In the measuring section (Figure 3.2d), a lateral access (with a choice of 3 different positions) was implemented to insert optical fibers used in conjunction with the μ PIV system (described in Chapter 3.6). These optical fibers are fastened to a holder (as in Figure 3.6) inside the measuring section. Attached to the holder, a SPM driver is used to guide the SPM flow coming from the diaphragm by gravitational settling toward the camera field of view along a two-wall separation chamber of 5 mm width. A pipe was placed at a corner inside the measuring section to remove bubbles trapped below the surface of the diaphragm. Several additional holes were made for draining and cleaning of the column and for future need.

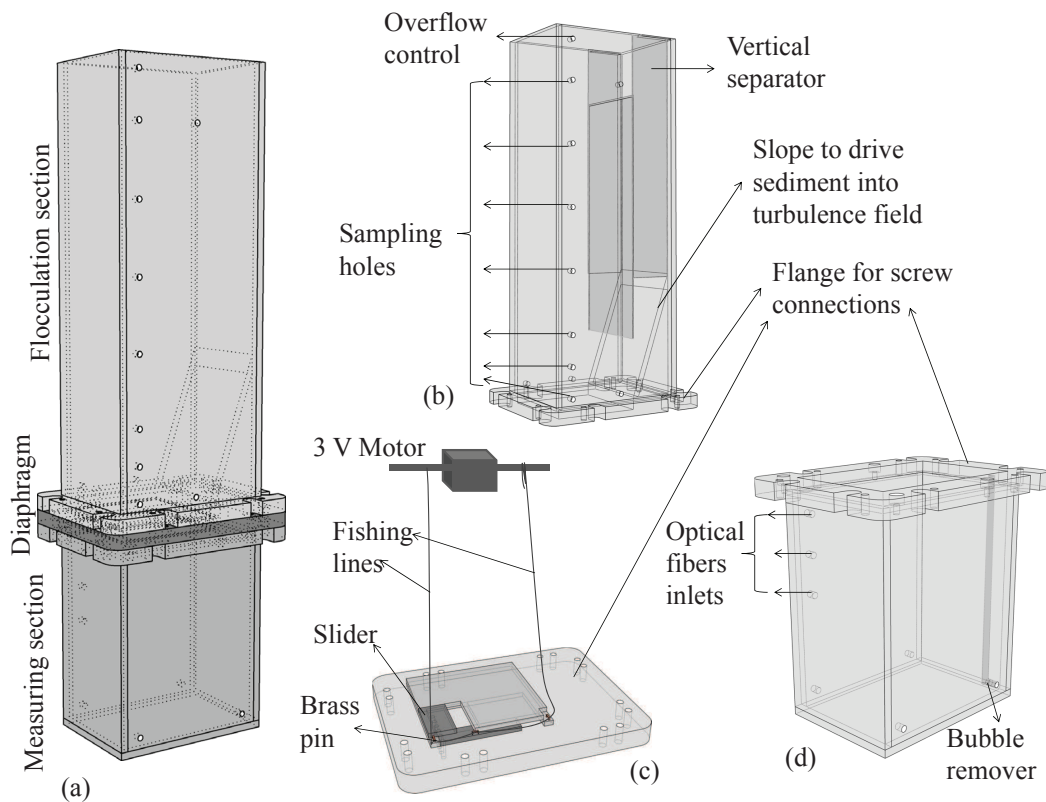


Figure 3.2: Schematic drawings of (a) the settling column, (b) the flocculation section, (c) the diaphragm, and (d) the measuring section.

3.4 Turbulence generating system

An isotropic (*i.e.*, all averages relating to the properties of turbulence do not change under rotations or reflections of the coordinate system, Tennekes and Lumley, 1972) and homogenous (*i.e.*, the mean velocity of the turbulence field is uniform in space, Tennekes and Lumley, 1972) turbulence is generated in the flocculation section by using an oscillating grid, which is a technique widely used in sediment related experiments (e.g., Wolanski et al., 1992; Van Leussen, 1994; Liem et al., 1999; Gratiot et al., 2005; Maggi, 2005). The turbulence shear rate G induced by the oscillating grid can be determined from the geometry, stroke, and frequency of the grid using analytical and empirical equations proposed in previous literature (e.g., Hopfinger and Toly, 1976; Fernando and De Silva, 1993; Bache and Rasool, 1996; Matsunaga et al., 1999).

3.4.1 Grid geometry

The oscillating grid consists of eight horizontal square elements vertically and evenly spaced from each other ($H = 60$ mm spacing), and connected through their centers with a stainless steel rod. Each grid element (120 mm \times 120 mm, Figure 3.3a), made of plastic, has 16 square meshes with mesh size $M = 28.5$ mm and is made of diamond-shaped bars with bar diameter $d = 6$ mm. The grid element has a solidity (*i.e.*, the ratio of the area of diamond-shaped bars to the total grid area) of approximately 43.75 %.

The grid element was made by plastic because plastic is very light in weight, non-reactive to chemicals, non-adhesive and has high resistance to oxidation and corrosion. The grid was designed to a size that gave 10 mm of clearance between the edge of the grid and the inner wall of the flocculation section. This is to provide sufficient space to introduce the slider mechanism on the diaphragm and yet to be small enough to minimise wall effect. The use of diamond-shaped bars enhances the turbulence field as a few studies observed that diamond-shaped prism created the strongest eddies and the highest vorticity compared to circular and square prisms (e.g., Tonui and Sumner, 2011; Ghozlani et al., 2012).

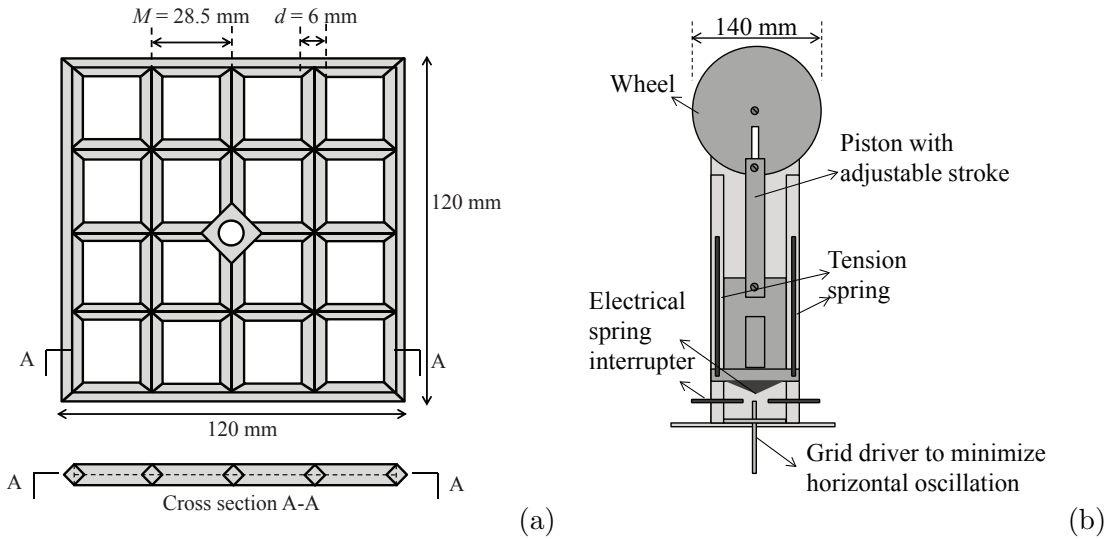


Figure 3.3: (a) the plan view and the cross-sectional view of a grid element, and (b) schematic drawing of the grid oscillation system.

3.4.2 Oscillation control

The grid is driven vertically by a 12 V DC motor connected to a 140 mm diameter wheel and a piston rod with adjustable stroke S (Figure 3.3b) that transformed rotational motion of the motor into vertical motion perpendicular to the grid element plane. Note that, S is defined here as the distance from the top to the bottom dead center of the piston, indicating the furthest possible travel of the grid in one direction.

The downward motion of the wheel is facilitated as a result of gravitational effect and, thus, the wheel moves faster downward than upward. This irregularity of the wheel motion is reduced with the aid of tension springs attached to the piston. A driver (a hollow rigid metal tube) is used to guide the stainless steel bar connecting the grid elements to minimise any undesired rotational and horizontal oscillations.

The frequency of the grid f_g (*i.e.*, the number of oscillations per second) is measured using an electrical spring interrupter, which consists of two springs and a metal plate attached to the bottom end of the piston (Figure 3.3b). The two springs are connected to a 5 V electricity supply and a signal is detected when the metal plate touches the springs. The signal is then sent to the micro-controlling system to allow instantaneous, real-time monitoring, and adjustment of the frequency.

3.4.3 Determination of turbulence shear rate

The root mean square velocity u_{rms} of turbulence induced by an oscillating grid with one grid element can be determined as (Hopfinger and Toly, 1976)

$$u_{rms} = c_g S^{\frac{3}{2}} M^{\frac{1}{2}} f_g Z_g^{-1} \left(\frac{S f_g M}{\nu} \right)^{(m_g-1)}, \quad (3.1)$$

where Z_g is the vertical distance away from the grid, ν is the water kinetic viscosity, while c_g and m_g are dimensionless coefficients depending on the shape of the grid bars, respectively. Hopfinger and Toly (1976) proposed $c_g = 0.25$ and $m_g = 1.0$ to be used for grids with square bars. Because the grid bars used here were diamond-shaped, the coefficients $c_g = 3.0$ and $m_g = 0.67$ were then determined based on experiments in Maggi (2005), where a grid made of diamond-shaped bars with $d = 8$ mm and square meshes with $M = 75$ mm was used.

Using Eq. (3.1), the turbulence energy dissipation rate ε was determined as (*e.g.*, Batchelor, 1953; Tennekes and Lumley, 1972)

$$\varepsilon = \frac{b_g u_{rms}^3}{l}, \quad (3.2)$$

where $b_g = 1$ (Tennekes and Lumley, 1972) and $l = \beta_g Z_g$ is the integral time scale with $\beta_g = 0.1$ (Noh and Fernando, 1993). Because the oscillating grid used here consists of multiple grid elements, the effective energy dissipation rate ε_{eff} at a certain location was determined as the sum of ε contributed by each grid element at that location (Villermaux et al., 1995). Since ε decays rapidly with increasing Z_g (*i.e.*, $\varepsilon \propto Z_g^{-4}$), ε_{eff} at a point between two grid elements was therefore considered as the sum of ε_1 and ε_2 contributed only by the two adjacent grid elements. Given that all grid elements have same geometry and equal spacing, we obtained

$$\varepsilon_{eff} = \varepsilon_1 + \varepsilon_2 = \frac{b_g}{\beta_g Z_g} \left(c_g^3 S^{\frac{9}{2}} M^{\frac{3}{2}} f_g^3 \left(\frac{S f_g M}{\nu} \right)^{(3m_g-3)} [Z_g^{-3} + (H - Z_g)^{-3}] \right), \quad (3.3)$$

where H is the spacing between the two grid elements. The turbulence shear rate G can then be expressed as $G = \sqrt{\varepsilon_{eff}/\nu}$, with ε_{eff} as in Eq. (3.3). With the grid geometry described above (i.e., $S = 60$ mm, $M = 28.5$ mm and $H = 60$ mm) and the grid frequency f_g ranging between 0.4 Hz and 1.2 Hz, the turbulence shear rate G at $Z_g = S/2$ ranged from 32 s^{-1} to 96 s^{-1} .

3.4.4 Discussion

The determination of G based on the Hopfinger and Toly (1976) approach is strongly dependent on the assumption that the turbulence induced by an oscillating grid is fully isotropic and homogenous. The energy dissipation rate ε was calculated based on the assumption that the overall root mean square of the fluctuating velocity is equal to the horizontal root mean square fluctuating velocity. In addition, by using the proposed linear relationship of the integral length scale l with position Z_g , the turbulence velocity derived in Eq. (3.1) is proportional to Z_g^{-1} under the assumption that the eddy viscosity is constant in the vertical direction.

The turbulence induced by the oscillating grid used in this chapter, however, may not be ideally isotropic and homogenous. Previous studies observed that grids with solidity $> 40\%$ tended to create secondary flows, which affected the isotropicity and homogeneity of the induced turbulence (e.g., Corrsin, 1963; Hopfinger and Toly, 1976; Fernando and De Silva, 1993). Although the solidity of the grid used here is just slightly greater than 40%, the possibility of having secondary flows could not be eliminated. Furthermore, Fernando and De Silva (1993) observed the existence of large-scale secondary flow and much slower decay of turbulence velocity when adopting the grid with end condition that has parallel bars adjacent to the column wall (i.e., similar to the end condition of the grid used in this chapter). They suggested that secondary circulation could be minimised by cutting away the grid bars at the edges so as to create reflection symmetry with respect to the column wall (Fernando and De Silva, 1993). The use of diamond-shaped bars may also promote secondary circulation. The axial oscillation tests for circular, square, and diamond-shaped prisms conducted in Tonui and Sumner (2011) suggested that the triangular-shaped afterbody of the diamond-shaped prism aided in the formation of large concentrations of secondary vortices. Moreover, the isotropicity and homogeneity of turbulence may also be affected by wall effects, even though the clearance between the grid and the column wall was kept to a minimum. Due to the existence of secondary flow and wall effects, the assumption of constant eddy viscosity, and that $u = w$, may not hold fully. However, the secondary flow and wall effects in this facility are mainly concentrated at the near wall and, therefore, the assumption of being isotropic and homogenous will still hold for the turbulence field in the water volume inside the grid.

3.5 Water quality measuring system

A multi-parameter water quality meter (TOA-DKK, WQC-24), equipped with sensors to measure up to 12 parameters (Table 3.1), is used to measure the physical and chemical properties of the suspension tested in the flocculation section. The water quality meter has a height of 510 mm and a width of 110 mm, and is connected to a data logger with LCD digital display. The water quality meter has an internal memory capacity that can record a maximum of 3360 data and the data can be continuously and automatically measured and recorded even with the water quality meter disconnected from the data logger. For indefinite recording of data, the measured data can be communicated and saved instantaneously to a PC through a RS-232C cable connected to the data logger. The water quality meter is fully waterproof and has a submerging depth limit of 5 m (depending on the type of sensor mounted to the water quality meter). Prior to experiments, each of

the parameters listed in Table 3.1 is calibrated according to the procedures suggested in the manual provided by the manufacturer.

Standard module parameters	Indication range	Precision	Measuring method
pH	0.00 - 14.00	0.01	Glass electrode method
Dissolved oxygen (DO)	0.00 - 20.00 mg/L	0.01 mg/L	Galvanization diaphragm electrode method
Electric conductivity (EC)	0.00 - 10.00 S/m	0.1 mS/m	AC 4 electrodes method
Salinity	0.0 - 40.0 %	0.1 %	Conversion from EC value
Total dissolved solid (TDS)	0.0 - 100.0 g/L	0.1 g/L	Converted from EC value
Sea water specific gravity	0.0 - 50.0 σ_t	0.1 σ_t	Converted from EC value
Water temperature	-5.0 - 55.0 °C	0.1 °C	Platinum thin film resistive element
Turbidity	0.0 - 800.0 NTU	0.1 NTU	90° scattered light measurement method
Depth	0.0 - 100.0 m	0.1 m	Diaphragm pressure sensor type
Ion module parameters	Measuring range	Precision	Measuring method
Chloride ion Cl ⁻	1 - 35000 mg/L	0.01 mg/L	Selective ion membrane
Ammonium ion NH ₄ ⁺	0.09 - 1800 mg/L	0.01 mg/L	Selective ion membrane
Nitrate ion NO ₃ ⁻	0.62 - 62000 mg/L	0.01 mg/L	Selective ion membrane

Table 3.1: Table of parameters measured by the water quality meter (TOA-DKK, WQC-24) equipped with the Standard and Ion modules. Table adapted from “Hand-held Water Quality Meter WQC-24 Instruction Manual” provided by the manufacturer.

3.6 μ PIV system

The measurement of SPM geometrical characteristics is conducted by using a micro particle image velocimetry (μ PIV) system that has long been used in most areas of experimental fluid mechanics as a promising tool to detect single particle in space as well as in time, to track the flow motion and to determine the particle distribution within regions ranging from several millimeters down to a few micrometers (e.g., Grant, 1997; Santiago et al., 1998; Chakraborti et al., 2000; Maggi, 2005). The μ PIV system, which consists of an imaging system and an illumination system, enables the tracking of characteristics and motion of settling SPM in an untouched environment.

3.6.1 Imaging system

A digital charge-coupled device (CCD) camera (Prosilica GC2450) and a high magnification lens (Navitar 12X Body Tube) are used to acquire images of settling SPM. The CCD camera and the magnification lens are mounted on a height-adjustable camera stand equipped with a cooling system to prevent over heating of the camera (Figure 3.4).

The CCD camera has a size of 2448×2050 pixel, 8-bit grayscale depth with a frame rate of 15 Hz at full size. The magnification lens is equipped with a continuous zoom that enables variation in the field of view (FOV) over a wide range of magnification steps, ranging from 0.58 to 7.0. At the lowest magnification step (*i.e.*, 0.58), a pixel has a size of approximately $4.435 \mu\text{m}^2$, whereas, at the highest magnification step (*i.e.*, 7.0), the size of a pixel is approximately $0.375 \mu\text{m}^2$. The depth of field (DOF) of the lens was also qualitatively determined to be approximately ± 5 mm from the focal distance.

The CCD camera is connected to a host computer and SPM images are acquired using *Image Acquisition Toolbox* in Matlab. This toolbox allows the adjustment of camera properties (*e.g.*, gain and shutter speed) and enables automatic image acquisition at specified time.

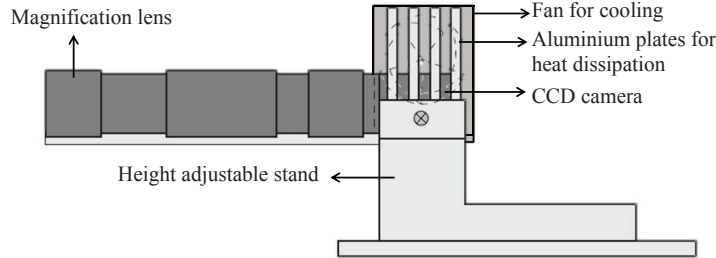


Figure 3.4: Schematic drawing of the CCD camera and the high magnification lens mounted on the height-adjustable camera stand.

3.6.2 Illumination system

A Cree LED (cool white colour) of 3.7 W, 400 lumens is used to illuminate the settling SPM. Light from the Cree LED is transported and shined directly onto the settling SPM through optical fibers that are inserted into the measuring section. The use of optical fibers enables the light to be shined directly onto the region where the measurements are to be taken without the need for the light to travel through the Perspex wall of the measuring section, hence, minimising the attenuation of the light beam.

An optical box (Figure 3.5), made of aluminium plates, was designed to hold the Cree LED and optical fibers in place. As the Cree LED radiates a great amount of heat, aluminium plates and a fan are used to dissipate the heat and control the temperature. Four optical fibers are inserted into an aluminium tube and are placed as close as possible to the bulb of the Cree LED so as to capture the maximum light intensity.

The other ends of the optical fibers are inserted into the measuring section and are fixed onto a holder (Figure 3.6a) attached to a positioning stand (Figure 3.6b). The optical fibers are tightly fastened between two plastic plates with one of the plates having round grooves cut at different angles to concentrate the light beams from the optical fibers into a point where the region of measurement is. A mask of less than 1 mm opening is attached to the plastic plates to create a thin vertical light sheet. The SPM driver is attached to the optical fibers holder approximately 5 mm from the mask to channel the flow of settling SPM.

The optical fibers holder is held in the measuring section by attaching it onto a positioning stand (Figure 3.6b) made of a 90 mm \times 280 mm vertical plate and a 140 mm \times 110 mm base plate. The optical fibers holder is positioned in such a way that the center of the 5 mm gap between the mask and the SPM driver coincides with the center of the sampling hole on the diaphragm. This is to allow SPM to flow within the plane of measurement. The vertical position of the optical fibers holder is designed to be adjustable.

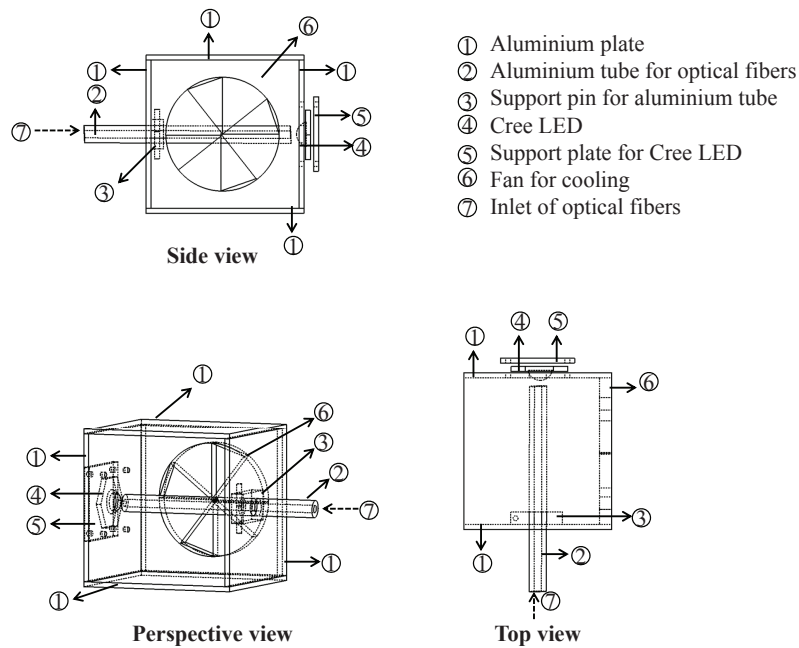


Figure 3.5: Schematic drawing of the optical box for holding Cree LED and optical fibers.

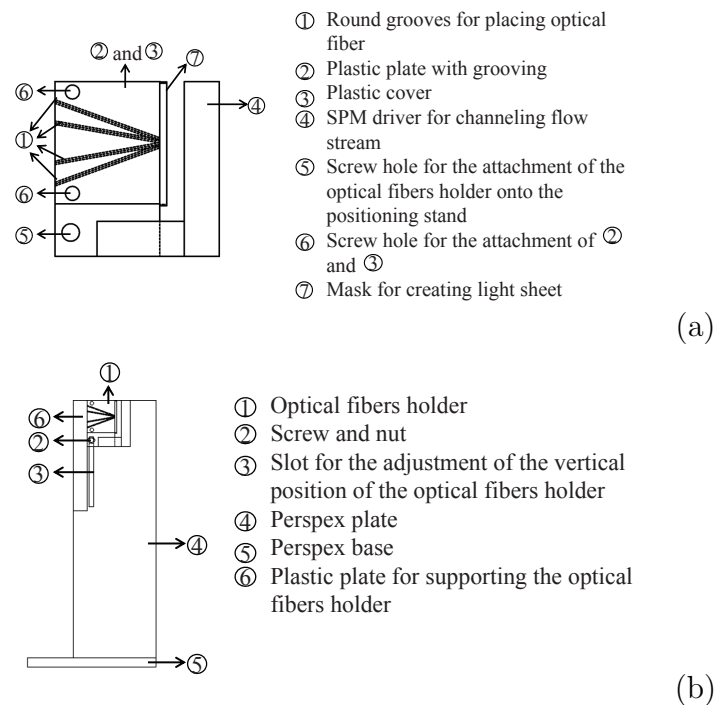


Figure 3.6: Schematic drawings of (a) the optical fibers holder, and (b) the positioning stand for holding the optical fibers holder.

3.7 Micro-controlling system

A micro-controlling system consisting of an *Arduino Uno*, two motor shields and a screw shield are connected to a PC and are used to automate each component of the facility, including the regulation of the oscillating grid frequency, the control over the illumination system, the slider, the water pumps, and the image acquisition. All operations can be scheduled and carried out automatically under the supervision of a script coded in the Matlab2011b environment (Figure 3.7).

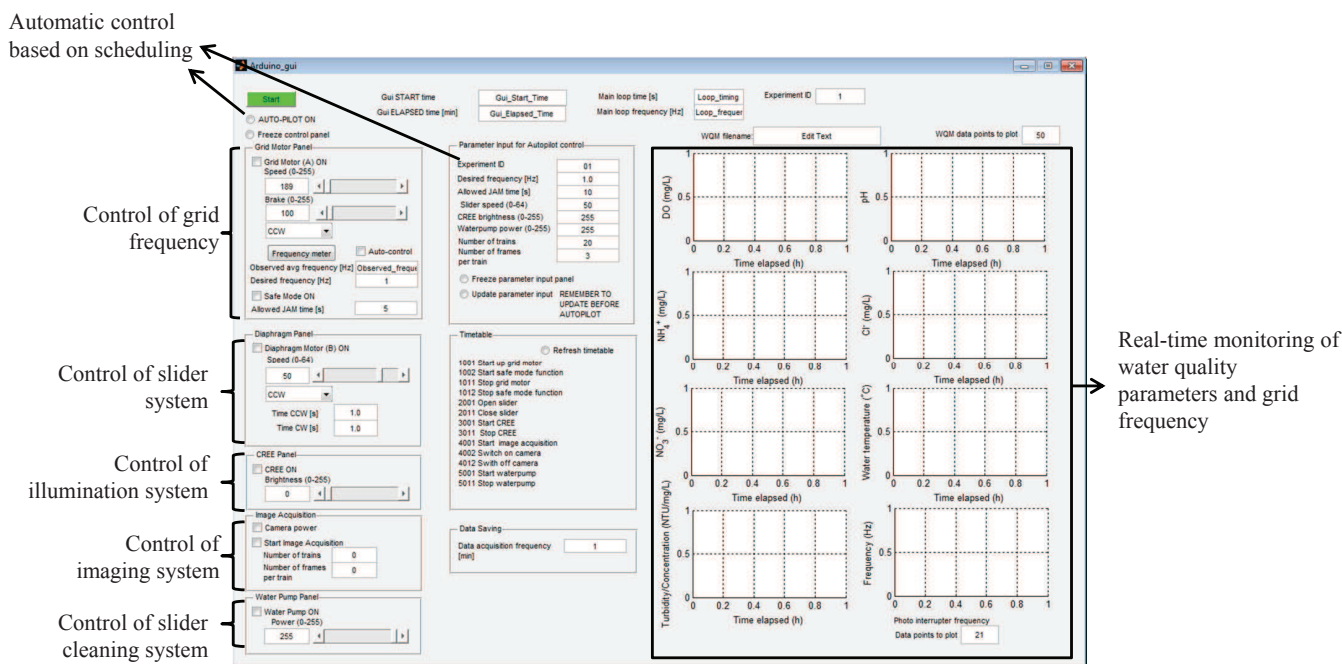


Figure 3.7: The interface built in Matlab2011b environment used for monitoring and controlling all components of the facility.

3.8 Sample preparation

All SPM samples tested were prepared using Q38 kaolinite, with particle size ranging between 0.6 μm to 38 μm . Experiments were carried out for three different SPM types: nutrient- and biomass-free (NFBF, used as the control); nutrient-affected and biomass-free (NABF); and nutrient- and biomass-affected (NABA).

NFBF was prepared using only kaolinite, while different concentrations of ammonium nitrate NH_4NO_3 were used in NABF and NABA. To set biomass-affected condition, NABA was inoculated with microbial strains present in natural sediment (dry mass = 1.07 g) collected from the shore at the Blackwattle Bay, Sydney, NSW, Australia, in a shallow water area on January the 1st, 2015 (summer). The sediment sample was sieved to remove debris and large mineral particles before adding to NABA samples. Strains were not characterized in this study, but after some incubation trials and nutrient concentration measurements, it was found that heterotrophic metabolism was favoured; to sustain heterotrophic growth, glucose was added in NABA as the carbon source at C:N ratio of 5:1 (e.g., Goldman et al., 1987; Tezuka, 1990).

All samples were prepared in a 500 mL beaker using deionized water and were gently mixed for approximately 30 minutes using a magnetic stirrer to hydrate dry kaolinite. NABA samples were

next incubated for 21 days at 21 °C prior to testing in the settling column, while no incubation was done for NFBF and NABF. Deionized water was used to minimize the number of parameters that could affect flocculation (e.g., salinity and pH). Because microbial strains used for inoculation were sampled in a semi-saline environment, using deionized water may have favoured growth of some strains that could adapt to low salinity; from earlier experiments (Middelburg and Nieuwenhuize, 2000), heterotrophic microorganisms adapted to estuarine waters can increase NH_4^+ and NO_3^- uptake rates when salinity decreases; thus, the procedure used here emphasised on strains that can grow in low salinity at the expenses of higher uptake of mineral N ions.

Finally, three different kaolinite concentrations C_K and three different NH_4NO_3 concentrations were tested for each SPM type, resulting in a total of 21 samples being tested (see summary in Table 3.2).

Table 3.2: Characteristics of SPM samples during the incubation in 500 mL beaker and the testing in settling column. The total liquid volumes contained in the flocculation section of the settling column and the beaker were 15 L and 0.5 L, respectively. ^aNutrient- and biomass free SPM prepared using only kaolinite mineral; ^bnutrient-affected and biomass-free SPM prepared using kaolinite mineral and ammonium nitrate; and ^cnutrient- and biomass-affected SPM prepared using kaolinite mineral, ammonium nitrate and glucose with inoculation of sedimentary microbial communities. *Note that NFBF and NABF samples were only mixed in beaker for 30 minutes and were not incubated. C_K and $[\text{NH}_4\text{NO}_3]$ denote the concentrations of kaolinite and ammonium nitrate, respectively.

Suspension type	Incubation conditions				Column conditions	
	Kaolinite (g)	NH_4NO_3 (g)	C_K (g/L)	$[\text{NH}_4\text{NO}_3]$ (mM)	C_K (g/L)	$[\text{NH}_4\text{NO}_3]$ (mM)
NFBF ^{a,*}	1.5	-	3	-	0.1	-
	3.0	-	6	-	0.2	-
	6.0	-	12	-	0.4	-
NABF ^{b,*}	1.5	0.06	3	1.5	0.1	0.05
	1.5	0.12	3	3.0	0.1	0.1
	1.5	0.24	3	6.0	0.1	0.2
	3.0	0.06	6	1.5	0.2	0.05
	3.0	0.12	6	3.0	0.2	0.1
	3.0	0.24	6	6.0	0.2	0.2
	6.0	0.06	12	1.5	0.4	0.05
	6.0	0.12	12	3.0	0.4	0.1
	6.0	0.24	12	6.0	0.4	0.2
NABA ^c	1.5	0.06	3	1.5	0.1	0.05
	1.5	0.12	3	3.0	0.1	0.1
	1.5	0.24	3	6.0	0.1	0.2
	3.0	0.06	6	1.5	0.2	0.05
	3.0	0.12	6	3.0	0.2	0.1
	3.0	0.24	6	6.0	0.2	0.2
	6.0	0.06	12	1.5	0.4	0.05
	6.0	0.12	12	3.0	0.4	0.1
	6.0	0.24	12	6.0	0.4	0.2

3.9 Experimental protocols

One SPM sample at a time was transferred from the beaker and was tested in the settling column, which was filled with 15 L of tap water. Each sample was mixed at grid frequency $f_g = \{0.4, 0.6, 0.8, 1.0, 1.2\}$ Hz, corresponding to turbulence shear rate $G = \{32, 48, 64, 80, 96\} \text{ s}^{-1}$. Each G was kept constant for 3 to 4 hours, while SPM imagery was conducted every 15 minutes. During image recording, the oscillating grid was put to halt to avoid interference with the SPM flow field, and the slider on the diaphragm was opened to allow SPM to settle freely into the camera view. Each recording took approximately 4 minutes to complete. The water quality parameters listed in Table 3.1 were acquired every 30 seconds, while, averages of measurements in a 10-minute time frame were used in the analyses presented in Chapter 7. The grid frequency was changed to the next test value at the end of the 3 to 4 hours period and the imagery procedures were repeated. The same protocol were applied to all the samples listed in Table 3.2.

3.10 Image processing

Acquired grayscale images (with intensity ranging between 0 and 255) of SPM were processed to separate individual aggregates from the background. A power function was first used to increase the image contrast; high frequency background noise was then removed by Fast Fourier Transform (FFT) filtering. The image intensity was then normalized using a two-threshold operation (*imadjust* function in Matlab2011b) before converting the images to binary. Dilation and erosion operations (*imdilate* and *imerode* functions in Matlab2011b) were systematically applied to all images for edge correction. Individual SPM images were then extracted from images that encompassed the entire camera view.

A SPM image was considered to be out-of-focus when the focus level F was smaller than the given threshold $F_{thres} = 10$. The focus level F of a SPM was determined using Brenner's method as (e.g., Brenner et al., 1976; Firestone et al., 1991; Pertuz et al., 2013),

$$F = \sum_i \sum_j (I_{i,j} - I_{i,2+j})^2, i + 2 < (\text{image size}), \quad (3.4)$$

where I is the grayscale image intensity matrix with i and j the pixel coordinates in that matrix. F describes an increase in focus when the intensity difference between a pixel and its adjacent two pixels increases.

3.11 Summary

This chapter presents the experimental facility and protocols specifically designed and developed to achieve the aim and primary objectives of this thesis. The facility is able to replicate and integrate hydrodynamic, chemical, and biological processes into one, unique setup. The use of μ PIV system to acquire images of settling SPM without disruption of test material can ensure that the geometrical characteristics of SPM are fully preserved. Protocols for sample preparation and testing were designed to explore how SPM structure and water quality change with increased nutrients and microbial activity, and in different environmental conditions, such as turbulence intensity and mineral concentration.

Chapter 4

Reconstructing SPM capacity dimension from light intensity spectra

Contents of this chapter were published in Tang and Maggi (2015c)¹ during PhD candidature of the author.

4.1 Introduction

The extent to which microorganisms can modify the internal architecture and space-filling capacity of SPM was quantified in this thesis through the use of the three-dimensional (3D) capacity dimension $d_0(S_3)$. The two-dimensional (2D) optical projection S_2 of SPM acquired in experiments can be used to retrieve $d_0(S_3)$ by using the method proposed in Maggi and Winterwerp (2004) (described in Chapter 2.3.2). This method, however, was found to underestimate the actual $d_0(S_3)$ of small aggregates (e.g., Maggi, 2008; Vahedi and Gorczyca, 2011). Because biomass-affected SPM is anticipated to have high irregularity in its shape and internal structure, a method that could better capture these irregularities was developed for this thesis and is described in sections below.

The underestimation of the method in Maggi and Winterwerp (2004) may stem from the use of only the outermost projection segmentation (i.e., the perimeter-based fractal dimension $d_P(S_2)$ of the boundary of S_2) to estimate $d_0(S_3)$. It is hypothesised here that the estimation can be improved if additional information were retrieved from the interior part of the projection. Because the scattering of light depends on surface topography, the light intensity of 2D optical images of SPM can be used as a proxy to its internal fractal architecture. Exploiting this information may therefore improve estimation of $d_0(S_3)$. It is proposed here that the perimeter-based fractal dimension of each intensity contour line, instead of just the outermost boundary of S_2 , can be employed for this purpose.

This chapter presents a method that uses the light intensity and multiple perimeter segmentations of 2D images to estimate $d_0(S_3)$ of SPM. To achieve this, projections (images) of SPM were first shown to have a characteristic intensity-based $d_P(S_2)$ spectrum; next, mathematical functions were developed to describe the $d_P(S_2)$ spectrum and to determine the optimal $d_P(S_2)$ that can accurately return $d_0(S_3)$ of SPM. Although this method may be applicable to granular aggregates other than SPM, this method was specifically designed and tested for use in this thesis to quantify changes in SPM internal architecture as a result of various biotic and abiotic processes.

¹Tang F.H.M., and Maggi F. (2015). Reconstructing the fractal dimension of granular aggregates from light intensity spectra, *Soft Matter*, 11(47), 9150-9159.

4.2 Methods

This section outlines the basis upon which the method was developed and introduces the procedure used to validate it against a control set of numerically-generated and stereolithographically-fabricated aggregates with known $d_0(S_3)$, and experimentally-acquired sedimentary aggregates with benchmark values of $d_0(S_3)$.

4.2.1 Earlier approach

The method proposed in Maggi and Winterwerp (2004) yields $d_0(S_3)$ of a SPM from $d_P(S_2)$ of its projection S_2 as

$$d_0(S_3) = \sqrt{\frac{a(\ell)}{d_P(S_2) - b(\ell)}} \text{ for } d_P(S_2) < 2, \quad (4.1)$$

where $\ell = L/L_p$ is the dimensionless aggregate size with L as the SPM size and L_p as the primary particle size, and $a(\ell)$ and $b(\ell)$ are the functions

$$a(\ell) = 9 \left(z(\ell) - \frac{2[k(\ell)]^2 - 9z(\ell)}{[k(\ell)]^2 - 9} \right), \quad (4.2a)$$

$$b(\ell) = \frac{2[k(\ell)]^2 - 9z(\ell)}{[k(\ell)]^2 - 9}, \quad (4.2b)$$

with $z(\ell) = (\log[4\ell - 4]) / (\log[\ell])$ and $k(\ell) = z(\ell)[z(\ell) - 1] + 1$. In Eq. (4.1), $d_P(S_2)$ is defined as (Meakin, 1998),

$$d_P(S_2) = 2 \frac{\log[N_P]}{\log[N_A]}, \quad (4.3)$$

where N_P and N_A are the dimensionless perimeter (i.e., the number of pixels at the outermost boundary of S_2) and area of the projection S_2 (i.e., the number of pixels contained within that boundary after filling holes), respectively. Note that $d_P(S_2)$ ranges between $[Z(\ell), 2]$, where $Z(\ell)$ is a function of ℓ defined as (Maggi and Winterwerp, 2004),

$$Z(\ell) = \begin{cases} 2 \frac{\log[\ell]}{\log[\ell]} = 2 & \text{for } \ell = 1, \\ 2 \frac{\log[4\ell - 4]}{\log[\ell^2]} \leq 2 & \text{for } \ell \geq 2, \\ 1 & \text{for } \ell = \infty. \end{cases} \quad (4.4)$$

The method proposed in this chapter improves and extends the approach described above after introducing the following additional quantities.

4.2.2 Perimeter-based fractal dimension spectrum

Consider the normalized intensity $I \in [0, 1]$ of a grayscale image (projection) S_2 of a SPM S_3 ; depending on the grayscale depth, N is the number of levels in I depending on its range of validity (e.g., 256 for a 8-bit grayscale depth). The subset $S_2(I \geq I^*) = S_{2,I^*}$ is defined as the set of pixels with $I \geq I^*$; because every subset S_{2,I^*} has a perimeter-based fractal dimension $d_P(S_{2,I^*}) = d_{P,I^*}$, then the set S_2 is associated with N subsets $S_{2,I}$ and N perimeter-based fractal dimensions $d_{P,I}$. The set of points defined by I and $d_{P,I}$ is the perimeter-based fractal dimension spectrum. Note that d_{P,I^*} is defined as in Eq. (4.3) with $N_P = N_P(S_{2,I})$ and $N_A = N_A(S_{2,I})$ the dimensionless perimeter and area of subset $S_{2,I}$.

4.2.3 Analytical description of the spectrum

Light intensity I is not uniformly distributed across the projection S_2 when irregular aggregates are characterized by surface asperities. Hence, from a conceptual point of view, every subset $S_{2,I}$ is expected to be distinct from one another and be associated with information of surface characteristics of S_2 at that I . Consider projections of SPM as in Figure 4.1; the first subset $S_{2,0}$ at the lowest intensity shows the exterior outlook of the SPM with some level of segmentation, while $S_{2,0 < I < 1}$ reveals how interior parts of S_2 become increasingly more heterogeneous and segmented as I increases, thus, unfolding the fractal nature of the SPM surface. With emerging fractal characteristics, $d_{P,I}$ is generally expected to increase from $d_{P,0}$ of the outermost boundary to reach a maximum at some intermediate intensity. However, as I increases to 1, subsets $S_{2,I \rightarrow 1}$ would show less heterogeneity and segmentation and would eventually collapse into a projection $S_{2,1}$ with ideally no perimeter segmentation (Figure 4.1); in this instance, $d_{P,1} = Z(\ell)$ as per Eq. (4.4).

Because the surface characteristics of SPM with low $d_0(S_3)$ are expected to be distinct from those with high $d_0(S_3)$, the spectrum $d_{P,I}$ of SPM is presumed to depend on $d_0(S_3)$. For example, consider an aggregate A with high $d_0(S_3)$ and an aggregate B with low $d_0(S_3)$ (Figure 4.1); subsets $S_{2,I}$ of A are expected to be less segmented than those of B. This implies that A would show lower values of $d_{P,I}$ at intermediate intensity as compared to B, signifying that the concavity of spectra decreases as $d_0(S_3)$ increases.

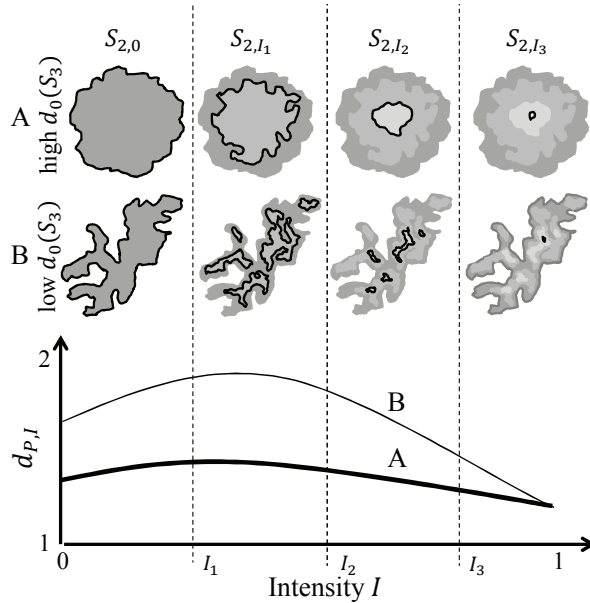


Figure 4.1: Conceptual perimeter-based fractal dimension spectra $d_{P,I}$ of S_2 projections of SPM aggregate A with high capacity dimension $d_0(S_3)$ and SPM aggregate B with low capacity dimension $d_0(S_3)$.

Since $d_{P,I}$ may increase from $d_{P,0}$ at $I = 0$ to a maximum value, and eventually decrease to $Z(\ell)$ at $I = 1$, $d_{P,I}$ may be described by a nonlinear (second-order) function of I as

$$d_{P,I} = AI^2 + BI + C. \quad (4.5)$$

To determine A , B and C in Eq. (4.5), three conditions are required:

Condition 1 (for $I = 0$): By substituting $I = 0$ into Eq. (4.5), we obtain

$$C = d_{P,0}, \quad (4.6)$$

where $d_{P,0}$ is the outermost perimeter-based fractal dimension as in Eq. (4.3).

Condition 2 (for $I = 1$): Because the spectrum $d_{P,I}$ would eventually decrease to $d_{P,I} = Z(\ell)$ at $I = 1$, using Eq. (4.5) with $C = d_{P,0}$ (Eq. (4.6)) allows writing B as a function of A as,

$$B(A) = Z(\ell) - d_{P,0} - A, \quad (4.7)$$

where $Z(\ell)$ is the known function of Eq. (4.4).

Condition 3 (for $\frac{dd_{P,I}}{dI}$ and $\frac{d^2d_{P,I}}{dI^2}$): To reflect the characteristics of the spectrum qualitatively depicted in Figure 4.1, the first derivative of Eq. (4.5) has to be positive at $I = 0$ and the second derivative has to be negative as

$$\left. \frac{dd_{P,I}}{dI} \right|_{I=0} = B(A) \geq 0, \quad (4.8a)$$

$$\frac{d^2d_{P,I}}{dI^2} = 2A \leq 0, \forall I. \quad (4.8b)$$

Assuming that Eqs. (4.8) are linearly proportional to each other by a factor α , then it is possible to write

$$\frac{d^2d_{P,I}}{dI^2} = -\alpha \left. \frac{dd_{P,I}}{dI} \right|_{I=0}, \quad (4.9)$$

$$2A = -\alpha B(A), \quad (4.10)$$

$$A = -\frac{\alpha(Z(\ell) - d_{P,0})}{2 - \alpha}, \quad (4.11)$$

where $B(A)$ of Eq. (4.7) was used in Eq. (4.10). By making A and $B(A)$ explicit in Eqs. (4.8), then we obtain

$$\left. \frac{dd_{P,I}}{dI} \right|_{I=0} = \frac{2}{2 - \alpha}(Z(\ell) - d_{P,0}) \geq 0, \quad (4.12a)$$

$$\frac{d^2d_{P,I}}{dI^2} = -\frac{2\alpha}{2 - \alpha}(Z(\ell) - d_{P,0}) \leq 0. \quad (4.12b)$$

Because $d_P(S_2) \in [Z(\ell), 2]$, then $(Z(\ell) - d_{P,0}) \leq 0$ and Eqs. (4.12) satisfy the inequalities only if $(2 - \alpha) \leq 0$, that is, only if $\alpha \geq 2$. When $\alpha \rightarrow 2$, $dd_{P,I}/dI \rightarrow \infty$ for $I \rightarrow 0$ (Eq. (4.12a)) and $d^2d_{P,I}/dI^2 \rightarrow -\infty$ (Eq. (4.12b)); on the other hand, $dd_{P,I}/dI \rightarrow 0$ for $I \rightarrow 0$ while $d^2d_{P,I}/dI^2 \rightarrow 2(Z(\ell) - d_{P,0})$ when $\alpha \rightarrow \infty$. Even though $\alpha \rightarrow \infty$ satisfies the conditions in Eqs. (4.12), a finite value of α has to be assumed to practically use Eq. (4.9); hence, an arbitrary value $\alpha = \tilde{\alpha}$ is introduced here, while an explicit value is derived later in Section 4.3.1.

As conceptually depicted in Figure 4.1, $d^2d_{P,I}/dI^2$ is not constant but is a function of $d_0(S_3)$ through α . Note also that $d_0(S_3)$ is the unknown that we aim to determine and, therefore, α has to be written as a function of $d_{P,0}$ instead. Because $d^2d_{P,I}/dI^2 \rightarrow -\infty$ is expected for SPM with an infinitely segmented perimeter (i.e., $d_P(S_2) = 2$), then $\alpha = 2$ for $d_{P,0} = 2$; in contrast, $d^2d_{P,I}/dI^2 \rightarrow 2(Z(\ell) - d_{P,0})$ is expected for aggregates with no perimeter segmentation (i.e., $d_P(S_2) = Z(\ell)$), hence, $\alpha = \tilde{\alpha}$ for $d_{P,0} = Z(\ell)$. In the absence of substantial evidence for the order of the function $\alpha(d_{P,0})$, the linear function

$$\alpha = \frac{(\tilde{\alpha} - 2)}{Z(\ell) - 2}d_{P,0} + \frac{2(Z(\ell) - \tilde{\alpha})}{Z(\ell) - 2}, \quad (4.13)$$

was used with $\alpha \in [2, \tilde{\alpha}]$ and with $Z(\ell)$ defined in Eq. (4.4). The value of A in Eq. (4.11) can be calculated by knowing the value of α from Eq. (4.13).

Finally, using Eqs. (4.6), (4.7) and (4.11) from *Conditions 1, 2* and *3*, the parameters A , B and C that determine the analytical spectrum $d_{P,I}$ in Eq. (4.5) are

$$A = -\frac{[(\tilde{\alpha} - 2)d_{P,0} + 2(Z(\ell) - \tilde{\alpha})][Z(\ell) - d_{P,0}]}{(2 - d_{P,0})(\tilde{\alpha} - 2)}, \quad (4.14a)$$

$$B = [Z(\ell) - d_{P,0}] \left(1 + \frac{(\tilde{\alpha} - 2)d_{P,0} + 2[Z(\ell) - \tilde{\alpha}]}{(2 - d_{P,0})(\tilde{\alpha} - 2)} \right), \quad (4.14b)$$

$$C = d_{P,0}, \quad (4.14c)$$

where $\tilde{\alpha}$ is a known arbitrary constant, $Z(\ell)$ is calculated from Eq. (4.4), $d_{P,0}$ is assessed from the outermost boundary of S_2 using Eq. (4.3), and ℓ can be any positive value. Note that because A , B and C are functions of ℓ , the spectrum $d_{P,I}(\ell)$ is also a function of ℓ .

Global maximum: Since $d_{P,I}(\ell) \in [Z(\ell), 2]$, the global maximum $d_{P,\hat{I}}$ of Eq. (4.5) should not exceed 2. If $d_{P,\hat{I}} > 2$, we impose $d_{P,\hat{I}} = 2$. The parameters A and B are then recalculated in terms of the intensity \hat{I} that yields $d_{P,\hat{I}}$ by equating the first derivative of Eq. (4.5) to zero. We then obtain

$$A = \frac{d_{P,0} - Z(\ell)}{2\hat{I} - 1}, \quad (4.15a)$$

$$B = Z(\ell) - d_{P,0} - \frac{d_{P,0} - Z(\ell)}{2\hat{I} - 1}. \quad (4.15b)$$

The values of \hat{I} corresponding to $d_{P,\hat{I}} = 2$ can be determined by substituting Eqs. (4.15) and (4.6) for A , B and C into Eq. (4.5), which returns the quadratic function $(Z(\ell) - d_{P,0})\hat{I}^2 + 2(d_{P,0} - 2)\hat{I} + 2 - d_{P,0} = 0$. Of the two solutions, only $\hat{I} \in [0, 1]$ is valid for this problem.

4.2.4 The optimal perimeter-based fractal dimension

Among the N subsets $S_{2,I}$, there exists a subset $S_{2,\hat{I}}$ that yields the optimum $d_{P,\hat{I}}$ to estimate $d_0(S_3)$ of a SPM. Note that, $d_{P,\hat{I}}$ can be any point within the spectrum $d_{P,I}(\ell)$, but $d_{P,\hat{I}} = d_{P,0}$ is very unlikely because $d_{P,0}$ only provides segmentation of the outermost boundary. This may be a possible explanation of why the method in Maggi and Winterwerp (2004) underestimated $d_0(S_3)$ of DLA and CCA aggregates tested in Maggi (2008). We then define a continuous function $f(\ell)$ of ℓ that intersects the analytical spectrum $d_{P,I}(\ell)$ and identify $d_{P,\hat{I}}$ as

$$(\hat{I}(\ell), d_{P,\hat{I}}(\ell)) = d_{P,I}(\ell) \cap f(\ell). \quad (4.16)$$

The function $f(\ell)$ is not known theoretically but an empirical expression for it will be presented along with experiments in Section 4.3.2. The derivation of $d_{P,\hat{I}}(\ell)$ is considered semi-analytical as it involves both analytical (i.e., $d_{P,I}(\ell)$) and empirical components (i.e., $f(\ell)$). After determining $d_{P,\hat{I}}(\ell)$ from Eq. (4.16), $d_0(S_3)$ can then be reconstructed using Eq. (4.1) with $d_P(S_2) = d_{P,\hat{I}}(\ell)$.

4.2.5 Control set of test aggregates

The semi-analytical method developed above was validated against a control set of different aggregates, including numerically-generated and stereolithographically-fabricated aggregates with known $d_0(S_3)$ and experimentally-acquired SPM with benchmark values of $d_0(S_3)$.

Numerically-generated aggregates: Particle aggregation governed by different kinetics would normally produce aggregates of different geometrical structures. In order to account for these differences, diffusion-limited (DLA), cluster-cluster (CCA) and self-correlated (SCA) aggregation kinetics were used.

DLA was introduced by Witten Jr and Sander (1981) to account for aggregation by Brownian (diffusion) motion that forms branch-like aggregates. CCA allows diffusion and aggregation not only of single particles but also clusters of particles, forming bridged and closed-ring aggregates (Meakin, 1983; Kolb et al., 1983; Vicsek, 1989; Meakin, 1998). SCA aggregates, on the other hand, are produced using static accretion, where particles are randomly attached onto existing ones without involving motion explicitly (Maggi and Winterwerp, 2004; Maggi, 2015b). The probability of an existing particle to receive a new one depends on an exponential distribution function, where an exponent tunes the resulting $d_0(S_3)$ of that aggregate.

In this chapter, we used 8 3D DLA and 10 3D CCA aggregates of 1000 primary particles already used in Maggi (2008), and 18 3D SCA aggregates used in Maggi (2015b). Hence, a total of 36 numerical aggregates with $d_0(S_3)$ ranging between 1.73 and 2.71 were available to our analyses. Among all, 9 of them were used to determine the function $f(\ell)$ in Eq. (4.16) and the other 27 were used for validation. A summary of the characteristics of the numerical aggregates is given in Table 4.1.

Projections $S_{2,x}$, $S_{2,y}$ and $S_{2,z}$ of numerical aggregates along the three principle directions were computed, and were then converted into 8-bit grayscale images. To assign a grayscale to those images, the light intensity observed at a point of the projected plane was calculated as the number of primary particles located at that point but in the direction normal to the projected plane. For this approach, we used the principle of superposition of the effects along with Mie theory (Mie, 1908), assuming therefore that light scatter is proportional to the mass. This approach may not universally apply to any type of aggregates, but it is particularly suited to aggregates of granular (e.g., sediment, dusts, aerosols, etc.) and biological nature (e.g., cells, microbes clusters, etc.), where individual particles are translucent at those scales. Grayscale projections of numerical aggregates reconstructed using the procedure above resulted in observations similar to images of natural SPM acquired through experiments (see images in the first three columns as compared to those in the fourth column of Figure 4.2a).

Table 4.1: Characteristics of DLA, CCA and SCA numerical aggregates.

Aggregate type	DLA	CCA	SCA
Number of aggregates for calibration	3	3	3
Number of aggregates for validation	5	7	15
Actual $d_0(S_3)$	1.82 - 1.86	1.73 - 1.84	1.91 - 2.71
Primary particles	1000	1000	704 - 8374
Dimensionless size	44	55	31

Stereolithographically-fabricated aggregates: Five of the 18 numerical SCA aggregates described above were fabricated by stereolithography (3D printing) using an Objet Eden-250 3D printing apparatus. Aggregates, having 5 cm linear size, were fabricated with Fullcure 720 resin (Objet), which has a specific density of 1.22 g cm^{-3} (Maggi, 2015b). For each stereolithographic SCA aggregate, photographic images were acquired in 8-bit grayscale and in three different directions. These images (Figure 4.2b, top row) have relatively similar outlook, though with higher light intensities, as compared to the grayscale reconstructed projections of their corresponding SCA numerical aggregates (Figure 4.2b,

bottom row). These images of stereolithographic aggregates were then used for validation.

Experimentally-acquired SPM: Two types of sediment suspensions were prepared: a natural suspension rich in organic matter collected from Blackwattle Bay, Glebe Council, Sydney, NSW, Australia; and a pure kaolinite suspension (type Q38, with particle size ranging between 0.6 μm to 38 μm). Sampling was conducted using the setup and procedure described in Chapter 6.2.1. SPM images were acquired in 8-bit grayscale using a μPIV system described in Chapter 3.6 and images were processed with the algorithm described in Chapter 3.10. Note that both organic and mineral SPM generally have projections similar to those of numerical aggregates, but they appeared closer to SCA aggregates as compared to DLA and CCA (Figure 4.2a).

4.2.6 Statistical estimators

Accuracy of estimations was evaluated using the correlation coefficient $R = \text{cov}(c, o)/(\sigma_c \sigma_o)$, normalized root mean square error (residuals) $\text{NRMSE} = \left(\frac{1}{n_o} \sum_{i=1}^{n_o} (c_i - o_i)^2 \right)^{1/2} / (\max\{o\} - \min\{o\})$, and percent error $\text{PE} = |o - c|/o \times 100$, where cov is covariance, c and o are the calculated and observed values, respectively, n_o is the sample size, and σ_c and σ_o are the standard deviation of c and o , respectively.

4.3 Results

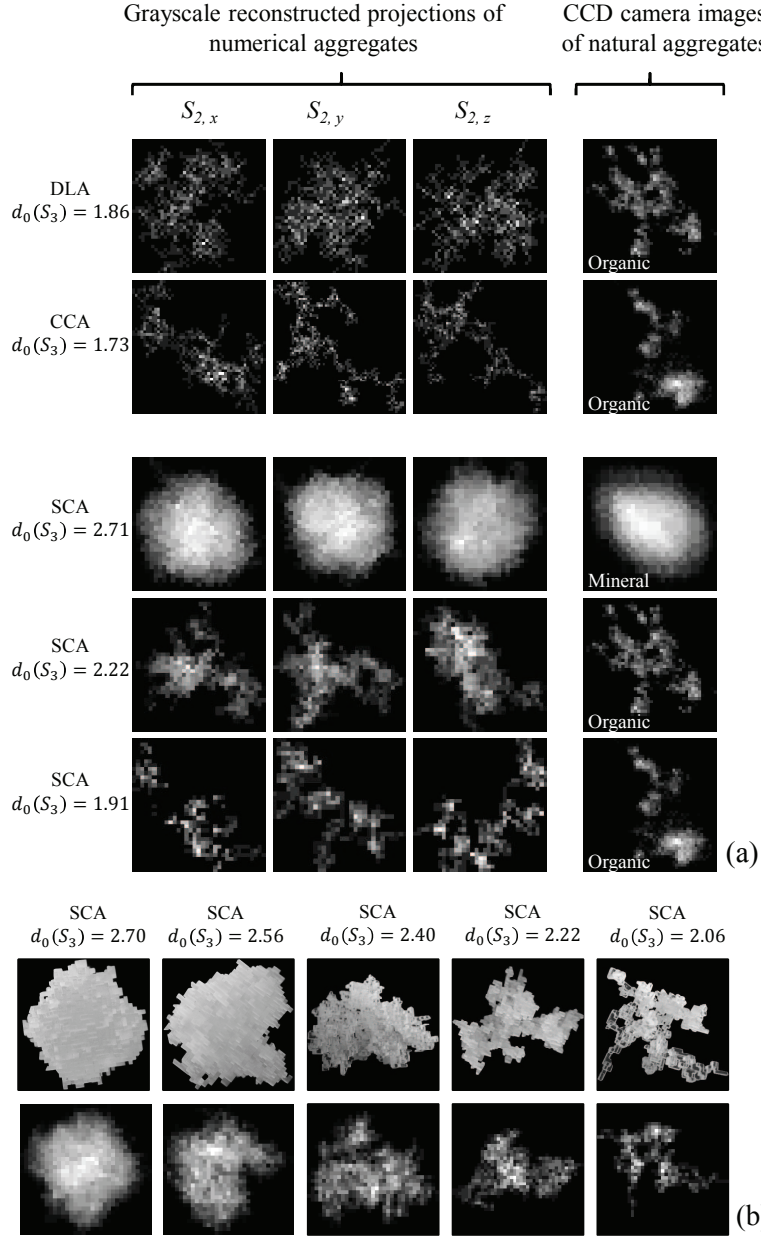
4.3.1 Projection-based and analytical spectra $d_{P,I}$ of numerical aggregates

The spectra $d_{P,I}$ of numerical DLA, CCA and SCA aggregates were calculated from their grayscale projections after subsets $S_{2,I}$ were resized to the same ℓ (see dotted lines for three illustrative values of ℓ in Figure 4.3a - c). Projection-based spectra ranged wide intervals in $d_{P,0}$ (at $I = 0$), curvature, and $d_{P,1}$ (at $I = 1$) regardless of ℓ , but appeared correlated with $d_0(S_3)$ of the original aggregates as conceptually depicted in Figure 4.1. In particular, $d^2 d_{P,I}/dI^2$ decreased with $d_{P,0}$ decreasing, hence, with $d_0(S_3)$ increasing. All spectra $d_{P,I}$ shared nearly the same value $d_{P,1} < d_{P,0}$ at $I = 1$ and had a maximum at intensities $\hat{I} \in [0.25, 0.5]$ for all $d_0(S_3)$ tested here.

This latter feature suggests a way to choose a suitable value $\alpha = \tilde{\alpha}$. By equating the first derivative of Eq. (4.5) to zero and using Eq. (4.10), \hat{I} can be expressed as $\hat{I} = -B(A)/2A = 1/\alpha$. If the assumption is taken that $\hat{I} \in [0.25, 0.5]$, then, $\alpha \in [2, \tilde{\alpha}]$ with $\tilde{\alpha} = 4$. Following this line, analytical spectra $d_{P,I}(\ell)$ of all the 36 numerical aggregates were derived based on the procedures described in Section 4.2.3 for $\tilde{\alpha} = 4$ and for $\ell = 2^m$, with $m \in [6, 13]$. Comparison between projection-based and analytical spectra of numerical aggregates are depicted in Figure 4.3a - c only for $\ell = 2^6, 2^8$ and 2^{13} , whereas Figure 4.3d reports NRMSE and R for all samples and ℓ values. Because $N_P(S_{2,I})$ and $N_A(S_{2,I})$ decreased with I increasing and led to less accurate $d_P(S_2)$, the spectrum for $I \in [0.5, 1]$ was not used in quantifying NRMSE and R. Neglecting these values of the spectrum, we found $\text{NRMSE} \leq 20\%$ and $R \geq 90\%$ regardless of ℓ , with slightly better accuracy at high ℓ (Figure 4.3d).

4.3.2 Empirical derivation of the function $f(\ell)$

The function $f(\ell) = \hat{I}(d_{P,\hat{I}}(\ell))$ describes the intensity \hat{I} corresponding to the optimum $d_{P,\hat{I}}$ of any spectrum $d_{P,I}(\ell)$ at any ℓ . To empirically derive $f(\ell)$, a calibration set comprising numerical aggre-



(a)

(b)

Figure 4.2: (a) example grayscale reconstructed projections of diffusion-limited (DLA), cluster-cluster (CCA), and self-correlated (SCA) aggregates in the three principle directions (first three columns) and experimental images of natural SPM (fourth column). (b) example images of stereolithographically-fabricated SCA aggregates (top row) as compared to their grayscale reconstructed projections (bottom row).

gates with known $d_{P,i}$ was used, where $d_{P,i}$ was calculated from the actual $d_0(S_3)$ by inverting Eq. (4.1) as

$$d_{P,i}(\ell) = \begin{cases} 2 & \text{for } d_0(S_3) \leq k(\ell), \\ \frac{a(\ell)}{[d_0(S_3)]^2} + b(\ell) & \text{for } d_0(S_3) > k(\ell), \end{cases} \quad (4.17)$$

with $a(\ell)$, $b(\ell)$ and $k(\ell)$ defined in Eq. (4.2). By knowing $d_{P,i}(\ell)$, the corresponding intensity $\dot{I}(\ell)$ can be solved for in Eq. (4.5) by substituting $d_{P,I}(\ell) = d_{P,i}(\ell)$. Solutions lead to three different

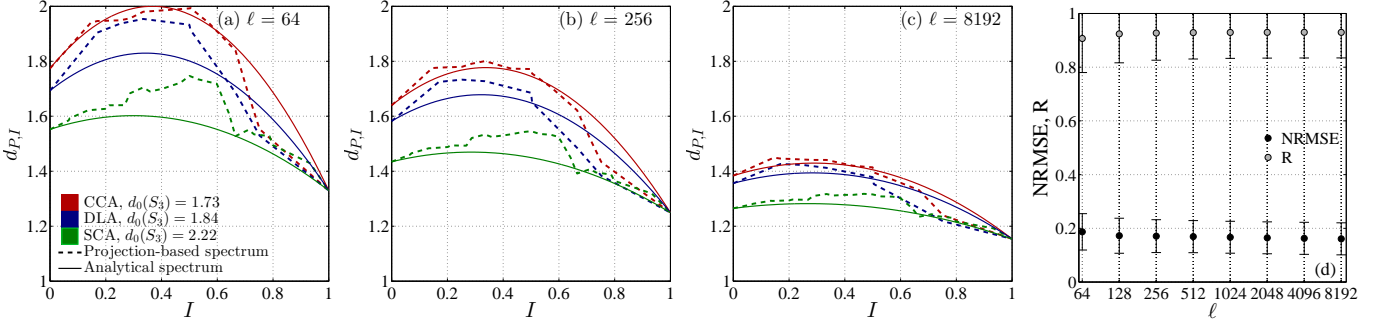


Figure 4.3: Example projection-based and analytical spectra $d_{P,I}(\ell)$ of diffusion-limited (DLA), cluster-cluster (CCA), and self-correlated (SCA) numerical aggregates for dimensionless aggregate size: (a) $\ell = 2^6$; (b) $\ell = 2^8$; and (c) $\ell = 2^{13}$. (d) NRMSE and R of analytical spectra $d_{P,I}(\ell)$ against projection-based spectra for all 36 numerical aggregates at different ℓ .

cases: (i) two solutions \hat{I}_1 and \hat{I}_2 with $\hat{I} = \max\{\hat{I}_1, \hat{I}_2\}$ and $\hat{I} \in [0, 1]$ when $d_{P,\hat{I}} < d_{P,i}$; (ii) one solution of \hat{I} when $d_{P,\hat{I}} = d_{P,i}$; and (iii) no real solution when $d_{P,\hat{I}} > d_{P,i}$; in this case, $\hat{I} = \hat{I}$ is imposed. The set of points $(\hat{I}(\ell), d_{P,\hat{I}}(\ell))$ relative to the calibration set in Figure 4.4a shows a trend that can be described by a second order function of the form,

$$f(\ell) = \beta_1(\ell)[d_{P,\hat{I}}(\ell)]^2 + \beta_2(\ell)d_{P,\hat{I}}(\ell) + \beta_3(\ell), \quad (4.18)$$

where $\beta_1(\ell)$, $\beta_2(\ell)$ and $\beta_3(\ell)$ are fitting parameters that depend on ℓ (Figure 4.4b). We noted that the concavity of $f(\ell)$ increased and that the goodness of fit also increased as a function of ℓ (NRMSE $< 20\%$ and $R > 80\%$, Figure 4.4a and inset therein). Additionally, fitting parameters showed monotonic trends (increasing or decreasing) as a function of ℓ (Figure 4.4b). A linear or nonlinear interpolation can be used to obtain specific values of $\beta_1(\ell)$, $\beta_2(\ell)$ and $\beta_3(\ell)$ at any given ℓ .

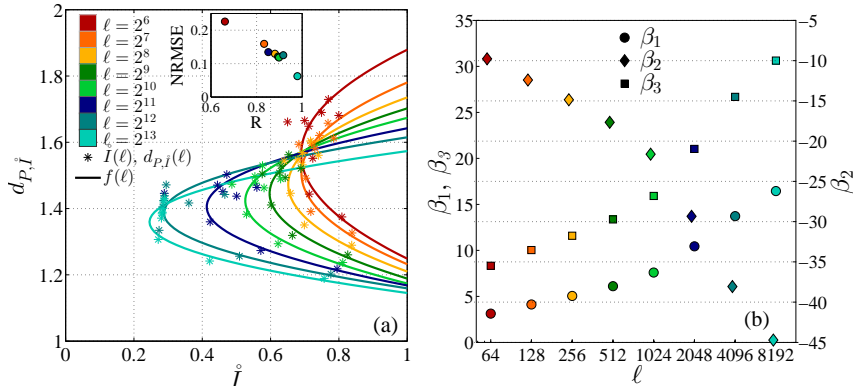


Figure 4.4: (a) least square fitting of $f(\ell)$ using calibration coordinates $(\hat{I}(\ell), d_{P,\hat{I}}(\ell))$ sets. (b) fitting parameters $\beta_1(\ell)$, $\beta_2(\ell)$, and $\beta_3(\ell)$ of the $f(\ell)$ function in Eq. (4.18) for dimensionless aggregate size $\ell = 2^m$, with $m \in [6, 13]$.

4.3.3 Validation against numerically-generated aggregates

A validation set consisting of 27 numerical aggregates (DLA, CCA and SCA) was used to test the accuracy of the method proposed in this chapter and to compare this method to the earlier approach in Maggi and Winterwerp (2004) for $\ell = 2^m$, with $m \in [6, 13]$.

Application of this method persistently achieved a better estimation of $d_0(S_3)$ as compared to the method in Maggi and Winterwerp (2004) regardless of ℓ as shown by statistical quantities in Figure 4.5. The method in Maggi and Winterwerp (2004) showed sensitivity to ℓ as PE fluctuated greatly over values of ℓ . In addition, accuracy decreased when the method was applied to aggregates with high $d_0(S_3)$ (Figure 4.6); these results agree with those in Vahedi and Gorczyca (2011), where greater errors were observed when the method in Maggi and Winterwerp (2004) was used to estimate $d_0(S_3)$ of small lime softening flocs that were expected to have high $d_0(S_3)$.

In contrast, the method proposed in this chapter showed less sensitivity to ℓ and was able to reconstruct $d_0(S_3)$ at a relatively high accuracy for all $d_0(S_3) \in [1.73, 2.71]$, improving the earlier approach by at least 50% with $PE \leq 2\%$ (except for $\ell = 8192$), $NRMSE \leq 8\%$ and $R \geq 98.5\%$ (Figure 4.5). This method also resulted in smaller standard deviation as compared to the method in Maggi and Winterwerp (2004), thus, implying a higher reliability (smaller uncertainty) for all ℓ and $d_0(S_3)$.

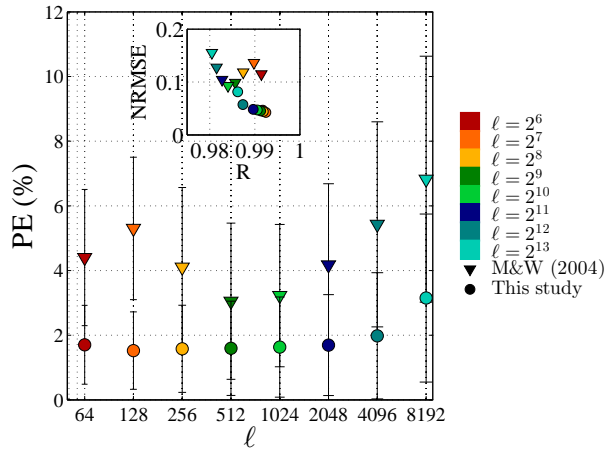


Figure 4.5: Percent error PE, normalized root mean square error (residuals) NRMSE and correlation coefficient R of estimated $d_0(S_3)$ for numerical aggregates obtained by using the methods in Maggi and Winterwerp (2004) (M&W (2004)) and in this chapter.

4.3.4 Validation against stereolithographically-fabricated aggregates

The projection-based spectra $d_{P,I}$ of stereolithographic aggregates showed a similar trend to those of numerical aggregates (Figure 4.7a - c), with the spectra increasing from $d_{P,0}$ to eventually converge to $I = 1$ and $d_{P,1} \leq d_{P,0}$. The second half of the spectra, however, showed a steep increase and reached a maximum at $0.9 < \hat{I} < 1$; this was explained by the aggregate showing anisotropy due to fabrication layering, with material deposited as thin films causing high-intensity light to be reflected from the surface - images of stereolithographic aggregates in Figure 4.2b (top row) showed higher light intensities than all other reconstructed and real projections. After excluding $I \in [0.5, 1]$, the analytical spectra $d_{P,I}$ captured the projection-based spectra relatively well for all tested ℓ , with $NRMSE \leq 20\%$ (shown in insets of Figure 4.7a - c).

The method presented in this chapter achieved $1.8\% < PE < 3.4\%$ with lower standard deviation in the reconstruction of $d_0(S_3)$ of stereolithographic aggregates as compared to the earlier approach in Maggi and Winterwerp (2004) ($PE > 3.6\%$) for all ℓ tested (Figure 4.7d).

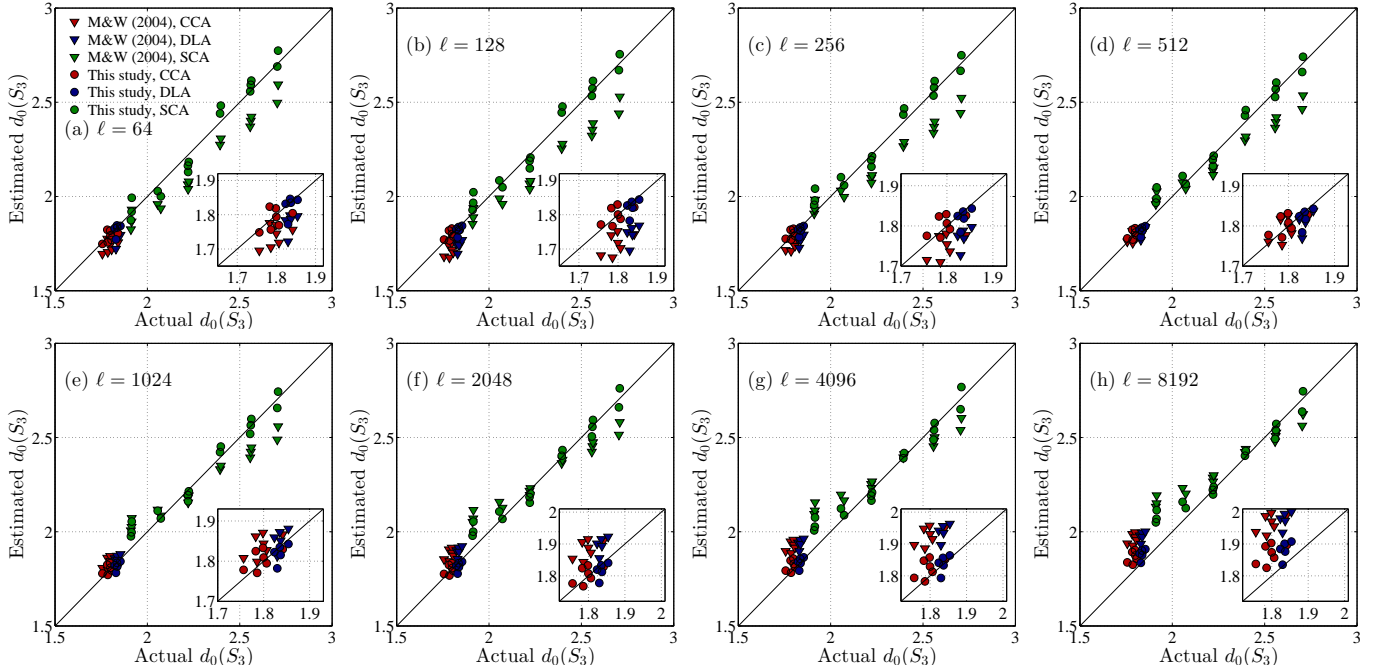


Figure 4.6: Estimated $d_0(S_3)$ using the methods in Maggi and Winterwerp (2004) (M&W (2004)) and in this chapter against actual $d_0(S_3)$ for dimensionless aggregate size $\ell = 2^m$ with $m \in [6, 13]$.

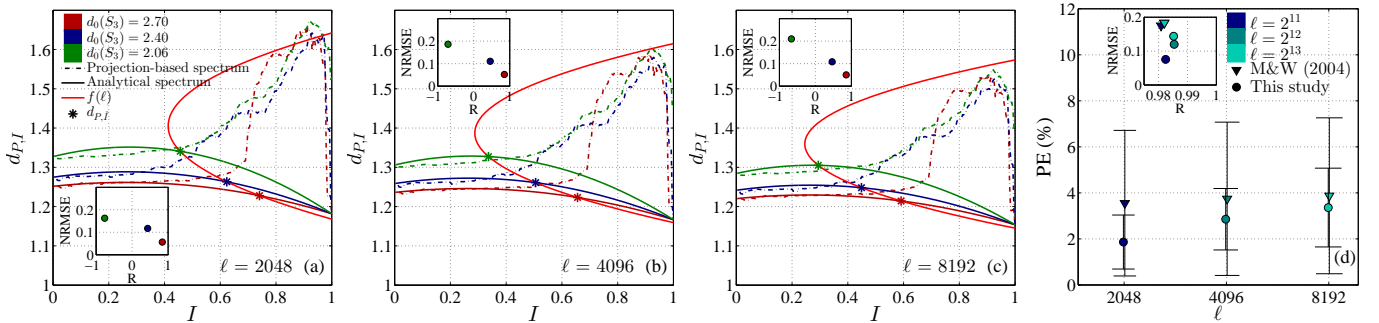


Figure 4.7: Projection-based and analytical spectra $d_{P,I}$ of stereolithographic self-correlated (SCA) aggregates for dimensionless aggregate size: (a) $\ell = 2048$; (b) $\ell = 4096$; and (c) $\ell = 8192$. (d) percent error PE, normalized root mean square error (residuals) NRMSE, and correlation coefficient R of estimated $d_0(S_3)$ for stereolithographic aggregates obtained by using the methods in Maggi and Winterwerp (2004) (M&W (2004)) and in this chapter.

4.3.5 Application to experimentally-acquired SPM

For natural SPM (mineral and organic), $d_0(S_3)$ can be estimated both directly using the method proposed in this chapter as well as the earlier approach in Maggi and Winterwerp (2004), or indirectly using their settling velocities calculated from images acquired through the experiments.

When applying the method in this chapter, we observed that the projection-based spectra $d_{P,I}$ of organic natural SPM were substantially different from those of mineral SPM (Figure 4.8a and b). Organic SPM possessed spectra with distinct curvature and were similar to spectra of numerical aggregates with low $d_0(S_3)$. In contrast, spectra of mineral SPM were relatively flat. More importantly, the analytical spectra $d_{P,I}$ of both organic and mineral SPM matched relatively well with the first half of their projection-based spectra (NRMSE < 16.5% and R > 95%). Application of the method

in this chapter returned $d_0(S_3) \in [2.78, 2.87]$ for mineral SPM and $d_0(S_3) \in [1.99, 2.15]$ for organic SPM. On the other hand, the earlier approach in Maggi and Winterwerp (2004) resulted in slightly lower values of $d_0(S_3)$ for both mineral ($d_0(S_3) \in [2.56, 2.68]$) and organic ($d_0(S_3) \in [1.94, 2.07]$) SPM.

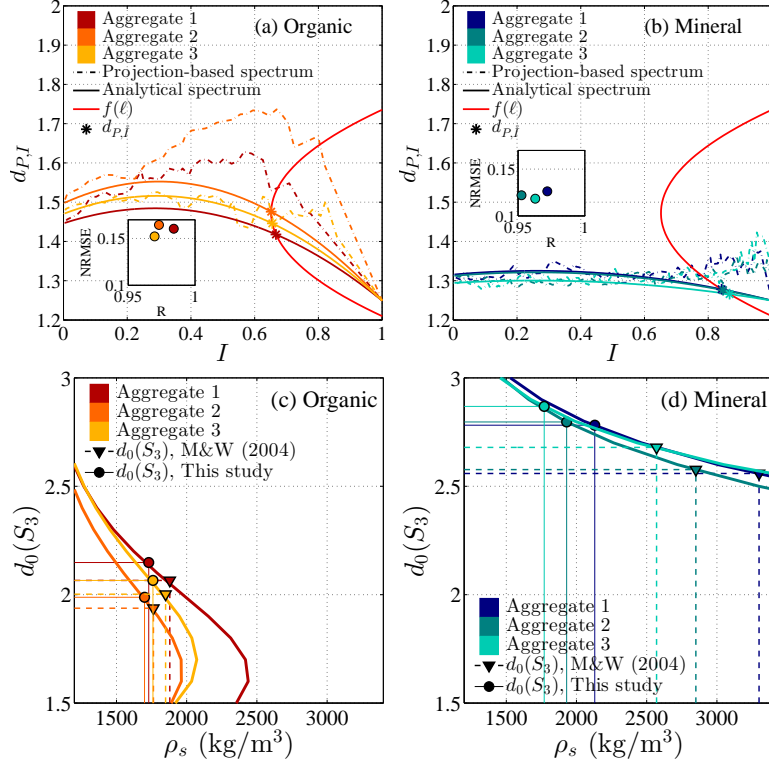


Figure 4.8: Projection-based and analytical spectra $d_{P,I}$ of (a) organic and (b) mineral SPM for dimensionless aggregate size $\ell = 256$; relationship between aggregate density ρ_s and capacity dimension $d_0(S_3)$ according to force balance equation for (c) organic and (d) mineral SPM.

To validate estimated $d_0(S_3)$ using 2D optical projections, $d_0(S_3)$ of natural SPM was also determined from their settling velocities v following the force balance equation $F_g - F_b = F_v + F_i$, where $F_g = \frac{\pi}{6} L^3 \rho_s g$ is the gravitational force, $F_b = \frac{\pi}{6} L^3 \rho_f g$ is the buoyancy force, $F_v = 6\sqrt{\pi} \mu v \left(\frac{\pi}{4} L^2\right)^{[(a/d_0(S_3))+b]/2}$ is viscous drag and $F_i = \frac{\pi}{16} L^2 \rho_f v^2$ is impact drag (e.g., Maggi, 2013; Maggi and Tang, 2015). Here, μ is the fluid dynamic viscosity, g is the gravitational acceleration, L is the characteristic aggregate size, ℓ is the dimensionless aggregate size, ρ_s and ρ_f are the sediment and fluid densities, respectively, where $a = 9/8$ and $b = 7/8$ of Eq. (4.2) were used with experimental data as in Maggi (2013). Here, $L_p = 0.6 \mu\text{m}$ and $L_p = 2.4 \mu\text{m}$ were used for mineral and organic SPM as per average values in the data base available in Maggi (2013), while $\mu = 1.0 \times 10^{-3} \text{ Pa s}$ and $\rho_f = 1000 \text{ kg/m}^3$ were used.

By knowing the SPM settling velocity v and the size L from experiments, ρ_s and $d_0(S_3)$ remain unknown in the force balance equation. Figure 4.8c and d show the relationship between ρ_s and $d_0(S_3)$ derived using experimental v and L of both organic and mineral SPM, respectively. The estimated $d_0(S_3)$ of mineral SPM yielded $1800 \text{ kg/m}^3 < \rho_s < 2200 \text{ kg/m}^3$ using the approach in this chapter, whereas, the approach in Maggi and Winterwerp (2004) returned $\rho_s \geq 2600 \text{ kg/m}^3$. Because kaolinite mineral has a density not generally exceeding 2600 kg/m^3 , results using Maggi and Winterwerp (2004) might have lower reliability in this circumstance (note, though, that only a few aggregates were used as an illustration, Figure 4.8d). In contrast, both methods returned values

of ρ_s of organic SPM that match previous literature (Maggi, 2013; Curran et al., 2007; Lee et al., 1996), with the method in this chapter returning slightly lower values of ρ_s ($1700 \text{ kg/m}^3 < \rho_s < 1800 \text{ kg/m}^3$) as compared to the earlier approach ($1800 \text{ kg/m}^3 < \rho_s < 1900 \text{ kg/m}^3$) (Figure 4.8c).

4.4 Recommendations

Although the concept that drives the derivation of the method proposed in this chapter is based on the light intensity spectrum of grayscale images, the application of this method does not require the assessment of the full projection-based spectrum $d_{P,I}$; instead, it requires only the determination of $d_{P,0}$ to derive both the analytical spectrum $d_{P,I}$ and the empirical function $f(\ell)$ used to reconstruct $d_0(S_3)$. This method, therefore, provides a simple and effective alternative to improve estimation of $d_0(S_3)$ of SPM from two-dimensional images. The algorithm of this method (a Matlab function script) is provided in Appendix B and as supplementary document in Tang and Maggi (2015c).

Even though the applications of this method to different types of aggregates (*e.g.*, DLA, CCA, SCA and natural SPM) were shown to give good estimation of $d_0(S_3)$ (NRMSE $\leq 10\%$ and R $\geq 98\%$), there exist exceptional cases where the application of this method is biased. For example, derivation of $d_{P,I}$ is not applicable to extensive fractal structures that do not have a definite boundary, and this method would not be appropriate. In addition, application of this method to Euclidean solids with fractal surface would result in biased estimation of $d_0(S_3)$; in fact, a fully solid Euclidean body has $d_0(S_3) = 3$ but its planar projection would show significant perimeter segmentation as a result of its surface roughness and, thus, the application of this method to reconstruct its $d_0(S_3)$ would result in false values. Hence, we recommend this method to be particularly suitable for applications with compact fractal sets such as granular aggregates. If part of the projection-based spectrum of a body looks like any of those presented here, it is presumed that the method proposed here can return a reliable estimation of $d_0(S_3)$.

4.5 Summary

In this chapter, a semi-analytical method to reconstruct the 3D capacity dimension $d_0(S_3)$ of SPM from its 2D grayscale images was presented. This method in this thesis serves as a tool to quantify the internal architecture and space-filling capacity of SPM, and to measure the extent to which SPM structure is governed by microbial activity. This method makes use of the light intensity and perimeter segmentation spectrum of a SPM image to determine the optimum perimeter-based fractal dimension associated to the actual $d_0(S_3)$ of the SPM. The integration of an analytical expression of the spectrum and an empirical intersecting function derived from control aggregates of various nature (*e.g.*, diffusion-limited, cluster-cluster, and self-correlated aggregates) makes this method particularly effective, robust, and user-friendly in that it only requires a binary projection image of SPM under investigation to retrieve its $d_0(S_3)$. Although this method is a generic tool that can be used to estimate $d_0(S_3)$ of any granular aggregates, it was specifically tested against natural SPM to ensure its suitability in this thesis. This method resulted in an average error of 2%, which improved largely the method in Maggi and Winterwerp (2004).

Chapter 5

Characteristics of SPM in nutrient- and biomass-affected waters

Parts of the contents in this chapter were published in Tang and Maggi (2016a)¹ during PhD candidature of the author.

5.1 Introduction

This chapter presents the analyses of SPM characteristics, including size L , capacity dimension d_0 , and settling velocity v , acquired through experiments described in Chapter 3. The analyses aim at investigating the influence of microorganisms on SPM dynamics and how biomass-free and biomass-affected SPM respond to different abiotic conditions, such as the increase of dissolved NH_4^+ and NO_3^- concentrations, turbulence shear rate G , and mineral concentration C_K . The probability distributions of L , d_0 , and v were calculated in all experiments (Appendix C) and were published as supplementary material in Tang and Maggi (2016a), while statistical parameters (e.g., average, median, standard deviation, range, skewness and kurtosis) are summarized in this chapter for synthesis. The statistical (information) entropy of L and d_0 distributions was also assessed to examine how microorganisms can modify not only the physical attributes of SPM, but also the uncertainty and information content of their habitat.

5.2 Data analyses

5.2.1 Analyses of size, capacity dimension, and settling velocity

In experiments described in Chapter 3, 21 suspensions (Table 3.2) with various SPM types (either biomass-free or biomass-affected), C_K and $[\text{NH}_4\text{NO}_3]$ were tested against five G and, hence, resulted in a total of 105 sets of experiments with a total of 154,240 SPM aggregates acquired for analyses.

The size L of a SPM aggregate was calculated as the length of the minimum square enveloping the aggregate image (Maggi, 2003), and its capacity dimension d_0 was reconstructed from the optimal perimeter-based fractal dimension d_P following the algorithm described in Chapter 4.

The settling velocity v was determined as the vertical downwards distance Δy traveled by the aggregate over the time difference Δt between two frames. The positions of aggregates in the first

¹Tang F.H.M., and Maggi F. (2016). A mesocosm experiment of suspended particulate matter dynamics in nutrient- and biomass-affected waters, *Water Research*, 89, 76-86.

and second frames were matched using a probabilistic method, that is, the probability $\Pr(X=X')$ that an aggregate X at position $P = (x, y)$ in the first frame is the aggregate X' at position $P' = (x', y')$ in the second frame was assessed as

$$\Pr(X=X') = \left(1 - \frac{\Delta D_{X'}}{D_{max}}\right) \times \left(1 - \frac{\Delta L_{X'}}{L_{max}}\right) \times \left(1 - \frac{\Delta A_{agg_{X'}}}{A_{agg_{max}}}\right), \quad (5.1)$$

where $\Delta D_{X'} = \sqrt{(x - x')^2 + (y - y')^2}$ is the distance traveled by aggregate X from position P to position P' , D_{max} is the maximum distance that aggregate X can travel (i.e., the diagonal of the camera field view); $\Delta L_{X'}$ and $\Delta A_{agg_{X'}}$ are the differences in size L and area A_{agg} between aggregate X and aggregate X' , respectively; while, L_{max} and $A_{agg_{max}}$ are the maximum L and A_{agg} that aggregate X can have (i.e., the size and area of the camera field view, respectively). Eq. (5.1) denotes that aggregate X' has a high probability to be aggregate X if $\Delta D_{X'}$, $\Delta L_{X'}$ and $\Delta A_{agg_{X'}}$ are very small. The vertical traveled distance Δy of an aggregate and, hence, its settling velocity v , can then be determined after mapping the positions of the aggregates in the two frames. To include only aggregates with velocity contributed purely by gravitational effect, aggregates that were either not moving or floating upwards, and aggregates that traveled horizontally by $|\Delta x| > 0.1\Delta y$ were excluded from the analyses of settling velocity.

5.2.2 Statistical quantification

Statistical parameters (e.g., average, median, standard deviation, range, skewness and kurtosis) of L , d_0 , and v of SPM in all experiments were then analysed and compared. The skewness $\gamma_{1,o}$ of an observed variable o was calculated as the standardized third central moment as $\gamma_{1,o} = 1/n_o \sum_{i=1}^{n_o} (o_i - \bar{o})^3 / (1/n_o \sum_{i=1}^{n_o} (o_i - \bar{o})^2)^{3/2}$, where n_o and \bar{o} are the total number and mean of observed variable o , respectively. The excess kurtosis $\gamma_{2,o}$ of an observed variable o can be determined as the standardized fourth moment about the mean as $\gamma_{2,o} = (1/n_o \sum_{i=1}^{n_o} (o_i - \bar{o})^4 / (1/n_o \sum_{i=1}^{n_o} (o_i - \bar{o})^2)^2) - 3$. Note that, a normal distribution has $\gamma_1 = \gamma_2 = 0$.

One-way analysis of variance (ANOVA) was conducted to test the null hypothesis that nutrient- and biomass-free (NFBF), nutrient-affected and biomass-free (NABF), and nutrient- and biomass-affected (NABA) aggregates have equal average L , d_0 , and v (*anova1* function in Matlab2011b). If the null hypothesis is rejected (i.e., $p < 0.01$), multiple comparison *post hoc* test using Tukey's procedure was carried out to identify the SPM type that is different from the others (*multcompare* function in Matlab2015a).

The correlation coefficient R between SPM characteristics (L , d_0 , and v) and C_K and $[\text{NH}_4\text{NO}_3]$ were also calculated as $R(o, o') = \text{cov}(o, o') / \sigma_o \sigma_{o'}$, where o and o' are two different quantities, respectively.

5.2.3 Background of statistical entropy

The concept of entropy is still nowadays a much debated topic since it was first introduced in thermodynamics by Clausius in the 19th century as a measure of macroscopic properties of a system. Clausius (1864) defined the change in entropy of a system from state X to X' (i.e., $E(X') - E(X)$) as the sum of infinite small increments of heat added (dq) to the system divided by the absolute temperature T at which the heat was supplied, such that, $E(X') - E(X) = \int_X^{X'} dq/T$. Boltzmann (1896) later proposed that macroscopic properties of a system are governed by the dynamics at microscopic level and a macrostate can result from many different microstates or different configurations

of molecular motion. Boltzmann's investigations revealed a connection between thermodynamics entropy and the statistical concept of uncertainties (or information) following his definition of entropy as (Boltzmann, 1896)

$$E = k_B \ln W, \tag{5.2}$$

where k_B is the Boltzmann constant and W is the number of microstates. This equation quantitatively measures the atomic or molecular disorderliness of a system, which can be interpreted as the uncertainty associated in predicting the microstate of that system.

Independently, Shannon (1948) proposed a quantity, also named entropy, to measure the uncertainty (or information) of a well-defined question Q given the knowledge P about Q (in mathematical term, P is the probability distribution of the possible answers to Q) as

$$E(Q|P) = -k_S \sum_{i=1}^{N_Q} p_{r_i} \ln p_{r_i}, \tag{5.3}$$

where N_Q is the number of possible answers to Q , p_{r_i} is the probability assigned to each answer i , and k_S is an arbitrary dimensional constant. To not create confusion, we clarify here that an increase in either Boltzmann entropy Eq. (5.2) or Shannon entropy Eq. (5.3) signifies an increase in uncertainty and a decrease in information. Many studies have shown that Boltzmann and Shannon entropy are similar in many ways (e.g., Raymond, 1950; Brillouin, 1951; Tribus and McIrvine, 1971). For example, assuming a macrostate that has 2 possible microstates (i.e., $W = 2$ in Eq. (5.2) and $N_Q = 2$ in Eq. (5.3)) with equal probabilities (i.e., $p_{r_1} = p_{r_2} = 0.5$), Shannon entropy yields the same result as the Boltzmann entropy by substituting the arbitrary constant k_S in Eq. (5.3) with k_B (i.e., $E = k_B \ln 2$).

Many studies tried to establish a connection between information, energy, and entropy. Among many, Maxwell (1871) was one of the pioneers who demonstrated that entropy can be decreased with the presence of information. Brillouin (1951) later suggested that the acquisition of information requires a source of illumination (in the case of Maxwell's demon), which is, in fact, a source of energy. This shows the interconnectedness between energy and information, i.e., energy is required to obtain information and information is required to harness energy (Tribus and McIrvine, 1971). Following this line, many scientists showed that the second law of thermodynamics is always obeyed as the net entropy of a system will always be positive even though the uncertainty or disorderliness of the system was decreased (e.g., Brillouin, 1951; Evans, 1969). We note that information has a role in affecting the entropy of a system but it does not represent the overall entropy.

This chapter is not aiming at describing the overall entropy of a system; instead, it aims at quantifying the uncertainties and disorderliness introduced by SPM-attached microorganisms to their habitat. To this purpose, analyses were proceeded by adopting the entropy defined by Shannon (1948) as in Eq. (5.3).

The questions $Q(L)$ and $Q(d_0)$ in Eq. (5.3) were defined here as: what could be the size L and capacity dimension d_0 of a SPM aggregate randomly selected from a suspension. The knowledge P about Q was the experimentally-acquired probability distributions of L and d_0 . The number of possible answers to Q (N_Q in Eq. (5.3)) was determined by the number of bins N_b of the probability distributions. Selection of N_b can be tricky because the disorderliness of a system could become $E(Q|P) \rightarrow \infty$ when $N_b \rightarrow \infty$, provided that there exists infinite number of observations n_o with infinite precision δ_o . In experiments where n_o and δ_o are finite, $E(Q|P)$ increases to an asymptotic value where further increase in N_b will no longer lead to any increase in $E(Q|P)$. Because this asymptotic value is generally limited by δ_o for samples with sufficiently large n_o , we suggest here

that probability distributions can be calculated with bin width $\Delta x = \delta_o$ and, hence, $N_Q = N_b = (x_{max} - x_{min})/\Delta x$ with x_{max} and x_{min} the maximum and minimum values of a set of observations, respectively. Note also that, $p_{r_i} \ln p_{r_i} = 0$ when $p_{r_i} = 0$ is assigned to an answer i (i.e., $\lim_{x \rightarrow 0^+} x \ln x = 0$ according to L'Hôpital's rule) and $k_S = 1$ was used throughout this chapter (i.e., $E(Q|P)$ is dimensionless).

5.3 Results

5.3.1 SPM size distribution

NFBF experiments were observed to have the smallest average \bar{L} and median \tilde{L} aggregate size (Figure 5.1, first row, green markers), followed by NABF experiments (blue markers) with approximately 16% increase, and by NABA experiments (red markers), with 60% greater \bar{L} and \tilde{L} than NFBF. Generally, \bar{L} and \tilde{L} decreased with increasing G regardless of suspension type. An increase in $[\text{NH}_4\text{NO}_3]$ did not lead to a detectable variation in NABF experiments, but \bar{L} increased in NABA experiments at $G < 64 \text{ s}^{-1}$ with correlation $R(\bar{L}, [\text{NH}_4\text{NO}_3])$ generally greater than 0.9 (Figure 5.2a). Although an increasing C_K led to increasing \bar{L} in NFBF and NABF aggregates (i.e., $R(\bar{L}, C_K) > 0$, Figure 5.2b), a conclusive pattern describing the effect of C_K on \bar{L} of NABA SPM could not be determined within the C_K range tested in this study due to relatively low $R(\bar{L}, C_K)$.

The standard deviations σ_L of NFBF and NABF aggregate size distributions were relatively similar, while σ_L of NABA size distributions was approximately 120% greater than NFBF (Figure 5.1, second row). The NABA size distributions also spanned across a wider size range as compared to NFBF and NABF.

All experiments showed $\gamma_{1,L} > 0$ and $\gamma_{2,L} > 0$, meaning that the size distributions were right-skewed with heavier tails than a normal distribution (Figure 5.1, third row). This feature was not significantly affected by G and C_K , confirming the concept of invariancy of the size distribution shape against G and C_K hypothesized in Hunt (1982) and Milligan and Hill (1998). NABA size distributions generally had distinctively greater $\gamma_{1,L}$ and $\gamma_{2,L}$, hence, resulting in a shape significantly different than that of NFBF and NABF.

From the above results, many aspects can be highlighted, and the most important are the following. First, all data points relative to NABA experiments (red) in Figure 5.1 scattered distinctively away from NABF (blue) and NFBF (green) experiments, clearly indicating that the presence of biomass led to a sharp differentiation in flocculated SPM, which was especially visible at low G values. One-way ANOVA (Table 5.1) confirmed that the variance in \bar{L} for NABA as compared to NFBF and NABF aggregates was significant (i.e., $p < 0.01$), while no significant difference was found for NABF as compared to NFBF aggregates (i.e., $p > 0.01$). Results agree with earlier literature where biomass-affected aggregates were found to be bigger than mineral aggregates as a result of microbial colonization (e.g., Kiørboe, 2001; Grossart et al., 2006) and the binding due to EPS and TEP (e.g., Jackson, 1995; Tan et al., 2012). NABA aggregates had size relatively similar to aggregates found in activated sludge (i.e., in the range between 10 and 1000 μm , e.g., Li and Ganczarczyk, 1987; Andreadakis, 1993), but the NABA suspensions were too different from activated sludge (typical of waste water treatment reactors), which generally has higher organic matter content and higher concentrations of various types of both organic and mineral nutrients, to set a comparison.

Second, an increasing turbulence shear had the effect of homogenizing \bar{L} and \tilde{L} toward smaller values in all experiments, and to decrease σ_L . This trend has largely been documented for mineral aggregates (e.g., Spicer and Pratsinis, 1996; Milligan and Hill, 1998; Maggi, 2005), while these results as well as those in Wingender et al. (1999) and Sheng et al. (2006) suggest that also biomass-affected

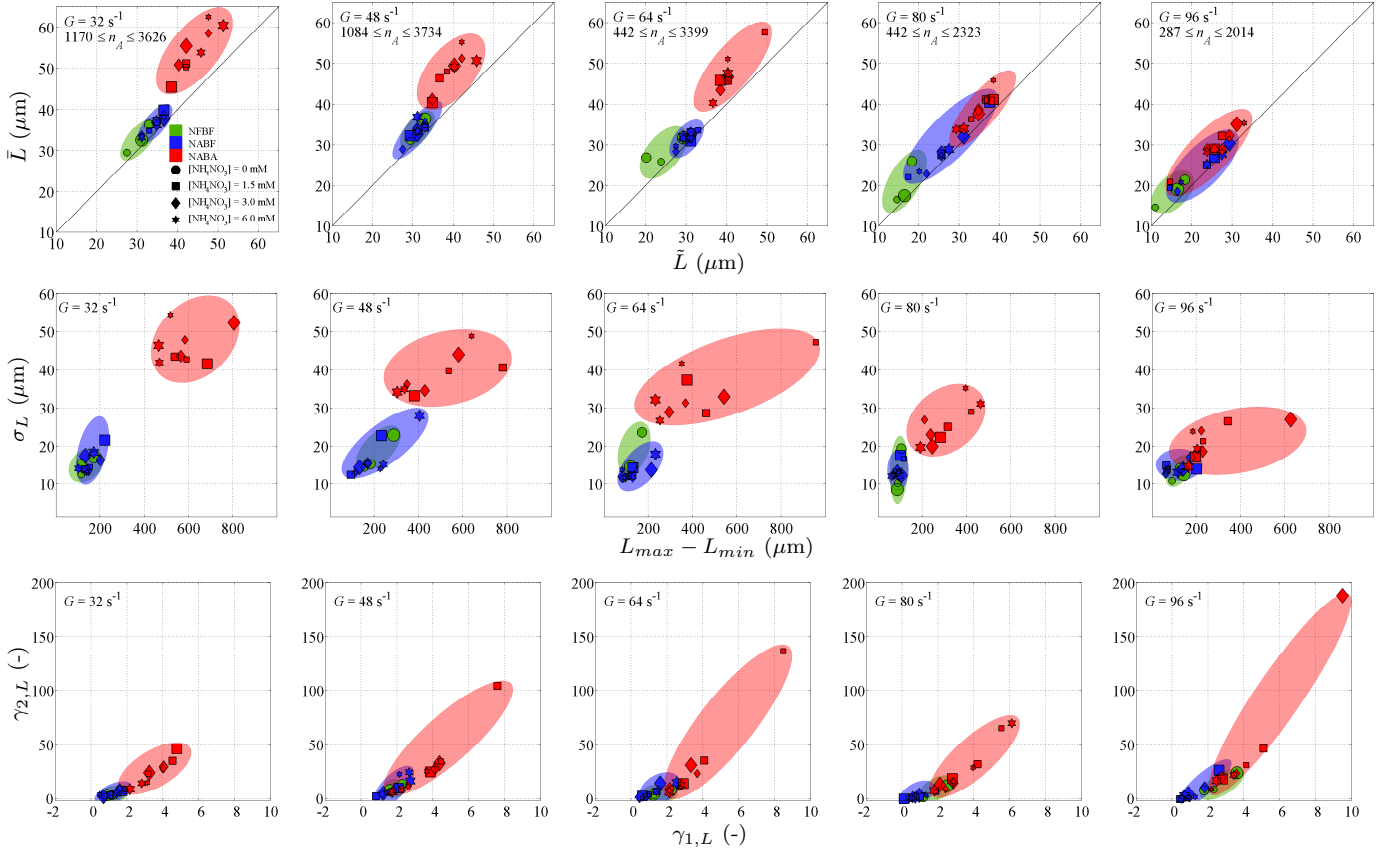


Figure 5.1: Average \bar{L} against median \tilde{L} (first row), standard deviation σ_L against size range ($L_{max} - L_{min}$) (second row), and excess kurtosis $\gamma_{2,L}$ against skewness $\gamma_{1,L}$ (third row) of SPM size distributions for nutrient- and biomass-free (NFBF), nutrient-affected and biomass-free (NABF) and, nutrient- and biomass-affected (NABA) suspension types with $[\text{NH}_4\text{NO}_3] = \{0, 1.5, 3.0, 6.0\}$ mM, $G = \{32, 48, 64, 80, 96\}$ s⁻¹ (first to fifth column), and $C_K = \{0.1, 0.2, 0.4\}$ g/L (corresponding to small, medium, and large markers, respectively), while, n_A is the number of aggregates analysed in an experimental set.

aggregates undergo a similar increase in breakup rate or detachment of superficial matter (cells and metabolic products).

Finally, an increase in free ion concentrations after NH_4NO_3 amendments slightly increased \bar{L} in NABF experiments, possibly due to a compression of the double layer around kaolinite minerals. The greater increase in \bar{L} and \tilde{L} in NABA associated with the presence of biomass was enhanced by increased $[\text{NH}_4\text{NO}_3]$ because NH_4NO_3 promotes biomass growth that eventually aids in SPM aggregation. This effect was somehow reduced when G increased as shown by $R(\bar{L}, [\text{NH}_4\text{NO}_3])$ becoming negative. This result suggests that the strength of bonding in NABA aggregates at high $[\text{NH}_4\text{NO}_3]$ was smaller than at low $[\text{NH}_4\text{NO}_3]$ either because aggregates were larger, or because different microorganisms have developed at different $[\text{NH}_4\text{NO}_3]$. Along this line, Sheng et al. (2006) observed that aggregates colonized by aerobic microorganisms had higher strength in withstanding shear than aggregates colonized by anaerobic microorganisms.

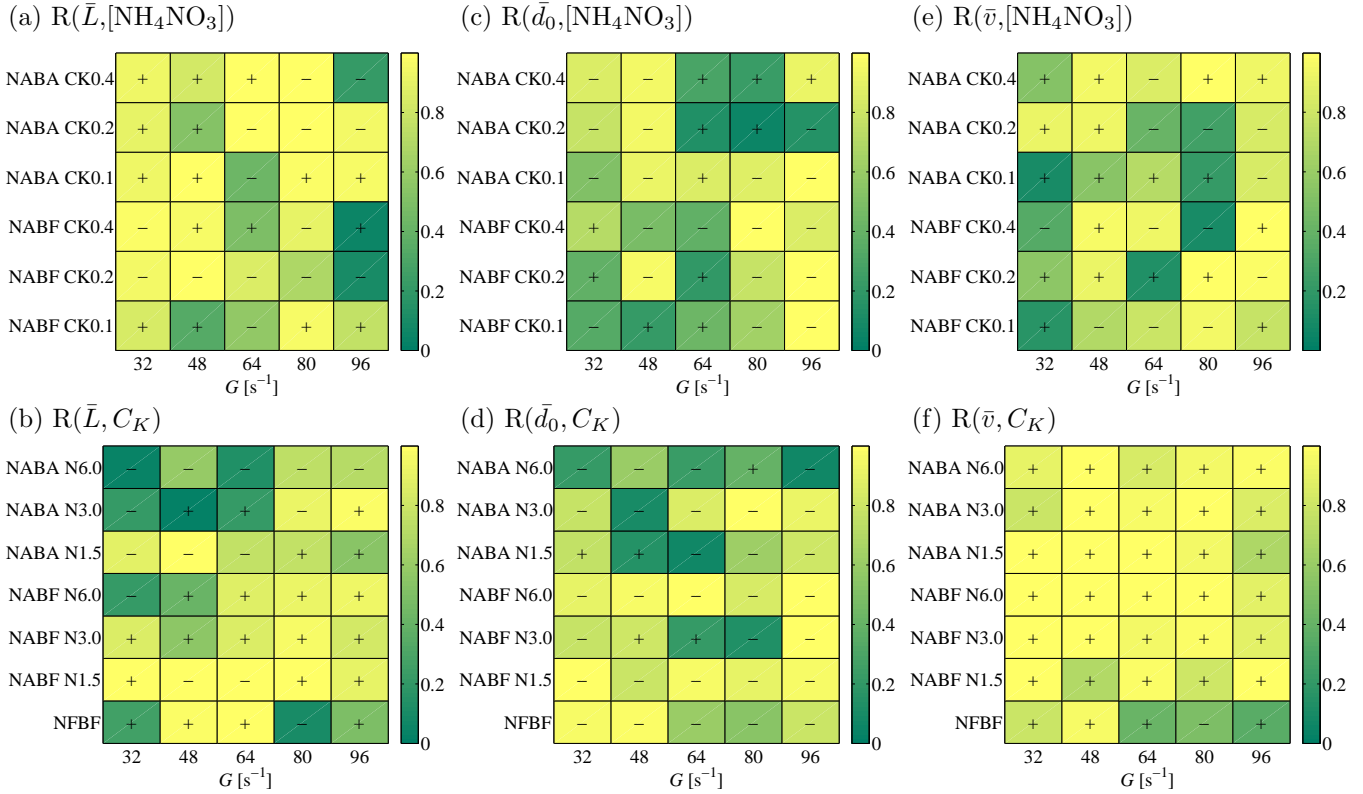


Figure 5.2: Correlation of \bar{L} (first column), \bar{d}_0 (second column), and \bar{v} (third column) with NH_4NO_3 concentration $[\text{NH}_4\text{NO}_3]$ (first row) and kaolinite concentration C_K (second row) for nutrient- and biomass-free (NFBF), nutrient-affected and biomass-free (NABF), and nutrient- and biomass-affected (NABA) suspension types, and for G ranging between 32 s^{-1} and 96 s^{-1} . CK0.1, CK0.2, and CK0.4 denote $C_K = 0.1$ g/L, $C_K = 0.2$ g/L, and $C_K = 0.4$ g/L, respectively. N1.5, N3.0, and N6.0 denote $[\text{NH}_4\text{NO}_3] = 1.5$ mM, $[\text{NH}_4\text{NO}_3] = 3.0$ mM and $[\text{NH}_4\text{NO}_3] = 6.0$ mM, respectively. '+' and '-' indicate positive and negative correlation, respectively.

Table 5.1: Results of one-way analysis of variance (ANOVA) and multiple comparison *post hoc* test for the null hypothesis that nutrient- and biomass-free (NFBF), nutrient-affected and biomass-free (NABF) and nutrient- and biomass-affected (NABA) aggregates are equal in size L , capacity dimension d_0 , and settling velocity v . Significance $p < 0.01$ indicates that the null hypothesis is rejected.

Test	L Significance p	d_0 Significance p	v Significance p
One-way ANOVA	<0.01	<0.01	<0.01
Multiple comparison post hoc test			
NFBF and NABF	0.15	0.50	0.065
NFBF and NABA	<0.01	<0.01	<0.01
NABF and NABA	<0.01	<0.01	0.037

5.3.2 SPM capacity dimension distribution

Experimental d_0 was observed to range between 1.8 and 3.0, matching those in Chu et al. (2004) and Vahedi and Gorczyca (2011). Figure 5.3 (first row) and ANOVA test (Table 5.1) show that NFBF and NABF experiments had significantly similar averages \bar{d}_0 (i.e., $p > 0.01$), while a significant

difference was observed between NABA and the other two SPM types (i.e., $p < 0.01$), with NABA experiments having the lowest \bar{d}_0 . This, therefore, highlights the role biomass plays in altering not only the size (Chapter 5.3.1) but also the aggregate internal architecture and surface irregularity. Observed \bar{d}_0 increased with increasing G regardless of suspension type. $[\text{NH}_4\text{NO}_3]$ did not affect \bar{d}_0 in NABF experiments (i.e., relatively low $R(\bar{d}_0, [\text{NH}_4\text{NO}_3])$, Figure 5.2c), but led to decreasing \bar{d}_0 in NABA experiments at $G < 64 \text{ s}^{-1}$ ($R(\bar{d}_0, [\text{NH}_4\text{NO}_3]) < -0.8$). An increasing C_K decreased slightly \bar{d}_0 in NFBBF and NABF experiments ($R(\bar{d}_0, C_K) < -0.7$, Figure 5.2d), while no effect was found in NABA experiments.

The standard deviation σ_{d_0} and range ($d_{0_{max}} - d_{0_{min}}$) of the three SPM types were relatively close (Figure 5.3, second row), with NABA aggregates having slightly higher σ_{d_0} .

Finally, $\gamma_{1,d_0} < 0$ and $\gamma_{2,d_0} > 0$ were found for all experiments, meaning that the capacity dimension distributions were left-skewed with heavier tails than a normal distribution (Figure 5.3, third row).

Results are overall consistent with earlier studies, with biomass-affected aggregates having generally lower fractal dimension than biomass-free aggregates be conclusive enough a result after Logan and Wilkinson (1990); Kilps et al. (1994); Vahedi and Gorczyca (2011); Tan et al. (2012); Maggi and Tang (2015). Additionally, our experiments also show that the effect of turbulence in increasing \bar{d}_0 applies to biomass-affected aggregates as much as mineral-only aggregates (e.g., Meakin and Jullien, 1988; Clark and Flora, 1991), suggesting that the biomass and its byproduct do not necessarily increase the aggregate resistance to shear.

5.3.3 Capacity dimension and size of SPM

To examine if the biomass had an impact on the correlation between d_0 and L , d_0 values of aggregates of the same SPM type and mixed under the same G were bin averaged and plotted against their corresponding L (Figure 5.4). The scaling law in Maggi (2005); Khelifa and Hill (2006); Maggi (2007) was used

$$d_0 = \delta \left(\frac{L}{L_p} \right)^\gamma, \quad (5.4)$$

where δ and L_p are capacity dimension and size of the primary particle, respectively, and γ is the characteristic rate of change in d_0 over L/L_p . An unconstrained fitting was used to determine the values of δ and γ , while, L_p values were constrained to be within the minimum L and the first decile of the aggregate size distribution.

The γ values in Eq. (5.4) were found to be always negative, indicating that d_0 generally decreased as a function of L (Figure 5.4). The L_p values ranged between $5.7 \mu\text{m}$ and $12.7 \mu\text{m}$ with NABA experiments having slightly greater L_p than NFBBF and NABF; the δ values ranged between 2.78 and 2.89 with no clear trend found between each SPM type.

By comparing Eq. (5.4) after fitting δ , L_p and γ (Figure 5.4), we observed that d_0 was relatively similar for $L < 10 \mu\text{m}$ regardless of SPM type, whereas, NABA experiments had higher d_0 for $L \geq 10 \mu\text{m}$ compared to NFBBF, except for the case of $G = 80 \text{ s}^{-1}$.

These analyses allow us to refine our current understanding and state that the presence of biological matter alone does not lead to low aggregate d_0 ; instead, it is the greater \bar{L} from an increased aggregation rate, facilitated by the presence of biomass, that results in lower \bar{d}_0 of biomass-affected as compared to biomass-free aggregates.

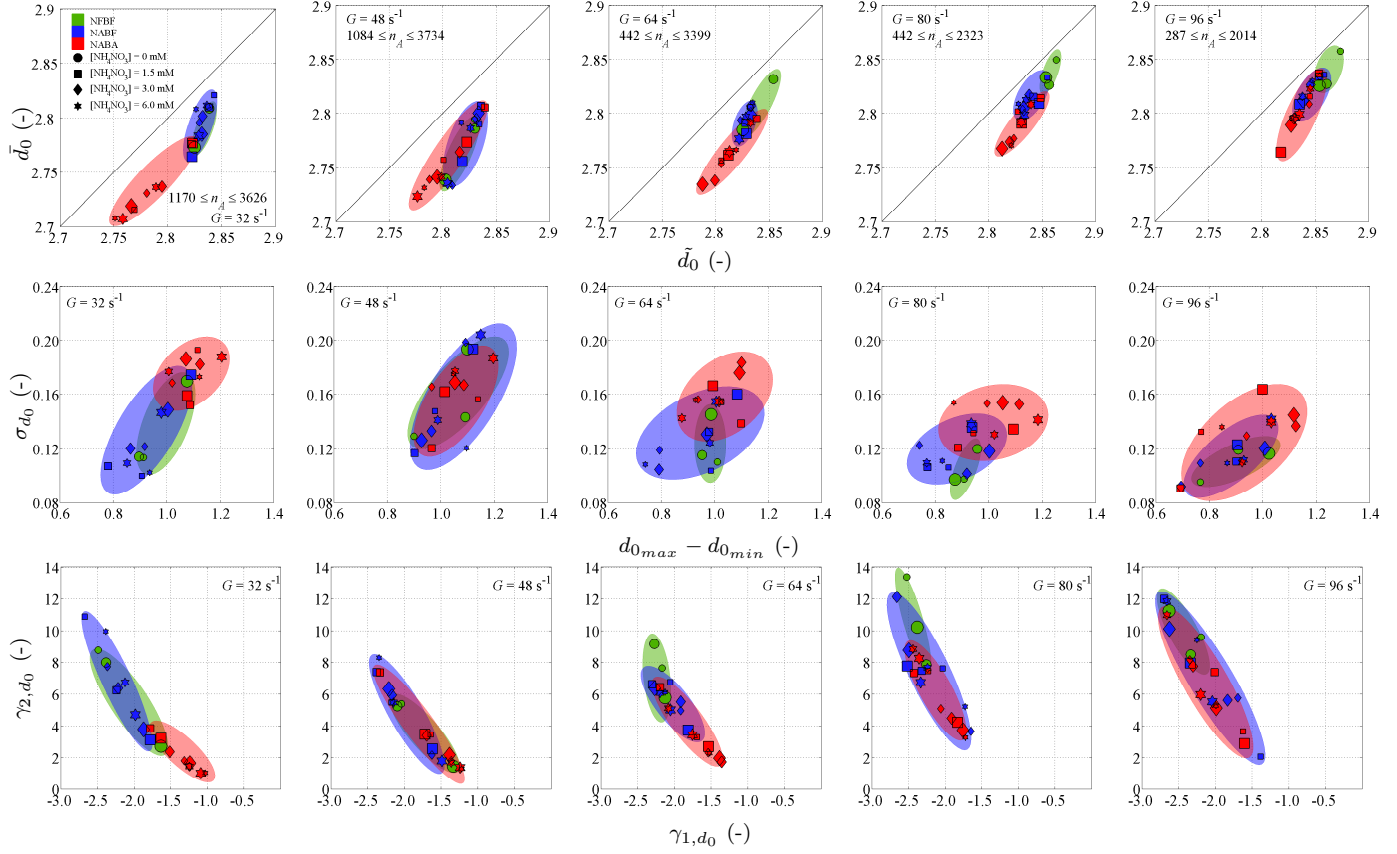


Figure 5.3: Average \bar{d}_0 against median \tilde{d}_0 (first row), standard deviation σ_{d_0} against capacity dimension range ($d_{0,max} - d_{0,min}$) (second row), and excess kurtosis γ_{2,d_0} against skewness γ_{1,d_0} (third row) of SPM capacity dimension distributions for nutrient- and biomass-free (NFBF), nutrient-affected and biomass-free (NABF) and, nutrient- and biomass-affected (NABA) suspension types with $[\text{NH}_4\text{NO}_3] = \{0, 1.5, 3.0, 6.0\}$ mM, $G = \{32, 48, 64, 80, 96\}$ s⁻¹ (first to fifth column), and $C_K = \{0.1, 0.2, 0.4\}$ g/L (corresponding to small, medium, and large markers, respectively), while, n_A is the number of aggregates analysed in an experimental set.

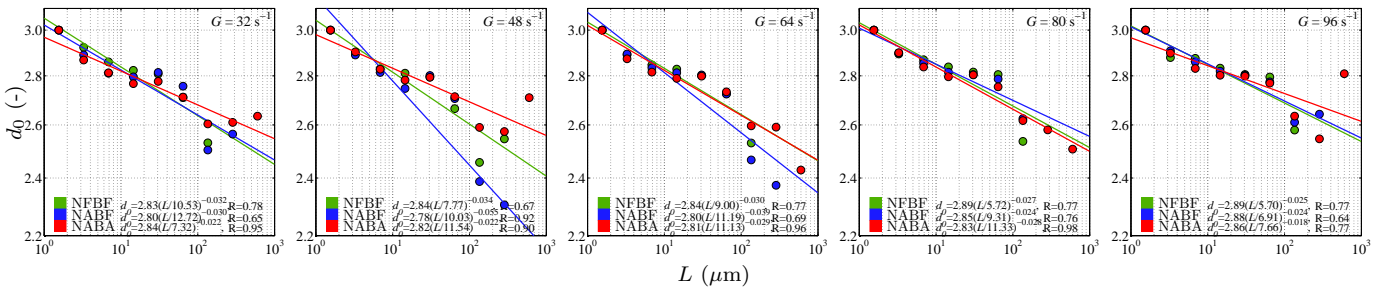


Figure 5.4: Bin-averaged capacity dimension d_0 against aggregate size L for experiments of nutrient- and biomass-free (NFBF, green), nutrient-affected and biomass-free (NABF, blue) and nutrient- and biomass-affected (NABA, red) with $G = \{32, 48, 64, 80, 96\}$ s⁻¹ (left to right). The correlation coefficient R represents the goodness of fit of Eq. (5.4) against experiments.

5.3.4 SPM settling velocity distribution

All experimental data accumulated on the 1:1 line in the (\bar{v}, \tilde{v}) plot (Figure 5.5, first row), suggesting that the settling velocity distributions were close to normal regardless of SPM type (i.e., skewness

$\gamma_{1,v} \simeq \gamma_{2,v} \simeq 0$, Figure 5.5, third row). NFBF aggregates were found to have the lowest \bar{v} , followed by an increasing order of NABA and NABF aggregates. An increase in G resulted in a slight decrease in \bar{v} , especially in NABA aggregates. The correlation between \bar{v} and $[\text{NH}_4\text{NO}_3]$ was found to be relatively weak (Figure 5.2e), whereas, an increasing C_K was observed to cause a slight increase in \bar{v} of all SPM types ($R(\bar{v}, C_K) > 0.8$, Figure 5.2f).

Note also that all distributions at low G (regardless of SPM type and $[\text{NH}_4\text{NO}_3]$) had relatively similar values of σ_v , $\gamma_{1,v}$ and $\gamma_{2,v}$, denoting that the settling velocity distributions were not substantially affected by the presence of nutrient and biomass.

In general, results compare well with most data sets in the database available in Maggi and Tang (2015), with individual aggregates having v ranging between 0.06 mm/s and 2.45 mm/s. As opposed to the shared consensus that an increasing L leads to an increasing v , the substantial increase in \bar{L} due to biomass presence (Figure 5.1, first row) resulted only in 0.1 mm/s greater \bar{v} than biomass-free aggregates. In fact, the null hypothesis that NABF and NABA aggregates had no substantial variation in \bar{v} could not be rejected by the ANOVA and *post hoc* tests (i.e., $p > 0.01$, Table 5.1). Thanks to our previous analyses (Section 3.2), we can now explain this as a result of NABA aggregates having lower \bar{d}_0 as compared to NABF aggregates and, hence, the effect of increasing \bar{L} on \bar{v} was counterbalanced by the effect of decreasing \bar{d}_0 .

When the biomass was not present, addition of NH_4NO_3 in NABF experiments did not alter substantially \bar{L} and \bar{d}_0 as compared to NFBF, but \bar{v} was found to be significantly higher than in NFBF aggregates (i.e., $p < 0.01$, Table 5.1). It is put forth here that NH_4NO_3 may have modified the surface charge of kaolinite mineral in addition to suppressing the electrical double layer, and this may have facilitated face-to-face aggregation and increased the aggregate compactness without being captured by d_0 .

Finally, an increasing \bar{v} observed with increasing C_K was in agreement with findings in previous literature when $C_K < 3000$ mg/L (e.g., Thorn, 1981; Ross, 1988; Milligan and Hill, 1998). Because C_K was not strongly correlated to \bar{L} and \bar{d}_0 , this increase in \bar{v} may have been caused by other factors.

5.3.5 Settling velocity and size of SPM

An increasing bin-averaged v was observed with increasing L regardless of SPM types (Figure 5.6, first row), confirming the findings reported in most previous studies (e.g., Gibbs, 1985; Lick et al., 1993; Jarvis et al., 2006). More importantly, NABA aggregates were found to have slightly lower or approximately similar v as compared to NABF aggregates of the same size, agreeing with analyses in Maggi (2013), and Maggi and Tang (2015) that v within the same L range was statistically similar regardless of SPM composition. This slightly lower v observed for NABA aggregates could be explained by the fact that NABA aggregates contained mostly biological matter (e.g., cells and metabolic products) that have lower density than kaolinite mineral.

5.3.6 Entropy of size and capacity dimension

The entropy of settling velocity v distributions was not analysed here even though measurements were available from experiments because v was found in the previous sections to be relatively invariant of SPM type.

Two general trends of the entropy of SPM size distribution $E[Q(L)|P(L)]$ and capacity dimension distribution $E[Q(d_0)|P(d_0)]$ were observed in Figure 5.7. On the one hand, $E[Q(d_0)|P(d_0)]$ was generally higher than $E[Q(L)|P(L)]$ for all tested suspensions, implying that SPM was more uncertain in its internal architecture relative to its size. On the other hand, NABA SPM had significantly

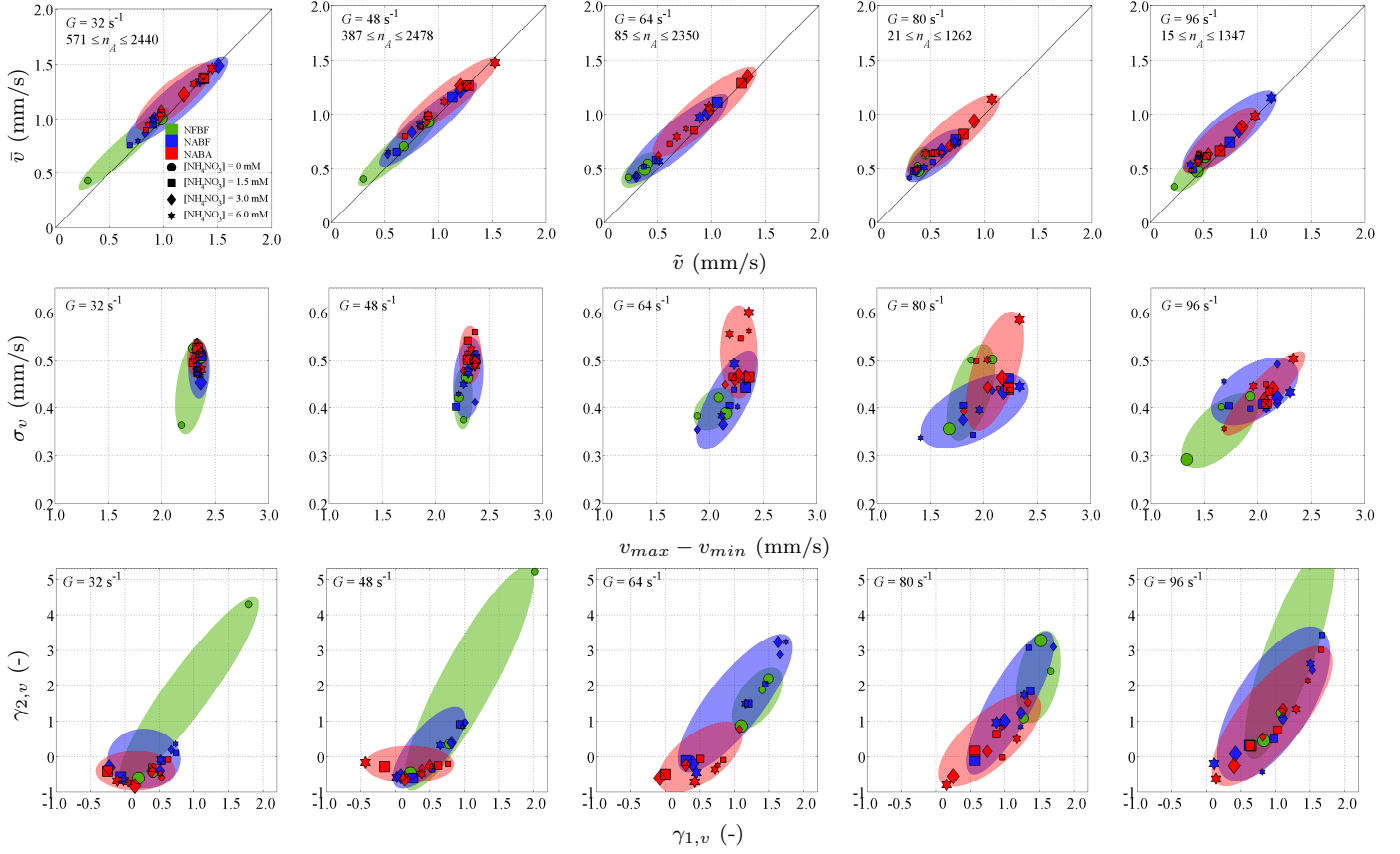


Figure 5.5: Average \bar{v} against median \tilde{v} (first row), standard deviation σ_v against settling velocity range ($v_{max} - v_{min}$) (second row), and excess kurtosis $\gamma_{2,v}$ against skewness $\gamma_{1,v}$ (third row) of SPM settling velocity distributions for nutrient- and biomass-free (NFBF), nutrient-affected and biomass-free (NABF) and, nutrient- and biomass-affected (NABA) suspension types with $[\text{NH}_4\text{NO}_3] = \{0, 1.5, 3.0, 6.0\}$ mM, $G = \{32, 48, 64, 80, 96\}$ s $^{-1}$ (first to fifth column), and $C_K = \{0.1, 0.2, 0.4\}$ g/L (corresponding to small, medium, and large markers, respectively), while, n_A is the number of aggregates analysed in an experimental set.

higher $E[Q(L)|P(L)]$ than biomass-free SPM (NFBF and NABF) in all tested abiotic conditions. NABA suspensions, however, showed significantly greater $E[Q(d_0)|P(d_0)]$ than that of biomass-free suspensions (Figure 5.7, first column) only in low turbulence conditions (i.e., $G = 32$ s $^{-1}$).

ANOVA analyses showed that $E[Q(L)|P(L)]$ and $E[Q(d_0)|P(d_0)]$ of NFBF and NABF suspensions were not significantly affected by the increase of G ; conversely, $E[Q(L)|P(L)]$ and $E[Q(d_0)|P(d_0)]$ of NABA suspensions decreased significantly with increasing G (results of ANOVA are not shown here). In all tested suspension types, C_K and $[\text{NH}_4\text{NO}_3]$ did not show significant effect on either $E[Q(L)|P(L)]$ or $E[Q(d_0)|P(d_0)]$.

The results shown here suggest that microorganisms can shift the information content and the disorderliness of SPM physical state away from abiotic conditions; this finding could be explained with the following reasonings. Microbial metabolism and growth are irreversible processes that increase the internal entropy of living cells (Von Stockar and Liu, 1999) according to the second law of thermodynamics. However, all organisms, including microorganisms, need to maintain themselves in a low state of entropy in order to maintain their highly ordered structures (e.g., chromosomes) and to evade from decaying into an inert state of equilibrium, which is eventually the death. Schrödinger (1944) suggested that organisms can achieve this because they are “fed on negative entropy”, mean-

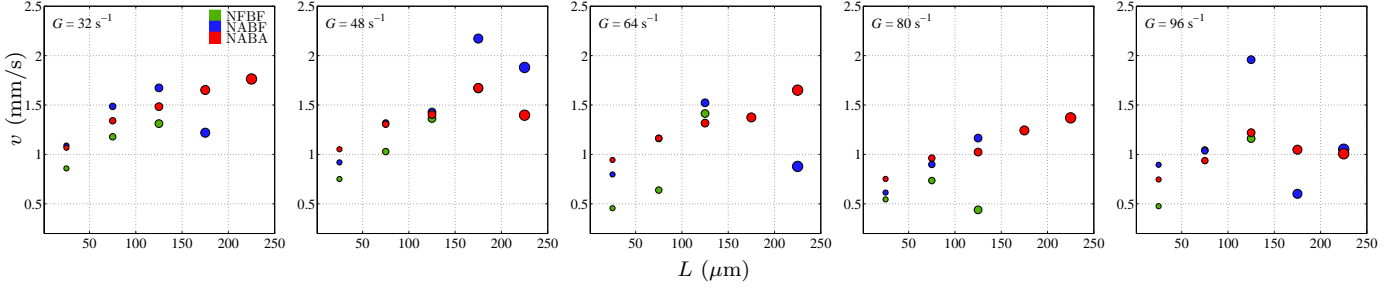


Figure 5.6: Bin-averaged settling velocity v against aggregate size L for experiments of nutrient- and biomass-free (NFBF, green), nutrient-affected and biomass-free (NABF, blue) and nutrient- and biomass-affected (NABA, red) with $G = \{32, 48, 64, 80, 96\} \text{ s}^{-1}$ (left to right).

ing that the internal entropy produced during metabolism is transferred to the external environment; in other words, microorganisms increase the entropy, or the disorderliness, of the environment to create a sharp transmembrane entropy gradient between living cells and the non-living habitat in order for them to carry out highly specific tasks required for living (Gatenby and Frieden, 2007). Along this line, Jacob et al. (2006) proposed that microorganisms consume also the latent information embedded in their habitat, i.e., microorganisms have the natural intelligence to extract information in the environment, and process and store the information within cells (e.g., Camilli and Bassler, 2006; Gatenby and Frieden, 2007); these processes increase their own information content and could potentially decrease the information content of the environment. We indeed observed that microbial activities have introduced higher uncertainties (lower information) to the size and internal architecture of SPM (i.e., higher $E[Q(L)|P(L)]$ and $E[Q(d_0)|P(d_0)]$) as compared to biomass-free SPM.

These results also demonstrate that variations in abiotic factors (e.g., G , C_K , and $[\text{NH}_4\text{NO}_3]$) did not cause significant shift in $E[Q(L)|P(L)]$ and $E[Q(d_0)|P(d_0)]$ of biomass-free suspensions. This observation suggests that the presence of microorganisms is the major factor that controls $E[Q(L)|P(L)]$ and $E[Q(d_0)|P(d_0)]$, hence, strengthening the argument put forth in this thesis that microorganisms play a crucial role in modulating the characteristics of SPM. We noted also that $E[Q(L)|P(L)]$ and $E[Q(d_0)|P(d_0)]$ of biomass-affected suspensions were susceptible to the increase of G , i.e., the increase in entropy caused by microbial metabolism has been constrained by the high dissipation energy introduced into the system due to high turbulence.

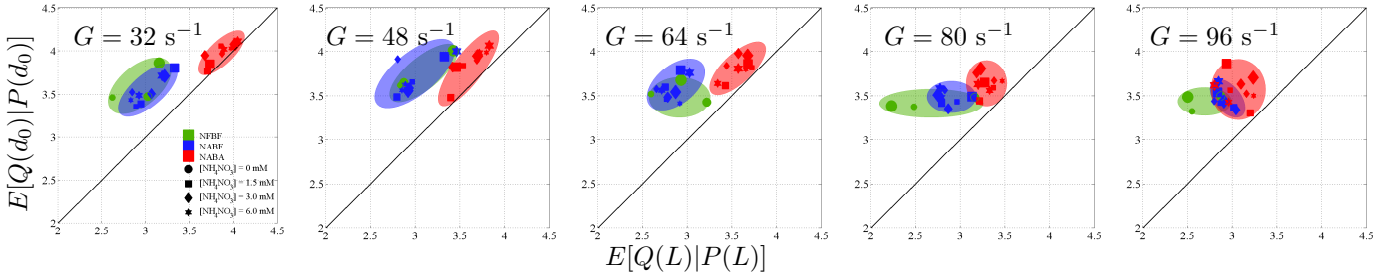


Figure 5.7: Entropy of SPM capacity dimension distribution $E[Q(d_0)|P(d_0)]$ against entropy of SPM size distribution $E[Q(L)|P(L)]$ for nutrient- and biomass-free (NFBF), nutrient-affected and biomass-free (NABF), and nutrient- and biomass-affected (NABA) suspensions with $[\text{NH}_4\text{NO}_3] = \{0, 1.5, 3.0, 6.0\} \text{ mM}$, mineral concentration $C_K = \{0.1, 0.2, 0.4\} \text{ g/L}$ (corresponding to small, medium, and large markers, respectively), and turbulence shear rate $G = \{32, 48, 64, 80, 96\} \text{ s}^{-1}$ (first to fifth column).

5.4 Summary

Many experimental findings emerged from the analyses presented in this chapter, the most important of which being the comprehensive picture given to the response of SPM characteristics against nutrient and microorganisms in isolated tests. Experimental evidence presented here has highlighted the role of microorganisms in modifying not only the structure and characteristics of SPM, but also in increasing the complexity and non-linearity of SPM flocculation dynamics, and its response to environmental factors.

The presence of microorganisms, along with nutrients, facilitated flocculation and resulted in average SPM size substantially larger (approximately 60% larger), and average capacity dimension slightly lower (approximately 2% lower) than biomass-free SPM, presuming that the addition of nutrients enhanced the growth and metabolic activity of SPM-attached living microorganisms. The addition of nutrients (NH_4^+ and NO_3^-) in pure mineral suspension (biomass-free) altered only slightly the size and capacity dimension of SPM; conversely, the size of biomass-affected SPM increased and the capacity dimension decreased with increasing nutrient concentration. Both biomass-free and biomass-affected SPM experienced breakup with increasing turbulence intensity, however, this effect of turbulence intensity was nonlinear with the availability of nutrients. The correlation between SPM characteristics and mineral SPM concentration was weak.

The entropy analyses presented in this chapter give further evidence to show that microorganisms have the ability to deviate the physical state of SPM away from that of pure mineral condition. It was first shown that entropy of both size $E[Q(L)|P(L)]$ and capacity dimension $E[Q(d_0)|P(d_0)]$ distributions of biomass-free SPM were not significantly altered by variations in abiotic conditions, including turbulence shear, nutrient concentration and mineral concentration. Microorganisms in a SPM suspension were then found to significantly increase $E[Q(L)|P(L)]$ and $E[Q(d_0)|P(d_0)]$. It was also observed that $E[Q(L)|P(L)]$ and $E[Q(d_0)|P(d_0)]$ of biomass-affected SPM were susceptible to increases in turbulence shear. These observations suggest that microorganisms increased the complexity and uncertainty of SPM flocculation and that the flocculation dynamics of a pure mineral SPM suspension was different from that of a suspension affected by microorganisms.

Although microorganisms were observed to substantially alter SPM size and capacity dimension, the average settling velocity of biomass-free and biomass-affected SPM were, however, nearly invariant because the effects of SPM size, density and capacity dimension on settling velocity are anisotropic; that is, an increase in size of biomass-affected SPM does not lead to a substantial increase in mass as it generally associates with a decrease in capacity dimension and a low excess density due to biological matter.

Although not all possible processes that may impact flocculation dynamics of SPM were examined, this chapter provides comprehensive experimental evidence of how important the nutrient and biomass feedback is on SPM, and contributes towards a wider understanding of flocculation processes in natural aquatic ecosystems.

Chapter 6

Stochastic collision and aggregation analysis of SPM

Contents of this chapter were published in Tang et al. (2014)¹ during PhD candidature of the author.

6.1 Introduction

In the previous chapter, we observed how microorganisms have altered the flocculation dynamics of SPM by growing upon available nutrients and secreting metabolites that increased the “stickiness” of SPM. These metabolites facilitated aggregation and resulted in SPM with substantially different characteristics from that of pure mineral SPM; generally, with larger size and higher irregularity in shape, surface asperity, and internal architecture (i.e., lower capacity dimension). These changes may have an impact in altering collision and aggregation kinematics, which in turn could feedback on flocculation dynamics.

This chapter aims at understanding how the shape and surface asperity of aggregated SPM can affect the probability of collision within the attraction zone of the double layer, and result in aggregation. Investigations were conducted by coupling experimental observations with a computational particle-based model (PBM). The investigations were first conducted by introducing a morphological approach based on the spheropolygon theory to describe the shape of SPM. In this approach, the surface asperity of SPM can be approximated at varying degree of accuracy depending on the number of vertices and radius sizes used to generate the spheropolygon. Spheropolygons generated from experimentally-acquired SPM images were then used within the PBM to assess various particle-particle interaction features, including (i) the probability of collision and aggregation in relation to the accuracy in approximating SPM shape and surface asperity; (ii) effect of particle relative axial displacement on aggregation kinetics; and (iii) particle interactions within the double layer barrier. Analysis of these results led to the discussion of morphological effects on SPM collision and aggregation kinematics.

¹Tang F.H.M., Alonso-Marroquin F., and Maggi F. (2014). Stochastic collision and aggregation analysis of kaolinite in water through experiments and the spheropolygon theory, *Water Research*, 53, 180-190.

6.2 Methods

6.2.1 Experiments

Kaolinite mineral (type Q38, with primary particle size ranging between $0.6 \mu\text{m}$ and $38 \mu\text{m}$) was hydrated in distilled water at a concentration of 8.8 g/L . A 20 ml suspension was poured into a 50 ml beaker and a magnetic stirrer was used to provide constant gentle mixing. SPM was sampled approximately 10 mm below the surface using a Pasteur pipette with 3 mm opening tip to reduce shear as recommended in Gibbs and Konwar (1982), and was gently transferred to a Perspex tank. During both sampling and transferring, the pipette tip was fully submerged in the solution and aggregates were gently released. These procedures could reduce suction and shear resulting from pipetting that may lead to floc breakup.

Images of SPM settling down the Perspex tank were acquired using the μPIV system described in Chapter 3.6 at a magnification level of 2.5, corresponding to resolution about $1 \mu\text{m}^2$ per pixel. Acquired images were then processed according to algorithms described in Chapter 3.10.

6.2.2 Definition of spheropolygon

A spheropolygon is defined as the Minkowski sum of a polygon with N_v vertices and a disk with radius r (also known as spheroradius) (Dobrohotoff et al., 2012)

$$P_s \oplus Q_s = \{u + v | u \in P_s, v \in Q_s\}, \quad (6.1)$$

where u and v are the sets of points belonging to the polygon P_s and disk Q_s , respectively. Note that \oplus is symmetric (*i.e.*, $P_s \oplus Q_s \equiv Q_s \oplus P_s$). An example of spheropolygon with $N_v = 16$ and $r = 4 \mu\text{m}$ is shown in Figure 6.1.

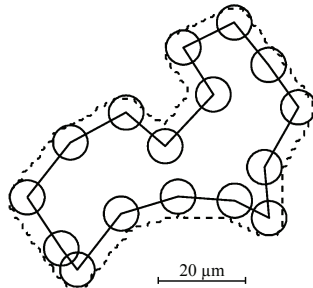


Figure 6.1: Polygon P_s with $N_v = 16$ (solid line) and disk Q_s with $r = 4 \mu\text{m}$ (circles) are shown with the spheropolygon $P_s \oplus Q_s$ drawn (dashed line).

6.2.3 Spheropolygon optimization

The shape of SPM was approximated at various degrees of accuracy by using spheropolygons with different values of N_v and r . Processed SPM images (binary) were used as the reference pixel image I_{ref} to generate a spheropolygon image I_{SP} . The error V in pixels was determined as $V = P(|I_{SP} - I_{ref}|)$, where $P(X)$ is a function that calculates the number of white pixels (*i.e.*, the number of *ones*) in the image matrix X .

Spheropolygon optimization consisted of minimising V by using an algorithm similar to that proposed in Dobrohotoff et al. (2012). To this end, each vertex with coordinates (x_k, y_k) with

$k = 1, \dots, N_v$ was incrementally moved in the plus and minus x and y directions from $-h$ to $+h$, with h the spatial discretisation length. The error V resulting from each movement was updated and used to determine its gradient $\nabla V = (\delta V/\delta x, \delta V/\delta y)$, where $\delta V/\delta x$ and $\delta V/\delta y$ are the central differences. The vertex position in the next iteration was calculated by solving the equation of motion of that vertex (Allen and Tildesley, 2012),

$$H\nabla V + c\frac{\delta x}{\delta t} = \frac{\delta^2 x}{\delta t^2},$$

where $H = 0.5$ is the force factor and $c = 2$ is the damping factor. Iterations continued until the minimum V and the optimal spheropolygon (here called spheropolyfloc) was found. Spheropolyfloc accuracy was expressed by the percent error relative to I_{ref}

$$\text{PE} = \frac{V}{P(I_{ref})} \times 100. \quad (6.2)$$

In this chapter, 17 values of N_v (ranging between 4 and 64), and 3 different values r (*i.e.*, $r = 1, 2$ and 4) were used to generate spheropolyflocs.

6.2.4 Spheropolyfloc interaction forces

Kinetic interactions between spheropolyflocs were modelled using a modified particle-based model (PBM) in a two-dimensional domain based on Alonso-Marroquin (2008). In this model, each spheropolyfloc undergoes gravitational \vec{F}_g and drag \vec{F}_d forces, whose modulus are defined respectively as (Stokes, 1851)

$$F_g = m_s g, \quad (6.3)$$

$$F_d = 6\pi r_{eq} \mu v, \quad (6.4)$$

where $m_s = \rho_s A_s$ is the spheropolyfloc mass per unit depth with ρ_s the surface density of spheropolyfloc and A_s the spheropolyfloc area, g is the gravitational acceleration, μ is the fluid dynamic viscosity, r_{eq} is the equivalent radius and v is the velocity.

Van der Waals attractive force \vec{F}_A and electrostatic repulsive force \vec{F}_R , were implemented into this PBM to account for the double layer forces, with their modulus being defined as (e.g., Hamaker, 1937; Bhattacharjee et al., 1998)

$$F_A = H_A \frac{r_{eq_i} r_{eq_j}}{6D_s^2 (r_{eq_i} + r_{eq_j})}, \quad (6.5)$$

$$F_R = -\phi^2 \frac{4\pi\epsilon_0\epsilon_r\kappa r_{eq_i} r_{eq_j}}{r_{eq_i} + r_{eq_j}} \exp(-\kappa D_s) \quad (6.6)$$

where H_A is the Hamaker constant, r_{eq_i} and r_{eq_j} are the equivalent radii of spheropolyflocs i (receiving particle) and j (approaching particle), respectively, D_s is the distance between the spheropolyflocs surface, $\epsilon_0 = 8.854 \times 10^{-12}$ F/m is the permittivity of vacuum, $\epsilon_r = 78.5$ is the dielectric constant of water at 25°C, $\kappa = 1/0.98 \text{ nm}^{-1}$ is the reciprocal Debye length, and ϕ is the surface electric potential.

Spheropolyfloc surface interactions were determined by vertex to edge contacts. At each contact point, the contact force \vec{F}_C was the resultant of elastic \vec{F}_E and viscous \vec{F}_V forces expressed in their

normal and tangential components as $\vec{F}_C = \vec{F}_{En} + \vec{F}_{Et} + \vec{F}_{Vn} + \vec{F}_{Vt}$. The modulus of elastic forces in \vec{F}_E are

$$F_{En} = -k_{s_n} \Delta x_n, \quad (6.7a)$$

$$F_{Et} = -k_{s_t} \Delta x_t. \quad (6.7b)$$

where k_{s_n} and k_{s_t} are the normal and tangential coefficients of stiffness, which account for the deformation of SPM, Δx_n is the overlapping length between two spheropolyflocs in contact, and Δx_t is the tangential elastic displacement. No sliding condition was assumed. The modulus of viscous forces in \vec{F}_V are defined as

$$F_{Vn} = -M_{eff} \lambda_n v_n, \quad (6.8a)$$

$$F_{Vt} = -M_{eff} \lambda_t v_t. \quad (6.8b)$$

where λ_n and λ_t are the normal and tangential coefficients of damping, v_n and v_t are the normal and tangential components of contact velocity, respectively, and $M_{eff} = (m_{s_i} m_{s_j}) / (m_{s_i} + m_{s_j})$ is the effective mass with m_{s_i} and m_{s_j} the masses of spheropolyflocs i and j , respectively.

A summary of parameters used in Eq. (6.5) to Eq. (6.8) is given in Table 6.1. k_{s_n} was estimated as $k_{s_n} = Y A_p / L$, where A_p is the projected area, L is the spheropolyfloc length perpendicular to that projected area, and Y is Young's modulus (Alonso-Marroquín et al., 2013). For Y in the order of magnitude of 10^6 N m^{-2} (McFarlane et al., 2005) and the ratio A_p / L , with $L = 2r_{eq}$, changing only slightly for the observed SPM aggregates, we obtained $k_{s_n} = 20 \text{ N m}^{-1}$. Values of k_{s_t} were derived to satisfy the relationship $k_{s_t} / k_{s_n} = (1 - 3\nu_p) / (1 + \nu_p)$ (Wang and Mora, 2008), with $\nu_p = 0.28$ being the typical Poisson ratio of clay (Vikash and Prashant, 2008). λ_n was calculated to satisfy a critical damping condition, i.e., collision time $t_c = \pi / \sqrt{\omega_0^2 - (\lambda_n/2)^2} \rightarrow \infty$, where $\omega_0 = \sqrt{k_{s_n} / M_{eff}}$ is the normal oscillation frequency of the contact between the two spheropolyflocs (Luding, 1998). The limit above implied that $\lambda_n \rightarrow 2\omega_0$. Finally, λ_t was calculated using the ratios $\lambda_t / \lambda_n = k_{s_t} / k_{s_n}$ for the restitution parameters in the normal and tangential directions. Typical values of Hamaker constant H_A and surface electric potential ϕ for kaolinite mineral were from Zhang and Zhang (2011).

Table 6.1: Values of parameters used in Eq. (6.5) - Eq. (6.8) for each spheropolyfloc collision type (I, II and III). ^(a) Values of λ_n depended on the effective mass of spheropolyflocs and were calculated as described in Chapter 6.2.4.

Parameters	Type I	Type II	Type III
k_{s_n} (N m ⁻¹)	20	20	20
k_{s_t} (N m ⁻¹)	2	2	2
λ_n (s ⁻¹)	^(a) 2.1×10^5	^(a) 7.4×10^5	^(a) 1.2×10^6
λ_t (s ⁻¹)	2.1×10^4	7.4×10^4	1.2×10^5
H_A (N m)	1.0×10^{-18}	1.0×10^{-18}	1.0×10^{-18}
ϕ (mV)	15	15	15
r_{eq_i} (μm)	16.41	4.95	4.62
r_{eq_j} (μm)	23.02	23.02	4.95

6.2.5 Ortho-axial and peri-axial collisions

Two different spheropolyflocs i (receiving) and j (approaching) with similar PE were used to model ortho-axial (frontal) and peri-axial (tangential) collisions in a gravitational field. Ortho-axial collision was modelled by aligning the spheropolyflocs center of mass, while these were displaced in peri-axial collision by a distance δ_s ranging from 0 to $\delta_{s_{max}} = R_i + R_j$, where R_i and R_j are the distances from the center of mass to the furthest possible contact point.

Experimental r_{eq} were divided into two classes ($r_{eq} \leq 5 \mu\text{m}$ and $r_{eq} > 5 \mu\text{m}$, with $5 \mu\text{m}$ the observed median aggregate size presented later in Chapter 6.3.1). Three types of collision were modelled to fully elucidate all possible collision kinetics: Type I, for both r_{eq_i} and r_{eq_j} greater than $5 \mu\text{m}$; Type II, for $r_{eq_i} \leq 5 \mu\text{m}$ and $r_{eq_j} > 5 \mu\text{m}$; and Type III, for both r_{eq_i} and r_{eq_j} smaller than $5 \mu\text{m}$. The orientation of colliding spheropolyflocs in ortho-axial collision were stochastically assigned 1000 times by generating a value n between 0 and 1 with a uniform distribution using *rand* function (in Matlab R2012a), and the angle of orientation θ was determined as $\theta = n2\pi$. Peri-axial collision was modelled using the same orientations of ortho-axial collision, but spheropolyflocs were displaced by various δ_s values.

The probability of collision and aggregation was then calculated from the set of 1000 stochastic simulations and was analysed for both ortho- and peri-axial collisions and for each of the three collision types (I, II and III).

6.3 Results

6.3.1 Experimental size distribution

A total of 2596 aggregates were detected in the experimental section described in Chapter 6.2.1, and were used in the analyses below. The equivalent radii r_{eq} of these aggregates ranged from $1.69 \mu\text{m}$ to $35.55 \mu\text{m}$, with an average r_{eq} of $6.53 \mu\text{m}$ and a median at about $5.44 \mu\text{m}$ (Figure 6.2).

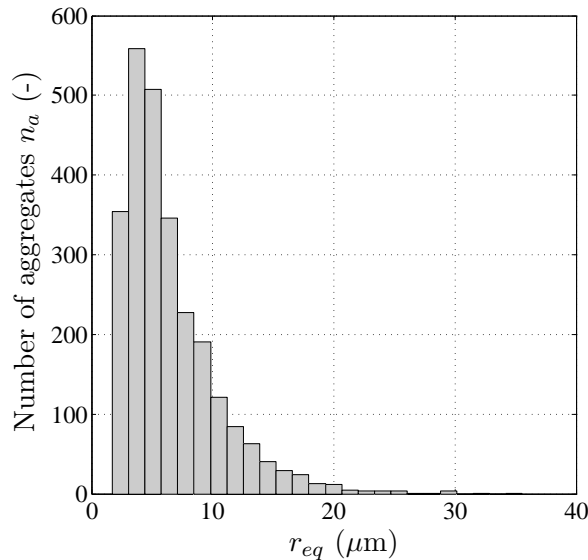


Figure 6.2: Equivalent radius r_{eq} histogram of experimental SPM aggregates.

6.3.2 Optimal spheropolyflocs

Spheropolyfloc optimization metrics against experimental SPM are depicted in Figure 6.3, with the average PE in the two size classes $r_{eq} \leq 5 \mu\text{m}$ and $r_{eq} > 5 \mu\text{m}$ shown as a function of N_v , and for $r = 1 \mu\text{m}$ (panel a), $r = 2 \mu\text{m}$ (panel b), and $r = 4 \mu\text{m}$ (panel c). The average PE of equivalent spheres (i.e., for $N_v = 1$ and $r = r_{eq}$) was represented in Figure 6.3 with dashed lines for comparison.

We note that all generated spheropolyflocs had substantially smaller PE than that of equivalent spheres. We also observe two specific patterns: on the one hand, PE increased with increasing r in all tests. On the other hand, PE of spheropolyflocs with $r_{eq} > 5 \mu\text{m}$ decreased with increasing N_v regardless of r values tested here. Spheropolyflocs with $r = 1 \mu\text{m}$ applied to aggregates with $r_{eq} \leq 5 \mu\text{m}$ resulted in a decreasing PE with increasing N_v until a minimum was reached at $N_v = 28$ (Figure 6.3a); beyond this point, PE seemed to oscillate and presumably reached a steady value. For $r = 2 \mu\text{m}$ and $r = 4 \mu\text{m}$ (Figure 6.3b and c), PE was relatively constant over N_v for $r_{eq} \leq 5 \mu\text{m}$.

In agreement with our results, Dobrohotoff et al. (2012) demonstrated that PE decreased concordantly with r . As the optimization algorithm used binary pixel images, $r = 1 \mu\text{m}$ (i.e., equivalent to 1 pixel) was the smallest possible spheroradius. For aggregates with $r_{eq} \leq 4 \mu\text{m}$, spheroradii $r \geq 2 \mu\text{m}$ (i.e., about or larger than r_{eq}) tended to result in greater PE. Image resolution, therefore, poses a limitation in the use of r ; it is suggested here that the condition $r < r_{eq}$ should be satisfied when using spheropolygons for this purpose.

When condition $r < r_{eq}$ is satisfied, optimization is strictly dependent on the number of vertices N_v in relation to the roundness of a body. As small aggregates have higher degree of roundness (i.e., larger capacity dimension), fewer vertices were needed as compared to large aggregates. Hence, assigning a value of N_v greater than the maximum number of vertices in experimental samples tended to produce greater PE. This may explain greater PE values against an increasing N_v for spheropolyflocs with $r_{eq} \leq 5 \mu\text{m}$ (Figure 6.3). Alongside, higher image resolution could potentially further decrease PE; however, we expect that PE would eventually decrease until a minimum point beyond which PE would reach a steady value even with increasing N_v , i.e., when the number of vertices is sufficient to describe the actual roundness of a body. Hence, image resolution only limits the use of the spheroradii, while the number of vertices is limited by the actual roundness of a body.

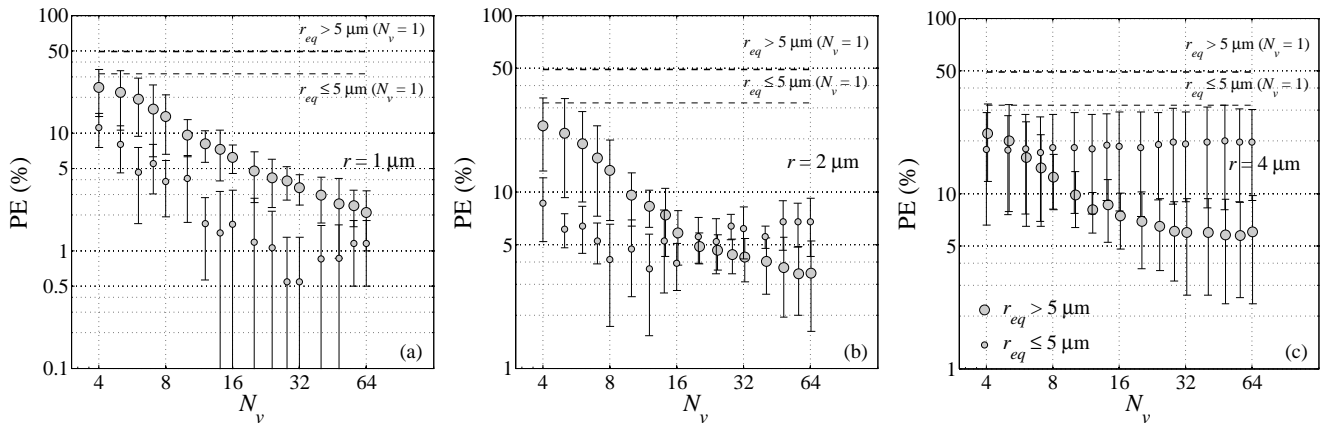


Figure 6.3: Average and standard deviation of the relative error percent PE(%) of generated spheropolyflocs in size class $r_{eq} \leq 5 \mu\text{m}$ (5 samples) and $r_{eq} > 5 \mu\text{m}$ (5 samples) as a function of number of vertices N_v and for spheroradius (a) $r = 1 \mu\text{m}$, (b) $r = 2 \mu\text{m}$ and (c) $r = 4 \mu\text{m}$, with dashed lines representing the average PE(%) of equivalent spheres (i.e., $N_v = 1$ and $r = r_{eq}$).

6.3.3 Collision probability in the double layer

The analysis of collision presented here includes both cases of equivalent spheres ($N_v = 1$ and $r = r_{eq}$) and spheropolyflocs ($N_v > 1$ and $r > 0$). Each case was investigated for the three collision types (I, II and III).

From a general viewpoint, a collision event C between equivalent spheres can result in two events: either $C(D_c < D_a)$, i.e., collision occurs within the attraction zone of the double layer, or $C(D_c \geq D_a)$, i.e., collision occurs outside the attraction zone. Spheres are considered to be within the attraction zone if the distance between centers of mass D_c is smaller than the critical distance D_a where $\vec{F}_A + \vec{F}_R = 0$, i.e., $D_c < D_a$. In either event $C(D_c < D_a)$ or $C(D_c \geq D_a)$, the collision outcome of spheres will not depend on the external shape but only on the relative size and surface electrochemical characteristics. For the cases analysed here, the size of experimental SPM aggregates spanned within a relatively narrow range and only differed by one order of magnitude, and thus, the difference in collision outcome was likely to depend more on electrochemical characteristics than size. Our results show that both ortho-axial ($\delta_s = 0$) and peri-axial ($0 < \delta_s \leq \delta_{smax}$) collisions between spheres of different sizes always resulted in collision within the attraction zone (see Figure 6.4 for $N_v = 1$), and this is regardless of whether the collision was of Type I, II or III.

Collisions between spheropolyflocs were modelled using two spheropolyflocs with spheroradius $r = 1 \mu\text{m}$ (tests with $r > 1 \mu\text{m}$ were excluded after our analysis in Chapter 6.3.2) and similar PE. The latter condition did not necessarily imply spheropolyflocs with identical N_v . Conversely to equivalent spheres, collision between spheropolyflocs within or outside the attraction zone is a stochastic event that depends on the surface asperities and relative orientation. To assess the effect of external shape, the probability $p_r[C(D_c < D_a)]$ that collision occurred within the attraction zone of the double layer was calculated for 1000 stochastic replicates in each collision type. Figure 6.4 shows that $p_r[C(D_c < D_a)]$ of Type I and II collisions decreased with increasing N_v and also with increasing δ_s . For Type III collision (between spheropolyflocs with $r_{eq} \leq 5 \mu\text{m}$), the probability $p_r[C(D_c < D_a)] = 1$ for all N_v and δ_s values. This complies with the fact that D_a was of similar order of magnitude as the size of SPM. Among the three collision types, Type I generally showed the lowest $p_r[C(D_c < D_a)]$, and was followed by Type II and III. The collision interaction between aggregates with $r_{eq} > 5 \mu\text{m}$ also showed the highest sensitivity to δ_s . This may be due to large aggregates ($r_{eq} > 5 \mu\text{m}$) having greater surface peculiarities than small aggregates ($r_{eq} \leq 5 \mu\text{m}$), thus leading to shape effects on collision outcome more evident than in other collision types.

These results give evidence that the outer shape of SPM may play an important role in determining whether a collision would occur within or outside the double layer field. Note, however, that this information is not enough to determine *a priori* if a collision within the attraction zone would have aggregation as an outcome.

6.3.4 Aggregation probability

If one presumes that aggregation were only be governed by the van der Waals attractive force \vec{F}_A , all collisions occurring within the attraction zone should lead to aggregation in opposition to those occurring outside; mathematically, this could be written as $p_r[A|C(D_c < D_a)] = 1$, where $A|C(D_c < D_a)$ is an event of aggregation when a collision occurred in the attraction zone. However, as anticipated earlier, collision within the attraction zone is neither a necessary condition nor is it sufficient for aggregation to happen in that zone. In fact, external shape is the factor that determines an outcome, and this factor is discussed in detail here for equivalent spheres and spheropolyflocs.

For the tests using equivalent spheres, the outcome of collision was found to always result in

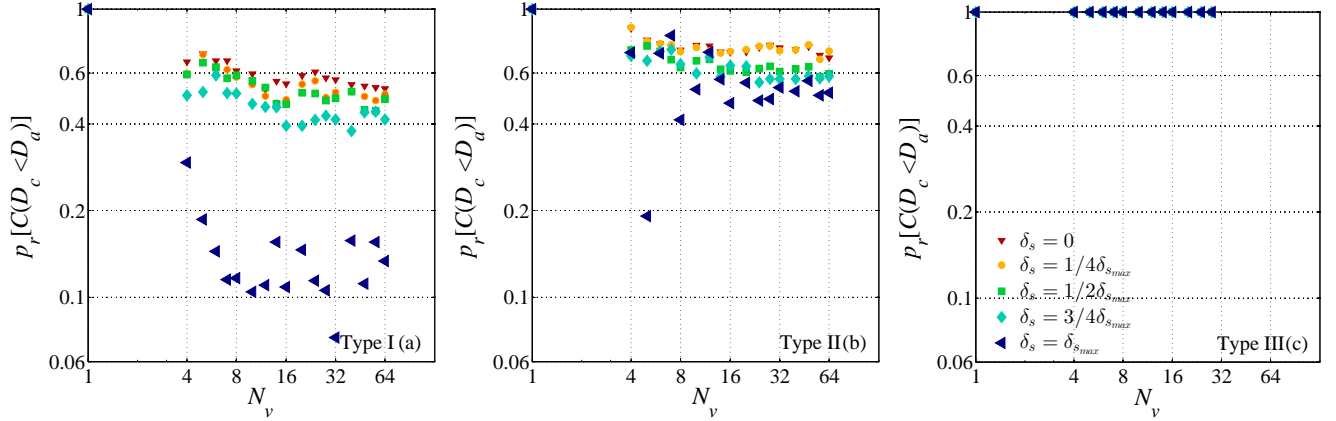


Figure 6.4: Probability of collision within the attraction zone $p_r[C(D_c < D_a)]$ for (a) Type I, (b) Type II, and (c) Type III collisions, with δ_s ranging from 0 to $\delta_{s_{max}}$. The number of vertices N_v on the x-axis refers to the approaching spheropolyfloc in each collision type.

aggregation ($Pr[A] = 1$) because spheres did not have surface peculiarities. The relative rotation over one another would never bring their centers of mass beyond D_a and, hence, $\vec{F}_A > \vec{F}_R$ would hold regardless of δ_s and collision type (Figure 6.5).

When spheropolyflocs collided and rotated over the surface of each other, surface asperities could move their centers of mass into or beyond D_a . Results in Figure 6.5 show that the aggregation probability after collision occurring within the attraction zone was $p_r[A|C(D_c < D_a)] < 1$ in all cases. Generally, $p_r[A|C(D_c < D_a)]$ decreased with increasing N_v and increasing δ_s for the three collision types. Type II collision showed the highest $p_r[A|C(D_c < D_a)]$, while Type I and III collisions had lower probability. Note that although Type I and III involved spheropolyflocs of different size classes, these had very similar aggregate size ratios r_{eqj}/r_{eqi} and, hence, were expected to have similar probability of aggregation (e.g., Overbeek, 1952; Hogg et al., 1966).

On the other hand, the aggregation probability after collision occurring outside the attraction zone was $p_r[A|C(D_c \geq D_a)] > 0$ in Type I and II collisions (Figure 6.6). These probabilities $p_r[A|C(D_c \geq D_a)]$ decreased with increasing N_v and increasing δ_s . In Type I collision, $p_r[A|C(D_c \geq D_a)]$ always equalled 0 when $\delta_s = \delta_{s_{max}}$. We also observed that in general, $p_r[A|C(D_c \geq D_a)] < p_r[A|C(D_c < D_a)]$ in all cases, and that both Type I and II collisions had relatively similar $p_r[A|C(D_c \geq D_a)]$. The probability $p_r[A|C(D_c \geq D_a)]$ in Type III collision was not shown because collisions always occurred inside the attraction zone as depicted in Figure 6.4c. These results demonstrate the importance of external shape, not only in determining the location of collision in the double layer, but also in conditioning whether a collision would result in aggregation.

6.3.5 Relative trajectory of spheropolyflocs

With the capability to track the relative position of interacting spheropolyflocs, we could analyse their trajectory before and after collision.

We identified four types of trajectory, each representing one possible interaction mechanism: Trajectory A (Figure 6.7a) describes two spheropolyflocs colliding within D_a and rotating over the surface of each other with their centers of mass always inside the attraction zone, thus, resulting in aggregation; Trajectory B (Figure 6.7b) represents a collision within the attraction zone with the centers of mass of spheropolyflocs falling beyond D_a during rotation, thus, causing them to repel and depart from each other; Trajectory C (Figure 6.7c) shows a collision occurring beyond D_a that

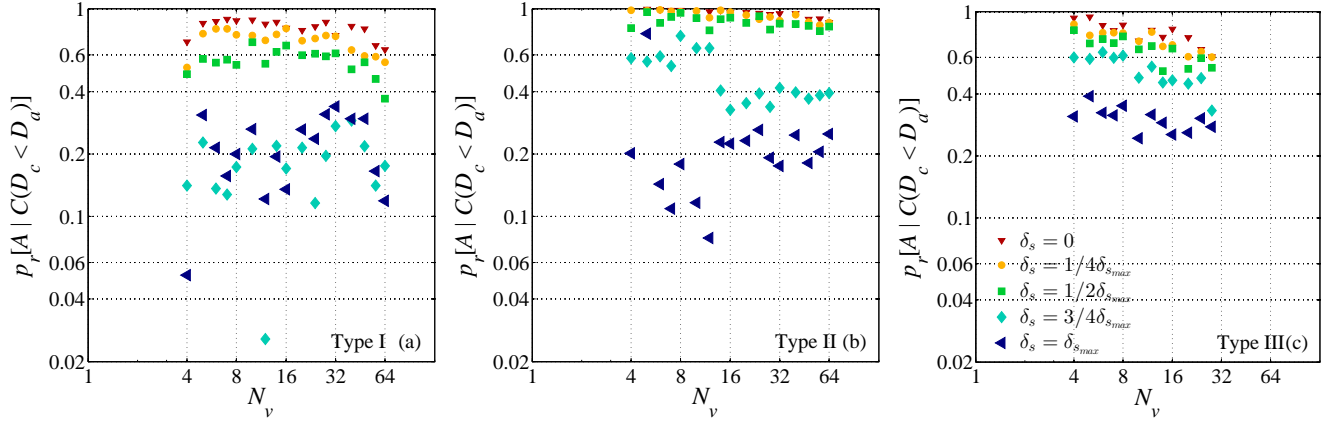


Figure 6.5: Conditional probability of aggregation after collision within the attraction zone $p_r[A|C(D_c < D_d)]$ for (a) Type I, (b) Type II, and (c) Type III collisions, with δ_s ranging from 0 to $\delta_{s_{max}}$. The number of vertices N_v on the x-axis refers to the approaching spheropolyfloc in each collision type.

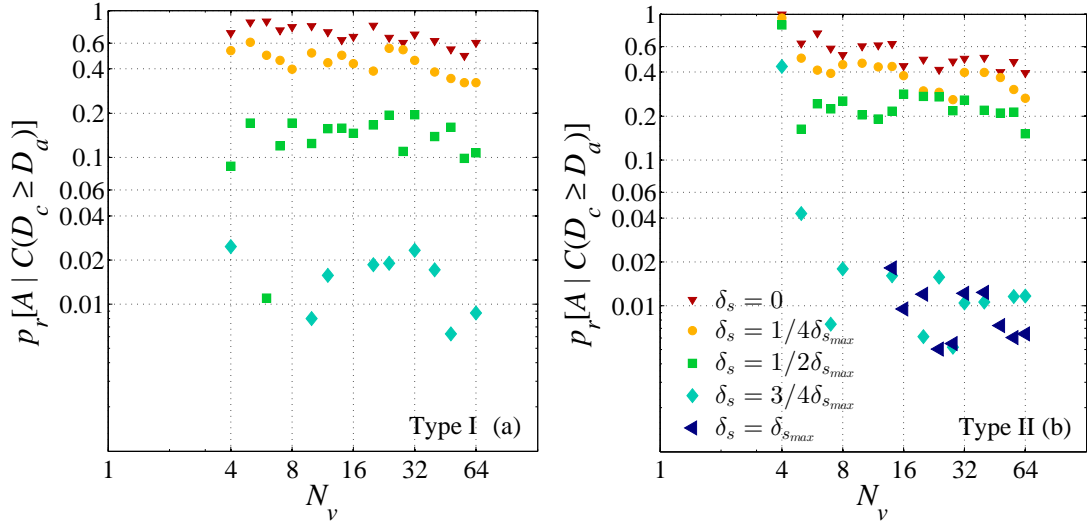


Figure 6.6: Conditional probability of aggregation after collision outside the attraction zone $p_r[A|C(D_c \geq D_d)]$ for (a) Type I, (b) Type II, and (c) Type III collisions, with δ_s ranging from 0 to $\delta_{s_{max}}$. The number of vertices N_v on the x-axis refers to the approaching spheropolyfloc in each collision type.

results in aggregation after relative rotation moves their centers of mass into the attraction zone; and finally, Trajectory D (Figure 6.7d) describes the case where a collision occurs outside the attraction zone and does not lead to aggregation.

Interaction mechanisms from spheropolyflocs in each of the three collision types were investigated. The probability of the four types of trajectory was calculated from 5000 stochastic replicates with δ_s ranging from 0 to $\delta_{s_{max}}$ (Figure 6.8). Here, we observed very distinct patterns in the occurrence of different relative trajectories among the three collision types. Trajectory D was observed in approximately 50% of Type I collision, and the probability increased with increasing N_v . In Type II collision, Trajectory A was observed to be the most frequent interaction mechanism but the occurrence of this trajectory decreased as N_v increased. On the other hand, only Trajectory A and B

were observed in Type III collision, with the probability of Trajectory A decreasing with increasing N_v .

These results suggest that the relative size of colliding spheropolyflocs influences the way and mechanisms by which they interacted, and implies that the effect of external shape observed in one collision type may not be directly applicable to collision of another type.

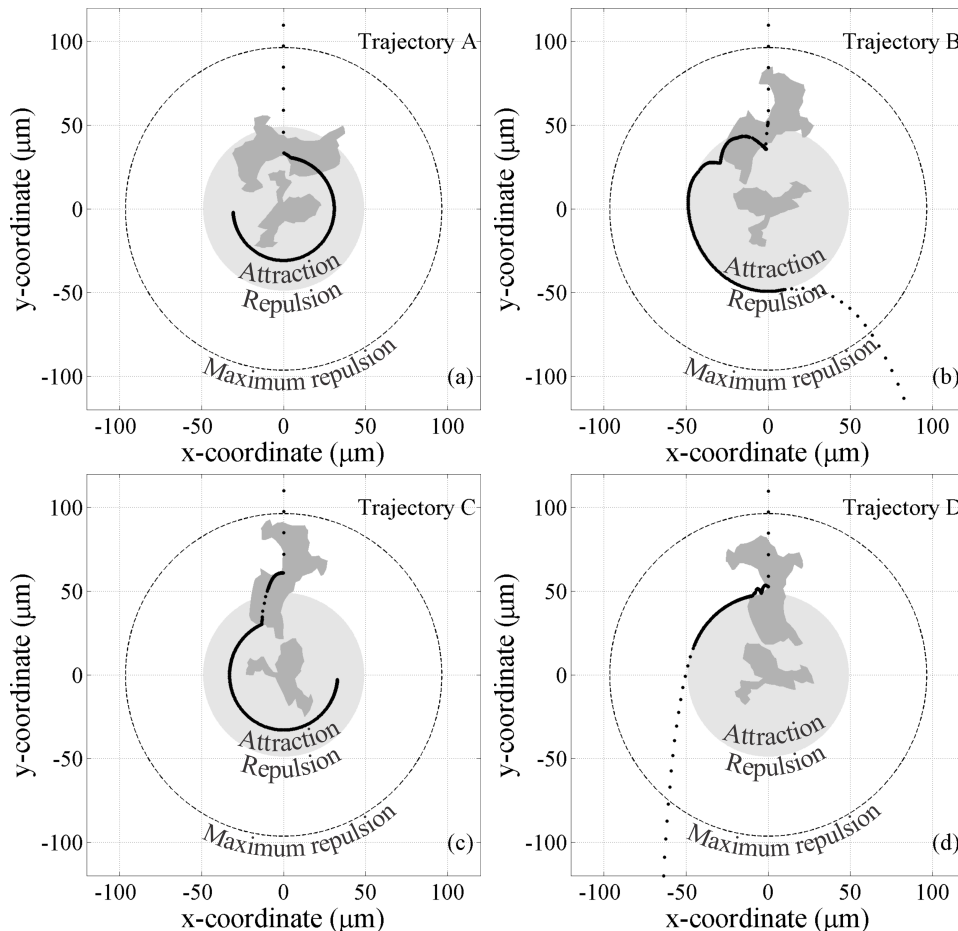


Figure 6.7: Trajectories of spheropolyflocs with $N_v = 64$ and $r = 1 \mu\text{m}$ in Type I ortho-axial collision ($\delta_s = 0$) for the cases where the collision occurred (a) within D_a and resulted in aggregation (Trajectory A), (b) within D_a and did not lead to aggregation (Trajectory B), (c) beyond D_a and led to aggregation (Trajectory C) and (d) beyond D_a with no aggregation observed (Trajectory D).

6.4 Discussion

This chapter highlighted several aspects of collision dynamics of irregularly-shaped SPM aggregates, but we also recall that there are several additional aspects that need to be discussed.

The internal aggregate architecture, porosity and fractal dimension are presumably affecting collision interaction and aggregation probability, whereas the aggregates in this PBM were considered as solid bodies. Some previous studies suggest that collisions between porous and fractal aggregates resulted in a higher aggregation probability as compared to that of rigid, non-porous spheres (e.g., Serra and Logan, 1999; Kim and Stolzenbach, 2004). Pores formed would increase the capture efficiency of particles and aggregates, and hence the probability of aggregation, presumably due to

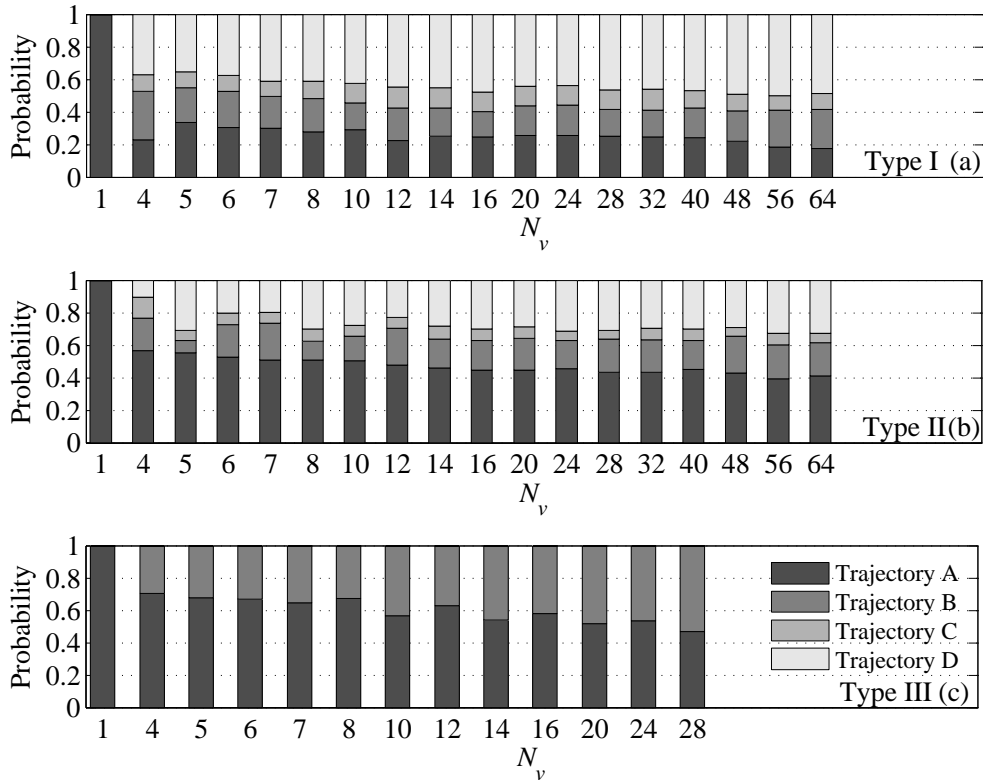


Figure 6.8: Probability of four different types of trajectory (A, B, C and D) in 5000 stochastic replicates with δ_s ranging from 0 to $\delta_{s_{max}}$ for (a) Type I, (b) Type II, and (c) Type III collisions. The number of vertices N_v on the x-axis refers to the approaching spheropolyfloc in each collision type.

flow through internal open pores (e.g., Li and Logan, 1997; Kim and Stolzenbach, 2004). Higashitani et al. (2001) suggested that deformation of the internal structure of aggregates, which led to aggregate breakup, is important for porous aggregates, especially when water flows through the pores. However, in this chapter, we assumed that the effect of collision-induced deformation has a second order relevance on the collision outcome, while we recognised this aspect to possibly cause nonlinearities that may require further investigation. Note that pores could be included in the approach presented here using aggregate made of several spheropolyflocs solidly attached to their neighbours. The case was not presented here yet as it was beyond the purpose of this chapter; however, research in this direction is expected to elucidate interaction mechanisms to further detail.

The analysis presented here was limited to binary collisions between equivalent spheres and spheropolyflocs, and hence, the possible effect of simultaneous collision of multiple aggregates was excluded. We do believe, though, that the time scales of binary collision can be considered much smaller than the time lapse needed between two sequential collisions to occur. Multiple collision can therefore be dealt with as a sequence of binary collision, provided that the integration time step is small enough (smaller than the average collision time lapse).

Hydrodynamics is the driving force of most processes and mechanisms in natural water bodies and, hence, the interaction between fluid and particles dynamics could be important. Flocculation, and aggregation and breakup rates are known to be highly affected by the turbulence shear rate (e.g., Van Leussen, 1994; Maggi, 2005). Some earlier studies have suggested that by taking into consideration wake effects, the presence of a large particle may cause an increase in the settling

velocity of a small particle and may tend to cause a small particle to elude from capture (e.g., McCave, 1984; Han and Lawler, 1991; Zhu et al., 1994). However, fluid motion was not described in this model and, therefore, the effects of wake and hydrodynamics on the aggregation dynamics of SPM were not included explicitly. Although these may be important aspects to be elucidated with this model, results in Chapter 6.3.3-6.3.4 highlighted the role of the outer aggregate shape on the probability of aggregation, that is the main focus of this chapter.

The drag force acting on a particle would potentially be affected by its shape. However, in this chapter, a simplified assumption was adopted, that is, replacing the complex shape by an equivalent sphere in the calculation of Stokes' velocity. Although considering the shape of aggregates within Navier-Stokes equations would improve the estimation of settling velocity, the collision dynamics would not be significantly affected. Taking into account the shape within the Navier-Stokes framework would be beneficial in sediment dynamics modelling where the Stokes' settling velocity was required to be superseded by a more accurate expression (Maggi, 2015b).

Overall, the morphological analyses in this chapter have highlighted the capability of spheropolygon theory to capture the details of SPM external shape and the extent to which it can affect collision and aggregation in a two-dimensional binary system.

6.5 Summary

This chapter puts forth evidence to illustrate that shape and surface asperity played an important role in governing the collision and aggregation kinematics of SPM. First, the analyses show that surface asperity controlled the location of collision between two aggregates, i.e., the probability for SPM to collide within the attraction zone of the double layer decreased with increasing degree of surface asperity. Second, the aggregation of SPM was not merely governed by van der Waals forces; in fact, shape and surface asperity are the factors that determine if the centers of mass of the two colliding SPM were always close enough for the van der Waals forces to keep them together. It was shown that a collision within the attraction zone did not necessary lead to aggregation, whereas, collision outside the attraction zone still had a probability to result in aggregation. Third, the size of SPM was observed to have a secondary effect on its collision and aggregation dynamics. The trajectory analyses depict that collisions between large aggregates had approximately 70% probability to not result in aggregation as compared to collisions between small aggregates that always occurred within the attraction zone with higher probability (approximately 50%) to aggregate; this is because large SPM commonly has more irregular shape (i.e., lower capacity dimension as shown in Chapter 5) than small SPM. The results presented here lead one to infer that the collision and aggregation dynamics of pure mineral SPM with small size and high capacity dimension are substantially different from those of biomass-affected SPM, which has generally larger size and lower capacity dimension. The analyses then suggest that the increase in shape and surface irregularity due to microorganisms has posed a negative feedback on SPM flocculation, hence, limiting the growth of biomass-affected SPM.

Chapter 7

Dynamics of microbial colonies living on SPM

Contents of this chapter were included in manuscript (Tang and Maggi, 2016b)¹ submitted to *Ecosystems*.

7.1 Introduction

After observing how microorganisms have modified the physical characteristics, and the collision and aggregation dynamics of SPM in Chapters 5 and 6, this chapter extends the investigation to focus on understanding how microorganisms can alter also the chemistry, and how this can feedback on the microbial colonies living on SPM. In particular, this chapter emphasises biogeochemical processes and ecological functions governed by NH_4^+ and NO_3^- to highlight the dynamic interrelationships between mineral, dissolved and adsorbed chemicals, and microorganisms. Investigations were conducted by coupling the water quality data acquired in experiments described in Chapter 3 with a biogeochemical model that considers various abiotic and biotic processes in sedimentary ecosystems, such as chemical adsorption on SPM, aqueous complexation, gas dissolution, microbial metabolism, and necromass dynamics, as well as, the exchange of information between different microbial functional groups (e.g., competition for limiting substrates and facilitation) to create an ecological feedback loop. The model was first calibrated and validated against experiments, and was next used to investigate the effects of nutrient leaching on the steady-state dynamics of microbial communities. The descriptions of the microbial reaction network and modelling approach are presented in the following sections.

7.2 Methods

7.2.1 Reaction network

The reaction network in Figure 7.1 shows the metabolic pathways of NH_4^+ and NO_3^- mediated by microorganisms, adsorption onto clay mineral, aqueous complexation, and gas dissolution. The network consists of 12 dissolved chemicals (NH_4^+ , NO_3^- , NO_2^- , $\text{C}_6\text{H}_{12}\text{O}_6$, H^+ , OH^- , HCO_3^- , $\text{O}_2(\text{aq})$, $\text{CO}_2(\text{aq})$, $\text{NH}_3(\text{aq})$, $\text{HNO}_3(\text{aq})$, $\text{H}_2\text{O}(\text{aq})$), 3 gases ($\text{O}_2(\text{g})$, $\text{CO}_2(\text{g})$, $\text{NH}_3(\text{g})$), 2 protected chemicals ($\text{NH}_4^+(\text{p})$,

¹Tang F.H.M., and Maggi F. (2016). Nitrogen-modulated dynamics of microbial colonies living on suspended sediment, submitted to *Ecosystems*, Manuscript ID: ECO-16-0150.

$\text{NO}_3^-(p)$), 5 living microbial functional groups, and the necromass. The functional groups are hypothesised to reflect those living in the estuarine ecosystem where samples were taken, and include: (1) aerobic oxygenic photolithoautotrophic bacteria B_{PHOTO} (e.g., cyanobacteria; Gottschalk, 1986; Dworkin et al., 2006; Raven, 2009); (2) aerobic chemoorganoheterotrophic bacteria B_{HET} (e.g., pseudomonads, bacilli, *Mesonnia*; Gottschalk, 1986; Wilson et al., 2010); (3) aerobic chemolithoautotrophic nitrifying bacteria B_{NIT} (e.g., *Nitrosomonas*, *Nitrobacter*; Van Kessel, 1977; Gottschalk, 1986; Raven, 2009); (4) anaerobic chemoorganoheterotrophic denitrifying bacteria B_{DEN} (Van Kessel, 1977); and (5) anaerobic chemoorganoheterotrophic dissimilatory nitrate reducing bacteria B_{DNR} (Van Kessel, 1977). B_{PHOTO} and B_{HET} can assimilate both NH_4^+ and NO_3^- , B_{NIT} uptakes NH_4^+ , whereas B_{DEN} and B_{DNR} uptake NO_3^- .

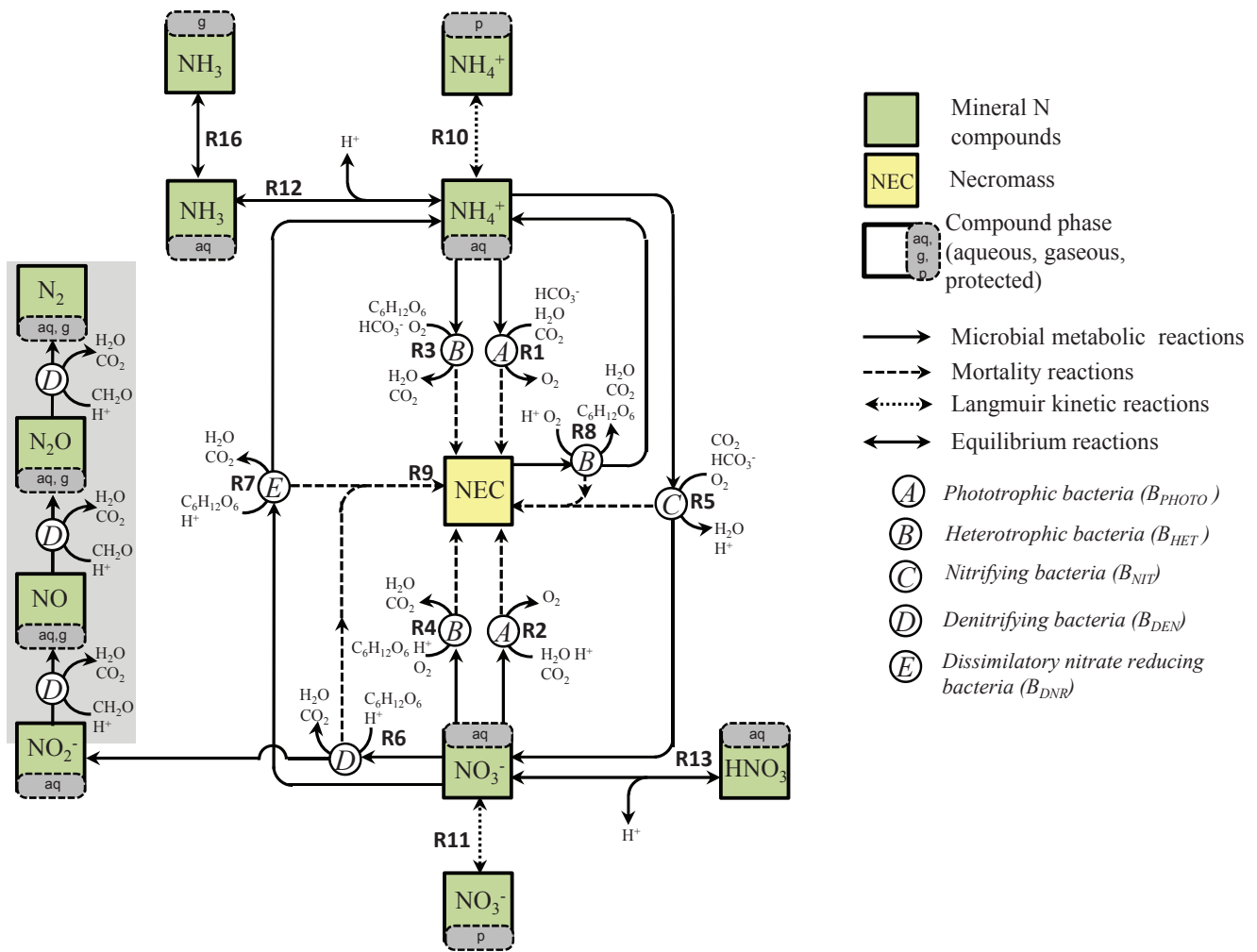


Figure 7.1: Biogeochemical reaction network of SPM micro-ecosystem described in the model. Pathways shaded in grey were not included in the model.

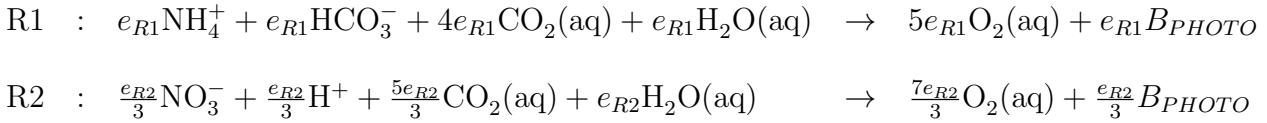
A generic microbial metabolic reaction R_M was described as the sum of catabolic (energy producing) R_C and anabolic (biomass yielding) R_A reactions according to Rittmann and McCarty (2001),

$$R_M = (1 - e)R_C + eR_A, \quad (7.1)$$

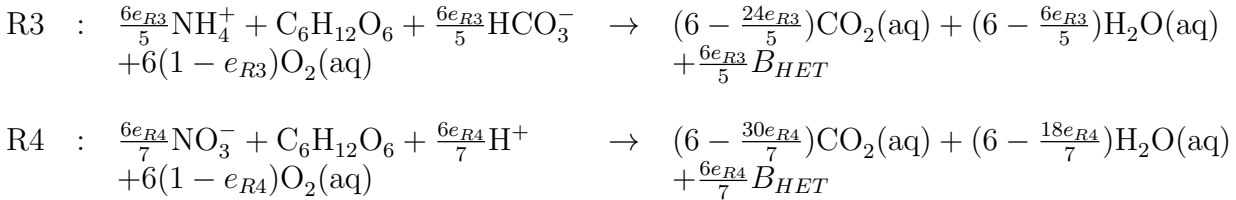
where e is the fraction of electrons used for anabolism, $R_C = R_a - R_d$, and $R_A = R_s - R_d$, with R_a the electron acceptor half-reaction, R_d the electron donor half-reaction, and R_s the cell synthesis

half-reaction. Energy produced in catabolic reactions R_C was assumed to satisfy cell maintenance requirement. For simplicity, all microbial functional groups were assumed to have the same chemical formula $C_5H_7O_2N$ for solid, dry mass, though this may differ among microbial strains, substrate preferences, and nutrient availability (e.g., Rittmann and McCarty, 2001; Ebeling et al., 2006).

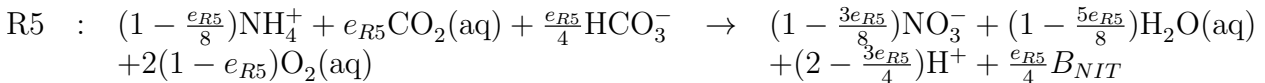
B_{PHOTO} requires both photosystems I and II, where H_2O undergoes photolysis and is used as e^- donor to produce energy (NADPH and ATP) and releases H^+ and O_2 as oxidization products (e.g., Kelly, 1971; Raven, 2009). Energy produced is used to reduce CO_2 (Kelly, 1971) to form glyceraldehyde-3-phosphate, which is used as general building block for cell synthesis (Rittmann and McCarty, 2001) in conjunction with either NH_4^+ or NO_3^- as nitrogen source. The overall metabolic reactions of phototrophic NH_4^+ (R1) and NO_3^- (R2) assimilation were written as,



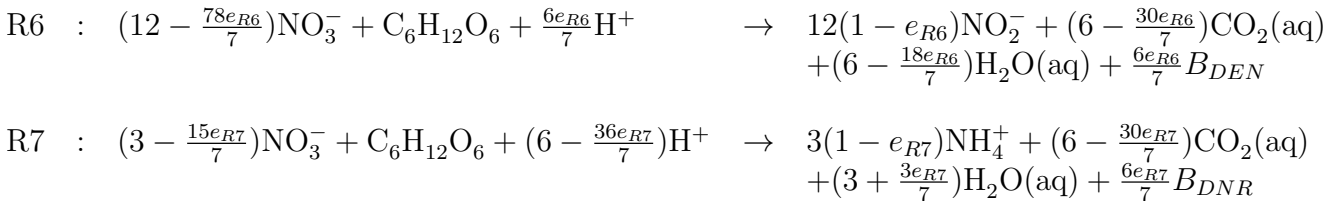
B_{HET} assimilates either NH_4^+ (R3) or NO_3^- (R4) for biomass synthesis by using $C_6H_{12}O_6$ as e^- donor and O_2 as e^- acceptor (Gottschalk, 1986), with the overall metabolic reactions expressed as,



B_{NIT} performs nitrification by oxidizing NH_4^+ to NO_3^- to produce energy using O_2 as e^- acceptor, with a fraction of NH_4^+ assimilated into the biomass (Rittmann and McCarty, 2001; Ebeling et al., 2006). This metabolic reaction (R5) was written as,

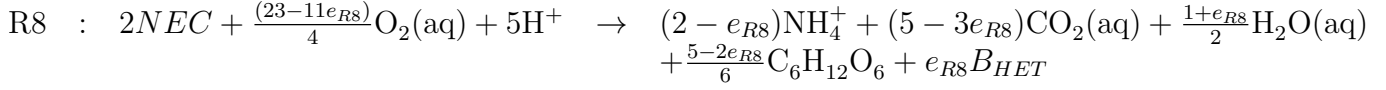


Anaerobic chemoorganoheterotrophs were divided into two different functional groups, with one being responsible for NO_3^- denitrification to NO_2^- , and the other for NO_3^- dissimilatory reduction to NH_4^+ (DNR). Both B_{DEN} and B_{DNR} oxidize $C_6H_{12}O_6$ to CO_2 with NO_3^- as the e^- acceptor. A fraction of NO_3^- is utilized in cell building reactions. Because N in any other forms except NH_4^+ and NO_3^- was not measured in the experiments, denitrification of NO_2^- to N_2 was not included in the model. The overall metabolic reactions for denitrification (R6) and DNR (R7) were expressed as,



Microorganisms from all functional groups were assumed to perish (R9) into biodegradable necromass NEC , which was assumed to have the same chemical formula as living-microorganisms

($C_5H_7O_2N$). NEC was then depolymerized and ammonified to NH_4^+ and $C_6H_{12}O_6$ by B_{HET} in oxic condition (e.g., Canfield et al., 2005; Riley et al., 2014), with the overall metabolic reaction (R8) expressed as,



Protection of NH_4^+ (R10) and NO_3^- (R11) onto kaolinite as a result of adsorption, ion exchange, physical protection in mineral and organic matrix, and other uncharacterized processes (Riley et al., 2014) was considered in the reaction network (Figure 7.1), with these protected ions being not available to microorganisms (Knicker and Hatcher, 1997). NH_4^+ and NO_3^- were also considered to be in equilibrium with $NH_3(\text{aq})$ (R12) and $HNO_3(\text{aq})$ (R13), respectively, whereas, $NH_3(\text{g})$ (R16), $O_2(\text{g})$ (R17) and $CO_2(\text{g})$ (R18) dissolution reactions were also accounted for explicitly. Derivations of Redox metabolic reactions R1 to R7 are reported in Appendix D and all reactions R1 to R18 are listed in Table 7.1.

7.2.2 Biogeochemical modelling

The reaction network in Figure 7.1 was solved in the general-purpose multiphase and multicomponent solver BRTSim-v2 (Maggi, 2015a). All chemicals in protected and biological phases were defined in the solver as primary species, all chemicals in gaseous phase were considered as secondary species, whereas those in the aqueous phase were defined as either primary or secondary species. Secondary species were solved only in equilibrium reactions with primary species and were not involved in kinetic reactions. All kinetic reactions involving secondary species were then rewritten in terms of corresponding equilibrium primary species (Table 7.1).

Aqueous complexation and gaseous dissolution reactions were solved in BRTSim-v2 as equilibrium reactions using the mass action law (Maggi, 2015a),

$$K_\beta = \prod_R [X_R]^{-x_R} \cdot \prod_P [X_P]^{x_P}, \quad (7.2)$$

where K_β is the equilibrium constant in phase β (either aqueous or gaseous), $[X_R]$ and $[X_P]$ are the concentrations [mol/L] (for aqueous phase) or partial pressure fraction [-] (for gaseous phase) of reactants X_R and products X_P , respectively, while, x_R and x_P are their corresponding stoichiometric numbers. The equilibrium equations considered in this model are listed in Table 7.1 together with their corresponding equilibrium constants, which were obtained from the EQ3/6 database (Wolery, 1992).

Protection was described using Langmuir adsorption kinetics (e.g., Langmuir, 1918; Atkins and De Paula, 2005) as

$$\frac{d[X(\text{p})]}{dt} = k_a[X(\text{aq})](Q_m - [X(\text{p})]) - k_d[X(\text{p})], \quad (7.3)$$

where $[X(\text{p})]$ and $[X(\text{aq})]$ are the concentrations [mol/L] of chemical X in protected (p) and aqueous (aq) phases, respectively, k_a and k_d are the adsorption and desorption rate constants, respectively, $Q_m = q_m C_K$, with q_m the maximum adsorption capacity [mol of X adsorbed/g of kaolinite], and C_K the kaolinite concentration [g/L]. Note that at equilibrium ($d[X(\text{p})]/dt = 0$), $K_L = k_a/k_d = [X(\text{p})]/([X(\text{aq})](Q_m - [X(\text{p})]))$ is the Langmuir equilibrium constant.

Microbial metabolism was described in the BRTSim-v2 solver by Michaelis-Menten-Monod kinetics with reaction rate R_r written as (Maggi, 2015a),

$$R_r = \hat{\mu}_s \cdot \frac{[B_x]}{Y_b} \cdot \prod_p [X_p]^{n_p} \cdot \prod_i \frac{[X_i]}{[X_i] + K_{M_i} (1 + \sum_j \frac{[X_j]}{K_{M_j}})} \cdot \prod_m \frac{K_{H_m}}{K_{H_m} + [X_m]}, \quad (7.4)$$

where $\hat{\mu}_s$ is the maximum specific biomass growth rate, $[B_x]$ is the concentration of microbial functional group B_x and Y_b is the biomass yield. Note that the maximum specific rate of substrate utilization is $\mu_s = \hat{\mu}_s / Y_b$. The third factor on the right-hand side describes the n_p -order kinetic product with $[X_p]$ the concentration of reactant X_p and $n_p = \{1, 2, 3, \dots, n\}$ for first, second, third, and n -order kinetics, respectively. The fourth factor on the right-hand side expresses the Michaelis-Menten-Monod kinetic terms, where $[X_i]$ is the concentration of reactant X_i with K_{M_i} its half-saturation concentration. The term in the parenthesis describes the competitive substrate consumption between reactant X_i and reactants X_j with concentrations $[X_j]$ and half-saturation concentrations K_{M_j} . The last term on the right-hand side expresses a decrease in R_r due to the presence of inhibitor X_m with concentration $[X_m]$ and inhibition constant K_{H_m} . The rate of change in the concentration $[X_n]$ of a generic reactant or product X_n in a reaction was then written as

$$\frac{d[X_n]}{dt} = \sum_i (x_{n_i} \cdot R_{r_i}), \quad (7.5)$$

where x_{n_i} is the stoichiometric number of X_n in reaction i . The rate of change in biomass concentration $[B_x]$ was described as Monod kinetics (Monod, 1949) and was expressed in a generic form as,

$$\frac{d[B_x]}{dt} = \sum_i Y_{b_i} R_{r_i} - \delta_m [B_x], \quad (7.6)$$

where the microbial mortality rate $\delta_m = 2 \times 10^{-6} \text{ s}^{-1}$ was assumed after Servais et al. (1985) and Billen et al. (1990) for all functional groups.

Competition between microorganisms from different functional groups for the same substrate was included in Michaelis-Menten kinetics in Eq. (7.4). Here, all substrates (including $\text{O}_2(\text{aq})$, H^+ , and HCO_3^-) involved in biochemical reactions were considered to exhibit Michaelis-Menten kinetics. To reduce the number of unknown parameters, aerobic (R3-R5, R8) and autotrophic (R1-R2, R5) reactions were assumed to have the same K_M values for $\text{O}_2(\text{aq})$ and HCO_3^- . Competitive substrate consumption in Eq. (7.4) relative to NH_4^+ and NO_3^- was included for N assimilation by B_{PHOTO} (R1 and R2) and B_{HET} (R3 and R4), whereas $\text{C}_6\text{H}_{12}\text{O}_6$ competition was also included for heterotrophic N assimilation (R3 and R4).

An inhibitory pH effect was explicitly accounted for at high pH as a Michaelis-Menten term with $K_M = 1 \times 10^{-9} \text{ mol/L}$ for H^+ and at low pH as an inhibition term with $K_H = 1 \times 10^{-5} \text{ mol/L}$ (e.g., Boon and Laudelout, 1962; Saleh-Lakha et al., 2009). O_2 inhibition on anaerobic reactions (R6 and R7) was also explicitly included. Finally, $\text{C}_6\text{H}_{12}\text{O}_6$ inhibition on depolymerization and ammonification (R8) was considered here because B_{HET} is expected to have higher preference for simple (i.e., $\text{C}_6\text{H}_{12}\text{O}_6$ over complex C sources such as necromass (Goldman and Dennett, 1991).

Table 7.1: Summary of microbial metabolic reactions, Langmuir adsorption kinetic reactions, and equilibrium aqueous complexation and gas dissolution reactions included in the reaction network. Note that R1 to R8 were written in the form used to code in the BRTSim-v2 solver. ^aParameter assumed after Servais et al. (1985) and Billen et al. (1990). ^bParameters calibrated based on NABF experiments. ^cParameters from EQ3/6 at 25°C (Wolery, 1992). ^dInterpolated parameters at 21°C.

Microbial metabolic kinetic reactions		Electron donor	Electron acceptor	Respiration type
R1	$\frac{1}{2}e_{R1}NH_4^+ + 2e_{R1}H^+ + \frac{5}{2}e_{R1}HCO_3^- \rightarrow \frac{5}{2}e_{R1}O_2(aq) + \frac{3}{2}e_{R1}H_2O(aq) + \frac{1}{2}e_{R1}B_{PHOTO}$	H ₂ O	CO ₂	Aerobic
R2	$\frac{5}{14}e_{R2}NO_3^- + \frac{15}{7}e_{R2}H^+ + \frac{25}{14}e_{R2}HCO_3^- \rightarrow \frac{5}{2}e_{R2}O_2(aq) + \frac{5}{7}e_{R2}H_2O(aq) + \frac{5}{14}e_{R2}B_{PHOTO}$	H ₂ O	CO ₂	Aerobic
R3	$\frac{6}{5}e_{R3}NH_4^+ + C_6H_{12}O_6 + 6(1 - e_{R3})O_2(aq) \rightarrow (6 - \frac{24}{5}e_{R3})H^+ + (6 - 6e_{R3})HCO_3^- + \frac{18}{5}e_{R3}H_2O(aq) + \frac{6}{5}e_{R3}B_{HET}$	C ₆ H ₁₂ O ₆	O ₂	Aerobic
R4	$\frac{6}{7}e_{R4}NO_3^- + C_6H_{12}O_6 + 6(1 - e_{R4})O_2(aq) \rightarrow (6 - \frac{36}{7}e_{R4})H^+ + (6 - \frac{30}{7}e_{R4})HCO_3^- + \frac{12}{7}e_{R4}H_2O(aq) + \frac{6}{7}e_{R4}B_{HET}$	C ₆ H ₁₂ O ₆	O ₂	Aerobic
R5	$(1 - \frac{1}{8}e_{R5})NH_4^+ + 2(1 - e_{R5})O_2(aq) + \frac{5}{4}e_{R5}HCO_3^- \rightarrow (1 - \frac{3}{8}e_{R5})NO_3^- + (2 - \frac{7}{4}e_{R5})H^+ + (1 + \frac{3}{8}e_{R5})H_2O(aq) + \frac{1}{4}e_{R5}B_{NIT}$	NH ₄ ⁺	O ₂	Aerobic
R6	$(12 - \frac{78}{7}e_{R6})NO_3^- + C_6H_{12}O_6 \rightarrow 12(1 - e_{R6})NO_2^- + (6 - \frac{36}{7}e_{R6})H^+ + (6 - \frac{30}{7}e_{R6})HCO_3^- + \frac{12}{7}e_{R6}H_2O(aq) + \frac{6}{7}e_{R6}B_{DEN}$	C ₆ H ₁₂ O ₆	NO ₃ ⁻	Anaerobic
R7	$(3 - \frac{15}{7}e_{R7})NO_3^- + C_6H_{12}O_6 \rightarrow 3(1 - e_{R7})NH_4^+ + \frac{6}{7}e_{R7}H^+ + (6 - \frac{30}{7}e_{R7})HCO_3^- + (\frac{33}{7}e_{R7} - 3)H_2O(aq) + \frac{6}{7}e_{R7}B_{DNR}$	C ₆ H ₁₂ O ₆	NO ₃ ⁻	Anaerobic
R8	$2NEC + \frac{(23-11e_{R8})}{4}O_2(aq) + 3e_{R8}H^+ + (\frac{9}{2} - \frac{7}{2}e_{R8})H_2O(aq) \rightarrow (2 - e_{R8})NH_4^+ + (5 - 3e_{R8})HCO_3^- + \frac{(5-2e_{R8})}{6}C_6H_{12}O_6 + e_{R8}B_{HET}$	NEC	O ₂	Aerobic
Microbial mortality reaction		$\frac{\partial m}{\partial t}$ [s ⁻¹]		
R9	$B_x \rightarrow NEC$	^a 2×10^{-6}		
Langmuir adsorption kinetic reactions		K_L [L mol ⁻¹]	q_m [mol g ⁻¹]	q_0 [mol g ⁻¹]
R10	$NH_4^+(aq) \leftrightarrow NH_4^+(p)$	^b 443.3	^b 1.07×10^{-3}	^b 1.06×10^{-4}
R11	$NO_3^-(aq) \leftrightarrow NO_3^-(p)$	^b 1608.4	^b 1.45×10^{-3}	^b 3.41×10^{-9}
Equilibrium aqueous complexation reactions		$\log(K_{(aq)})$ at 25°C	$\log(K_{(aq)})$ at 21°C	
R12	$NH_4^+ \leftrightarrow H^+ + NH_3(aq)$	^c -9.24	^d -9.37	
R13	$HNO_3(aq) \leftrightarrow H^+ + NO_3^-$	^c 1.30	^d 1.35	
R14	$OH^- + H^+ \leftrightarrow H_2O(aq)$	^c 13.99	^d 14.13	
R15	$CO_2(aq) + H_2O(aq) \leftrightarrow H^+ + HCO_3^-$	^c -6.34	^d -6.37	
Equilibrium gas dissolution reactions		$\log(K_{(g)})$ at 25°C	$\log(K_{(g)})$ at 21°C	
R16	$NH_3(g) \leftrightarrow NH_3(aq)$	^c 1.80	^d 1.88	
R17	$O_2(aq) \leftrightarrow O_2(g)$	^c 2.90	^d 2.87	
R18	$CO_2(g) + H_2O(aq) \leftrightarrow H^+ + HCO_3^-$	^c -7.81	^d -7.78	

7.2.3 Model calibration and validation

Langmuir kinetic parameters k_a , k_d , q_m in Eq. (7.3), and the initial amount of ions q_0 protected in one gram of kaolinite were calibrated for both NH_4^+ and NO_3^- adsorption processes against nutrient-affected and biomass-free (NABF) experiments conducted in Chapter 3, where both the ions were present; the competition between NH_4^+ and NO_3^- to adsorb onto the same sites on kaolinite was, therefore, implicitly accounted for.

The remaining 38 unknown parameters (i.e., $\hat{\mu}_s$, K_M , K_H , e , and initial biomass concentrations $[B_x]_0$) were calibrated against the nutrient- and biomass-affected (NABA) experiment conducted at $[\text{NH}_4\text{NO}_3] = 6$ mM, $[\text{C}_6\text{H}_{12}\text{O}_6] = 11.6$ mM, and $C_K = 3$ g/L; in total, 192 experimental data points corresponded to four state variables (NH_4^+ , NO_3^- , pH, and $\text{O}_2(\text{aq})$) were available for calibration. The model was calibrated with PEST (Doherty, 2005), which uses the Gauss-Marquardt-Levenberg algorithm (Levenberg, 1944) to minimize the errors between model-generated state variables and experimental measurements.

The model structure and calibrated parameters were validated against eight other NABA experiments conducted at $[\text{NH}_4\text{NO}_3]$, $[\text{C}_6\text{H}_{12}\text{O}_6]$ and C_K different than those for the calibration (Table 3.2). Model goodness-of-fit was measured using the correlation coefficient (R), the normalized root mean square error (NRMSE), Nash-Sutcliffe efficiency (NSE, Nash and Sutcliffe, 1970), index of agreement (IA, e.g., Willmott, 1982; Willmott et al., 1985), and percent bias (PBIAS, Sorooshian et al., 1993),

$$R = \frac{\text{cov}(c, o)}{\sigma_c \sigma_o}, \quad \text{with} \quad -1 \leq R \leq 1, \quad (7.7a)$$

$$\text{NRMSE} = \frac{\sqrt{\frac{1}{n_o} \sum_{i=1}^{n_o} (c_i - o_i)^2}}{\max\{o\} - \min\{o\}} \times 100, \quad \text{with} \quad 0 \leq \text{NRMSE} < \infty, \quad (7.7b)$$

$$\text{NSE} = 1 - \frac{\sum_{i=1}^{n_o} (o_i - c_i)^2}{\sum_{i=1}^{n_o} (o_i - \bar{o})^2}, \quad \text{with} \quad -\infty < \text{NSE} \leq 1, \quad (7.7c)$$

$$\text{IA} = 1 - \frac{\sum_{i=1}^{n_o} (o_i - c_i)^2}{\sum_{i=1}^{n_o} (|c_i - \bar{o}| + |o_i - \bar{o}|)^2}, \quad \text{with} \quad 0 \leq \text{IA} \leq 1, \quad (7.7d)$$

$$\text{PBIAS} = \frac{\sum_{i=1}^{n_o} (c_i - o_i)}{\sum_{i=1}^{n_o} o_i} \times 100, \quad \text{with} \quad -\infty < \text{PBIAS} < \infty, \quad (7.7e)$$

where c and o are the calculated and observed values of the state variables, respectively, n_o is the number of observations, σ_c and σ_o are the standard deviation of c and o , respectively, and \bar{o} is the average of o .

Modelled values match observations when $R \rightarrow 1$, $\text{NRMSE} \rightarrow 0\%$, $\text{NSE} \rightarrow 1$, $\text{IA} \rightarrow 1$, and $\text{PBIAS} \rightarrow 0\%$. $\text{NSE} = 0$ implies that c is as accurate as \bar{o} , while, $\text{NSE} < 0$ signifies that \bar{o} is a better prediction than the model. PBIAS measures model over- ($\text{PBIAS} > 0$) or underestimation ($\text{PBIAS} < 0$). A validation test was considered satisfactory if conditions $R \geq 0.8$, $\text{NRMSE} \leq 15\%$, $\text{NSE} \geq 0$, $\text{IA} \geq 0.8$, and $-15\% \leq \text{PBIAS} \leq 15\%$ were satisfied, and signified that model structure and parameter uncertainty were suitable to describe that experiment.

7.2.4 Analyses of nitrogen leaching

The calibrated model was used to investigate how inorganic NH_4^+ and NO_3^- leaching modulates the dynamics of microbial diversity. A total of 400 simulations were run for leaching rates, $R_{\text{NH}_4^+}$ and $R_{\text{NO}_3^-}$ ranging between 8.64×10^{-9} and 8.64×10^{-3} mol L⁻¹ day⁻¹, with $R_{\text{NH}_4^+}/R_{\text{NO}_3^-}$ ratios

ranging from 10^{-6} to 10^6 . $R_{\text{NH}_4^+}$ and $R_{\text{NO}_3^-}$ tested here cover leaching rates commonly observed in both urban (approximately 2.15×10^{-12} mol-N L⁻¹ s⁻¹, Birch et al., 2010) and agricultural (approximately 7.11×10^{-11} to 2.9×10^{-9} mol-N L⁻¹ s⁻¹, Brown et al., 1982) ecosystems. All simulations were initialized with equal biomass across all functional groups. C:N ratio was kept at 8:1 as commonly found in estuarine sediment (Matson and Brinson, 1990), while C_K was kept at 0.1 g/L. Microbial metabolism was assumed not to be limited by $[\text{H}^+]$ and $[\text{HCO}_3^-]$, which were assumed to be continuously recharged in natural aquatic ecosystem through various buffering processes not explicitly included in the model; hence, pH was kept at 7 and $[\text{HCO}_3^-]$ was maintained at 6×10^{-5} mol L⁻¹ so as to be in equilibrium with pH 7 and atmospheric $\text{CO}_2(\text{g})$. Simulations were run for a period of 50 years to reach steady state.

Dynamics of microbial diversity was analysed by calculating the biomass fraction of a functional group relative to total living biomass concentration at the end of the 50-year simulation period. Analysis of N partitioning into protected ($\text{NH}_4^+(\text{p})$ and $\text{NO}_3^-(\text{p})$), aqueous (NH_4^+ , NO_3^- , NO_2^- , $\text{NH}_3(\text{aq})$, and $\text{HNO}_3(\text{aq})$), gaseous ($\text{NH}_3(\text{g})$), and biological (B_{PHOTO} , B_{HET} , B_{NIT} , B_{DEN} , B_{DNR} , and NEC) phases was also conducted at the end of 50-year simulation. Finally, the N mass flow through each metabolic reactions (R1 to R8) was calculated to determine the dominating biogeochemical partitioning.

7.3 Results

7.3.1 Calibrated model parameters

Calibration of Langmuir parameters for NH_4^+ and NO_3^- adsorption on clay (Table 7.1) matched relatively well those in the literature (e.g., Li and Bowman, 2001; Cengeloglu et al., 2006; Copcia et al., 2010).

Experimentally-determined kinetic parameters relative to reactions R1 to R8 are listed in Table 7.2. The maximum specific biomass growth rate $\hat{\mu}_s$ ranged from about 1×10^{-5} to about 4×10^{-4} s⁻¹; ammonification and depolymerization in R8, and heterotrophic NO_3^- assimilation in R3 had the highest and lowest $\hat{\mu}_s$, respectively. The biomass yield Y_b was the highest in phototrophic NH_4^+ assimilation in R1 and the lowest in R8. No correlation was found between $\hat{\mu}_s$ and Y_b (i.e., $R = -0.38$). K_M values spanned across a wide range of values from 8×10^{-6} to 6×10^{-2} mol/L (Table 7.2). The $\text{O}_2(\text{aq})$ inhibition constant K_H in denitrification in R6 was higher than in DNR in R7, implying that B_{DEN} had higher tolerance to $\text{O}_2(\text{aq})$ than B_{DNR} . The reaction velocity of R8 was reduced by more than 50% when $[\text{C}_6\text{H}_{12}\text{O}_6] > 6.18 \times 10^{-5}$ mol/L, thus accounting for B_{HET} to prefer simpler monosaccharides as a C source to NEC .

Qualitatively, the model matched relatively well the measured NH_4^+ and NO_3^- concentrations, pH, and the net O_2 consumption $[\text{O}_2(\text{aq})]_C$ (Figure 7.2, first column). In general, $[\text{NH}_4^+]$, $[\text{NO}_3^-]$, $[\text{C}_6\text{H}_{12}\text{O}_6]$, and pH decreased during incubation, while $[\text{O}_2(\text{aq})]_C$ increased.

During incubation, $[\text{NH}_4^+]$ decreased initially and was nearly constant afterwards as a result of production by B_{DNR} and B_{HET} in reaction R7 and R8 (contributing about 97.5% and 2.5%, respectively) and consumption by B_{NIT} in R5 (contributing about 99.86%), and by B_{PHOTO} and B_{HET} in R1 and R3 (contributing less than 0.14%) (Figure 7.2a). NO_3^- gradually decreased because of consumption by B_{DEN} (74.9%), B_{DNR} (25%), and B_{HET} and B_{PHOTO} (contributing less than 0.01%) (Figure 7.2b). NO_3^- produced by B_{NIT} was unable to sustain uptake by other microbial functional groups. $\text{C}_6\text{H}_{12}\text{O}_6$ production from NEC was negligible while consumption could be attributed mainly to B_{DNR} and B_{DEN} (about 98.5%) and to a smaller extent to B_{HET} (1.5%) (Figure 7.2e). At the end of incubation, $\text{C}_6\text{H}_{12}\text{O}_6$ was predicted to stabilize at a high concentration, suggesting that

heterotrophic growth was not limited by carbon. After the initial phase, pH stabilized at about 5 by the end of incubation (Figure 7.2c). The net oxygen consumption $[O_2(aq)]_C$, calculated as consumption by aerobic bacteria minus production by phototrophic bacteria (Figure 7.2d), increased during incubation and implied that the ecosystem had more intense aerobic respiration than photosynthesis. By tracking the mass flow of total N through each microbial metabolic reaction, R6 contributed 59% of total N consumption, followed by R5 (approximately 21%), R7 (approximately 19.7%), and R8 (approximately 0.5%). NH_4^+ and NO_3^- consumption by B_{PHOTO} and B_{HET} (R1 to R4) resulted in less than 0.04% of total N consumption.

All microbial functional groups showed an initial increase in their concentrations (Figure 7.2, right column), and reached a maximum between day 7 and 14. In contrast, $[NEC]$ increased steadily during incubation. The biomass fraction in each functional group fluctuated during the whole test depending on substrate availability and environmental conditions (e.g., pH, $O_2(aq)$).

Note that, a sharp change in concentrations was observed at day 21 after transferring incubated samples into the settling column for testing as described in Chapter 3.9.

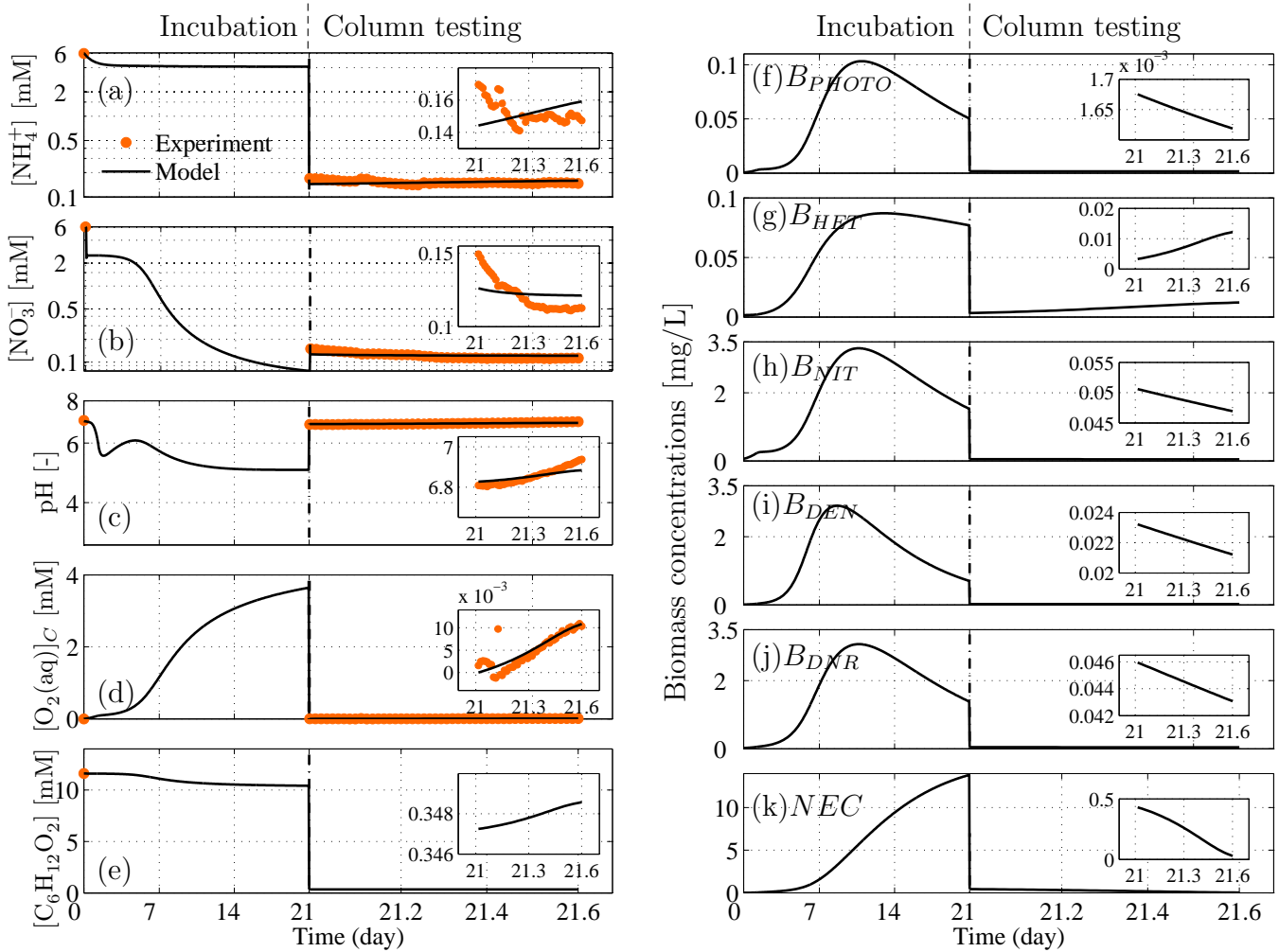


Figure 7.2: Comparison between experimental measurements and modelled results for (a) $[NH_4^+]$, (b) $[NO_3^-]$, (c) pH, (d) the net oxygen consumption $[O_2(aq)]_C$, (e) $[C_6H_{12}O_6]$, and biomass concentrations for (f) phototrophic bacteria B_{PHOTO} , (g) heterotrophic bacteria B_{HET} , (h) nitrifying bacteria B_{NIT} , (i) denitrifying bacteria B_{DEN} , (j) dissimilatory nitrate reducing bacteria B_{DNR} , and (k) necromass NEC .

Table 7.2: Summary of calibrated parameters for microbial metabolic reactions R1 to R8. ^aValues of μ_s relative to reactions R1 to R8 written as in Table 7.1. Note that, the value of μ_s changes depending on the stoichiometry represented in the reactions. ^bCompetiton term was included in R1 and R2 to account for competitive substrate consumption between NH_4^+ and NO_3^- . ^cCompetiton term was included in R3 and R4 to account for competitive substrate consumption between NH_4^+ and NO_3^- . ^dCompetiton term was included in R3 and R4 to account for competitive substrate consumption of $\text{C}_6\text{H}_{12}\text{O}_6$.

Parameter values		R1	R2	R3	Reactions		R6	R7	R8	
					R4	R5				
Maximum specific rate of substrate utilization μ_s [$\times 10^{-5} \text{ s}^{-1}$]		88.45 ^a	594.88 ^a	7.27 ^a	177.98 ^a	442.94 ^a	54.53 ^a	42.74 ^a	883.15 ^a	
Maximum specific biomass growth rate $\hat{\mu}_s$ [$\times 10^{-5} \text{ s}^{-1}$]		2.66	10.78	1.00	12.48	16.49	5.57	4.35	40.78	
Fraction of electron used for cell synthesis e [-]		0.06	0.05	0.11	0.08	0.15	0.12	0.12	0.05	
Biomass yield Y_b [mol of B_x /mol of e^- donor]		1.0	0.33	0.13	0.069	0.038	0.10	0.10	0.025	
Biomass yield Y_b [g of dry B_x /g of e^- donor]		6.28	2.09	0.083	0.043	0.24	0.065	0.065	0.025	
Michaelis-Menten constant K_M [mol/L]		NH_4^+	^b 3.01×10^{-3}	-	^c 1.41×10^{-5}	-	3.55×10^{-2}	-	-	
		NO_3^-	-	^b 5.29×10^{-2}	-	^c 1.28×10^{-2}	-	4.64×10^{-3}	6.15×10^{-4}	-
		$\text{C}_6\text{H}_{12}\text{O}_6$	-	-	^d 5.72×10^{-2}	^d 5.16×10^{-3}	-	1.47×10^{-3}	8.10×10^{-4}	-
		$\text{O}_2(\text{aq})$	-	-	4.43×10^{-5}	4.43×10^{-5}	4.43×10^{-5}	-	-	4.43×10^{-5}
		HCO_3^-	7.90×10^{-6}	7.90×10^{-6}	-	-	7.90×10^{-6}	-	-	-
		NEC	-	-	-	-	-	-	-	-
Inhibition constant K_H [mol/L]		H^+	1×10^{-9}	1×10^{-9}	1×10^{-9}	1×10^{-9}	1×10^{-9}	1×10^{-9}	1×10^{-9}	1×10^{-9}
		$\text{O}_2(\text{aq})$	1×10^{-5}	1×10^{-5}	1×10^{-5}	1×10^{-5}	1×10^{-5}	1×10^{-5}	1×10^{-5}	1×10^{-5}
		$\text{C}_6\text{H}_{12}\text{O}_6$	-	-	-	-	-	1.91×10^{-3}	1.51×10^{-4}	-
Initial biomass concentration $[B_x]_0$ [mg of dry B_x /L]		B_{PHOTO}	6.1×10^{-4}							
		B_{HET}	1.6×10^{-3}							
		B_{NIT}	6.5×10^{-2}							
		B_{DEN}	9.0×10^{-3}							
		B_{DNR}	2.2×10^{-2}							

7.3.2 Goodness-of-fit analyses

Analyses of goodness-of-fit show that the modelled concentrations in Figure 7.2 matched relatively well the experimental $[\text{NH}_4^+]$, $[\text{NO}_3^-]$, pH, and net oxygen consumption $[\text{O}_2(\text{aq})]_C$, with $R \geq 0.9$, $\text{NRMSE} \leq 17\%$, $\text{NSE} \geq 0.7$, $\text{IA} \geq 0.85$, and $-0.1\% \leq \text{PBIAS} \leq 5\%$ (Figure 7.3, cells marked with red asterisk).

Validation tests conducted with experiments at different $[\text{NH}_4\text{NO}_3]$ and C_K (Figure 7.3) also showed relatively good agreement against experiments, with 84% of state variables having $R \geq 0.8$, 50% having $\text{NRMSE} \leq 15\%$, 53% having $\text{NSE} \geq 0$, 56% having $\text{IA} \leq 0.8$, and 38% having $-15\% \leq \text{PBIAS} \leq 15\%$; in average, 56.2% of validation tests passed the benchmark values stated in Section 7.2.3. In all validation tests, $[\text{NH}_4^+]$ and $[\text{NO}_3^-]$ were captured by the model at relatively high accuracy (86 % passing goodness-of-fit benchmark analyses), while the model prediction of pH and $[\text{O}_2(\text{aq})]_C$ was less accurate and often underestimated the state variable values.

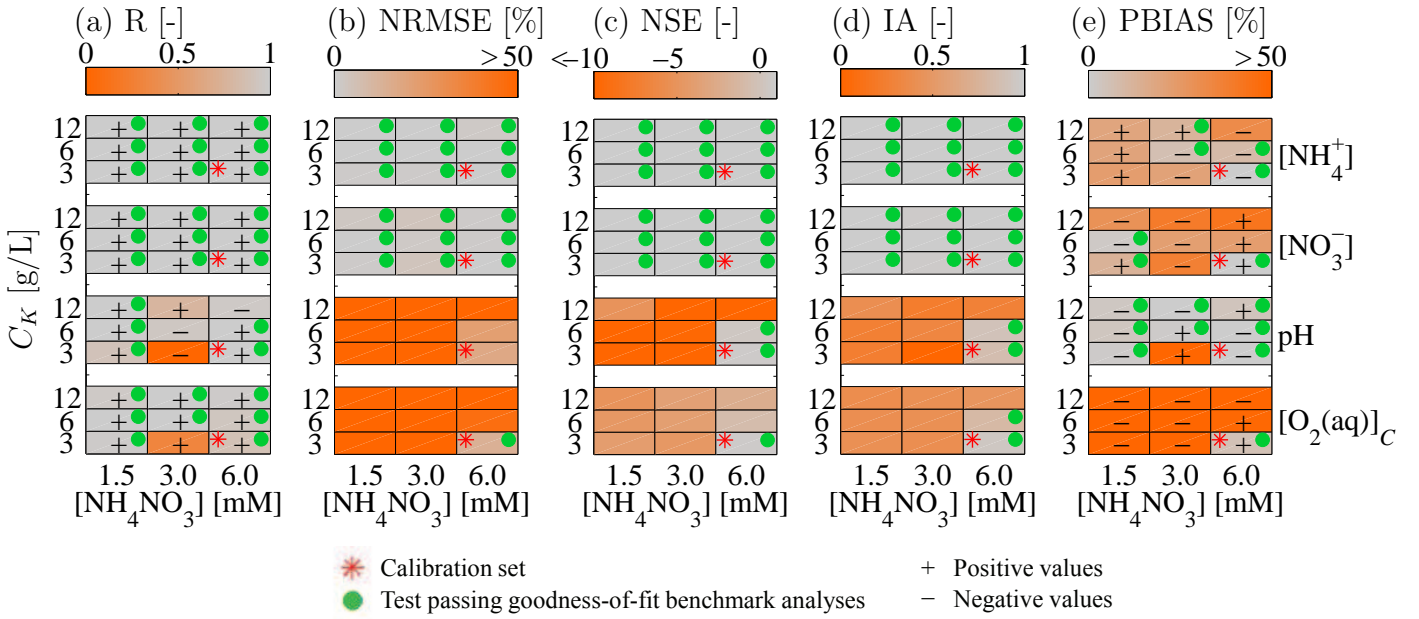


Figure 7.3: Goodness-of-fit analyses of the modelled against experimental $[\text{NH}_4^+]$, $[\text{NO}_3^-]$, pH, and the net oxygen consumption $[\text{O}_2(\text{aq})]_C$ using (a) correlation coefficient R, (b) normalized root mean square error NRMSE, (c) Nash-Sutcliffe efficiency NSE, (d) index of agreement IA, and (e) percent bias PBIAS. The red asterisk indicates calibration set and the green dot represents validation tests that passed the good-of-fit benchmark analyses. '+' and '-' signs indicate positive and negative values in R and PBIAS tests, respectively. Note that kaolinite concentration C_K and $[\text{NH}_4\text{NO}_3]$ plotted corresponded to the initial concentrations in incubation.

7.3.3 Effect of N leaching on microbial dynamics

50-year simulations were carried out to investigate how ecosystem and microbial communities responded to NH_4^+ and NO_3^- leaching rates $R_{\text{NH}_4^+}$ and $R_{\text{NO}_3^-}$ ranging between 8.64×10^{-9} and 8.64×10^{-3} $\text{mol L}^{-1} \text{day}^{-1}$. In all tested scenarios, a steady-state was reached at the end of the 50-year simulation period.

Total living biomass B_{TOT} (Figure 7.4a) generally increased with increasing $R_{\text{NH}_4^+}$ and $R_{\text{NO}_3^-}$ up to 11.3 g/L at the highest $R_{\text{NH}_4^+}$ and $R_{\text{NO}_3^-}$. No trace of living biomass was observed at the lowest

leaching rates (indicated by “NB” in Figure 7.4). Necromass *NEC* (not shown here) accumulated in the ecosystem at high leaching rates because depolymerization and ammonification in R8 was inhibited by the presence of $C_6H_{12}O_6$ and because other decomposition pathways (e.g., fermentation by fungus) were not included in the reaction network.

B_{PHOTO} dominated the ecosystem when $R_{NO_3^-} \leq 5 \times 10^{-4} \text{ mol L}^{-1} \text{ day}^{-1}$ and was out-competed when $R_{NO_3^-} > 5 \times 10^{-4} \text{ mol L}^{-1} \text{ day}^{-1}$ and $R_{NO_3^-} \gg R_{NH_4^+}$ (Figure 7.4b). B_{PHOTO} was synthesised mainly by NH_4^+ assimilation (R1) when $R_{NO_3^-}$ was low regardless of $R_{NH_4^+}$ and by NO_3^- assimilation (R2) when both $R_{NO_3^-}$ and $R_{NH_4^+}$ were high. These results show that B_{PHOTO} was able to effectively utilize low NH_4^+ concentrations and had a higher preference for NH_4^+ over NO_3^- ; similar observations have previously been reported in Caperon and Meyer (1972), McCarthy et al. (1977), and Cochlan and Harrison (1991).

B_{HET} survived only at leaching rates smaller than $1 \times 10^{-5} \text{ mol L}^{-1} \text{ day}^{-1}$, and contributed to less than 8% of total living biomass (Figure 7.4c). Approximately 50 to 70% of B_{HET} was synthesis from NH_4^+ assimilation (R3), about 30 to 25% by depolymerizing *NEC* (R8), and less than 20% by assimilating NO_3^- (R4). B_{HET} survived in low NH_4^+ concentrations because of a low K_M for NH_4^+ in R3, and it showed a higher preference for NH_4^+ over NO_3^- . However, its growth was greatly suppressed by B_{PHOTO} due to high K_M for $C_6H_{12}O_6$ in R3. Similar experimental observations were also found in Tufail (1987) and Kirchman and Wheeler (1998).

B_{NIT} was completely out-competed by B_{PHOTO} and B_{HET} at steady-state (Figure 7.4d), as opposed to the transient incubation phase (Figure 7.2h), where B_{NIT} was more abundant than other microorganisms. B_{PHOTO} was experimentally observed to suppress nitrification by more than 80% in Risgaard-Petersen et al. (2004), whereas B_{HET} was found to reduce by more than 90% the B_{NIT} concentration in the presence of glucose (Verhagen and Laanbroek, 1991).

A small fraction of B_{DNR} was observed at intermediate $R_{NO_3^-}$, with no B_{DEN} surviving in that regime (Figure 7.4e - f). B_{DNR} survived better than B_{DEN} in low $[NO_3^-]$ because of lower K_M for both NO_3^- and $C_6H_{12}O_6$. However, B_{DEN} gradually overcame B_{DNR} because competition between them decreased with increasing $R_{NO_3^-}$. At this point, $O_2(aq)$ inhibition on B_{DNR} was higher than B_{DEN} , thus DNR reaction velocity became slower than denitrification reaction. Although B_{DEN} dominated the ecosystem at high $R_{NO_3^-}$, it was out-competed by B_{PHOTO} when $R_{NH_4^+}$ increased.

7.3.4 Effect of N leaching on aqueous NH_4^+ and NO_3^-

$[NH_4^+(aq)]$ and $[NO_3^-(aq)]$ were negatively correlated ($R = -0.99$, Figure 7.5), with $[NH_4^+(aq)]$ maintained at a relatively high concentration even if $R_{NH_4^+}$ was low because B_{HET} and B_{DNR} were more active in converting *NEC* and NO_3^- into NH_4^+ through R8 and R7, respectively, at low leaching rates. Conversely, $[NO_3^-]$ was low at low $R_{NO_3^-}$ because B_{NIT} did not survive (Figure 7.1) and, therefore, there was no recharge of NO_3^- in the ecosystem.

7.3.5 Effect of N leaching on total N phase partitioning

Figure 7.6 shows how N compounds were partitioned into protected ($NH_4^+(p)$ and $NO_3^-(p)$), aqueous ($NH_4^+(aq)$, $NO_3^-(aq)$, $NO_2^-(aq)$, $NH_3(aq)$, and $HNO_3(aq)$), gaseous ($NH_3(g)$), and biological (B_{PHOTO} , B_{HET} , B_{NIT} , B_{DEN} , B_{DNR} , and *NEC*) phases at steady-state for all N leaching scenarios. In general, the majority of N was partitioned into aqueous and biological phases, with negligible fractions being either protected on clay or released to the atmosphere as gases.

Protected N was less than 1% of the total N introduced in the ecosystem, and was lower with

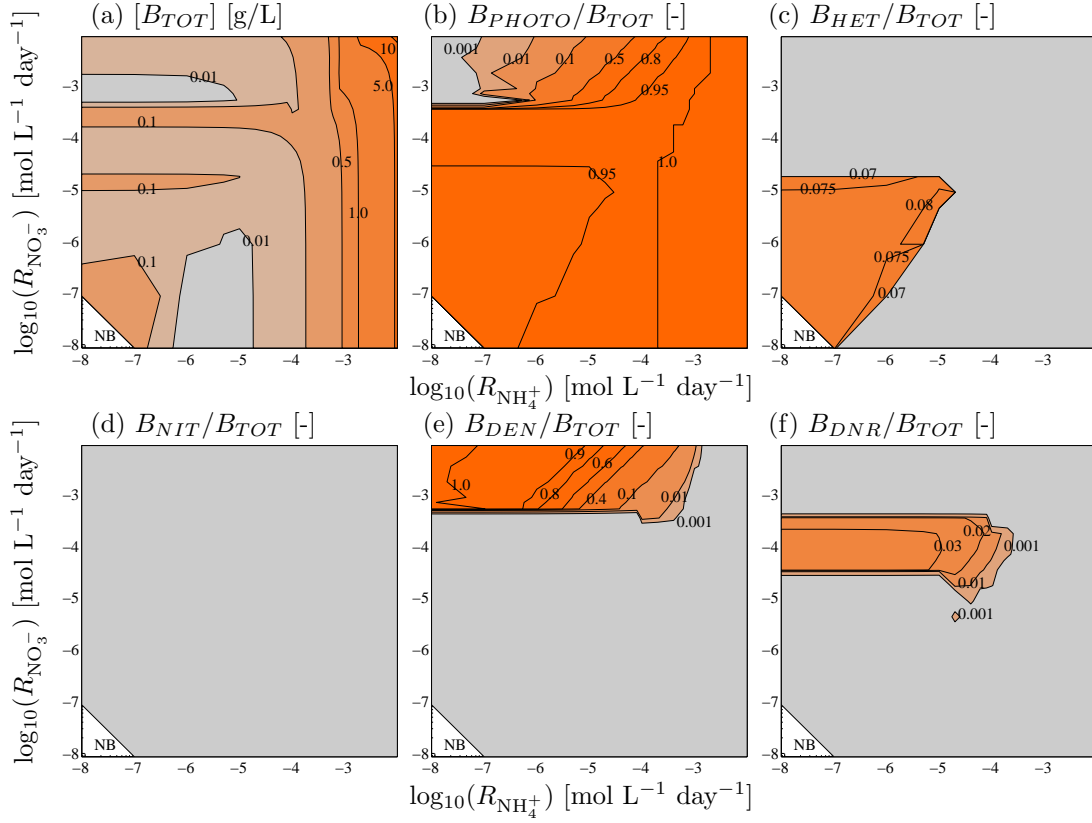


Figure 7.4: (a) Concentrations of total living biomass B_{TOT} and biomass fraction relative to B_{TOT} for (b) phototrophic bacteria B_{PHOTO} , (c) heterotrophic bacteria B_{HET} , (d) nitrifying bacteria B_{NIT} , (e) denitrifying bacteria B_{DEN} , and (f) dissimilatory nitrate reducing bacteria B_{DNR} at steady-state (end of 50-year simulation period) and for leaching rates $R_{NH_4^+}$ and $R_{NO_3^-}$ ranging between 8.64×10^{-9} and 8.64×10^{-3} mol L⁻¹ day⁻¹. NB indicates no trace of living biomass detected.

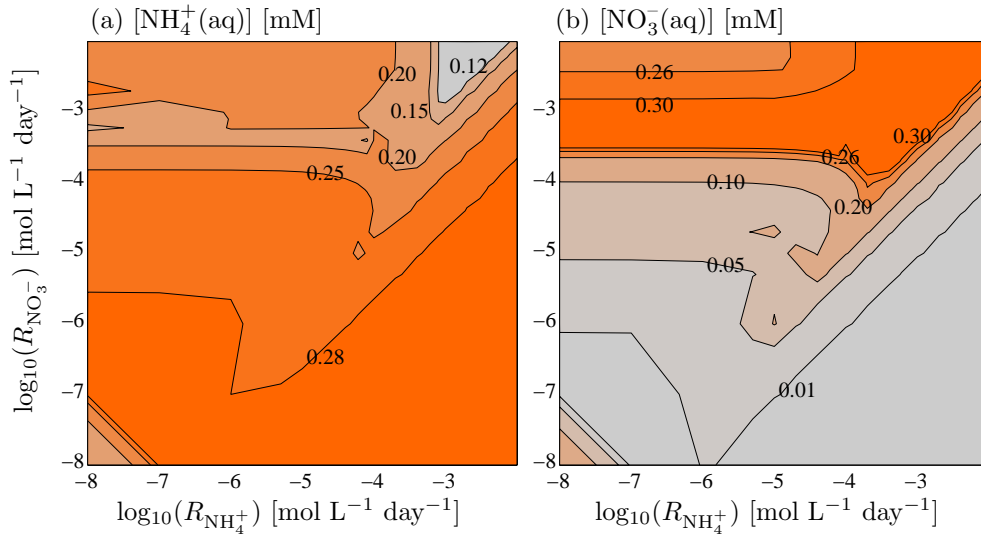


Figure 7.5: Concentrations of (a) NH_4^+ and (b) NO_3^- in the aqueous phase at steady-state (end of 50-year simulation period) for leaching rates $R_{NH_4^+}$ and $R_{NO_3^-}$ ranging between 8.64×10^{-9} and 8.64×10^{-3} mol L⁻¹ day⁻¹.

increasing leaching rates (Figure 7.6a); it was regulated by biomass and by $[\text{NH}_4^+(\text{aq})]$ and $[\text{NO}_3^-(\text{aq})]$ at steady-state more than by Langmuir adsorption.

Aqueous N generally decreased with increasing $R_{\text{NH}_4^+}$ and $R_{\text{NO}_3^-}$ for $R_{\text{NO}_3^-} \leq 5 \times 10^{-4} \text{ mol L}^{-1} \text{ day}^{-1}$; an opposite trend was found for $R_{\text{NO}_3^-} > 5 \times 10^{-4} \text{ mol L}^{-1} \text{ day}^{-1}$ (Figure 7.6b). This resulted from B_{DEN} dominating the ecosystem at high $R_{\text{NO}_3^-}$ and producing NO_2^- that accumulated in the ecosystem. Because NO_2^- denitrification to $\text{N}_2(\text{g})$ was not modelled, N gas released to the atmosphere was negligible (Figure 7.6c).

Finally, the fraction of N accumulated in the biological phase was high (Figure 7.6d) and negatively correlated to aqueous N fraction, implying that a great portion of aqueous inorganic N was immobilized into biomass.

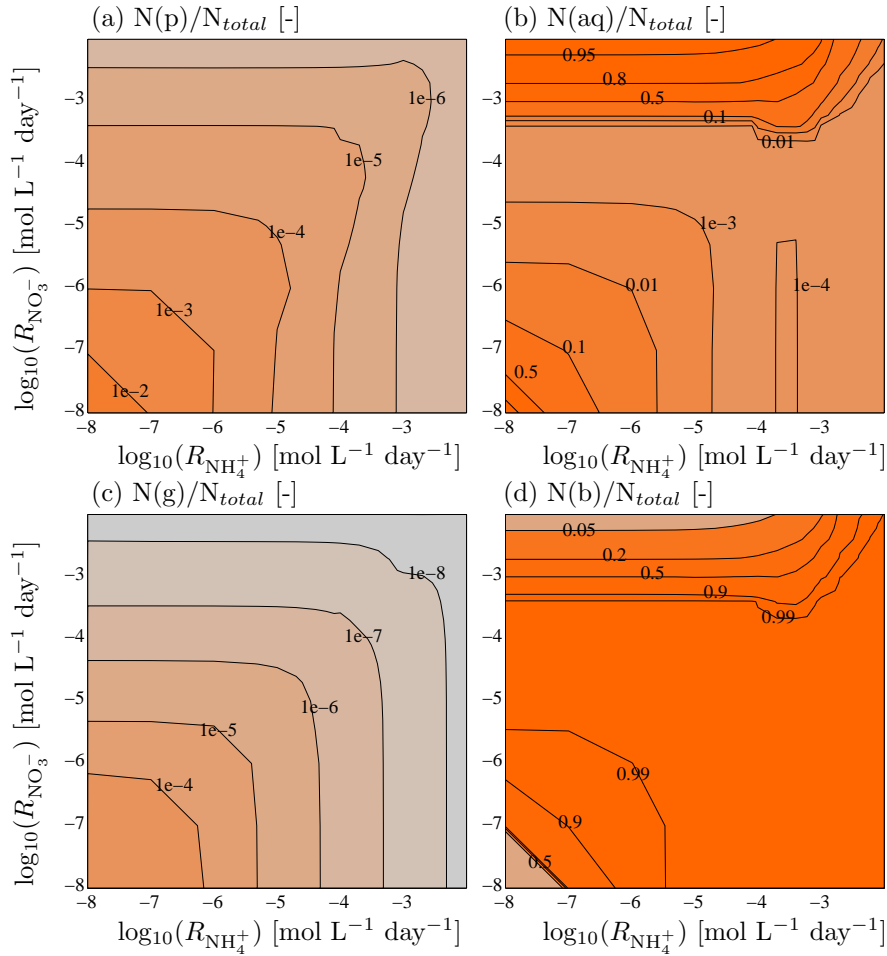


Figure 7.6: Partitioning of total N (N_{total}) into (a) protected (p), (b) aqueous (aq), (c) gaseous (g), and (d) biological (b) phases at steady-state (end of 50-year simulation period) for leaching rates $R_{\text{NH}_4^+}$ and $R_{\text{NO}_3^-}$ ranging between 8.64×10^{-9} and $8.64 \times 10^{-3} \text{ mol L}^{-1} \text{ day}^{-1}$.

7.3.6 N leaching and N mass flow through reactions

Figure 7.7 shows the mass flow of total N through each microbial metabolic reaction at steady-state for $R_{\text{NH}_4^+}/R_{\text{NO}_3^-} = 1$.

At low leaching rates ($\leq 1 \times 10^{-5} \text{ mol L}^{-1} \text{ day}^{-1}$), more than 50% of total N was consumed by B_{HET} through depolymerization and ammonification in R8, whereas phototrophic and heterotrophic

NH_4^+ assimilation (R1 and R3) contributed to approximately 47 and 3% of total N consumption, respectively. Depolymerization of NEC was high due to low $\text{C}_6\text{H}_{12}\text{O}_6$ availability at low leaching rates; though, the concentration of B_{HET} synthesised from NEC was smaller than that produced by R3 (Chapter 7.3.3) because of smaller biomass yield Y_b in R8 than in R3 (Table 7.2). Apart from competition, facilitative interactions were also observed between B_{PHOTO} and B_{HET} . Depolymerization and ammonification of NEC by B_{HET} released NH_4^+ and $\text{C}_6\text{H}_{12}\text{O}_6$ to the ecosystem, and this facilitated phototrophic and heterotrophic NH_4^+ assimilation and increased the abundance of B_{PHOTO} and B_{HET} , which eventually decayed into NEC ; this therefore resulted in a positive feedback loop that enabled the ecosystem to sustain itself even though the input of nutrients was low.

With increasing leaching rates, R3 and R8 were gradually out-competed, while R1 kept consuming approximately 45% of total N; in contrast, N fraction uptake by phototrophic NO_3^- assimilation (R2) increased to approximately 50% of the total N consumption at the highest leaching rate (Figure 7.7). Because phototrophic NH_4^+ assimilation in R1 had high Y_b , the concentration of B_{PHOTO} increases rapidly with increasing $[\text{NH}_4^+]$, hence, creating intra-species competition for NH_4^+ . When $[\text{NH}_4^+]$ was unable to sustain B_{PHOTO} , a fraction of B_{PHOTO} would have to switch their diet to consume NO_3^- . Although both denitrification (R6) and DNR (R7) had lower K_M for NO_3^- than R2 (Table 2), R6 and R7 were eventually overtaken by R2 at high leaching rates because phototrophic reactions in R1 and R2 had higher Y_b than R6 and R7.

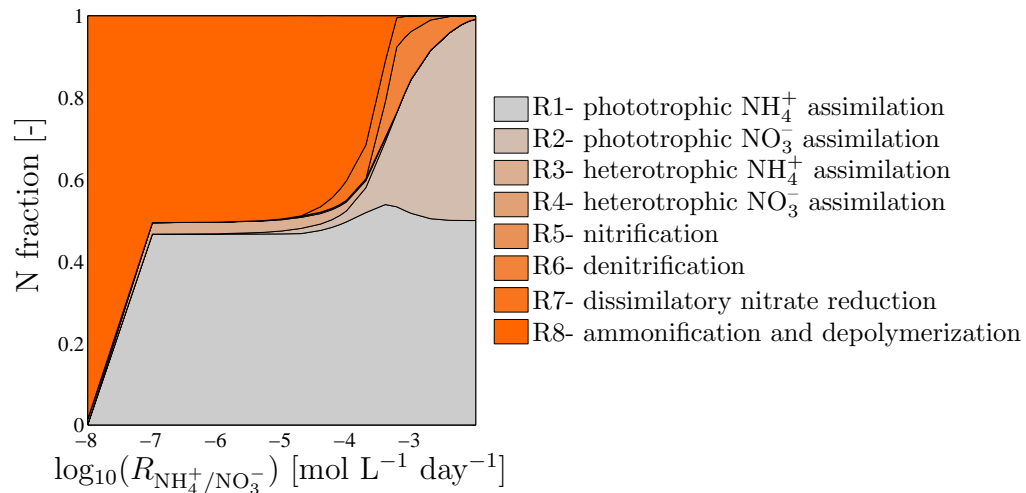


Figure 7.7: Mass flow of total N N_{total} through microbial metabolic reaction R1 to R8 at steady-state (end of 50-year simulation period) for leaching rates $R_{\text{NH}_4^+}$ and $R_{\text{NO}_3^-}$ ranging between 8.64×10^{-9} and $8.64 \times 10^{-3} \text{ mol L}^{-1} \text{ day}^{-1}$, and for $R_{\text{NH}_4^+}/R_{\text{NO}_3^-} = 1$.

7.4 Discussion

In this chapter, microbial functional groups included different microbial species that performed similar ecological functions, hence assuming that members of the same group were equipped with same enzymes for the same metabolic mechanisms; in fact, no significant variation was found in Michaelis-Menten constant K_M when experiments were conducted with different microbial species of the same functional group (Caperon and Meyer, 1972). However, several studies showed that K_M values may greatly depend on the ambient nutrient concentrations of the original habitat (e.g.,

MacIsaac and Dugdale, 1969; Caperon and Meyer, 1972); for instance, phytoplankton populations obtained from eutrophic ecosystems were observed to have much higher K_M values for NO_3^- as compared to those living in oligotrophic ecosystems (MacIsaac and Dugdale, 1969). The microbial communities used to inoculate sediment mixtures in the experiments conducted in Chapter 3 were sampled from an estuary that has relatively high $[\text{NH}_4^+]$ and $[\text{NO}_3^-]$ (approximately 1.2 mM of NH_4^+ and 6.6 mM of NO_3^-) and, hence, the parameters calibrated here may reflect only the metabolic characteristics of microorganisms adapted to high nutrient concentrations and may not be applicable to ecosystem where nutrients are strongly limiting. This may also explain why none of the functional groups was able to survive at low N leaching rates (Figure 7.4). Along this line, the capability of microorganisms to adapt to a specific nutrient condition (Eppley and Coatsworth, 1968) was not accounted for in the model, and we assumed that enzymes responsible for metabolism were not altered after long-term presence in such an environment. If microbial adaptation were included, the model may result in different microbial interactions and different patterns of diversity at steady-state (Williams and Lenton, 2010).

Microorganisms were found to attach on SPM at a few orders of magnitude higher concentration than those living freely in ambient water (e.g., Caron et al., 1986; Turley and Mackie, 1994). These two groups of microorganisms were not differentiated in the model and, hence the calibrated parameters reflected the combined effects resulting from metabolism of both aggregate-attached and free-living microorganisms; however, we note that aggregate-attached bacteria may have higher enzymatic activity and reaction rate than free-living bacteria as evident in Goulder (1977) and Grossart et al. (2007). Several studies also observed the grazing of aggregate-attached microorganisms by heterotrophic microflagellates and suggested that the abundance of bacteria living attached to SPM was controlled by heterotrophic grazing (e.g., Caron, 1987; Kiørboe et al., 2004). Although we note that antagonistic relationships such as predation, grazing, scavenging, and inhibition by metabolites of other species occur among microbial communities (e.g., Cole, 1982; Guerrero et al., 1986; Pernthaler, 2005), these interactions were not explicitly included in the model; indeed, we assume that these interactions were implicitly accounted for through mortality.

Although microorganisms may grow better in environments where micronutrients are available to them (MacIsaac and Dugdale, 1969), experiments herein were conducted with only inorganic N (NH_4^+ and NO_3^-) and $\text{C}_6\text{H}_{12}\text{O}_6$ without accounting for other macro- and micronutrients. Because sulfur-based compounds were not added to the test samples, chemolithoautotrophic denitrification that uses sulfur as electron donor (Batchelor and Lawrence, 1978) was not included in the reaction network. NO_2^- , on the other hand, was very likely present in the test samples and it was accounted for in the model as an intermediate product of denitrification. However, anaerobic ammonium oxidation (Anammox) that uses NO_2^- as electron acceptor (Dalsgaard et al., 2005) was not considered in the reaction network, though, we did not exclude the possibility of having Anammox bacteria in the test samples.

Temperature has been reported in literature as one of the factors that alters the enzymatic activities of microorganisms (Toseland et al., 2013). For instance, microbial affinity for NO_3^- in phototrophic and heterotrophic assimilation was found to decrease with decreasing temperature (Reay et al., 1999), whereas a reduction in nitrification and denitrification rates were also observed as temperature decreased (e.g., Tourna et al., 2008; Saleh-Lakha et al., 2009; Wang et al., 2015). Apart from biochemical reactions, chemical adsorption on clay is also sensitive to temperature (Almeida et al., 2009). In this study, temperature in both experiments and model was kept constant at 21°C and, hence, the parameters calibrated here reflected only the microbial metabolism and adsorption kinetics specific to that temperature.

The model considered a comprehensive ecological feedback loop that explicitly accounted for the

biomass of different functional groups and the necromass, which are not normally included in most aquatic biogeochemical models (Robson, 2014). Some models did consider explicitly the biomass with one or more functional groups, however, most of these models focused on biogeochemical cycling processes (e.g., Allen and Clarke, 2007; Kaufman and Borrett, 2010) with little emphasis on the dynamics of microbial diversity (e.g., Bruce et al., 2006; Prokopkin et al., 2010). Although the calibrated parameters were specific to the microbial strains and environmental conditions tested here, the reaction network and model structure presented herein provide a modelling framework that could be applied to predict, monitor, and manage water quality and microbial communities, not only in natural aquatic ecosystems, but also in engineered environments such as wastewater treatment plants, bioremediation plants, bioreactors, aquaculture farms, and microalgae cultivation plant.

7.5 Summary

This chapter presents a biogeochemical model coupled with experimental observations to illustrate the role of microorganisms in modifying the chemical composition of a SPM suspension and the dynamics of the microbial community affected by changes in the environment quality.

Microorganisms controlled the water quality of their habitat with different functional groups responsible for transforming different nutrients and performing different ecological functions. It was observed that the concentration of NH_4^+ in aqueous was not linearly correlated to the increase of nutrient leaching; in fact, NH_4^+ was observed at relatively high concentrations at low nutrient leaching rates because the low nutrient condition favoured the metabolic reaction of heterotrophic microorganisms that converted necromass into NH_4^+ . Variation in chemical composition caused by anthropogenic nutrient leaching was observed to result in a shift in the ecological balance of the microbial community, i.e., the added chemicals either favoured or suppressed the growth of certain microbial functional groups. For example, denitrifying microorganisms were found to dominate an ecosystem subject to high NO_3^- and low NH_4^+ leaching, while, the ecosystem was dominated by phototrophic microorganisms when NH_4^+ leaching was increased. The competitive and facilitative interactions between microbial functional groups were found to be susceptible to the change in environmental conditions. For example, heterotrophic microorganisms were out-competed by phototrophs at high NH_4^+ and NO_3^- leaching, while, both phototrophs and heterotrophs coexisted in facilitative relationship in low nutrient conditions with heterotrophs providing NH_4^+ to phototrophs through the necromass ammonification process. In addition, the feeding behaviour of microorganisms was also found to be altered by changes in nutrient availability. Phototrophs were observed to have higher preference for NH_4^+ over NO_3^- in low nutrient conditions, whereas, their preferences for both NH_4^+ and NO_3^- were approximately equal when the availability of both NH_4^+ and NO_3^- was high.

This chapter provides a picture of how microorganisms modulated the sediment and water qualities of an aquatic ecosystem and how changes in chemical composition in the ecosystem altered the ecological functions and dynamics of the microbial community, which in turn modified SPM characteristics and further feedback on the water quality of the ecosystem.

Chapter 8

Conclusions and perspectives

8.1 Conclusions

The dynamics of suspended particulate matter (SPM) modulated by microbial activity was extensively investigated in this doctoral thesis to establish a comprehensive understanding on the interrelationships between mineral, chemical, and biological components of a SPM suspension. Experimental evidence and numerical analyses were put forth to address these feedback mechanisms.

Microorganisms were first shown through experiments to facilitate SPM aggregation, presumably through the excretion of sticky metabolites that act as “biological glue” to provide adhesion to SPM in addition to van der Waals forces. SPM suspensions inoculated with microorganisms were observed to have average size approximately 60% larger and average capacity dimension approximately 2% lower than SPM free from microbial colonization. Correlation analyses of size and capacity dimension suggest that the presence of microorganisms alone did not result in low capacity dimension; instead, it stemmed from the increased aggregation facilitated by microorganisms. Microorganisms were also found to increase the uncertainty and complexity of the size and capacity dimension distributions of SPM. The size and capacity dimension distributions of biomass-affected SPM were found to have higher statistical entropy than those of biomass-free SPM, providing further confirmation to the argument that microorganisms can shift the equilibrium of SPM away from that of abiotic condition.

Biomass-affected and biomass-free SPM have different responses towards variation in environmental conditions. The size and capacity dimension of biomass-affected SPM were observed to increase and decrease, respectively, with increasing nutrient concentration because of nutrient-enhanced microbial metabolism, which facilitated aggregation. On the other hand, the addition of nutrients (i.e., NH_4^+ and NO_3^-) increased only slightly the size of mineral SPM, with size and capacity dimension not significantly altered when nutrient concentration was increased. In addition, the response of biomass-affected SPM to hydrodynamic forcing (e.g., turbulence) was found to be different from that of biomass-free SPM. The entropy of SPM size and capacity dimension distributions in biomass-affected conditions decreased with increasing turbulence shear rate, whereas, the entropy was not significantly affected by turbulence in pure mineral suspension. These analyses provide strong evidence that phenomena observed in a pure mineral suspension cannot be used to draw inference on the flocculation dynamics of a suspension affected by microorganisms.

It is worth pointing out that the settling velocity of biomass-free and biomass-affected SPM was found to be nearly invariant, even though microorganisms were observed to play an important role in modifying SPM size and capacity dimension. This was explained by the fact that the effects of size, density, and capacity dimension on settling velocity are anisotropic.

Microorganisms were next found to alter SPM collision and aggregation dynamics through the

modification of SPM size, shape, and surface asperity. Numerical analyses, based on the spheropolygon theory, suggest that biomass-affected SPM with generally large size and low capacity dimension had lower probability of aggregation as compared to biomass-free SPM that had smaller size and higher roundness. The analyses also show that shape and surface asperity have a very significant control over SPM collision and aggregation kinematics. This implies that neglecting the effect of shape and surface asperity can bias the estimation of flocculation rate.

Microorganisms assimilate nutrients and transform molecules from one form to another and, hence, they modify the chemical composition of a SPM suspension. Analyses based on water quality data acquired from experiments coupled with a biogeochemical model reveal that the fraction of nutrients absorbed on mineral and that present in aqueous phase were in fact controlled by microbial activity. Steady-state analyses further reveal that changes in nutrient concentration as a result of anthropogenic leaching can in turn feedback on microbial growth and metabolism. Increased nutrient concentration favoured growth of one microbial functional group and suppressed growth of others, hence, changing the ecological balance of a microbial community. The interactions between microbial functional groups and the feeding behaviour of microorganisms were also found to be sensitive to the change in nutrient availability. A shift in ecological balance can then impose a feedback on SPM flocculation because different types of microorganisms have different affinity to adhere to SPM and produce metabolites with different strength and stickiness.

This thesis demonstrates that microorganisms are effectively engineering the physical structure and chemical properties of SPM and have a very significant control over SPM flocculation dynamics. The interactions between minerals, nutrients, and microorganisms are interconnected with high complexity and nonlinearity, i.e., these interactions continuously feedback on one another. A summary of the feedback loop describing SPM flocculation mediated by microorganisms is depicted in Figure 8.1.

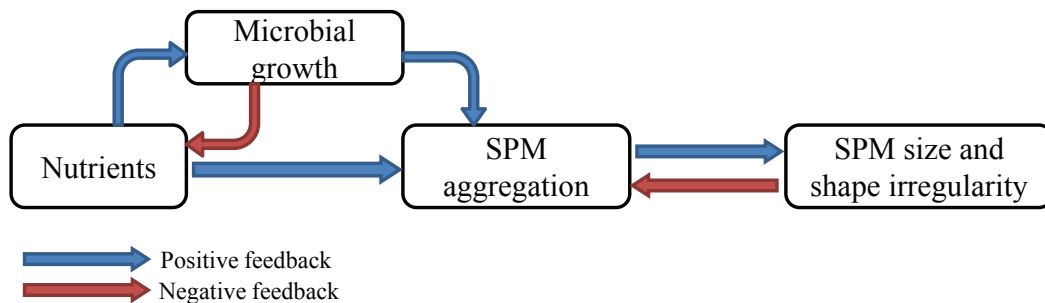


Figure 8.1: Feedback loop describing the interactions between SPM, nutrients, and microorganisms.

8.2 Perspectives

The knowledge and tools developed in this thesis have a high prospect to be used in different research areas. A general opinion on possible applications and future improvements is illustrated in this section.

The experimental facility designed and developed in Chapter 3 is a unique tool that allows the user to control and monitor various physical, chemical, and biological processes simultaneously and systematically. It is a user-friendly tool that has the capability to conduct automated regulation

of turbulence intensity and measurements. The usability of this facility could be further improved by implementing an automated control system to regulate the chemical composition of the test suspension. This implementation will allow the user to maintain a constant pH or a constant chemical concentration condition throughout an experiment. In addition, the quantification of microbiological processes in experiments could be improved if a method for direct detection of microorganisms is developed, possibly through optical imaging techniques. This will then allow a better quantification of SPM-attached microorganisms and will allow a better picture of the interactions between free-living and SPM-attached microorganisms.

The flocculation of SPM modulated by microorganisms could only be partially explored in this thesis with a focus on the interactions between microorganisms and inorganic nitrogen. The growth of microorganisms can be substantially affected by other nutrients (e.g., phosphate and sulfur) and contaminants (e.g., glyphosate and DDT); hence, investigations can be extended to examine the effects or the combined effects of other chemicals. In addition, the impacts of other environmental parameters (e.g., water temperature rise and decreased pH) on microbiological flocculation can be investigated using the facility presented here. The application of this facility, however, is not only restricted to sediment research; instead, it can be used for investigations in ecological and environmental studies. For example, it can be used to explore how the clustering of microorganisms is affected by different chemical, hydrodynamical, and environmental conditions by quantifying the size and fractal dimension of these microbial clusters.

The semi-analytical method developed in Chapter 4 to estimate the three-dimensional capacity dimension of SPM is a generic tool that is applicable to granular aggregates of various origin, such as dusts, aerosols, biological cells, microbial clusters, proteins, and gel networks. It requires the user to input only a binary image of the test sample with no parameter required to be calibrated; the algorithm is robust and user-friendly.

The biogeochemical reaction network and model structure presented in Chapter 7 provide a modelling framework that can be used in both environmental and engineering contexts. It can be used as a tool to predict, monitor, and manage sediment and water quality, and microbial dynamics in natural aquatic ecosystems as well as in engineered environments, including wastewater treatment plants, bioremediation plants, bioreactors, aquaculture farms, and microalgae cultivation plants. The prediction of the model could, however, be improved by implementing an approach to account for the capability of microorganisms to adapt to a specific chemical concentration or a specific environmental condition after long period of exposure to that condition. This implementation will allow investigations of long-term effects (e.g., thousands of years) with kinetic parameters of microbial metabolic reactions calibrated against experiments conducted in an experimental time scale (e.g., in weeks/months). With the suggested improvements, the model framework together with measurements acquired from controlled experiments can therefore be used to investigate the long-term impacts of climate change and ocean acidification on the dynamics of aquatic microorganisms.

The ability of microorganisms to alter the information content of SPM size and capacity dimension distributions (observed in Chapter 5) may be exploited as a method to indicate the presence of microorganisms in a suspension. Such a method, if developed, can be incorporated into a commercial particle size analyzer to allow for *in-situ* detection of SPM-attached microorganisms.

Appendix A

Photographs of the facility

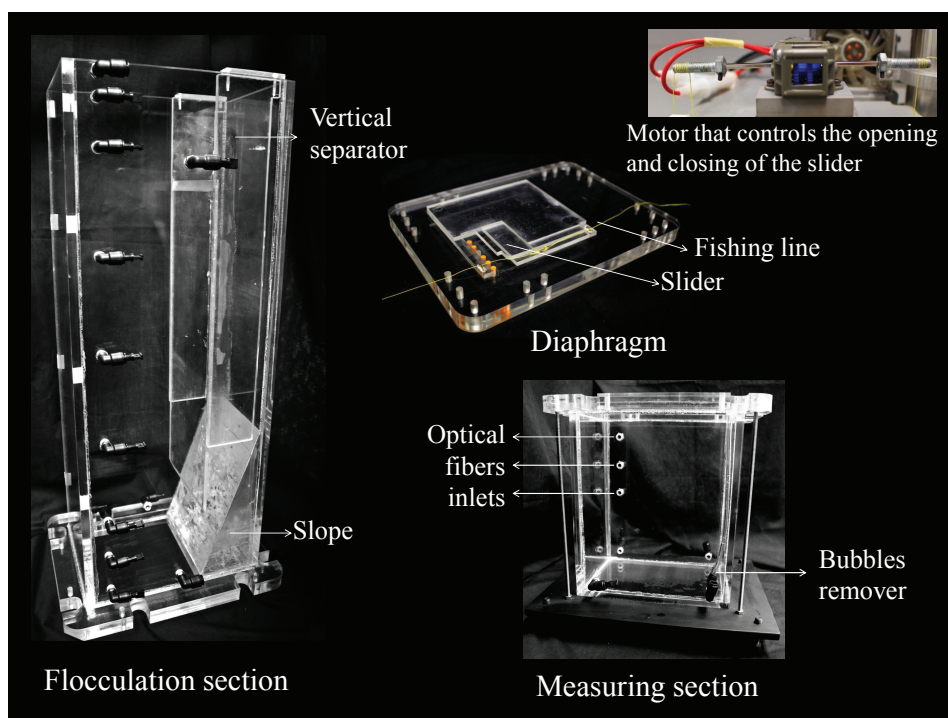


Figure A.1: Components of the settling column including the floculation section, the measuring section, and the diaphragm.

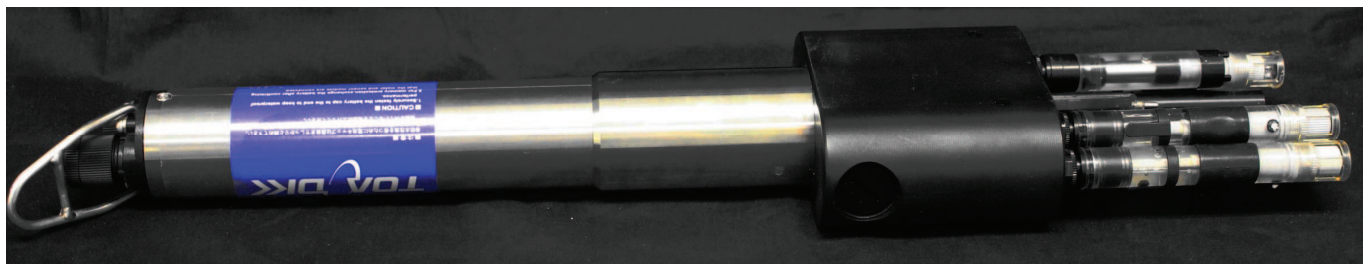


Figure A.2: The multi-parameter water quality meter (TOA-DKK, WQC-24) equipped with Standard and Ion modules.

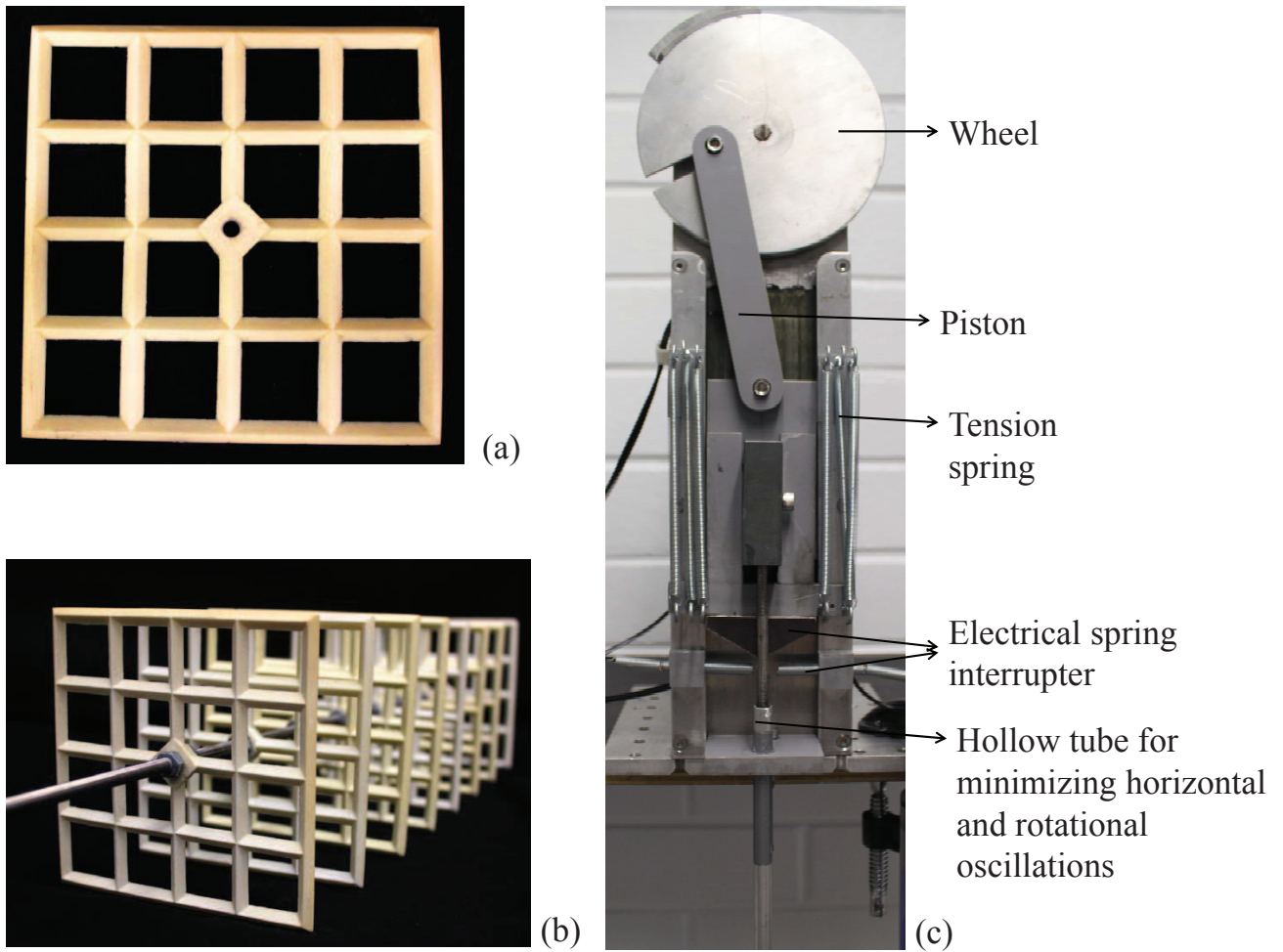


Figure A.3: Photographs of (a) a grid element, (b) evenly spaced grid elements connected through a stainless steel bar, and (c) the grid oscillation system.

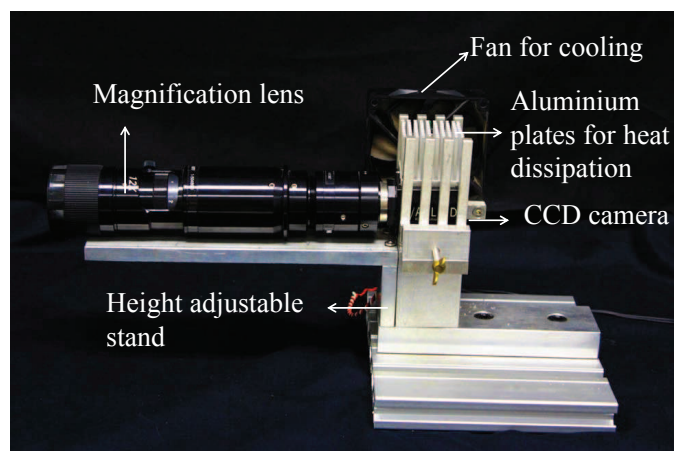
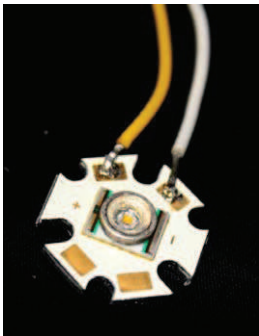
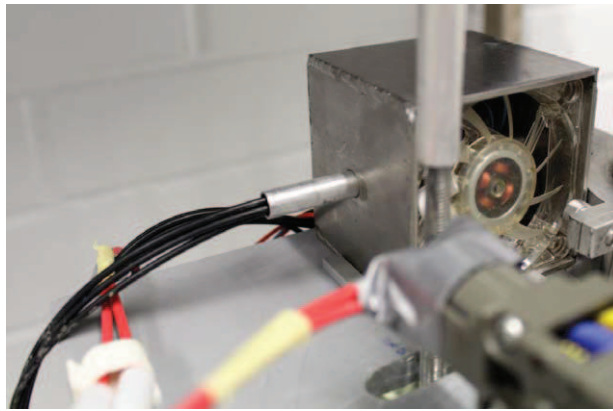


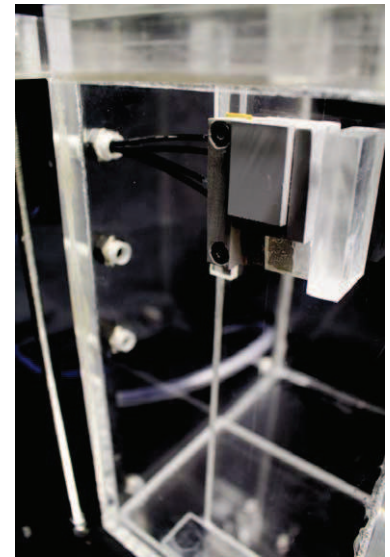
Figure A.4: Photograph of the CCD camera and the high magnification lens mounted on the height-adjustable camera stand.



(a)



(b)



(c)

Figure A.5: Photographs of (a) a Cree LED, (b) the optical box, and (c) the optical fibers holder fixed on the positioning stand.

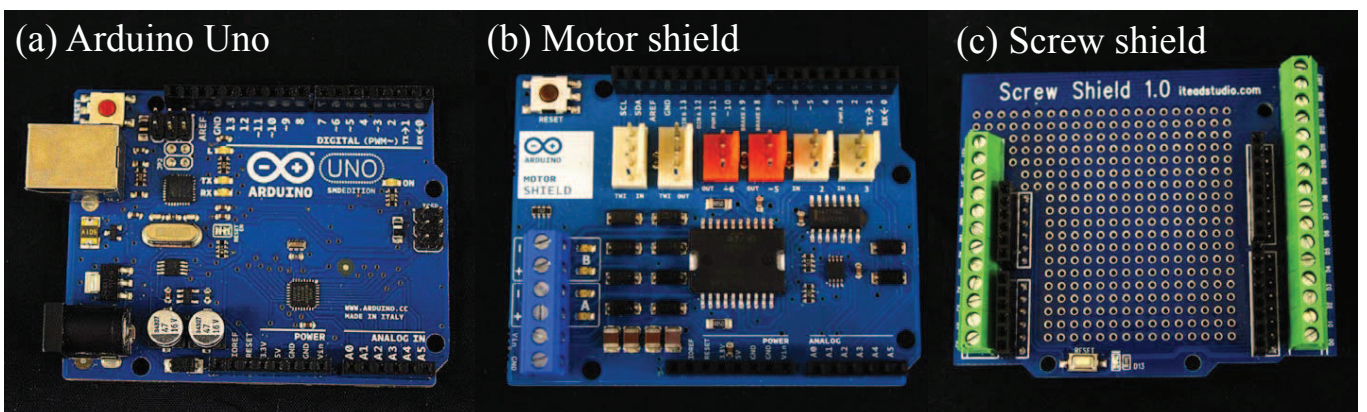


Figure A.6: Photographs of (a) the *Arduino Uno* board, (b) the motor shield, and (c) the screw shield used in the micro-controlling system.

Appendix B

Algorithms for reconstructing SPM capacity dimension

The algorithms used to reconstruct the 3D capacity dimension $d_0(S_3)$ of SPM from its 2D image described in Chapter 4 are presented here as a Matlab function script (*CapacityDimension3D*). This function script was published as supplementary document in Tang and Maggi (2015c)¹.

The function *CapacityDimension3D(FILENAME, ELL)* reads a binary image from the file specified by FILENAME (e.g., BW_CCA_1-7323.bmp), resizes the image to the desired dimensionless aggregate size ELL (e.g., ELL=1024), and returns the estimated $d_0(S_3)$. Note that, this function allows only the input of binary image and ELL has to be greater than the original image size.

B.1 Matlab function

```
function d0_3D = CapacityDimension3D(filename,ell)

image01 = imread(filename); %raw black and white image
%%% Check if the image is black and white
if max(max(image01))> 1;
    disp('Error-- Please input a binary image of aggregate.')
    return
end

image02 = imfill(image01, 'holes'); %fill holes

%%% Check the size of the raw image
if mean(size(image01,1),size(image01,2))> ell
    sprintf('Error-- Desired resolution ell has to be greater than original image ..
    .. size = %2.2d.',mean(size(image01,1),size(image01,2)))
    return
end

%%% Resize image to desire resolution ell
image03= imresize(image02, [ell ell],'nearest');
image03= uint8(image03);
```

¹Tang F.H.M., and Maggi F. (2015). Reconstructing the fractal dimension of granular aggregates from light intensity spectra, *Soft Matter*, 11(47), 9150-9159.

```

%%% Dimensionless area of aggregate N_A
[s1 t1] = find(image03==1);
N_A = length(s1);

%%% Dimensionless perimeter of aggregate N_P
image04= bwperim(image03);
[s2 t2] = find(image04==1);
N_P = length(s2);

%%% Outermost perimeter-based fractal dimension dP_0
dP_0 = 2* log10(N_P)/log10(N_A); % Eq.(4)

%%% Perimeter-based fractal dimension at I=1
Z= 2* log10(4*ell - 4)/log10(ell^2); % Eq.(5)

%%% Alpha with \tilde{\alpha}=4
alpha= (4-2)*dP_0/(Z-2) + 2*(Z-4)/(Z-2); %Eq.(14)

%%% Analytical dP_I spectrum, dP_I = AI^2+BI+C (Eq. (6))
A = -1* alpha* (Z - dP_0)/(2-alpha); %Eq. (12)
B = Z - dP_0 - A; %Eq. (8)
C = dP_0; %Eq. (7)

%%% Check if the spetrum exceed the global maximum =2;
I_max= -1*B/(2*A);
dP_I_max= A * I_max^2 + B .* I_max + C;

if dP_I_max > 2 % dP_I_max = 2
    tmpA = Z - dP_0;
    tmpB = 2*(dP_0 - 2);
    tmpC = 2 - dP_0;

    tmpI(1) = (-tmpB + sqrt(tmpB^2- 4*tmpA*tmpC))/2*tmpA;
    tmpI(2) = (-tmpB - sqrt(tmpB^2- 4*tmpA*tmpC))/2*tmpA;

    tmpI_max = tmpI(tmpI>0);

    if length(tmpI_max)>1
        tmpI_max = tmpI(tmpI<1);
        tmpI_max = min(tmpI_max);
    end

    A= (dp_0 - Z)/(2*tmpI_max -1); %Eq. (16)
    B= Z - dP_0 - A;
end

%%% Function f(ell)= beta1*dp_I^2 + beta2*dp_I + beta3 Eq. (19)
ell_given = [64 128 256 512 1024 2048 4096 8192];
beta1_given = [3.12 4.12 5.05 6.11 7.59 10.44 13.72 16.45];
beta2_given = [-9.77 -12.41 -14.86 -17.67 -21.62 -29.34 -38.07 -44.71];
beta3_given = [8.33 10.03 11.59 13.37 15.92 21.03 26.69 30.64];

%%% Linear interpolation to find beta1, beta2 and beta3 Fig.(4b)
beta1= interp1(ell_given, beta1_given, ell);
beta2= interp1(ell_given, beta2_given, ell);
beta3= interp1(ell_given, beta3_given, ell);

```

```

%%% Determine optimum perimeter-based fractal dimension dP_I_opt
%% Equation 1: dP_I = AI^2+BI+C
%% Equation 2: I = beta1*dp_I^2 + beta2*dp_I + beta3
%% Solve for intersect between Equation 1 and Equation 2 Eq.(17)
syms tmpdP_I_opt
tmpdP_I_opt = solve(A*(beta1*tmpdP_I_opt^2+beta2*tmpdP_I_opt+beta3)^2 + ..
.. B*(beta1*tmpdP_I_opt^2+beta2*tmpdP_I_opt+beta3)+C-tmpdP_I_opt);
tmpdP_I_opt= double(tmpdP_I_opt);
%%% Select solution for dP_I_opt
tmpdP_I_opt= tmpdP_I_opt(tmpdP_I_opt==real(tmpdP_I_opt)); %% only get real numbers
tmpdP_I_opt = tmpdP_I_opt(tmpdP_I_opt>=Z); %%% dP has to be greater than Z
tmpdP_I_opt = tmpdP_I_opt(tmpdP_I_opt<=2); %%% dP has to be smaller than 2

%%% if no real solution (i.e., dP_I_opt>dP_I_max), then I_opt = I_max
if isempty(tmpdP_I_opt)==1
    %% Find I_max
    I_max= -1* B/ (2 * A);
    dP_I_opt= A * I_max^2 + B * I_max + C;
else
    %%% Check if I_opt is in the range of 0 and 1
    I_opt= beta1*tmpdP_I_opt.^2+beta2*tmpdP_I_opt+beta3;
    [ss tt] = find(I_opt>=0 & I_opt<=1);

    tmpdP_I_opt = tmpdP_I_opt(tt);

    %%% Get the maximum if there are more than one solution
    dP_I_opt= max(tmpdP_I_opt);
end

%%% 3D Capacity Dimension d0_3D Eq.(2)
k= Z * (Z - 1) + 1;

a = 9 * (Z - ((2* k ^2 - 9 * Z)/(k^2 - 9)));
b = (2* k^2 - 9*Z)/(k^2 - 9);

d0_3D= sqrt(a ./ (dP_I_opt - b));

```

Appendix C

SPM size, capacity dimension, and settling velocity distributions

The cumulative frequency of SPM size L , capacity dimension d_0 and settling velocity v distributions for all experiments described in Chapter 3 are presented in Table C.1, Table C.2, and Table C.3, respectively (in following pages). The data sets presented here were previously published as supplementary material in Tang and Maggi (2016a)¹.

¹Tang F.H.M., and Maggi F. (2016). A mesocosm experiment of suspended particulate matter dynamics in nutrient- and biomass-affected waters, *Water Research*, 89, 76-86.

Table C.1: Cumulative frequency of SPM size L distribution for nutrient- and biomass-free (NFBF), nutrient-affected and biomass-free (NABF), and nutrient- and biomass-affected (NABA) experiments and for different ammonium nitrate concentrate $[\text{NH}_4\text{NO}_3]$, kaolinite concentration C_K and turbulence shear rate G .

Suspension type	$[\text{NH}_4\text{NO}_3]$ (mM)	C_K (g/L)	G (s^{-1})	Aggregate size L (μm)													
				1- 2.5	2.5- 4	4- 6	6- 10	10- 16	16- 25	25- 40	40- 63	63- 100	100- 159	159- 251	251- 398	398- 631	631- 1000
NFBF	0.0	0.1	32	0.0053	0.0069	0.0084	0.0152	0.0472	0.3938	0.8332	0.9779	0.9970	1.0000	1.0000	1.0000	1.0000	1.0000
NFBF	0.0	0.1	48	0.0088	0.0157	0.0238	0.0389	0.0740	0.3526	0.7911	0.9711	0.9994	1.0000	1.0000	1.0000	1.0000	1.0000
NFBF	0.0	0.1	64	0.0012	0.0035	0.0104	0.0290	0.1566	0.5313	0.8933	0.9907	1.0000	1.0000	1.0000	1.0000	1.0000	1.0000
NFBF	0.0	0.1	80	0.0176	0.0396	0.0989	0.2132	0.5407	0.8593	0.9824	0.9912	1.0000	1.0000	1.0000	1.0000	1.0000	1.0000
NFBF	0.0	0.1	96	0.0255	0.0488	0.1380	0.4204	0.6900	0.8620	0.9575	0.9979	1.0000	1.0000	1.0000	1.0000	1.0000	1.0000
NFBF	0.0	0.2	32	0.0070	0.0105	0.0133	0.0211	0.0400	0.2015	0.6397	0.9487	0.9951	1.0000	1.0000	1.0000	1.0000	1.0000
NFBF	0.0	0.2	48	0.0091	0.0140	0.0178	0.0265	0.0433	0.2542	0.7511	0.9610	0.9947	0.9990	1.0000	1.0000	1.0000	1.0000
NFBF	0.0	0.2	64	0.0452	0.0679	0.1222	0.2285	0.3914	0.5860	0.7896	0.9389	0.9819	0.9955	1.0000	1.0000	1.0000	1.0000
NFBF	0.0	0.2	80	0.0222	0.0378	0.0867	0.2289	0.4022	0.5822	0.7578	0.9578	0.9978	1.0000	1.0000	1.0000	1.0000	1.0000
NFBF	0.0	0.2	96	0.0237	0.0364	0.0820	0.2168	0.4262	0.6539	0.8998	0.9945	0.9964	1.0000	1.0000	1.0000	1.0000	1.0000
NFBF	0.0	0.4	32	0.0289	0.0489	0.0690	0.1081	0.1502	0.2932	0.7108	0.9551	0.9973	0.9997	1.0000	1.0000	1.0000	1.0000
NFBF	0.0	0.4	48	0.0330	0.0514	0.0711	0.1133	0.1749	0.2901	0.6248	0.8956	0.9832	0.9978	0.9997	1.0000	1.0000	1.0000
NFBF	0.0	0.4	64	0.0116	0.0155	0.0266	0.0404	0.0869	0.3132	0.7737	0.9685	0.9972	1.0000	1.0000	1.0000	1.0000	1.0000
NFBF	0.0	0.4	80	0.0071	0.0141	0.0212	0.1114	0.4838	0.8773	0.9774	0.9972	1.0000	1.0000	1.0000	1.0000	1.0000	1.0000
NFBF	0.0	0.4	96	0.0127	0.0227	0.0581	0.1431	0.4561	0.8144	0.9518	0.9858	0.9972	1.0000	1.0000	1.0000	1.0000	1.0000
NABF	1.5	0.1	32	0.0035	0.0069	0.0090	0.0193	0.0386	0.2215	0.7012	0.9634	0.9945	1.0000	1.0000	1.0000	1.0000	1.0000
NABF	1.5	0.1	48	0.0126	0.0158	0.0221	0.0339	0.0603	0.2104	0.7191	0.9602	0.9949	0.9996	1.0000	1.0000	1.0000	1.0000
NABF	1.5	0.1	64	0.0060	0.0112	0.0149	0.0224	0.0395	0.1945	0.7422	0.9776	0.9993	1.0000	1.0000	1.0000	1.0000	1.0000
NABF	1.5	0.1	80	0.0339	0.0566	0.1086	0.2489	0.4344	0.6561	0.8665	0.9842	0.9910	1.0000	1.0000	1.0000	1.0000	1.0000
NABF	1.5	0.1	96	0.0301	0.0630	0.1616	0.3589	0.5068	0.6932	0.8932	0.9973	1.0000	1.0000	1.0000	1.0000	1.0000	1.0000
NABF	1.5	0.2	32	0.0016	0.0037	0.0053	0.0112	0.0255	0.1586	0.6184	0.9548	0.9979	1.0000	1.0000	1.0000	1.0000	1.0000
NABF	1.5	0.2	48	0.0065	0.0091	0.0130	0.0221	0.0355	0.1959	0.7243	0.9753	1.0000	1.0000	1.0000	1.0000	1.0000	1.0000
NABF	1.5	0.2	64	0.0040	0.0086	0.0129	0.0244	0.0438	0.1983	0.7816	0.9810	0.9975	1.0000	1.0000	1.0000	1.0000	1.0000
NABF	1.5	0.2	80	0.0013	0.0103	0.0116	0.0450	0.1493	0.4607	0.8353	0.9794	1.0000	1.0000	1.0000	1.0000	1.0000	1.0000
NABF	1.5	0.2	96	0.0178	0.0468	0.0891	0.1938	0.3274	0.5367	0.8040	0.9911	1.0000	1.0000	1.0000	1.0000	1.0000	1.0000
NABF	1.5	0.4	32	0.0187	0.0306	0.0415	0.0643	0.0977	0.1739	0.5635	0.8959	0.9806	0.9966	1.0000	1.0000	1.0000	1.0000
NABF	1.5	0.4	48	0.0399	0.0624	0.0876	0.1468	0.2164	0.3907	0.7212	0.9261	0.9866	0.9973	1.0000	1.0000	1.0000	1.0000
NABF	1.5	0.4	64	0.0294	0.0441	0.0597	0.0874	0.1262	0.2713	0.7852	0.9762	0.9994	1.0000	1.0000	1.0000	1.0000	1.0000
NABF	1.5	0.4	80	0.0199	0.0303	0.0390	0.0555	0.0780	0.1473	0.5442	0.8449	0.9983	1.0000	1.0000	1.0000	1.0000	1.0000
NABF	1.5	0.4	96	0.0153	0.0230	0.0392	0.0813	0.1751	0.4766	0.8488	0.9866	0.9981	0.9990	1.0000	1.0000	1.0000	1.0000

continue from Table C.1

Suspension type	[NH ₄ NO ₃] (mM)	C _K (g/L)	G (s ⁻¹)	Aggregate size L (μm)													
				1- 2.5	2.5- 4	4- 6	6- 10	10- 16	16- 25	25- 40	40- 63	63- 100	100- 159	159- 251	251- 398	398- 631	631- 1000
NABF	3.0	0.1	32	0.0046	0.0085	0.0116	0.0170	0.0417	0.2323	0.7215	0.9730	0.9977	1.0000	1.0000	1.0000	1.0000	1.0000
NABF	3.0	0.1	48	0.0109	0.0158	0.0227	0.0360	0.1141	0.3956	0.8370	0.9807	0.9980	1.0000	1.0000	1.0000	1.0000	1.0000
NABF	3.0	0.1	64	0.0073	0.0084	0.0136	0.0272	0.0942	0.4094	0.8628	0.9906	0.9990	1.0000	1.0000	1.0000	1.0000	1.0000
NABF	3.0	0.1	80	0.0267	0.0401	0.0869	0.1693	0.3096	0.5791	0.9310	0.9911	1.0000	1.0000	1.0000	1.0000	1.0000	1.0000
NABF	3.0	0.1	96	0.0392	0.0784	0.1653	0.3109	0.4846	0.7535	0.9300	0.9972	1.0000	1.0000	1.0000	1.0000	1.0000	1.0000
NABF	3.0	0.2	32	0.0093	0.0151	0.0186	0.0302	0.0581	0.1794	0.6231	0.9448	0.9942	0.9994	1.0000	1.0000	1.0000	1.0000
NABF	3.0	0.2	48	0.0127	0.0176	0.0242	0.0374	0.0655	0.2220	0.7323	0.9648	0.9930	0.9996	1.0000	1.0000	1.0000	1.0000
NABF	3.0	0.2	64	0.0099	0.0156	0.0206	0.0419	0.0667	0.2484	0.7828	0.9901	1.0000	1.0000	1.0000	1.0000	1.0000	1.0000
NABF	3.0	0.2	80	0.0064	0.0177	0.0290	0.0548	0.1594	0.4605	0.7762	0.9903	1.0000	1.0000	1.0000	1.0000	1.0000	1.0000
NABF	3.0	0.2	96	0.0115	0.0172	0.0344	0.0860	0.2409	0.4665	0.7400	0.9675	0.9981	0.9981	1.0000	1.0000	1.0000	1.0000
NABF	3.0	0.4	32	0.0185	0.0265	0.0361	0.0596	0.0929	0.1782	0.5772	0.9300	0.9956	1.0000	1.0000	1.0000	1.0000	1.0000
NABF	3.0	0.4	48	0.0128	0.0225	0.0307	0.0463	0.0752	0.2601	0.7477	0.9693	0.9972	1.0000	1.0000	1.0000	1.0000	1.0000
NABF	3.0	0.4	64	0.0090	0.0183	0.0269	0.0482	0.0789	0.2397	0.7569	0.9757	0.9985	0.9996	1.0000	1.0000	1.0000	1.0000
NABF	3.0	0.4	80	0.0058	0.0097	0.0168	0.0304	0.0505	0.2655	0.7753	0.9812	0.9994	1.0000	1.0000	1.0000	1.0000	1.0000
NABF	3.0	0.4	96	0.0163	0.0327	0.0490	0.0772	0.1144	0.3279	0.7884	0.9818	0.9991	1.0000	1.0000	1.0000	1.0000	1.0000
NABF	6.0	0.1	32	0.0094	0.0168	0.0188	0.0255	0.0349	0.0914	0.5618	0.9772	0.9980	1.0000	1.0000	1.0000	1.0000	1.0000
NABF	6.0	0.1	48	0.0063	0.0103	0.0160	0.0229	0.0366	0.1571	0.6634	0.9771	0.9971	0.9994	1.0000	1.0000	1.0000	1.0000
NABF	6.0	0.1	64	0.0077	0.0116	0.0167	0.0488	0.1322	0.3979	0.7766	0.9769	1.0000	1.0000	1.0000	1.0000	1.0000	1.0000
NABF	6.0	0.1	80	0.0156	0.0253	0.0487	0.1170	0.2846	0.6238	0.9006	0.9922	1.0000	1.0000	1.0000	1.0000	1.0000	1.0000
NABF	6.0	0.1	96	0.0304	0.0491	0.1028	0.2383	0.4322	0.6986	0.8925	0.9836	1.0000	1.0000	1.0000	1.0000	1.0000	1.0000
NABF	6.0	0.2	32	0.0133	0.0217	0.0242	0.0380	0.0656	0.2562	0.7325	0.9694	0.9990	1.0000	1.0000	1.0000	1.0000	1.0000
NABF	6.0	0.2	48	0.0116	0.0156	0.0222	0.0400	0.0614	0.2543	0.7474	0.9671	0.9973	0.9987	1.0000	1.0000	1.0000	1.0000
NABF	6.0	0.2	64	0.0049	0.0067	0.0125	0.0267	0.0513	0.2648	0.8016	0.9844	0.9996	1.0000	1.0000	1.0000	1.0000	1.0000
NABF	6.0	0.2	80	0.0095	0.0217	0.0326	0.0719	0.1642	0.4545	0.8630	0.9946	1.0000	1.0000	1.0000	1.0000	1.0000	1.0000
NABF	6.0	0.2	96	0.0174	0.0244	0.0383	0.1028	0.2666	0.5453	0.8397	0.9948	1.0000	1.0000	1.0000	1.0000	1.0000	1.0000
NABF	6.0	0.4	32	0.0133	0.0267	0.0370	0.0573	0.0953	0.2280	0.6481	0.9319	0.9911	0.9995	1.0000	1.0000	1.0000	1.0000
NABF	6.0	0.4	48	0.0359	0.0524	0.0695	0.1134	0.1760	0.3400	0.6600	0.8858	0.9663	0.9934	0.9992	0.9997	1.0000	1.0000
NABF	6.0	0.4	64	0.0120	0.0214	0.0334	0.0638	0.1140	0.3346	0.7746	0.9550	0.9901	0.9987	1.0000	1.0000	1.0000	1.0000
NABF	6.0	0.4	80	0.0151	0.0238	0.0334	0.0635	0.1048	0.3757	0.8253	0.9905	1.0000	1.0000	1.0000	1.0000	1.0000	1.0000
NABF	6.0	0.4	96	0.0283	0.0442	0.0581	0.0988	0.1514	0.4037	0.8441	0.9886	0.9990	1.0000	1.0000	1.0000	1.0000	1.0000

continue from Table C.1

Suspension type	[NH ₄ NO ₃] (mM)	C _K (g/L)	G (s ⁻¹)	Aggregate size L (μm)													
				1- 2.5	2.5- 4	4- 6	6- 10	10- 16	16- 25	25- 40	40- 63	63- 100	100- 159	159- 251	251- 398	398- 631	631- 1000
NABA	1.5	0.1	32	0.0288	0.0455	0.0703	0.1049	0.1579	0.2548	0.4640	0.7510	0.9043	0.9775	0.9954	0.9988	1.0000	1.0000
NABA	1.5	0.1	48	0.0196	0.0259	0.0295	0.0384	0.0625	0.1812	0.5107	0.8089	0.9411	0.9777	0.9929	0.9982	1.0000	1.0000
NABA	1.5	0.1	64	0.0078	0.0117	0.0155	0.0243	0.0418	0.0836	0.3158	0.7182	0.9106	0.9786	0.9932	0.9981	0.9990	1.0000
NABA	1.5	0.1	80	0.0221	0.0361	0.0643	0.1185	0.1968	0.3373	0.6466	0.9016	0.9759	0.9960	0.9980	0.9980	1.0000	1.0000
NABA	1.5	0.1	96	0.0341	0.0739	0.1847	0.3551	0.5057	0.7301	0.8693	0.9659	0.9915	0.9972	1.0000	1.0000	1.0000	1.0000
NABA	1.5	0.2	32	0.0207	0.0245	0.0326	0.0477	0.0835	0.1808	0.4401	0.7828	0.9259	0.9755	0.9925	0.9981	1.0000	1.0000
NABA	1.5	0.2	48	0.0070	0.0117	0.0179	0.0241	0.0444	0.1604	0.5452	0.8520	0.9478	0.9821	0.9938	0.9984	0.9992	1.0000
NABA	1.5	0.2	64	0.0102	0.0172	0.0256	0.0349	0.0554	0.1150	0.4686	0.8533	0.9627	0.9902	0.9981	0.9995	1.0000	1.0000
NABA	1.5	0.2	80	0.0076	0.0110	0.0177	0.0329	0.0549	0.1554	0.5591	0.9071	0.9764	0.9916	0.9983	1.0000	1.0000	1.0000
NABA	1.5	0.2	96	0.0219	0.0337	0.0506	0.1113	0.2108	0.4216	0.7116	0.9528	0.9865	0.9916	0.9983	1.0000	1.0000	1.0000
NABA	1.5	0.4	32	0.0315	0.0475	0.0639	0.1244	0.1833	0.2882	0.5040	0.8172	0.9406	0.9810	0.9945	0.9980	0.9995	1.0000
NABA	1.5	0.4	48	0.0308	0.0401	0.0557	0.0819	0.1289	0.2602	0.6202	0.8839	0.9582	0.9832	0.9971	1.0000	1.0000	1.0000
NABA	1.5	0.4	64	0.0330	0.0471	0.0638	0.0972	0.1408	0.2261	0.5257	0.8187	0.9349	0.9776	0.9965	1.0000	1.0000	1.0000
NABA	1.5	0.4	80	0.0159	0.0237	0.0297	0.0405	0.0646	0.1438	0.5570	0.8997	0.9789	0.9966	0.9991	1.0000	1.0000	1.0000
NABA	1.5	0.4	96	0.0181	0.0229	0.0295	0.0648	0.1619	0.4581	0.8029	0.9733	0.9933	0.9981	1.0000	1.0000	1.0000	1.0000
NABA	3.0	0.1	32	0.0199	0.0256	0.0319	0.0504	0.0752	0.1256	0.3520	0.7040	0.8928	0.9659	0.9901	0.9979	1.0000	1.0000
NABA	3.0	0.1	48	0.0121	0.0204	0.0295	0.0477	0.0673	0.1415	0.4523	0.7625	0.9153	0.9834	0.9962	1.0000	1.0000	1.0000
NABA	3.0	0.1	64	0.0073	0.0122	0.0170	0.0261	0.0462	0.1197	0.4891	0.8451	0.9496	0.9885	0.9964	1.0000	1.0000	1.0000
NABA	3.0	0.1	80	0.0125	0.0175	0.0225	0.0424	0.0974	0.2185	0.5730	0.8864	0.9563	0.9913	1.0000	1.0000	1.0000	1.0000
NABA	3.0	0.1	96	0.0161	0.0252	0.0596	0.1537	0.3005	0.5252	0.7431	0.9518	0.9885	0.9931	1.0000	1.0000	1.0000	1.0000
NABA	3.0	0.2	32	0.0231	0.0282	0.0342	0.0504	0.0803	0.1863	0.4855	0.7838	0.9162	0.9726	0.9949	0.9983	1.0000	1.0000
NABA	3.0	0.2	48	0.0282	0.0370	0.0442	0.0652	0.1054	0.2671	0.6171	0.8689	0.9590	0.9823	0.9960	0.9992	1.0000	1.0000
NABA	3.0	0.2	64	0.0294	0.0430	0.0566	0.0881	0.1278	0.1963	0.5155	0.8303	0.9608	0.9924	0.9989	1.0000	1.0000	1.0000
NABA	3.0	0.2	80	0.0150	0.0208	0.0273	0.0488	0.0736	0.1823	0.6387	0.9147	0.9759	0.9948	1.0000	1.0000	1.0000	1.0000
NABA	3.0	0.2	96	0.0101	0.0241	0.0342	0.0684	0.1369	0.3435	0.7414	0.9531	0.9924	0.9987	1.0000	1.0000	1.0000	1.0000
NABA	3.0	0.4	32	0.0315	0.0534	0.0702	0.1161	0.1766	0.2784	0.4537	0.7052	0.8705	0.9567	0.9899	0.9996	0.9996	1.0000
NABA	3.0	0.4	48	0.0183	0.0306	0.0390	0.0619	0.0956	0.2087	0.4992	0.7936	0.9205	0.9755	0.9916	0.9969	1.0000	1.0000
NABA	3.0	0.4	64	0.0226	0.0352	0.0422	0.0768	0.1170	0.2039	0.4641	0.8091	0.9453	0.9905	0.9990	0.9995	1.0000	1.0000
NABA	3.0	0.4	80	0.0192	0.0266	0.0371	0.0632	0.0990	0.1984	0.6063	0.9308	0.9876	0.9982	1.0000	1.0000	1.0000	1.0000
NABA	3.0	0.4	96	0.0210	0.0343	0.0436	0.0709	0.1387	0.3164	0.6726	0.9299	0.9860	0.9961	0.9992	0.9992	1.0000	1.0000

continue from Table C.1

Suspension type	[NH ₄ NO ₃] (mM)	C _K (g/L)	G (s ⁻¹)	Aggregate size L (μm)													
				1- 2.5	2.5- 4	4- 6	6- 10	10- 16	16- 25	25- 40	40- 63	63- 100	100- 159	159- 251	251- 398	398- 631	631- 1000
NABA	6.0	0.1	32	0.0176	0.0264	0.0373	0.0505	0.0717	0.1376	0.3624	0.6750	0.8609	0.9444	0.9854	0.9956	1.0000	1.0000
NABA	6.0	0.1	48	0.0221	0.0277	0.0332	0.0526	0.0775	0.1716	0.4557	0.7454	0.8875	0.9594	0.9917	0.9991	0.9991	1.0000
NABA	6.0	0.1	64	0.0138	0.0231	0.0354	0.0538	0.0877	0.1938	0.4708	0.7846	0.9108	0.9677	0.9938	1.0000	1.0000	1.0000
NABA	6.0	0.1	80	0.0224	0.0247	0.0336	0.0516	0.0717	0.2040	0.5135	0.8341	0.9417	0.9888	0.9955	1.0000	1.0000	1.0000
NABA	6.0	0.1	96	0.0314	0.0348	0.0523	0.0941	0.1568	0.3206	0.6899	0.9164	0.9756	0.9965	1.0000	1.0000	1.0000	1.0000
NABA	6.0	0.2	32	0.0225	0.0356	0.0491	0.0818	0.1218	0.1852	0.3970	0.7126	0.9056	0.9755	0.9918	0.9996	1.0000	1.0000
NABA	6.0	0.2	48	0.0229	0.0295	0.0441	0.0665	0.1022	0.1758	0.4636	0.7805	0.9242	0.9863	0.9982	1.0000	1.0000	1.0000
NABA	6.0	0.2	64	0.0120	0.0186	0.0219	0.0383	0.0974	0.2287	0.5974	0.8884	0.9650	0.9945	0.9989	1.0000	1.0000	1.0000
NABA	6.0	0.2	80	0.0137	0.0256	0.0359	0.1111	0.2444	0.4239	0.6923	0.9214	0.9795	0.9932	0.9983	0.9983	1.0000	1.0000
NABA	6.0	0.2	96	0.0049	0.0099	0.0165	0.0659	0.2241	0.5206	0.7974	0.9671	0.9885	0.9951	1.0000	1.0000	1.0000	1.0000
NABA	6.0	0.4	32	0.0262	0.0373	0.0547	0.0849	0.1298	0.1894	0.3339	0.6385	0.8617	0.9578	0.9947	0.9996	1.0000	1.0000
NABA	6.0	0.4	48	0.0232	0.0405	0.0533	0.0841	0.1330	0.2033	0.3895	0.7358	0.9238	0.9872	0.9983	1.0000	1.0000	1.0000
NABA	6.0	0.4	64	0.0096	0.0122	0.0148	0.0331	0.0636	0.1681	0.4913	0.8162	0.9312	0.9791	1.0000	1.0000	1.0000	1.0000
NABA	6.0	0.4	80	0.0159	0.0329	0.0454	0.0782	0.1338	0.3333	0.6961	0.9342	0.9875	0.9989	1.0000	1.0000	1.0000	1.0000
NABA	6.0	0.4	96	0.0157	0.0329	0.0400	0.0627	0.1144	0.4028	0.8362	0.9843	0.9961	0.9992	1.0000	1.0000	1.0000	1.0000

Table C.2: Cumulative frequency of SPM capacity dimension d_0 distribution for nutrient- and biomass-free (NFBF), nutrient-affected and biomass-free (NABF), and nutrient- and biomass-affected (NABA) experiments and for different ammonium nitrate concentration $[\text{NH}_4\text{NO}_3]$, kaolinite concentration C_K and turbulence shear rate G .

Suspension type	$[\text{NH}_4\text{NO}_3]$ (mM)	C_K (g/L)	G (s^{-1})	Aggregate capacity dimension d_0 (-)													
				1.69-1.79	1.79-1.88	1.88-1.98	1.98-2.07	2.07-2.16	2.16-2.26	2.26-2.35	2.35-2.45	2.45-2.54	2.54-2.63	2.63-2.73	2.73-2.82	2.82-2.92	2.92-3
NFBF	0.0	0.1	32	0.0000	0.0000	0.0000	0.0000	0.0023	0.0061	0.0137	0.0206	0.0350	0.0647	0.1478	0.4136	0.9429	1.0000
NFBF	0.0	0.1	48	0.0000	0.0000	0.0000	0.0000	0.0019	0.0082	0.0169	0.0307	0.0558	0.1010	0.1926	0.4686	0.9423	1.0000
NFBF	0.0	0.1	64	0.0000	0.0000	0.0000	0.0012	0.0012	0.0035	0.0081	0.0162	0.0325	0.0650	0.1752	0.4432	0.9339	1.0000
NFBF	0.0	0.1	80	0.0000	0.0000	0.0000	0.0000	0.0022	0.0044	0.0066	0.0088	0.0110	0.0242	0.0791	0.2923	0.7956	1.0000
NFBF	0.0	0.1	96	0.0000	0.0000	0.0000	0.0000	0.0000	0.0021	0.0042	0.0106	0.0149	0.0234	0.0722	0.2569	0.7601	1.0000
NFBF	0.0	0.2	32	0.0000	0.0000	0.0000	0.0000	0.0021	0.0035	0.0126	0.0232	0.0330	0.0625	0.1566	0.4024	0.9389	1.0000
NFBF	0.0	0.2	48	0.0000	0.0000	0.0005	0.0010	0.0039	0.0144	0.0236	0.0467	0.0770	0.1117	0.2070	0.4617	0.9475	1.0000
NFBF	0.0	0.2	64	0.0000	0.0000	0.0000	0.0023	0.0023	0.0045	0.0113	0.0204	0.0271	0.0543	0.1176	0.3462	0.8371	1.0000
NFBF	0.0	0.2	80	0.0000	0.0000	0.0000	0.0022	0.0022	0.0044	0.0133	0.0200	0.0267	0.0822	0.1356	0.3378	0.8667	1.0000
NFBF	0.0	0.2	96	0.0000	0.0000	0.0000	0.0000	0.0036	0.0073	0.0091	0.0182	0.0310	0.0619	0.1348	0.3333	0.8616	1.0000
NFBF	0.0	0.4	32	0.0000	0.0000	0.0003	0.0020	0.0068	0.0190	0.0391	0.0714	0.1047	0.1583	0.2559	0.4903	0.8998	1.0000
NFBF	0.0	0.4	48	0.0000	0.0000	0.0011	0.0041	0.0138	0.0305	0.0611	0.1030	0.1549	0.2214	0.3387	0.5602	0.9127	1.0000
NFBF	0.0	0.4	64	0.0000	0.0000	0.0000	0.0033	0.0094	0.0127	0.0227	0.0426	0.0725	0.1168	0.2081	0.4853	0.9314	1.0000
NFBF	0.0	0.4	80	0.0000	0.0000	0.0000	0.0000	0.0014	0.0028	0.0028	0.0099	0.0197	0.0409	0.0874	0.3371	0.8717	1.0000
NFBF	0.0	0.4	96	0.0000	0.0000	0.0000	0.0028	0.0042	0.0057	0.0085	0.0184	0.0326	0.0581	0.1176	0.3555	0.8669	1.0000
NABF	1.5	0.1	32	0.0000	0.0000	0.0000	0.0000	0.0007	0.0048	0.0076	0.0152	0.0242	0.0462	0.1125	0.3775	0.9441	1.0000
NABF	1.5	0.1	48	0.0000	0.0000	0.0000	0.0028	0.0079	0.0146	0.0260	0.0461	0.0749	0.1182	0.1962	0.4346	0.9354	1.0000
NABF	1.5	0.1	64	0.0000	0.0000	0.0000	0.0007	0.0007	0.0015	0.0052	0.0104	0.0358	0.0641	0.1587	0.4449	0.9560	1.0000
NABF	1.5	0.1	80	0.0000	0.0000	0.0000	0.0000	0.0023	0.0023	0.0068	0.0136	0.0226	0.0430	0.1086	0.3552	0.8507	1.0000
NABF	1.5	0.1	96	0.0000	0.0000	0.0000	0.0000	0.0000	0.0000	0.0000	0.0027	0.0329	0.0767	0.1315	0.3096	0.7945	1.0000
NABF	1.5	0.2	32	0.0000	0.0000	0.0000	0.0000	0.0000	0.0016	0.0085	0.0218	0.0389	0.0660	0.1421	0.4018	0.9590	1.0000
NABF	1.5	0.2	48	0.0000	0.0000	0.0000	0.0000	0.0017	0.0048	0.0134	0.0269	0.0455	0.0728	0.1409	0.4174	0.9463	1.0000
NABF	1.5	0.2	64	0.0000	0.0000	0.0000	0.0011	0.0047	0.0108	0.0201	0.0370	0.0557	0.0941	0.1889	0.4659	0.9576	1.0000
NABF	1.5	0.2	80	0.0000	0.0000	0.0000	0.0000	0.0000	0.0039	0.0116	0.0193	0.0296	0.0605	0.1300	0.3887	0.9395	1.0000
NABF	1.5	0.2	96	0.0000	0.0000	0.0000	0.0000	0.0022	0.0089	0.0089	0.0178	0.0290	0.0445	0.0869	0.3408	0.8597	1.0000
NABF	1.5	0.4	32	0.0000	0.0000	0.0007	0.0037	0.0092	0.0252	0.0470	0.0759	0.1150	0.1705	0.2535	0.4974	0.9337	1.0000
NABF	1.5	0.4	48	0.0000	0.0003	0.0027	0.0070	0.0177	0.0329	0.0613	0.0927	0.1320	0.1880	0.2879	0.5139	0.8937	1.0000
NABF	1.5	0.4	64	0.0000	0.0000	0.0003	0.0021	0.0065	0.0153	0.0332	0.0538	0.0927	0.1406	0.2315	0.4672	0.9070	1.0000
NABF	1.5	0.4	80	0.0000	0.0000	0.0000	0.0009	0.0078	0.0095	0.0225	0.0399	0.0607	0.0789	0.1430	0.3718	0.9376	1.0000
NABF	1.5	0.4	96	0.0000	0.0000	0.0000	0.0000	0.0038	0.0067	0.0172	0.0239	0.0383	0.0737	0.1445	0.4316	0.9110	1.0000

continue from Table C.2

Suspension type	[NH ₄ NO ₃] (mM)	C _K (g/L)	G (s ⁻¹)	Aggregate capacity dimension d ₀ (-)													
				1.69-1.79	1.79-1.88	1.88-1.98	1.98-2.07	2.07-2.16	2.16-2.26	2.26-2.35	2.35-2.45	2.45-2.54	2.54-2.63	2.63-2.73	2.73-2.82	2.82-2.92	2.92-3
NABF	3.0	0.1	32	0.0000	0.0000	0.0000	0.0000	0.0054	0.0085	0.0123	0.0293	0.0478	0.0826	0.1667	0.4684	0.9537	1.0000
NABF	3.0	0.1	48	0.0000	0.0000	0.0030	0.0104	0.0212	0.0410	0.0746	0.1136	0.1595	0.2104	0.2993	0.5531	0.9506	1.0000
NABF	3.0	0.1	64	0.0000	0.0000	0.0000	0.0000	0.0000	0.0052	0.0147	0.0230	0.0492	0.0932	0.1895	0.4942	0.9455	1.0000
NABF	3.0	0.1	80	0.0000	0.0000	0.0000	0.0000	0.0000	0.0000	0.0067	0.0267	0.0535	0.0824	0.1693	0.4633	0.9020	1.0000
NABF	3.0	0.1	96	0.0000	0.0000	0.0000	0.0000	0.0000	0.0056	0.0056	0.0112	0.0196	0.0448	0.1176	0.3725	0.8151	1.0000
NABF	3.0	0.2	32	0.0000	0.0000	0.0000	0.0000	0.0012	0.0058	0.0134	0.0285	0.0465	0.0801	0.1574	0.4419	0.9559	1.0000
NABF	3.0	0.2	48	0.0000	0.0000	0.0000	0.0009	0.0026	0.0105	0.0202	0.0360	0.0607	0.0945	0.1833	0.4576	0.9371	1.0000
NABF	3.0	0.2	64	0.0000	0.0000	0.0000	0.0000	0.0000	0.0021	0.0057	0.0135	0.0312	0.0653	0.1561	0.4457	0.9432	1.0000
NABF	3.0	0.2	80	0.0000	0.0000	0.0000	0.0000	0.0032	0.0064	0.0064	0.0113	0.0258	0.0483	0.1176	0.3849	0.9388	1.0000
NABF	3.0	0.2	96	0.0000	0.0000	0.0000	0.0000	0.0000	0.0000	0.0019	0.0057	0.0172	0.0440	0.0994	0.3652	0.9140	1.0000
NABF	3.0	0.4	32	0.0000	0.0000	0.0000	0.0006	0.0036	0.0102	0.0259	0.0496	0.0863	0.1335	0.2088	0.4526	0.9308	1.0000
NABF	3.0	0.4	48	0.0000	0.0000	0.0000	0.0000	0.0023	0.0073	0.0170	0.0312	0.0518	0.0885	0.1670	0.4335	0.9417	1.0000
NABF	3.0	0.4	64	0.0000	0.0000	0.0000	0.0004	0.0022	0.0097	0.0194	0.0348	0.0580	0.0954	0.1642	0.4331	0.9368	1.0000
NABF	3.0	0.4	80	0.0000	0.0000	0.0000	0.0006	0.0026	0.0071	0.0149	0.0246	0.0440	0.0712	0.1431	0.4378	0.9391	1.0000
NABF	3.0	0.4	96	0.0000	0.0000	0.0000	0.0027	0.0027	0.0082	0.0154	0.0236	0.0427	0.0672	0.1353	0.4033	0.9328	1.0000
NABF	6.0	0.1	32	0.0000	0.0000	0.0000	0.0007	0.0027	0.0040	0.0087	0.0128	0.0282	0.0551	0.1136	0.4812	0.9489	1.0000
NABF	6.0	0.1	48	0.0000	0.0000	0.0006	0.0011	0.0034	0.0074	0.0160	0.0263	0.0434	0.0817	0.1789	0.5251	0.9531	1.0000
NABF	6.0	0.1	64	0.0000	0.0000	0.0000	0.0000	0.0000	0.0000	0.0090	0.0218	0.0359	0.0642	0.1297	0.4134	0.9345	1.0000
NABF	6.0	0.1	80	0.0000	0.0000	0.0000	0.0000	0.0000	0.0039	0.0039	0.0156	0.0331	0.0663	0.1676	0.4795	0.8908	1.0000
NABF	6.0	0.1	96	0.0000	0.0000	0.0000	0.0000	0.0023	0.0047	0.0117	0.0140	0.0234	0.0397	0.1028	0.3762	0.8294	1.0000
NABF	6.0	0.2	32	0.0000	0.0000	0.0000	0.0000	0.0010	0.0039	0.0089	0.0192	0.0341	0.0656	0.1412	0.4195	0.9314	1.0000
NABF	6.0	0.2	48	0.0000	0.0000	0.0000	0.0013	0.0044	0.0133	0.0271	0.0458	0.0698	0.1067	0.1876	0.4793	0.9471	1.0000
NABF	6.0	0.2	64	0.0000	0.0000	0.0000	0.0004	0.0018	0.0062	0.0152	0.0330	0.0548	0.0874	0.1636	0.4681	0.9474	1.0000
NABF	6.0	0.2	80	0.0000	0.0000	0.0000	0.0000	0.0000	0.0054	0.0136	0.0190	0.0312	0.0556	0.1330	0.4220	0.9281	1.0000
NABF	6.0	0.2	96	0.0000	0.0000	0.0000	0.0000	0.0035	0.0087	0.0139	0.0174	0.0209	0.0453	0.1341	0.4111	0.9164	1.0000
NABF	6.0	0.4	32	0.0000	0.0000	0.0000	0.0020	0.0054	0.0109	0.0267	0.0469	0.0775	0.1224	0.2172	0.4758	0.9423	1.0000
NABF	6.0	0.4	48	0.0000	0.0003	0.0017	0.0075	0.0218	0.0469	0.0764	0.1145	0.1567	0.2133	0.3195	0.5657	0.9186	1.0000
NABF	6.0	0.4	64	0.0000	0.0000	0.0000	0.0034	0.0090	0.0167	0.0351	0.0544	0.0793	0.1272	0.2296	0.5009	0.9379	1.0000
NABF	6.0	0.4	80	0.0000	0.0000	0.0000	0.0008	0.0056	0.0135	0.0222	0.0373	0.0667	0.0937	0.1652	0.4297	0.9317	1.0000
NABF	6.0	0.4	96	0.0000	0.0000	0.0005	0.0015	0.0050	0.0109	0.0223	0.0377	0.0645	0.1043	0.1832	0.4568	0.9131	1.0000

continue from Table C.2

Suspension type	[NH ₄ NO ₃] (mM)	C _K (g/L)	G (s ⁻¹)	Aggregate capacity dimension d ₀ (-)													
				1.69-1.79	1.79-1.88	1.88-1.98	1.98-2.07	2.07-2.16	2.16-2.26	2.26-2.35	2.35-2.45	2.45-2.54	2.54-2.63	2.63-2.73	2.73-2.82	2.82-2.92	2.92-3
NABA	1.5	0.1	32	0.0000	0.0000	0.0012	0.0052	0.0173	0.0375	0.0669	0.1049	0.1660	0.2611	0.3954	0.6536	0.9331	1.0000
NABA	1.5	0.1	48	0.0000	0.0009	0.0009	0.0009	0.0063	0.0143	0.0321	0.0562	0.0929	0.1688	0.2991	0.5830	0.9473	1.0000
NABA	1.5	0.1	64	0.0000	0.0000	0.0010	0.0039	0.0058	0.0117	0.0330	0.0564	0.0952	0.1681	0.2867	0.5685	0.9592	1.0000
NABA	1.5	0.1	80	0.0000	0.0000	0.0000	0.0020	0.0060	0.0120	0.0161	0.0281	0.0502	0.0863	0.1687	0.4819	0.9016	1.0000
NABA	1.5	0.1	96	0.0000	0.0000	0.0000	0.0000	0.0000	0.0028	0.0142	0.0227	0.0540	0.1080	0.1676	0.3949	0.8295	1.0000
NABA	1.5	0.2	32	0.0000	0.0000	0.0006	0.0006	0.0069	0.0132	0.0257	0.0508	0.0829	0.1412	0.2511	0.5009	0.9284	1.0000
NABA	1.5	0.2	48	0.0000	0.0000	0.0000	0.0008	0.0023	0.0055	0.0140	0.0249	0.0428	0.0779	0.1604	0.4120	0.9525	1.0000
NABA	1.5	0.2	64	0.0000	0.0000	0.0019	0.0023	0.0047	0.0088	0.0177	0.0331	0.0624	0.1127	0.1998	0.4169	0.9348	1.0000
NABA	1.5	0.2	80	0.0000	0.0000	0.0000	0.0000	0.0008	0.0076	0.0135	0.0253	0.0490	0.0701	0.1461	0.3590	0.9333	1.0000
NABA	1.5	0.2	96	0.0000	0.0000	0.0000	0.0000	0.0000	0.0000	0.0051	0.0084	0.0169	0.0304	0.0860	0.3052	0.8870	1.0000
NABA	1.5	0.4	32	0.0000	0.0000	0.0005	0.0015	0.0055	0.0180	0.0310	0.0500	0.0849	0.1513	0.2722	0.4945	0.9016	1.0000
NABA	1.5	0.4	48	0.0000	0.0000	0.0000	0.0029	0.0075	0.0180	0.0290	0.0557	0.0947	0.1487	0.2520	0.4983	0.9082	1.0000
NABA	1.5	0.4	64	0.0000	0.0000	0.0000	0.0035	0.0084	0.0189	0.0326	0.0598	0.1073	0.1707	0.2970	0.5403	0.9168	1.0000
NABA	1.5	0.4	80	0.0000	0.0000	0.0004	0.0009	0.0013	0.0052	0.0172	0.0349	0.0611	0.1184	0.2096	0.4598	0.9384	1.0000
NABA	1.5	0.4	96	0.0000	0.0000	0.0000	0.0038	0.0067	0.0162	0.0333	0.0590	0.1048	0.1686	0.2952	0.5162	0.9171	1.0000
NABA	3.0	0.1	32	0.0000	0.0000	0.0000	0.0035	0.0071	0.0213	0.0376	0.0738	0.1356	0.2307	0.3676	0.6423	0.9624	1.0000
NABA	3.0	0.1	48	0.0000	0.0000	0.0000	0.0015	0.0061	0.0174	0.0416	0.0741	0.1203	0.2080	0.3570	0.6127	0.9539	1.0000
NABA	3.0	0.1	64	0.0000	0.0000	0.0000	0.0006	0.0030	0.0158	0.0334	0.0583	0.1081	0.1774	0.2977	0.5784	0.9642	1.0000
NABA	3.0	0.1	80	0.0000	0.0000	0.0000	0.0037	0.0100	0.0175	0.0287	0.0474	0.0799	0.1336	0.2385	0.4956	0.9463	1.0000
NABA	3.0	0.1	96	0.0000	0.0000	0.0000	0.0023	0.0069	0.0115	0.0138	0.0229	0.0436	0.0849	0.1628	0.3968	0.8968	1.0000
NABA	3.0	0.2	32	0.0000	0.0009	0.0009	0.0068	0.0145	0.0291	0.0538	0.0838	0.1376	0.2051	0.3470	0.5949	0.9376	1.0000
NABA	3.0	0.2	48	0.0000	0.0000	0.0008	0.0048	0.0097	0.0169	0.0386	0.0636	0.1038	0.1641	0.2856	0.5213	0.9284	1.0000
NABA	3.0	0.2	64	0.0000	0.0000	0.0005	0.0060	0.0125	0.0266	0.0511	0.0886	0.1419	0.2257	0.3437	0.5797	0.9326	1.0000
NABA	3.0	0.2	80	0.0000	0.0000	0.0007	0.0020	0.0085	0.0117	0.0273	0.0514	0.0846	0.1380	0.2474	0.5143	0.9421	1.0000
NABA	3.0	0.2	96	0.0000	0.0013	0.0013	0.0038	0.0051	0.0089	0.0190	0.0317	0.0583	0.1001	0.1787	0.4601	0.9163	1.0000
NABA	3.0	0.4	32	0.0000	0.0000	0.0017	0.0055	0.0156	0.0269	0.0555	0.0984	0.1564	0.2473	0.4054	0.6758	0.9340	1.0000
NABA	3.0	0.4	48	0.0000	0.0000	0.0015	0.0046	0.0084	0.0161	0.0352	0.0688	0.1261	0.2156	0.3417	0.5971	0.9472	1.0000
NABA	3.0	0.4	64	0.0000	0.0000	0.0005	0.0050	0.0105	0.0261	0.0482	0.0809	0.1376	0.2160	0.3591	0.6128	0.9453	1.0000
NABA	3.0	0.4	80	0.0000	0.0000	0.0009	0.0018	0.0064	0.0137	0.0316	0.0527	0.0871	0.1581	0.2658	0.5422	0.9400	1.0000
NABA	3.0	0.4	96	0.0000	0.0000	0.0008	0.0008	0.0039	0.0125	0.0257	0.0436	0.0663	0.1216	0.1949	0.4747	0.9127	1.0000

continue from Table C.2

Suspension type	[NH ₄ NO ₃] (mM)	C _K (g/L)	G (s ⁻¹)	Aggregate capacity dimension d ₀ (-)													
				1.69-1.79	1.79-1.88	1.88-1.98	1.98-2.07	2.07-2.16	2.16-2.26	2.26-2.35	2.35-2.45	2.45-2.54	2.54-2.63	2.63-2.73	2.73-2.82	2.82-2.92	2.92-3
NABA	6.0	0.1	32	0.0000	0.0007	0.0007	0.0022	0.0073	0.0198	0.0410	0.0900	0.1654	0.2694	0.4502	0.7050	0.9583	1.0000
NABA	6.0	0.1	48	0.0000	0.0000	0.0009	0.0028	0.0074	0.0185	0.0434	0.0858	0.1494	0.2306	0.3644	0.6282	0.9419	1.0000
NABA	6.0	0.1	64	0.0000	0.0000	0.0000	0.0000	0.0046	0.0108	0.0262	0.0569	0.1092	0.1692	0.2708	0.5185	0.9431	1.0000
NABA	6.0	0.1	80	0.0000	0.0000	0.0000	0.0000	0.0045	0.0179	0.0269	0.0583	0.0852	0.1480	0.2534	0.5022	0.9417	1.0000
NABA	6.0	0.1	96	0.0000	0.0000	0.0000	0.0000	0.0035	0.0139	0.0174	0.0314	0.0627	0.1220	0.1882	0.4564	0.9199	1.0000
NABA	6.0	0.2	32	0.0000	0.0000	0.0000	0.0033	0.0090	0.0192	0.0413	0.0859	0.1398	0.2249	0.3700	0.5998	0.9325	1.0000
NABA	6.0	0.2	48	0.0000	0.0000	0.0004	0.0026	0.0088	0.0225	0.0463	0.0855	0.1388	0.2168	0.3336	0.5734	0.9374	1.0000
NABA	6.0	0.2	64	0.0000	0.0000	0.0000	0.0000	0.0044	0.0153	0.0263	0.0405	0.0667	0.1138	0.1947	0.4519	0.9256	1.0000
NABA	6.0	0.2	80	0.0000	0.0000	0.0000	0.0017	0.0068	0.0120	0.0154	0.0274	0.0444	0.0786	0.1658	0.4154	0.8855	1.0000
NABA	6.0	0.2	96	0.0000	0.0000	0.0000	0.0000	0.0033	0.0066	0.0115	0.0148	0.0280	0.0527	0.1219	0.3575	0.8946	1.0000
NABA	6.0	0.4	32	0.0000	0.0004	0.0013	0.0040	0.0102	0.0285	0.0622	0.1098	0.1765	0.2823	0.4304	0.6901	0.9373	1.0000
NABA	6.0	0.4	48	0.0000	0.0003	0.0010	0.0035	0.0104	0.0287	0.0596	0.1015	0.1617	0.2403	0.3854	0.6382	0.9321	1.0000
NABA	6.0	0.4	64	0.0000	0.0000	0.0000	0.0026	0.0052	0.0131	0.0348	0.0575	0.0923	0.1585	0.2657	0.5357	0.9512	1.0000
NABA	6.0	0.4	80	0.0000	0.0011	0.0011	0.0045	0.0079	0.0102	0.0193	0.0306	0.0612	0.1043	0.2018	0.4592	0.9331	1.0000
NABA	6.0	0.4	96	0.0000	0.0000	0.0008	0.0008	0.0024	0.0102	0.0227	0.0400	0.0650	0.0956	0.1685	0.4373	0.9169	1.0000

Table C.3: Cumulative frequency of SPM settling velocity v distribution for nutrient- and biomass-free (NFBF), nutrient-affected and biomass-free (NABF), and nutrient- and biomass-affected (NABA) experiments and for different ammonium nitrate concentration $[\text{NH}_4\text{NO}_3]$, kaolinite concentration C_K and turbulence shear rate G .

Suspension type	$[\text{NH}_4\text{NO}_3]$ (mM)	C_K (g/L)	G (s^{-1})	Aggregate settling velocity v (mm/s)													
				0.04-0.07	0.07-0.09	0.09-0.12	0.12-0.15	0.15-0.20	0.20-0.27	0.27-0.35	0.35-0.47	0.47-0.62	0.62-0.81	0.81-1.07	1.07-1.41	1.41-1.86	1.86-2.45
NFBF	0.0	0.1	32	0.0000	0.1366	0.1366	0.2960	0.2960	0.4221	0.5324	0.6865	0.7828	0.8459	0.9387	0.9737	0.9895	1.0000
NFBF	0.0	0.1	48	0.0000	0.1860	0.1860	0.3385	0.3385	0.4522	0.5995	0.7158	0.7984	0.8708	0.9380	0.9690	0.9897	1.0000
NFBF	0.0	0.1	64	0.0000	0.1856	0.1856	0.3608	0.3608	0.5361	0.5773	0.6907	0.7216	0.8041	0.9381	0.9794	0.9897	1.0000
NFBF	0.0	0.1	80	0.0000	0.1429	0.1429	0.2381	0.2381	0.3333	0.4286	0.6667	0.7619	0.8095	0.8571	0.9048	0.9524	1.0000
NFBF	0.0	0.1	96	0.0000	0.1333	0.1333	0.3333	0.3333	0.6000	0.7333	0.9333	0.9333	0.9333	0.9333	0.9333	1.0000	1.0000
NFBF	0.0	0.2	32	0.0000	0.0188	0.0188	0.0424	0.0424	0.0836	0.1272	0.2285	0.3039	0.4052	0.5642	0.7998	0.9399	1.0000
NFBF	0.0	0.2	48	0.0000	0.0284	0.0284	0.0885	0.0885	0.1503	0.2145	0.3558	0.4825	0.6401	0.8107	0.9245	0.9878	1.0000
NFBF	0.0	0.2	64	0.0000	0.0353	0.0353	0.1647	0.1647	0.2235	0.4000	0.6000	0.6824	0.8118	0.8706	0.9294	0.9882	1.0000
NFBF	0.0	0.2	80	0.0000	0.0446	0.0446	0.1250	0.1250	0.2946	0.3482	0.5089	0.5982	0.7054	0.8304	0.8839	0.9554	1.0000
NFBF	0.0	0.2	96	0.0000	0.0833	0.0833	0.1042	0.1042	0.2396	0.3542	0.4896	0.5625	0.7292	0.8646	0.9583	0.9792	1.0000
NFBF	0.0	0.4	32	0.0000	0.0156	0.0156	0.0395	0.0395	0.0708	0.1035	0.1946	0.2627	0.3460	0.5520	0.7711	0.9417	1.0000
NFBF	0.0	0.4	48	0.0000	0.0264	0.0264	0.0518	0.0518	0.0821	0.1181	0.1915	0.2723	0.3874	0.6412	0.8235	0.9723	1.0000
NFBF	0.0	0.4	64	0.0000	0.1103	0.1103	0.2580	0.2580	0.3826	0.4698	0.6103	0.6868	0.7616	0.9146	0.9751	0.9982	1.0000
NFBF	0.0	0.4	80	0.0000	0.1143	0.1143	0.2000	0.2000	0.2286	0.4000	0.6286	0.7714	0.7714	0.9714	0.9714	1.0000	1.0000
NFBF	0.0	0.4	96	0.0000	0.0471	0.0471	0.1882	0.1882	0.2706	0.3529	0.5882	0.7294	0.8941	0.9647	0.9882	1.0000	1.0000
NABF	1.5	0.1	32	0.0000	0.0383	0.0383	0.1014	0.1014	0.1577	0.2241	0.3502	0.4673	0.5676	0.7748	0.8806	0.9775	1.0000
NABF	1.5	0.1	48	0.0000	0.0299	0.0299	0.0680	0.0680	0.1048	0.1510	0.2570	0.3575	0.4878	0.6694	0.8210	0.9513	1.0000
NABF	1.5	0.1	64	0.0000	0.1179	0.1179	0.2336	0.2336	0.3472	0.4563	0.5895	0.7031	0.7773	0.8865	0.9454	0.9847	1.0000
NABF	1.5	0.1	80	0.0000	0.0448	0.0448	0.0746	0.0746	0.1493	0.2836	0.4627	0.6269	0.8060	0.9104	0.9851	0.9851	1.0000
NABF	1.5	0.1	96	0.0000	0.1061	0.1061	0.2727	0.2727	0.3333	0.4394	0.5909	0.7424	0.8333	0.9091	0.9697	0.9848	1.0000
NABF	1.5	0.2	32	0.0000	0.0037	0.0037	0.0217	0.0232	0.0532	0.0945	0.1844	0.2826	0.4063	0.6259	0.8283	0.9520	1.0000
NABF	1.5	0.2	48	0.0000	0.0322	0.0322	0.0785	0.0808	0.1399	0.2610	0.3530	0.5168	0.6829	0.8474	0.9476	0.9873	1.0000
NABF	1.5	0.2	64	0.0000	0.0503	0.0503	0.1258	0.1258	0.2123	0.3278	0.4921	0.6085	0.7618	0.8695	0.9489	0.9882	1.0000
NABF	1.5	0.2	80	0.0000	0.1371	0.1371	0.2686	0.2743	0.3829	0.5200	0.5943	0.6971	0.8114	0.9200	0.9714	0.9829	1.0000
NABF	1.5	0.2	96	0.0000	0.0357	0.0357	0.1357	0.1357	0.2500	0.3286	0.5143	0.6000	0.7071	0.8857	0.9429	1.0000	1.0000
NABF	1.5	0.4	32	0.0000	0.0040	0.0040	0.0062	0.0068	0.0159	0.0266	0.0482	0.0743	0.1332	0.2778	0.5357	0.8129	1.0000
NABF	1.5	0.4	48	0.0000	0.0036	0.0036	0.0093	0.0093	0.0145	0.0351	0.0924	0.1638	0.2522	0.4633	0.6885	0.8939	1.0000
NABF	1.5	0.4	64	0.0000	0.0055	0.0055	0.0111	0.0111	0.0221	0.0311	0.0736	0.1306	0.2332	0.5021	0.7494	0.9379	1.0000
NABF	1.5	0.4	80	0.0000	0.0642	0.0642	0.0994	0.0994	0.1491	0.1925	0.3230	0.4265	0.5549	0.7557	0.8841	0.9834	1.0000
NABF	1.5	0.4	96	0.0000	0.0366	0.0366	0.0595	0.0595	0.1167	0.1899	0.2952	0.4142	0.5606	0.8238	0.9268	0.9886	1.0000

continue from Table C.3

Suspension type	[NH ₄ NO ₃] (mM)	C _K (g/L)	G (s ⁻¹)	Aggregate settling velocity <i>v</i> (mm/s)													
				0.04-0.07	0.07-0.09	0.09-0.12	0.12-0.15	0.15-0.20	0.20-0.27	0.27-0.35	0.35-0.47	0.47-0.62	0.62-0.81	0.81-1.07	1.07-1.41	1.41-1.86	1.86-2.45
NABF	3.0	0.1	32	0.0000	0.0142	0.0142	0.0460	0.0460	0.0821	0.1389	0.2352	0.3490	0.4694	0.7068	0.8731	0.9573	1.0000
NABF	3.0	0.1	48	0.0000	0.0482	0.0482	0.1094	0.1094	0.1774	0.2627	0.4384	0.5650	0.7011	0.8562	0.9432	0.9897	1.0000
NABF	3.0	0.1	64	0.0000	0.1031	0.1031	0.2268	0.2268	0.3789	0.5206	0.6830	0.7861	0.8660	0.9304	0.9716	0.9948	1.0000
NABF	3.0	0.1	80	0.0000	0.2018	0.2018	0.2936	0.2936	0.4220	0.4771	0.6514	0.7523	0.8257	0.8991	0.9541	0.9817	1.0000
NABF	3.0	0.1	96	0.0000	0.0676	0.0676	0.1351	0.1351	0.2297	0.2973	0.5270	0.6081	0.6892	0.8649	0.9189	0.9595	1.0000
NABF	3.0	0.2	32	0.0000	0.0067	0.0067	0.0227	0.0227	0.0463	0.0842	0.1633	0.2643	0.3813	0.5884	0.7753	0.9209	1.0000
NABF	3.0	0.2	48	0.0000	0.0216	0.0216	0.0459	0.0459	0.0912	0.1420	0.2610	0.3772	0.5338	0.7383	0.8789	0.9624	1.0000
NABF	3.0	0.2	64	0.0000	0.1417	0.1417	0.3243	0.3243	0.4427	0.5223	0.6777	0.7748	0.8408	0.9320	0.9786	0.9922	1.0000
NABF	3.0	0.2	80	0.0000	0.0699	0.0699	0.2238	0.2238	0.3497	0.4615	0.6084	0.7063	0.8042	0.9021	0.9720	0.9930	1.0000
NABF	3.0	0.2	96	0.0000	0.0385	0.0385	0.1282	0.1282	0.2308	0.3397	0.5513	0.6410	0.7244	0.8590	0.9615	0.9936	1.0000
NABF	3.0	0.4	32	0.0000	0.0008	0.0008	0.0045	0.0045	0.0094	0.0119	0.0189	0.0352	0.0590	0.1766	0.4246	0.7832	1.0000
NABF	3.0	0.4	48	0.0000	0.0048	0.0048	0.0126	0.0126	0.0235	0.0355	0.0752	0.1191	0.2136	0.3971	0.6420	0.8821	1.0000
NABF	3.0	0.4	64	0.0000	0.0098	0.0098	0.0224	0.0224	0.0420	0.0644	0.1211	0.2035	0.3290	0.5952	0.7965	0.9471	1.0000
NABF	3.0	0.4	80	0.0000	0.0490	0.0490	0.1135	0.1135	0.1840	0.2688	0.4146	0.5221	0.6667	0.8483	0.9391	0.9785	1.0000
NABF	3.0	0.4	96	0.0000	0.0252	0.0252	0.0419	0.0419	0.0805	0.1174	0.2164	0.3188	0.4547	0.7265	0.8977	0.9799	1.0000
NABF	6.0	0.1	32	0.0000	0.0407	0.0407	0.0682	0.0694	0.1256	0.1722	0.3050	0.4151	0.5371	0.7464	0.8923	0.9713	1.0000
NABF	6.0	0.1	48	0.0000	0.0450	0.0450	0.1140	0.1140	0.1850	0.2680	0.4260	0.5590	0.6610	0.8430	0.9340	0.9890	1.0000
NABF	6.0	0.1	64	0.0000	0.1447	0.1447	0.3064	0.3064	0.4596	0.5957	0.6894	0.7830	0.8213	0.9106	0.9617	0.9915	1.0000
NABF	6.0	0.1	80	0.0000	0.1875	0.1875	0.2750	0.2750	0.4125	0.5250	0.7000	0.7875	0.8375	0.9250	0.9875	1.0000	1.0000
NABF	6.0	0.1	96	0.0000	0.0678	0.0678	0.1186	0.1186	0.2034	0.3729	0.5085	0.5932	0.6949	0.7966	0.9153	1.0000	1.0000
NABF	6.0	0.2	32	0.0000	0.0134	0.0134	0.0212	0.0212	0.0382	0.0679	0.1316	0.2229	0.3510	0.6362	0.8011	0.9498	1.0000
NABF	6.0	0.2	48	0.0000	0.0148	0.0148	0.0321	0.0321	0.0539	0.0917	0.1738	0.2777	0.4419	0.6947	0.8666	0.9583	1.0000
NABF	6.0	0.2	64	0.0000	0.0532	0.0532	0.1269	0.1269	0.2118	0.3122	0.4923	0.6286	0.7581	0.8937	0.9614	0.9914	1.0000
NABF	6.0	0.2	80	0.0000	0.1208	0.1208	0.2167	0.2167	0.3125	0.3917	0.6000	0.6958	0.7833	0.9083	0.9667	0.9875	1.0000
NABF	6.0	0.2	96	0.0000	0.0663	0.0663	0.1271	0.1271	0.2376	0.3978	0.5580	0.6851	0.7901	0.9006	0.9503	0.9890	1.0000
NABF	6.0	0.4	32	0.0000	0.0037	0.0037	0.0045	0.0045	0.0082	0.0163	0.0394	0.0684	0.1226	0.3262	0.5379	0.8410	1.0000
NABF	6.0	0.4	48	0.0000	0.0024	0.0024	0.0095	0.0095	0.0158	0.0215	0.0453	0.0869	0.1675	0.3737	0.6014	0.8835	1.0000
NABF	6.0	0.4	64	0.0000	0.0096	0.0096	0.0289	0.0289	0.0536	0.0873	0.1740	0.2593	0.4168	0.6293	0.7875	0.9512	1.0000
NABF	6.0	0.4	80	0.0000	0.0264	0.0264	0.0826	0.0826	0.1441	0.2144	0.3445	0.4446	0.5800	0.7996	0.9192	0.9807	1.0000
NABF	6.0	0.4	96	0.0000	0.0089	0.0089	0.0163	0.0163	0.0245	0.0275	0.0549	0.1084	0.1997	0.4603	0.7082	0.9406	1.0000

continue from Table C.3

Suspension type	[NH ₄ NO ₃] (mM)	C _K (g/L)	G (s ⁻¹)	Aggregate settling velocity <i>v</i> (mm/s)													
				0.04-0.07	0.07-0.09	0.09-0.12	0.12-0.15	0.15-0.20	0.20-0.27	0.27-0.35	0.35-0.47	0.47-0.62	0.62-0.81	0.81-1.07	1.07-1.41	1.41-1.86	1.86-2.45
NABA	1.5	0.1	32	0.0000	0.0178	0.0178	0.0492	0.0492	0.0868	0.1318	0.2333	0.3473	0.4655	0.6684	0.8410	0.9456	1.0000
NABA	1.5	0.1	48	0.0000	0.0585	0.0585	0.1146	0.1146	0.1732	0.2634	0.3927	0.4683	0.5829	0.6878	0.8366	0.9488	1.0000
NABA	1.5	0.1	64	0.0000	0.0656	0.0656	0.1803	0.1831	0.2377	0.3197	0.4344	0.5164	0.6120	0.7596	0.8743	0.9508	1.0000
NABA	1.5	0.1	80	0.0000	0.0957	0.0957	0.1739	0.1739	0.2435	0.3304	0.4696	0.6087	0.7043	0.7913	0.8696	0.9826	1.0000
NABA	1.5	0.1	96	0.0000	0.0000	0.0000	0.0465	0.0465	0.1628	0.2558	0.5116	0.5814	0.7907	0.8605	0.9302	0.9767	1.0000
NABA	1.5	0.2	32	0.0000	0.0119	0.0119	0.0202	0.0202	0.0451	0.0641	0.1176	0.1983	0.3064	0.5689	0.7684	0.9169	1.0000
NABA	1.5	0.2	48	0.0000	0.0167	0.0167	0.0417	0.0417	0.0633	0.0900	0.1717	0.2817	0.4283	0.6233	0.7800	0.9100	1.0000
NABA	1.5	0.2	64	0.0000	0.0309	0.0309	0.0635	0.0670	0.1047	0.1554	0.2506	0.3451	0.4798	0.6755	0.8781	0.9674	1.0000
NABA	1.5	0.2	80	0.0000	0.0645	0.0645	0.1532	0.1552	0.2298	0.2944	0.4274	0.5484	0.6673	0.8367	0.9395	0.9879	1.0000
NABA	1.5	0.2	96	0.0000	0.0723	0.0723	0.1205	0.1205	0.2410	0.3012	0.4639	0.6145	0.7169	0.8434	0.9337	0.9880	1.0000
NABA	1.5	0.4	32	0.0000	0.0152	0.0152	0.0248	0.0248	0.0352	0.0381	0.0562	0.0800	0.1324	0.2943	0.5067	0.7981	1.0000
NABA	1.5	0.4	48	0.0000	0.0146	0.0146	0.0271	0.0271	0.0448	0.0542	0.0772	0.0949	0.1522	0.3525	0.6048	0.8665	1.0000
NABA	1.5	0.4	64	0.0000	0.0053	0.0053	0.0084	0.0084	0.0138	0.0229	0.0405	0.0665	0.1429	0.3621	0.5859	0.8739	1.0000
NABA	1.5	0.4	80	0.0000	0.0323	0.0323	0.0581	0.0581	0.1009	0.1493	0.2575	0.3559	0.5109	0.7425	0.8991	0.9758	1.0000
NABA	1.5	0.4	96	0.0000	0.0806	0.0806	0.1373	0.1373	0.1881	0.2388	0.3582	0.4955	0.6687	0.8388	0.9522	0.9910	1.0000
NABA	3.0	0.1	32	0.0000	0.0024	0.0024	0.0109	0.0109	0.0169	0.0459	0.1197	0.2056	0.3458	0.5732	0.7328	0.8815	1.0000
NABA	3.0	0.1	48	0.0000	0.0211	0.0211	0.0475	0.0475	0.0778	0.1161	0.2018	0.2902	0.4274	0.6385	0.8351	0.9617	1.0000
NABA	3.0	0.1	64	0.0000	0.0633	0.0633	0.1444	0.1444	0.2242	0.3329	0.4580	0.5736	0.7194	0.8569	0.9216	0.9807	1.0000
NABA	3.0	0.1	80	0.0000	0.1007	0.1007	0.2014	0.2014	0.3333	0.4375	0.5903	0.6910	0.8194	0.8993	0.9549	0.9965	1.0000
NABA	3.0	0.1	96	0.0000	0.0351	0.0351	0.1053	0.1053	0.1316	0.1842	0.3684	0.4912	0.6491	0.8246	0.9211	0.9912	1.0000
NABA	3.0	0.2	32	0.0000	0.0101	0.0101	0.0336	0.0336	0.0487	0.0789	0.1393	0.2097	0.3574	0.5772	0.7768	0.9379	1.0000
NABA	3.0	0.2	48	0.0000	0.0176	0.0176	0.0380	0.0380	0.0583	0.0828	0.1560	0.2456	0.4084	0.6214	0.7951	0.9362	1.0000
NABA	3.0	0.2	64	0.0018	0.0136	0.0136	0.0236	0.0245	0.0371	0.0634	0.0987	0.1540	0.3197	0.5643	0.7835	0.9493	1.0000
NABA	3.0	0.2	80	0.0089	0.0355	0.0355	0.0811	0.1039	0.1686	0.2624	0.3283	0.4525	0.6375	0.8048	0.9227	0.9835	1.0000
NABA	3.0	0.2	96	0.0000	0.0433	0.0433	0.1022	0.1300	0.1858	0.2632	0.4149	0.5325	0.7214	0.8576	0.9381	0.9783	1.0000
NABA	3.0	0.4	32	0.0000	0.0024	0.0024	0.0047	0.0047	0.0102	0.0339	0.0820	0.1458	0.2301	0.4342	0.6186	0.8629	1.0000
NABA	3.0	0.4	48	0.0000	0.0050	0.0050	0.0062	0.0062	0.0112	0.0211	0.0533	0.0954	0.1747	0.3903	0.6183	0.8612	1.0000
NABA	3.0	0.4	64	0.0000	0.0017	0.0017	0.0043	0.0043	0.0096	0.0130	0.0321	0.0539	0.1364	0.2919	0.5395	0.8471	1.0000
NABA	3.0	0.4	80	0.0000	0.0182	0.0182	0.0357	0.0357	0.0658	0.1094	0.1735	0.2591	0.4271	0.6212	0.8312	0.9715	1.0000
NABA	3.0	0.4	96	0.0000	0.0172	0.0172	0.0408	0.0408	0.0690	0.1003	0.2006	0.2853	0.4734	0.6834	0.8715	0.9781	1.0000

continue from Table C.3

Suspension type	[NH ₄ NO ₃] (mM)	C _K (g/L)	G (s ⁻¹)	Aggregate settling velocity <i>v</i> (mm/s)													
				0.04-0.07	0.07-0.09	0.09-0.12	0.12-0.15	0.15-0.20	0.20-0.27	0.27-0.35	0.35-0.47	0.47-0.62	0.62-0.81	0.81-1.07	1.07-1.41	1.41-1.86	1.86-2.45
NABA	6.0	0.1	32	0.0000	0.0184	0.0184	0.0356	0.0395	0.0804	0.1397	0.2345	0.3228	0.4361	0.6113	0.7918	0.9341	1.0000
NABA	6.0	0.1	48	0.0000	0.0337	0.0337	0.0657	0.0673	0.1218	0.1763	0.2628	0.3462	0.4503	0.6619	0.8381	0.9519	1.0000
NABA	6.0	0.1	64	0.0000	0.0425	0.0425	0.0652	0.0652	0.1020	0.1785	0.3116	0.4363	0.5581	0.6742	0.8159	0.9405	1.0000
NABA	6.0	0.1	80	0.0000	0.0824	0.0824	0.1412	0.1412	0.2078	0.2824	0.4314	0.5451	0.6667	0.8392	0.9373	0.9765	1.0000
NABA	6.0	0.1	96	0.0000	0.0704	0.0704	0.1549	0.1690	0.3169	0.4225	0.6197	0.7606	0.8380	0.9225	0.9577	1.0000	1.0000
NABA	6.0	0.2	32	0.0000	0.0031	0.0031	0.0062	0.0062	0.0125	0.0226	0.0545	0.0981	0.1626	0.3502	0.5774	0.8241	1.0000
NABA	6.0	0.2	48	0.0000	0.0082	0.0082	0.0204	0.0204	0.0310	0.0539	0.1061	0.1731	0.2849	0.5184	0.7216	0.8955	1.0000
NABA	6.0	0.2	64	0.0000	0.0622	0.0622	0.1244	0.1244	0.1813	0.2513	0.3834	0.4715	0.5725	0.7202	0.8264	0.9404	1.0000
NABA	6.0	0.2	80	0.0000	0.0449	0.0449	0.1282	0.1282	0.1987	0.3526	0.5449	0.6282	0.6987	0.8013	0.8910	0.9744	1.0000
NABA	6.0	0.2	96	0.0000	0.0959	0.0959	0.2055	0.2055	0.2945	0.3630	0.5548	0.6712	0.7466	0.8836	0.9178	0.9795	1.0000
NABA	6.0	0.4	32	0.0000	0.0009	0.0009	0.0035	0.0035	0.0044	0.0070	0.0194	0.0379	0.0960	0.2201	0.4613	0.7685	1.0000
NABA	6.0	0.4	48	0.0000	0.0084	0.0084	0.0168	0.0168	0.0196	0.0204	0.0323	0.0477	0.0961	0.1839	0.4225	0.7607	1.0000
NABA	6.0	0.4	64	0.0000	0.0279	0.0279	0.0479	0.0479	0.0659	0.0938	0.1876	0.2794	0.3912	0.5429	0.7206	0.8703	1.0000
NABA	6.0	0.4	80	0.0000	0.0250	0.0250	0.0455	0.0455	0.0659	0.0977	0.1659	0.2182	0.3045	0.4659	0.6523	0.8659	1.0000
NABA	6.0	0.4	96	0.0000	0.0286	0.0286	0.0571	0.0571	0.0872	0.1278	0.1940	0.2707	0.3624	0.5564	0.7759	0.9549	1.0000

Appendix D

Derivations of microbial metabolic reactions

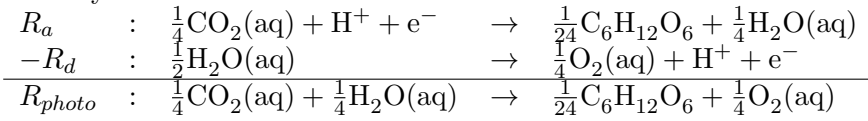
The derivations of microbial metabolic reactions R1 to R7 based on Eq. (7.1) and half-reactions reported in Rittmann and McCarty (2001) are presented below. Recall that the overall metabolic reaction R_M is written as Rittmann and McCarty (2001)

$$R_M = (1 - e)R_C + eR_A,$$

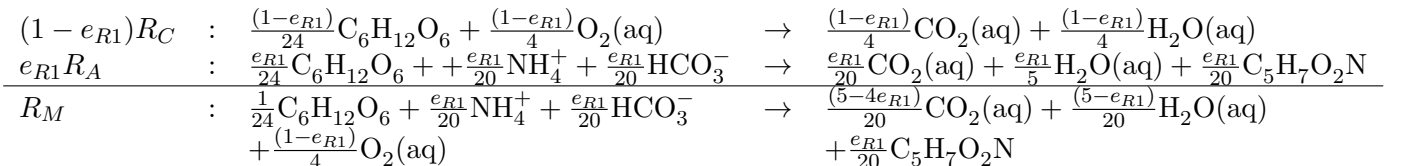
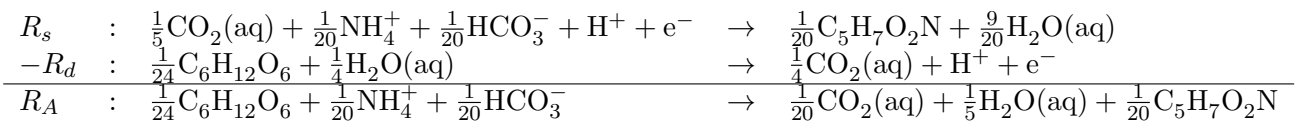
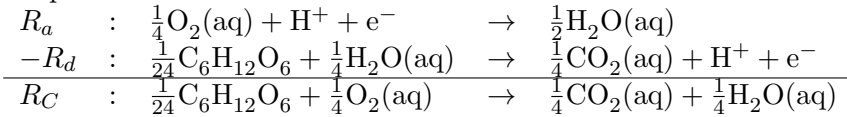
where e is the fraction of electrons used for cell synthesis, $R_C = R_a - R_d$ and $R_A = R_s - R_d$ are the catabolic and anabolic reactions, respectively, with R_a the electron acceptor half-reaction, R_d the electron donor half-reaction, and R_s the cell synthesis half-reaction. Note that phototrophic uptake of NH_4^+ and NO_3^- involves two processes: (i) the photosynthesis that transforms CO_2 into glucose (or other building blocks) with H_2O as electron donor and CO_2 as electron acceptor; and (ii) the respiration process that uses O_2 as electron acceptor and glucose as electron donor to synthesis energy and biomass.

R1: Phototrophic uptake of NH_4^+

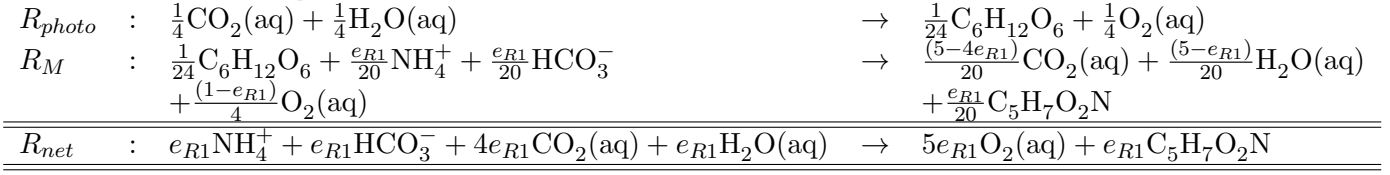
Photosynthesis:



Respiration:

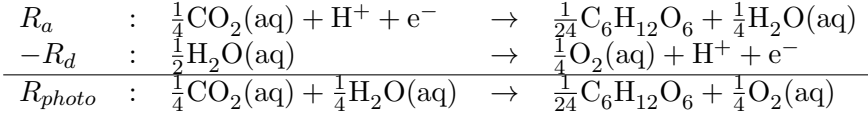


Net reaction ($R_{net} = R_{photo} + R_M$):

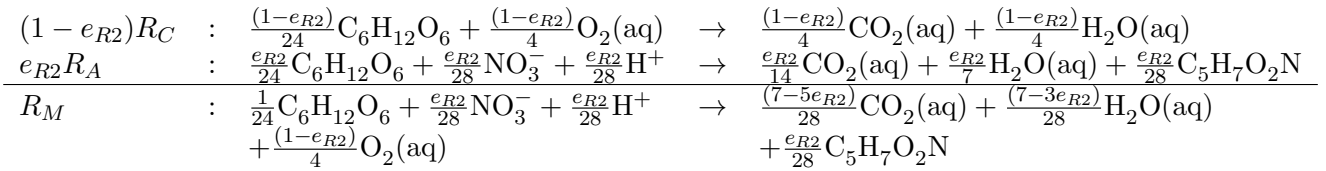
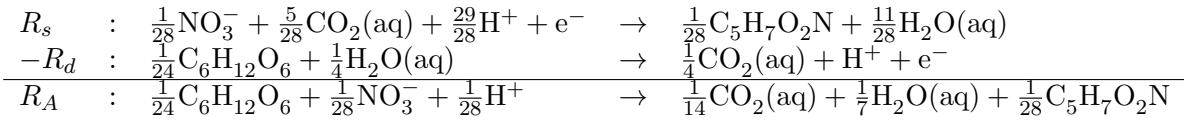
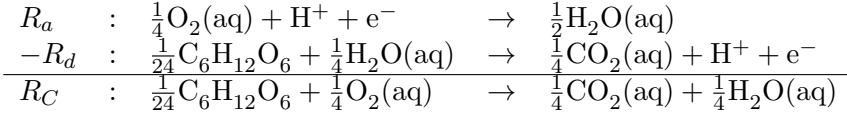


R2: Phototrophic uptake of NO_3^-

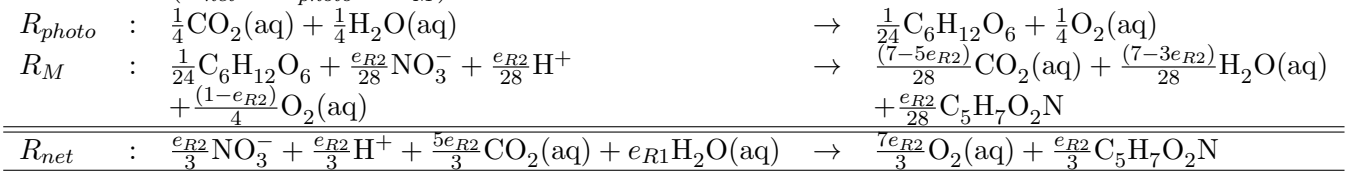
Photosynthesis:



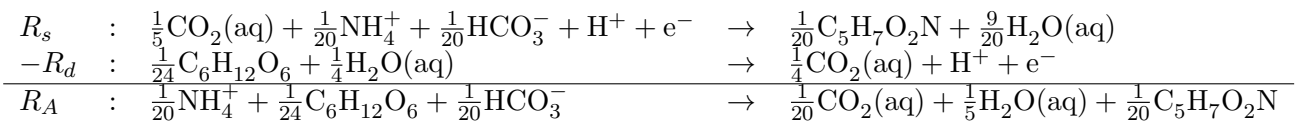
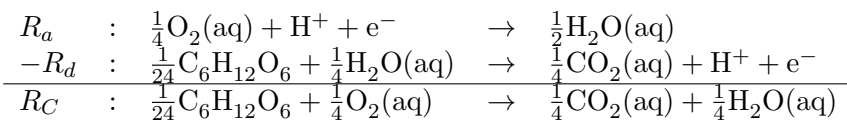
Respiration:

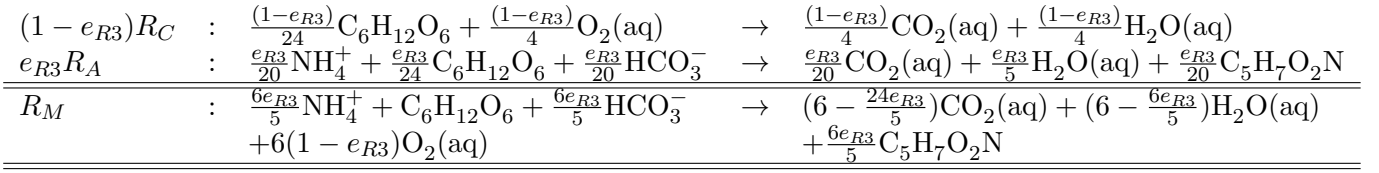


Net reaction ($R_{net} = R_{photo} + R_M$):

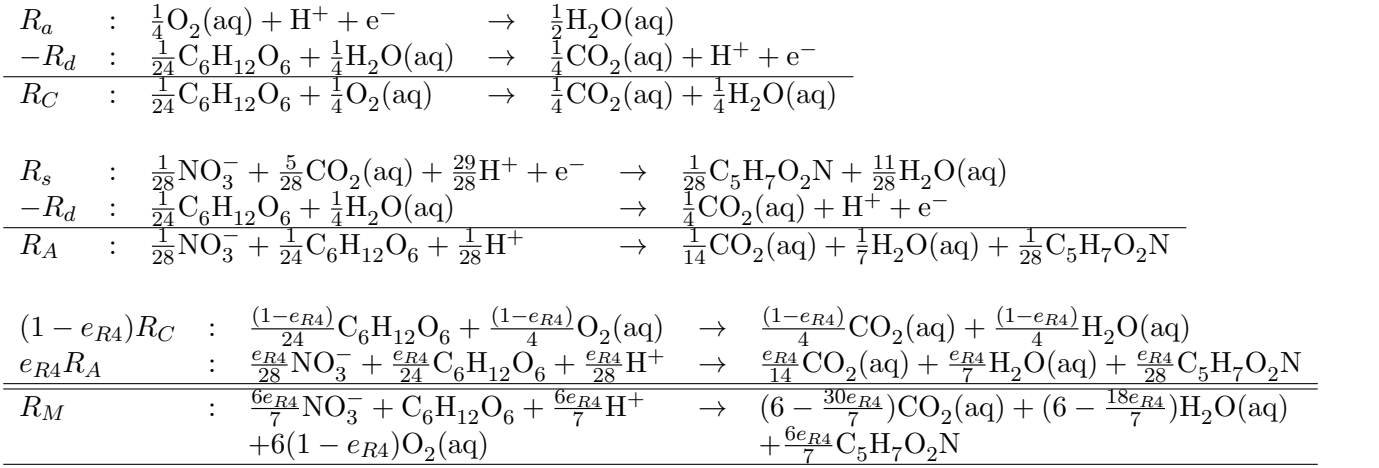


R3: Heterotrophic uptake of NH_4^+

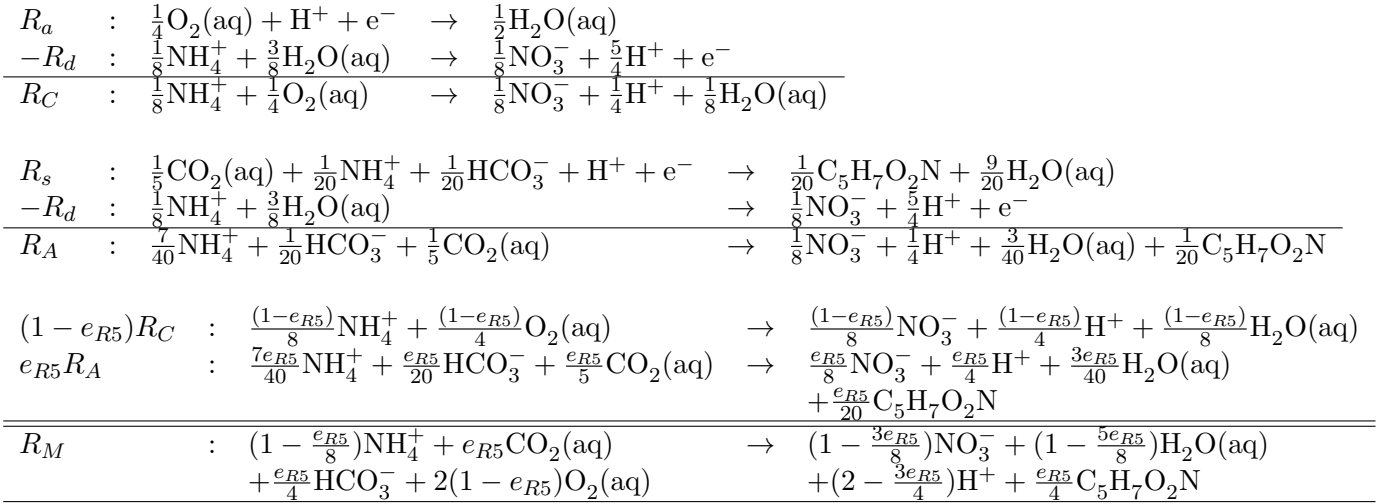




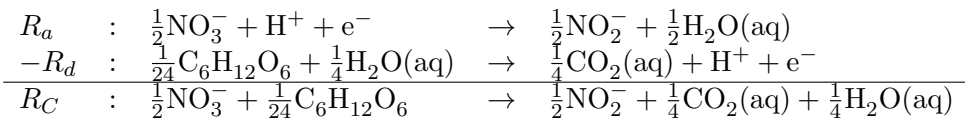
R4: Heterotrophic uptake of NO_3^-



R5: Nitrification



R6: Denitrification



Bibliography

- Abrahamson, J. (1975). Collision rates of small particles in a vigorously turbulent fluid. *Chemical Engineering Science*, 30(11):1371–1379.
- Absalon, C., Van Dellen, K., and Watnick, P. I. (2011). A communal bacterial adhesin anchors biofilm and bystander cells to surfaces. *PLoS Pathog*, 7(8):e1002210.
- Allredge, A. L., Passow, U., and Logan, B. E. (1993). The abundance and significance of a class of large, transparent organic particles in the ocean. *Deep Sea Research Part I: Oceanographic Research Papers*, 40(6):1131–1140.
- Allredge, A. L. and Silver, M. W. (1988). Characteristics, dynamics and significance of marine snow. *Progress in oceanography*, 20(1):41–82.
- Allen, J. and Clarke, K. (2007). Effects of demersal trawling on ecosystem functioning in the North Sea: a modelling study. *Marine Ecology Progress Series*, 336:63–75.
- Allen, M. P. and Tildesley, D. J. (2012). *Computer simulation in chemical physics*, volume 397. Springer Science & Business Media.
- Almeida, C., Debacher, N., Downs, A., Cottet, L., and Mello, C. (2009). Removal of methylene blue from colored effluents by adsorption on montmorillonite clay. *Journal of colloid and interface science*, 332(1):46–53.
- Alonso-Marroquin, F. (2008). Spheropolygons: a new method to simulate conservative and dissipative interactions between 2d complex-shaped rigid bodies. *EPL (Europhysics Letters)*, 83(1):14001.
- Alonso-Marroquín, F., Ramírez-Gómez, Á., González-Montellano, C., Balaam, N., Hanaor, D. A., Flores-Johnson, E., Gan, Y., Chen, S., and Shen, L. (2013). Experimental and numerical determination of mechanical properties of polygonal wood particles and their flow analysis in silos. *Granular Matter*, 15(6):811–826.
- Andreadakis, A. D. (1993). Physical and chemical properties of activated sludge floc. *Water Research*, 27(12):1707–1714.
- Ariathurai, R. and Krone, R. B. (1976). Finite element model for cohesive sediment transport. *Journal of the Hydraulics Division*, 102(3):323–338.
- Asper, V. L. (1987). Measuring the flux and sinking speed of marine snow aggregates. *Deep Sea Research Part A. Oceanographic Research Papers*, 34(1):1–17.
- Atkins, P. and De Paula, J. (2005). *Elements of physical chemistry*. Oxford University Press, USA, 4th edition.
- Azetsu-Scott, K. and Passow, U. (2004). Ascending marine particles: Significance of transparent exopolymer particles (TEP) in the upper ocean. *Limnology and Oceanography*, 49(3):741–748.
- Bache, D. and Rasool, E. (1996). Measurement of the rate of energy dissipation around an oscillating grid by an energy balance approach. *The Chemical Engineering Journal and the Biochemical Engineering Journal*, 63(2):105–115.
- Bainbridge, Z. T., Wolanski, E., Álvarez-Romero, J. G., Lewis, S. E., and Brodie, J. E. (2012). Fine sediment and nutrient dynamics related to particle size and floc formation in a Burdekin River flood plume, Australia. *Marine Pollution Bulletin*, 65(4):236–248.
- Bale, A. and Morris, A. (1987). In situ measurement of particle size in estuarine waters. *Estuarine, Coastal and Shelf Science*, 24(2):253–263.
- Batchelor, B. and Lawrence, A. W. (1978). Autotrophic denitrification using elemental sulfur. *Journal (Water Pollution Control Federation)*, pages 1986–2001.
- Batchelor, G. K. (1953). *The theory of homogeneous turbulence*. Cambridge University Press.
- Bhaskar, P. and Bhosle, N. B. (2006). Bacterial extracellular polymeric substance (EPS): a carrier of heavy metals in the marine food-chain. *Environment International*, 32(2):191–198.
- Bhattacharjee, S., Elimelech, M., and Borkovec, M. (1998). DLVO interaction between colloidal particles: beyond Derjaguins approximation. *Croatica Chemica Acta*, 71(4):883–903.

- Bibby, R. L. and Webster-Brown, J. G. (2005). Characterisation of urban catchment suspended particulate matter (Auckland region, New Zealand); a comparison with non-urban SPM. *Science of the Total Environment*, 343(1):177–197.
- Billen, G., Servais, P., and Becquevort, S. (1990). Dynamics of bacterioplankton in oligotrophic and eutrophic aquatic environments: bottom-up or top-down control? *Hydrobiologia*, 207(1):37–42.
- Birch, G. F., Cruickshank, B., and Davis, B. (2010). Modelling nutrient loads to Sydney estuary (Australia). *Environmental Monitoring and Assessment*, 167(1-4):333–348.
- Boltzmann, L. (1896). *Vorlesungen über Gastheorie*, volume 1. JA Barth.
- Boon, B. and Laudelout, H. (1962). Kinetics of nitrite oxidation by *Nitrobacter winogradskyi*. *Biochemical Journal*, 85(3):440.
- Brandt, B. W., Kooijman, S. A., et al. (2000). Two parameters account for the flocculated growth of microbes in biodegradation assays. *Biotechnology and Bioengineering*, 70(6):677–684.
- Brenner, J. F., Dew, B. S., Horton, J. B., King, T., Neurath, P. W., and Selles, W. D. (1976). An automated microscope for cytologic research a preliminary evaluation. *Journal of Histochemistry & Cytochemistry*, 24(1):100–111.
- Briggs, L. I., McCulloch, D. S., and Moser, F. (1962). The hydraulic shape of sand particles. *Journal of Sedimentary Research*, 32(4):645–656.
- Brillouin, L. (1951). Maxwell’s demon cannot operate: Information and entropy. i. *Journal of Applied Physics*, 22(3):334–337.
- Brönmark, C. and Hansson, L.-A. (2005). *The biology of lakes and ponds*. Oxford University Press.
- Brown, K., Thomas, J., and Doble, R. (1982). Nitrogen source effect on nitrate and ammonium leaching and runoff losses from greens. *Agronomy Journal*, 74(6):947–950.
- Bruce, L. C., Hamilton, D., Imberger, J., Gal, G., Gophen, M., Zohary, T., and Hambright, K. D. (2006). A numerical simulation of the role of zooplankton in C, N and P cycling in Lake Kinneret, Israel. *Ecological Modelling*, 193(3):412–436.
- Bruckner, C. G., Rehm, C., Grossart, H.-P., and Kroth, P. G. (2011). Growth and release of extracellular organic compounds by benthic diatoms depend on interactions with bacteria. *Environmental Microbiology*, 13(4):1052–1063.
- Camilli, A. and Bassler, B. L. (2006). Bacterial small-molecule signaling pathways. *Science*, 311(5764):1113–1116.
- Canfield, D. E., Kristensen, E., and Thamdrup, B. (2005). *Aquatic geomicrobiology*. Gulf Professional Publishing.
- Cantrell, K. J., Serne, R. J., and Last, G. V. (2002). Applicability of the linear sorption isotherm model to represent contaminant transport processes in site-wide performance assessments. *Pacific Northwest National Laboratory. Technical report PNNL-14576*.
- Caperon, J. and Meyer, J. (1972). Nitrogen-limited growth of marine phytoplankton. uptake kinetics and their role in nutrient limited growth of phytoplankton. *Deep Sea Research and Oceanographic Abstracts*, 19(9):619–632.
- Caron, D. A. (1987). Grazing of attached bacteria by heterotrophic microflagellates. *Microbial Ecology*, 13(3):203–218.
- Caron, D. A., Davis, P. G., Madin, L. P., and Sieburth, J. M. (1986). Enrichment of microbial populations in macroaggregates (marine snow) from surface waters of the North Atlantic. *Journal of Marine Research*, 44(3):543–565.
- Cengeloglu, Y., Tor, A., Ersoz, M., and Arslan, G. (2006). Removal of nitrate from aqueous solution by using red mud. *Separation and Purification Technology*, 51(3):374–378.
- Chakraborti, R. K., Atkinson, J. F., and Van Benschoten, J. E. (2000). Characterization of alum floc by image analysis. *Environmental science & technology*, 34(18):3969–3976.
- Chariton, A. A., Court, L. N., Hartley, D. M., Colloff, M. J., and Hardy, C. M. (2010). Ecological assessment of estuarine sediments by pyrosequencing eukaryotic ribosomal DNA. *Frontiers in Ecology and the Environment*, 8(5):233–238.
- Chen, S. and Eisma, D. (1995). Fractal geometry of in situ flocs in the estuarine and coastal environments. *Netherlands Journal of Sea Research*, 33(2):173–182.
- Chhabra, A. and Jensen, R. V. (1989). Direct determination of the $f(\alpha)$ singularity spectrum. *Physical Review Letters*, 62(12):1327.
- Cho, B. C. and Azam, F. (1988). Major role of bacteria in biogeochemical fluxes in the ocean’s interior. *Nature*, 332(6163):441–443.
- Christian, J. R., Lewis, M. R., and Karl, D. M. (1997). Vertical fluxes of carbon, nitrogen, and phosphorus in the North Pacific Subtropical Gyre near Hawaii. *Journal of Geophysical Research: Oceans*, 102(C7):15667–15677.

- Chu, C., Lee, D., and Peng, X. (2004). Structure of conditioned sludge flocs. *Water Research*, 38(8):2125–2134.
- Clark, M. M. and Flora, J. R. (1991). Floc restructuring in varied turbulent mixing. *Journal of Colloid and Interface Science*, 147(2):407–421.
- Clarke, L. P., Velthuisen, R. P., Camacho, M. A., Heine, J. J., Vaidyanathan, M., Hall, L. O., Thatcher, R. W., and Silbiger, M. L. (1995). MRI segmentation: methods and applications. *Magnetic Resonance Imaging*, 13(3):343–368.
- Clausius, R. (1864). *Abhandlungen über die mechanische Wärmetheorie*, volume 1. F. Vieweg.
- Clift, R., Grace, J. R., and Weber, M. E. (2005). *Bubbles, drops, and particles*. Courier Corporation.
- Cline, H. E., Dumoulin, C. L., Hart Jr, H. R., Lorensen, W. E., and Ludke, S. (1987). 3D reconstruction of the brain from magnetic resonance images using a connectivity algorithm. *Magnetic Resonance Imaging*, 5(5):345–352.
- Cloern, J. E. (2001). Our evolving conceptual model of the coastal eutrophication problem. *Marine Ecology Progress Series*, 210:223–253.
- Cochlan, W. P. and Harrison, P. J. (1991). Kinetics of nitrogen (nitrate, ammonium and urea) uptake by the picoflagellate *Micromonas pusilla* (Prasinophyceae). *Journal of Experimental Marine Biology and Ecology*, 153(2):129–141.
- Cole, J. J. (1982). Interactions between bacteria and algae in aquatic ecosystems. *Annual Review of Ecology and Systematics*, 13:291–314.
- Copcia, V., Hristodor, C., Luchian, C., Bilba, N., and Sandu, I. (2010). Ammonium nitrogen removal from aqueous solution by natural clay. *Rev. Chim. (Bucharest)*, 61:1192–1196.
- Corey, A. T. (1963). *Influence of shape on the fall velocity of sand grains*. Audio Visual Service, Colorado State University.
- Corrsin, S. (1963). Turbulence: experimental methods. *Handbuch der Physik*, 8(2):524–533.
- Crump, B. C., Armbrust, E. V., and Baross, J. A. (1999). Phylogenetic analysis of particle-attached and free-living bacterial communities in the Columbia River, its estuary, and the adjacent coastal ocean. *Applied and Environmental Microbiology*, 65(7):3192–3204.
- Curran, K. J., Hill, P. S., Milligan, T. G., Mikkelsen, O. A., Law, B. A., Durrieu de Madron, X., and Bourrin, F. (2007). Settling velocity, effective density, and mass composition of suspended sediment in a coastal bottom boundary layer, Gulf of Lions, France. *Continental Shelf Research*, 27(10):1408–1421.
- Dalsgaard, T., Thamdrup, B., and Canfield, D. E. (2005). Anaerobic ammonium oxidation (anammox) in the marine environment. *Research in Microbiology*, 156(4):457–464.
- Dashman, T. and Stotzky, G. (1982). Adsorption and binding of amino acids on homoionic montmorillonite and kaolinite. *Soil Biology and Biochemistry*, 14(5):447–456.
- Dietrich, W. E. (1982). Settling velocity of natural particles. *Water Resources Research*, 18(6):1615–1626.
- Dobrohotoff, P. B., Azeezullah, S. I., Maggi, F., and Alonso-Marroquin, F. (2012). Optimal description of two-dimensional complex-shaped objects using spheropolygons. *Granular Matter*, 14(5):651–658.
- Doherty, J. (2005). *PEST: Model-independent parameter estimation*. Watermark Computing, Corinda, Australia, 5th edn. edition.
- Domínguez-García, P. and Rubio, M. A. (2010). Three-dimensional morphology of field-induced chain-like aggregates of superparamagnetic microparticles. *Colloids and Surfaces A: Physicochemical and Engineering Aspects*, 358(1):21–27.
- Droppo, I. and Ongley, E. (1992). The state of suspended sediment in the freshwater fluvial environment: a method of analysis. *Water Research*, 26(1):65–72.
- Droppo, I. G. (2001). Rethinking what constitutes suspended sediment. *Hydrological Processes*, 15(9):1551–1564.
- Duarte, C. M. and Cebrian, J. (1996). The fate of marine autotrophic production. *Limnology and Oceanography*, 41(8):1758–1766.
- Dworkin, M., Falkow, S., Rosenberg, E., Schleifer, K.-H., and Stackebrandt, E. (2006). *The Prokaryotes: Vol. 2: Ecophysiology and Biochemistry*. Springer Science & Business Media.
- Ebeling, J. M., Timmons, M. B., and Bisogni, J. (2006). Engineering analysis of the stoichiometry of photoautotrophic, autotrophic, and heterotrophic removal of ammonia–nitrogen in aquaculture systems. *Aquaculture*, 257(1):346–358.
- Einstein, H. A. and Krone, R. B. (1962). Experiments to determine modes of cohesive sediment transport in salt water. *Journal of Geophysical Research*, 67(4):1451–1461.
- Eisma, D. (1986). Flocculation and de-flocculation of suspended matter in estuaries. *Netherlands Journal of Sea Research*, 20(2-3):183–199.
- Elfrink, B. and Baldock, T. (2002). Hydrodynamics and sediment transport in the swash zone: a review and perspec-

- tives. *Coastal Engineering*, 45(3):149–167.
- Ensminger, L. and Gieseking, J. (1939). The adsorption of proteins by montmorillonitic clays. *Soil Science*, 48(6):467–474.
- Eppley, R. W. and Coatsworth, J. L. (1968). Uptake of nitrate and nitrite by *Ditylum brightwellii*-kinetics and mechanisms. *Journal of Phycology*, 4(2):151–156.
- Evans, R. B. (1969). *A proof that essergy is the only consistent measure of potential work (for chemical systems)*. PhD thesis, Dartmouth College, University Microfilms, Ann Arbor, Michigan.
- Fernando, H. and De Silva, I. (1993). Note on secondary flows in oscillating-grid, mixing-box experiments. *Physics of Fluids A: Fluid Dynamics (1989-1993)*, 5(7):1849–1851.
- Firestone, L., Cook, K., Culp, K., Talsania, N., and Preston, K. (1991). Comparison of autofocus methods for automated microscopy. *Cytometry*, 12(3):195–206.
- Fredsøe, J. and Deigaard, R. (1992). *Mechanics of coastal sediment transport*, volume 3. World scientific.
- Freundlich, H. (1906). Over the adsorption in solution. *J. Phys. Chem*, 57(385471):1100–1107.
- Galloway, J. N. (1998). The global nitrogen cycle: changes and consequences. *Environmental Pollution*, 102(1):15–24.
- Gatenby, R. A. and Frieden, B. R. (2007). Information theory in living systems, methods, applications, and challenges. *Bulletin of mathematical biology*, 69(2):635–657.
- Gessner, P. K. and Hasan, M. M. (1987). Freundlich and Langmuir isotherms as models for the adsorption of toxicants on activated charcoal. *Journal of Pharmaceutical Sciences*, 76(4):319–327.
- Ghozlani, B., Hafsia, Z., and Maalel, K. (2012). Numerical study of flow around an oscillating diamond prism and circular cylinder at low Keulegan-Carpenter number. *Journal of Hydrodynamics, Ser. B*, 24(5):767–775.
- Gibbs, R. J. (1985). Estuarine flocs: their size, settling velocity and density. *Journal of Geophysical Research: Oceans*, 90(C2):3249–3251.
- Gibbs, R. J. and Konwar, L. N. (1982). Effect of pipetting on mineral flocs. *Environmental Science & Technology*, 16(2):119–121.
- Goldman, J. and Dennett, M. (1991). Ammonium regeneration and carbon utilization by marine bacteria grown on mixed substrates. *Marine Biology*, 109(3):369–378.
- Goldman, J. C., Caron, D. A., and Dennett, M. R. (1987). Regulation of gross growth efficiency and ammonium regeneration in bacteria by substrate C: N ratio. *Limnol. Oceanogr*, 32(6):1239–1252.
- Golterman, H. L., Sly, P. G., and Thomas, R. L. (1983). *Study of the relationship between water quality and sediment transport: a guide for the collection and interpretation of sediment quality data*. UNIPUB, New York, NY.
- Gottschalk, G. (1986). *Bacterial metabolism*. Springer Science & Business Media.
- Goulder, R. (1977). Attached and free bacteria in an estuary with abundant suspended solids. *Journal of Applied Bacteriology*, 43(3):399–405.
- Grant, I. (1997). Particle image velocimetry: a review. *Proceedings of the Institution of Mechanical Engineers, Part C: Journal of Mechanical Engineering Science*, 211(1):55–76.
- Gratiot, N., Michallet, H., and Mory, M. (2005). On the determination of the settling flux of cohesive sediments in a turbulent fluid. *Journal of Geophysical Research: Oceans*, 110(C6).
- Green, J. L., Bohannan, B. J., and Whitaker, R. J. (2008). Microbial biogeography: from taxonomy to traits. *Science*, 320(5879):1039–1043.
- Groffman, P. M. and Bohlen, P. J. (1999). Soil and sediment biodiversity: cross-system comparisons and large-scale effects. *BioScience*, 49(2):139–148.
- Grošelj, D., Jenko, F., and Frey, E. (2015). How turbulence regulates biodiversity in systems with cyclic competition. *Physical Review E*, 91(3):033009.
- Grossart, H., Kiørboe, T., Tang, K., Allgaier, M., Yam, E., and Ploug, H. (2006). Interactions between marine snow and heterotrophic bacteria: aggregate formation and microbial dynamics. *Aquatic Microbial Ecology*, 42:19–26.
- Grossart, H. P., Hietanen, S., and Ploug, H. (2003a). Microbial dynamics on diatom aggregates in Øresund, Denmark. *Marine Ecology Progress Series*, 249:69–78.
- Grossart, H.-P., Kiørboe, T., Tang, K., and Ploug, H. (2003b). Bacterial colonization of particles: growth and interactions. *Applied and Environmental Microbiology*, 69(6):3500–3509.
- Grossart, H.-P. and Simon, M. (1993). Limnetic macroscopic organic aggregates (lake snow): Occurrence, characteristics, and microbial dynamics in Lake Constance. *Limnology and Oceanography*, 38(3):532–546.
- Grossart, H.-P., Tang, K. W., Kiørboe, T., and Ploug, H. (2007). Comparison of cell-specific activity between free-

- living and attached bacteria using isolates and natural assemblages. *FEMS Microbiology Letters*, 266(2):194–200.
- Guerrero, R., Pedrós-Alió, C., Esteve, I., Mas, J., Chase, D., and Margulis, L. (1986). Predatory prokaryotes: predation and primary consumption evolved in bacteria. *Proceedings of the National Academy of Sciences*, 83(7):2138–2142.
- Hallas, L. E., Hahn, E. M., and Korndorfer, C. (1988). Characterization of microbial traits associated with glyphosate biodegradation in industrial activated sludge. *Journal of Industrial Microbiology*, 3(6):377–385.
- Hamaker, H. (1937). The Londonvan der Waals attraction between spherical particles. *Physica*, 4(10):1058–1072.
- Han, M. and Lawler, D. F. (1991). Interactions of two settling spheres: Settling rates and collision efficiency. *Journal of Hydraulic Engineering*, 117(10):1269–1289.
- Hart, B. T. (1982). Uptake of trace metals by sediments and suspended particulates: a review. *Hydrobiologia*, 91(1):299–313.
- Headley, J. V., Gandrass, J., Kuballa, J., Peru, K. M., and Gong, Y. (1998). Rates of sorption and partitioning of contaminants in river biofilm. *Environmental Science & Technology*, 32(24):3968–3973.
- Hedges, J. I. (1977). The association of organic molecules with clay minerals in aqueous solutions. *Geochimica et Cosmochimica Acta*, 41(8):1119–1123.
- Hedges, J. I. and Hare, P. (1987). Amino acid adsorption by clay minerals in distilled water. *Geochimica et Cosmochimica Acta*, 51(2):255–259.
- Hedges, J. I. and Keil, R. G. (1995). Sedimentary organic matter preservation: an assessment and speculative synthesis. *Marine Chemistry*, 49(2):81–115.
- Heisler, J., Glibert, P. M., Burkholder, J. M., Anderson, D. M., Cochlan, W., Dennison, W. C., Dortch, Q., Gobler, C. J., Heil, C. A., Humphries, E., et al. (2008). Eutrophication and harmful algal blooms: a scientific consensus. *Harmful Algae*, 8(1):3–13.
- Henrichs, S. M. and Sugai, S. F. (1993). Adsorption of amino acids and glucose by sediments of Resurrection Bay, Alaska, USA: functional group effects. *Geochimica et Cosmochimica Acta*, 57(4):823–835.
- Hentschel, H. G. E. and Procaccia, I. (1983). The infinite number of generalized dimensions of fractals and strange attractors. *Physica D: Nonlinear Phenomena*, 8(3):435–444.
- Higashitani, K. and Iimura, K. (1998). Two-dimensional simulation of the breakup process of aggregates in shear and elongational flows. *Journal of Colloid and Interface Science*, 204(2):320–327.
- Higashitani, K., Iimura, K., and Sanda, H. (2001). Simulation of deformation and breakup of large aggregates in flows of viscous fluids. *Chemical Engineering Science*, 56(9):2927–2938.
- Hill, P. S., Bowers, D. G., and Braithwaite, K. M. (2013). The effect of suspended particle composition on particle area-to-mass ratios in coastal waters. *Methods in Oceanography*, 7:95–109.
- Hill, P. S., Syvitski, J. P., Cowan, E. A., and Powell, R. D. (1998). In situ observations of floc settling velocities in Glacier Bay, Alaska. *Marine Geology*, 145(1):85–94.
- Hogg, R., Healy, T. W., and Fuerstenau, D. (1966). Mutual coagulation of colloidal dispersions. *Transactions of the Faraday Society*, 62:1638–1651.
- Hopfinger, E. and Toly, J.-A. (1976). Spatially decaying turbulence and its relation to mixing across density interfaces. *Journal of Fluid Mechanics*, 78(01):155–175.
- Horner-Devine, M. C., Carney, K. M., and Bohannon, B. J. (2004). An ecological perspective on bacterial biodiversity. *Proceedings of the Royal Society of London B: Biological Sciences*, 271(1535):113–122.
- Hu, K., Ding, P., Wang, Z., and Yang, S. (2009). A 2D/3D hydrodynamic and sediment transport model for the Yangtze Estuary, China. *Journal of Marine Systems*, 77(1):114–136.
- Huisman, J., Sharples, J., Stroom, J. M., Visser, P. M., Kardinaal, W. E. A., Verspagen, J. M., and Sommeijer, B. (2004). Changes in turbulent mixing shift competition for light between phytoplankton species. *Ecology*, 85(11):2960–2970.
- Hunt, B. R. and Kaloshin, V. Y. (1997). How projections affect the dimension spectrum of fractal measures. *Nonlinearity*, 10(5):1031.
- Hunt, J. R. (1982). Self-similar particle-size distributions during coagulation: theory and experimental verification. *Journal of Fluid Mechanics*, 122:169–185.
- Ize-Iyamu, O., Asia, I., and Egwakhide, P. (2007). Concentrations of residues from organochlorine pesticide in water and fish from some rivers in Edo State Nigeria. *International Journal of Physical Sciences*, 2(9):237–241.
- Jackson, G. A. (1995). TEP and coagulation during a mesocosm experiment. *Deep Sea Research Part II: Topical Studies in Oceanography*, 42(1):215–222.

- Jacob, E. B., Shapira, Y., and Tauber, A. I. (2006). Seeking the foundations of cognition in bacteria: From Schrödinger's negative entropy to latent information. *Physica A: Statistical Mechanics and its Applications*, 359:495–524.
- Jain, C. and Ram, D. (1997). Adsorption of lead and zinc on bed sediments of the river Kali. *Water Research*, 31(1):154–162.
- James, S. C., Jones, C. A., Grace, M. D., and Roberts, J. D. (2010). Advances in sediment transport modelling. *Journal of Hydraulic Research*, 48(6):754–763.
- Janke, N. (1966). Effect of shape upon the settling velocity of regular convex geometric particles. *Journal of Sedimentary Research*, 36(2).
- Jarvis, P., Jefferson, B., and Parsons, S. A. (2006). Floc structural characteristics using conventional coagulation for a high doc, low alkalinity surface water source. *Water Research*, 40(14):2727–2737.
- Jones, C. G., Lawton, J. H., and Shachak, M. (1994). Organisms as ecosystem engineers. In *Ecosystem Management*, pages 130–147. Springer.
- Kalender, W. A. (2006). X-ray computed tomography. *Physics in Medicine and Biology*, 51(13):R29.
- Karickhoff, S. W., Brown, D. S., and Scott, T. A. (1979). Sorption of hydrophobic pollutants on natural sediments. *Water Research*, 13(3):241–248.
- Kaufman, A. G. and Borrett, S. R. (2010). Ecosystem network analysis indicators are generally robust to parameter uncertainty in a phosphorus model of Lake Sidney Lanier, USA. *Ecological Modelling*, 221(8):1230–1238.
- Kelly, D. P. (1971). Autotrophy: concepts of lithotrophic bacteria and their organic metabolism. *Annual Reviews in Microbiology*, 25(1):177–210.
- Khelifa, A. and Hill, P. S. (2006). Models for effective density and settling velocity of flocs. *Journal of Hydraulic Research*, 44(3):390–401.
- Kilps, J. R., Logan, B. E., and Alldredge, A. L. (1994). Fractal dimensions of marine snow determined from image analysis of in situ photographs. *Deep Sea Research Part I: Oceanographic Research Papers*, 41(8):1159–1169.
- Kim, A. S. and Stolzenbach, K. D. (2004). Aggregate formation and collision efficiency in differential settling. *Journal of Colloid and Interface Science*, 271(1):110–119.
- Kinniburgh, D. G. (1986). General purpose adsorption isotherms. *Environmental Science & Technology*, 20(9):895–904.
- Kjørboe, T. (2001). Formation and fate of marine snow: small-scale processes with large-scale implications. *Scientia Marina*, 65(S2):57–71.
- Kjørboe, T., Andersen, K., and Dam, H. (1990). Coagulation efficiency and aggregate formation in marine phytoplankton. *Marine Biology*, 107(2):235–245.
- Kjørboe, T., Grossart, H.-P., Ploug, H., and Tang, K. (2002). Mechanisms and rates of bacterial colonization of sinking aggregates. *Applied and Environmental Microbiology*, 68(8):3996–4006.
- Kjørboe, T., Grossart, H.-P., Ploug, H., Tang, K., and Auer, B. (2004). Particle-associated flagellates: swimming patterns, colonization rates, and grazing on attached bacteria. *Aquatic Microbial Ecology*, 35(2):141–152.
- Kirchman, D. L. and Wheeler, P. A. (1998). Uptake of ammonium and nitrate by heterotrophic bacteria and phytoplankton in the sub-Arctic Pacific. *Deep Sea Research Part I: Oceanographic Research Papers*, 45(2):347–365.
- Klump, J. V. and Martens, C. S. (1981). Biogeochemical cycling in an organic rich coastal marine basin. nutrient sediment-water exchange processes. *Geochimica et Cosmochimica Acta*, 45(1):101–121.
- Knicker, H. and Hatcher, P. G. (1997). Survival of protein in an organic-rich sediment: possible protection by encapsulation in organic matter. *Naturwissenschaften*, 84(6):231–234.
- Kolb, M., Botet, R., and Jullien, R. (1983). Scaling of kinetically growing clusters. *Physical Review Letters*, 51(13):1123.
- Kranck, K. (1973). Flocculation of suspended sediment in the sea. *Nature*, 246:348–350.
- Kranck, K. (1975). Sediment deposition from flocculated suspensions. *Sedimentology*, 22(1):111–123.
- Kranenburg, C. (1994). The fractal structure of cohesive sediment aggregates. *Estuarine, Coastal and Shelf Science*, 39(6):451–460.
- Krishnappan, B. (1990). Modelling of settling and flocculation of fine sediments in still water. *Canadian Journal of Civil Engineering*, 17(5):763–770.
- Krone, R. B. (1962). Flume studies of the transport of sediment in estuarial shoaling processes. Technical report, Hydraulic Engineering Laboratory and Sanitary Engineering Research Laboratory, University of California, Berkeley.

- Krone, R. B. (1972). A field study of flocculation as a factor in estuarial shoaling processes. Technical report, DTIC Document.
- Kumar, R. G., Strom, K. B., and Keyvani, A. (2010). Floc properties and settling velocity of San Jacinto estuary mud under variable shear and salinity conditions. *Continental Shelf Research*, 30(20):2067–2081.
- Kumar, S., Finlay, J. C., and Sterner, R. W. (2011). Isotopic composition of nitrogen in suspended particulate matter of Lake Superior: implications for nutrient cycling and organic matter transformation. *Biogeochemistry*, 103(1-3):1–14.
- Kusters, K. A., Wijers, J. G., and Thoenes, D. (1997). Aggregation kinetics of small particles in agitated vessels. *Chemical Engineering Science*, 52(1):107–121.
- Langmuir, I. (1918). The adsorption of gases on plane surfaces of glass, mica and platinum. *Journal of the American Chemical Society*, 40(9):1361–1403.
- Lartiges, B., Deneux-Mustin, S., Villemin, G., Mustin, C., Barres, O., Chamerois, M., Gerard, B., and Babut, M. (2001). Composition, structure and size distribution of suspended particulates from the Rhine River. *Water Research*, 35(3):808–816.
- Lee, D. J., Chen, G. W., Liao, Y. C., and Hsieh, C. C. (1996). On the free-settling test for estimating activated sludge floc density. *Water Research*, 30(3):541–550.
- Leliaert, F., Zhang, X., Ye, N., Malta, E.-j., Engelen, A. H., Mineur, F., Verbruggen, H., and De Clerck, O. (2009). Research note: identity of the Qingdao algal bloom. *Phycological Research*, 57(2):147–151.
- Levenberg, K. (1944). A method for the solution of certain non-linear problems in least squares. *Quarterly of Applied Mathematics*, 2(2):164–168.
- Lévy, M., Jahn, O., Dutkiewicz, S., and Follows, M. J. (2014). Phytoplankton diversity and community structure affected by oceanic dispersal and mesoscale turbulence. *Limnology and Oceanography: Fluids and Environments*, 4(1):67–84.
- Li, D.-H. and Ganczarczyk, J. J. (1987). Stroboscopic determination of settling velocity, size and porosity of activated sludge flocs. *Water Research*, 21(3):257–262.
- Li, X. and Logan, B. E. (1997). Collision frequencies between fractal aggregates and small particles in a turbulently sheared fluid. *Environmental Science & Technology*, 31(4):1237–1242.
- Li, Z. and Bowman, R. S. (2001). Retention of inorganic oxyanions by organo-kaolinite. *Water Research*, 35(16):3771–3776.
- Lick, W., Huang, H., and Jepsen, R. (1993). Flocculation of fine-grained sediments due to differential settling. *Journal of Geophysical Research: Oceans*, 98(C6):10279–10288.
- Liem, L., Smith, D., and Stanley, S. (1999). Turbulent velocity in flocculation by means of grids. *Journal of Environmental Engineering*, 125(3):224–233.
- Logan, B. and Alldredge, A. (1989). Potential for increased nutrient uptake by flocculating diatoms. *Marine Biology*, 101(4):443–450.
- Logan, B. E. and Kilps, J. R. (1995). Fractal dimensions of aggregates formed in different fluid mechanical environments. *Water Research*, 29(2):443–453.
- Logan, B. E., Passow, U., Alldredge, A. L., Grossartt, H.-P., and Simont, M. (1995). Rapid formation and sedimentation of large aggregates is predictable from coagulation rates (half-lives) of transparent exopolymer particles (TEP). *Deep Sea Research Part II: Topical Studies in Oceanography*, 42(1):203–214.
- Logan, B. E. and Wilkinson, D. B. (1990). Fractal geometry of marine snow and other biological aggregates. *Limnology and Oceanography*, 35(1):130–136.
- Lubarsky, H. V., Hubas, C., Chocholek, M., Larson, F., Manz, W., Paterson, D. M., and Gerbersdorf, S. U. (2010). The stabilisation potential of individual and mixed assemblages of natural bacteria and microalgae. *PloS one*, 5(11):e13794.
- Luding, S. (1998). Collisions & contacts between two particles. In *Physics of Dry Granular Media*, pages 285–304. Springer.
- MacIsaac, J. and Dugdale, R. (1969). The kinetics of nitrate and ammonia uptake by natural populations of marine phytoplankton. *Deep Sea Research and Oceanographic Abstracts*, 16(1):45–57.
- Magbanua, F. S., Townsend, C. R., Hageman, K. J., Lange, K., Lear, G., Lewis, G. D., and Matthaei, C. D. (2013). Understanding the combined influence of fine sediment and glyphosate herbicide on stream periphyton communities. *Water Research*, 47(14):5110–5120.
- Maggi, F. (2003). Survey of the numerical characterisation of 2-D complex clusters. Technical report, TU Delft,

- Department of Hydraulic Engineering.
- Maggi, F. (2005). *Flocculation dynamics of cohesive sediment*. PhD thesis, TU Delft, Delft University of Technology.
- Maggi, F. (2007). Variable fractal dimension: A major control for floc structure and flocculation kinematics of suspended cohesive sediment. *Journal of Geophysical Research: Oceans (1978–2012)*, 112(C7).
- Maggi, F. (2008). Projection of compact fractal sets: application to diffusion-limited and cluster-cluster aggregates. *Nonlinear Processes in Geophysics*, 15(4):695–699.
- Maggi, F. (2013). The settling velocity of mineral, biomineral, and biological particles and aggregates in water. *Journal of Geophysical Research: Oceans*, 118(4):2118–2132.
- Maggi, F. (2015a). BRTsim version 1: A general-purpose multiphase and multicomponent computational solver for biogeochemical reaction-advection-dispersion processes in porous and non-porous media, 1st edn. Technical Report Research Report R954, The University of Sydney, Australia.
- Maggi, F. (2015b). Experimental evidence of how the fractal structure controls the hydrodynamic resistance on granular aggregates moving through water. *Journal of Hydrology*, 528:694–702.
- Maggi, F. and Tang, F. H. M. (2015). Analysis of the effect of organic matter content on the architecture and sinking of sediment aggregates. *Marine Geology*, 363:102–111.
- Maggi, F. and Winterwerp, J. C. (2004). Method for computing the three-dimensional capacity dimension from two-dimensional projections of fractal aggregates. *Physical Review E*, 69(1):011405.
- Markussen, T. N. and Andersen, T. J. (2014). Flocculation and floc break-up related to tidally induced turbulent shear in a low-turbidity, microtidal estuary. *Journal of Sea Research*, 89:1–11.
- Martin, J. H., Knauer, G. A., Karl, D. M., and Broenkow, W. W. (1987). VERTEX: carbon cycling in the northeast pacific. *Deep Sea Research Part A. Oceanographic Research Papers*, 34(2):267–285.
- Matson, E. A. and Brinson, M. M. (1990). Stable carbon isotopes and the C: N ratio in the estuaries of the Pamlico and Neuse Rivers, North Carolina. *Limnology and Oceanography*, 35(6):1290–1300.
- Matsunaga, N., Sugihara, Y., Komatsu, T., and Masuda, A. (1999). Quantitative properties of oscillating-grid turbulence in a homogeneous fluid. *Fluid Dynamics Research*, 25(3):147–165.
- Maxwell, J. C. (1871). *Theory of heat*. Reprinted (2012) by Courier Corporation.
- McCarthy, J. J., Taylor, W. R., and Taft, J. L. (1977). Nitrogenous nutrition of the plankton in the Chesapeake Bay. 1. Nutrient availability and phytoplankton preferences. *Limnol. Oceanogr*, 22(6):996–1011.
- McCave, I. (1984). Size spectra and aggregation of suspended particles in the deep ocean. *Deep Sea Research Part A. Oceanographic Research Papers*, 31(4):329–352.
- McCready, S., Birch, G. F., and Long, E. R. (2006). Metallic and organic contaminants in sediments of Sydney Harbour, Australia and vicinity: a chemical dataset for evaluating sediment quality guidelines. *Environment International*, 32(4):455–465.
- McFarlane, A. J., Addai-Mensah, J., Bremmell, K., et al. (2005). Rheology of flocculated kaolinite dispersions. *Korea-Australia Rheology Journal*, 17(4):181–190.
- McSwain, B., Irvine, R., Hausner, M., and Wilderer, P. (2005). Composition and distribution of extracellular polymeric substances in aerobic flocs and granular sludge. *Applied and Environmental Microbiology*, 71(2):1051–1057.
- Meadows, P. and Tufail, A. (1986). Bioturbation, microbial activity and sediment properties in an estuarine ecosystem. *Proceedings of the Royal Society of Edinburgh. Section B. Biological Sciences*, 90:129–142.
- Meadows, P. S., Meadows, A., and Murray, J. M. (2012). Biological modifiers of marine benthic seascapes: Their role as ecosystem engineers. *Geomorphology*, 157:31–48.
- Meakin, P. (1983). Formation of fractal clusters and networks by irreversible diffusion-limited aggregation. *Physical Review Letters*, 51(13):1119.
- Meakin, P. (1991). Fractal aggregates in geophysics. *Reviews of Geophysics*, 29(3):317–354.
- Meakin, P. (1998). *Fractals, scaling and growth far from equilibrium*, volume 5. Cambridge university press.
- Meakin, P. and Jullien, R. (1988). The effects of restructuring on the geometry of clusters formed by diffusion-limited, ballistic, and reaction-limited cluster–cluster aggregation. *The Journal of chemical physics*, 89(1):246–250.
- Mee, L. D. (1992). The Black Sea in crisis: a need for concerted international action. *Ambio*, 21(4):278–86.
- Mehta, A. J. (1989). On estuarine cohesive sediment suspension behavior. *Journal of Geophysical Research: Oceans*, 94(C10):14303–14314.
- Métivier, R., Bourven, I., Labanowski, J., and Guibaud, G. (2013). Interaction of erythromycin ethylsuccinate and acetaminophen with protein fraction of extracellular polymeric substances (EPS) from various bacterial aggregates.

- Environmental Science and Pollution Research*, 20(10):7275–7285.
- Middelburg, J. and Levin, L. (2009). Coastal hypoxia and sediment biogeochemistry. *Biogeosciences*, 6.
- Middelburg, J. J. and Nieuwenhuize, J. (2000). Nitrogen uptake by heterotrophic bacteria and phytoplankton in the nitrate-rich Thames estuary. *Marine Ecology Progress Series*, 203:13–21.
- Midgley, P. A. and Weyland, M. (2003). 3D electron microscopy in the physical sciences: the development of Z-contrast and EFTEM tomography. *Ultramicroscopy*, 96(3):413–431.
- Mie, G. (1908). Articles on the optical characteristics of turbid tubes, especially colloidal metal solutions. *Ann. Phys*, 25(3):377–445.
- Mietta, F., Chassagne, C., and Winterwerp, J. (2009). Shear-induced flocculation of a suspension of kaolinite as function of pH and salt concentration. *Journal of Colloid and Interface Science*, 336(1):134–141.
- Mikkelsen, O. A., Curran, K. J., Hill, P. S., and Milligan, T. G. (2007). Entropy analysis of in situ particle size spectra. *Estuarine, Coastal and Shelf Science*, 72(4):615–625.
- Milligan, T. G. and Hill, P. (1998). A laboratory assessment of the relative importance of turbulence, particle composition, and concentration in limiting maximal floc size and settling behaviour. *Journal of Sea Research*, 39(3):227–241.
- Monod, J. (1949). The growth of bacterial cultures. *Annual Reviews in Microbiology*, 3(1):371–394.
- More, T., Yan, S., Hoang, N., Tyagi, R., and Surampalli, R. (2012). Bacterial polymer production using pre-treated sludge as raw material and its flocculation and dewatering potential. *Bioresource Technology*, 121:425–431.
- Nash, J. E. and Sutcliffe, J. V. (1970). River flow forecasting through conceptual models part i a discussion of principles. *Journal of Hydrology*, 10(3):282–290.
- Ng, C., Losso, J. N., Marshall, W. E., and Rao, R. M. (2002). Freundlich adsorption isotherms of agricultural by-product-based powdered activated carbons in a geosmin–water system. *Bioresource Technology*, 85(2):131–135.
- Noh, Y. and Fernando, H. J. (1993). The role of molecular diffusion in the deepening of the mixed layer. *Dynamics of Atmospheres and Oceans*, 17(2):187–215.
- Ongley, E., Bynoe, M., and Percival, J. (1981). Physical and geochemical characteristics of suspended solids, Wilton Creek, Ontario. *Canadian Journal of Earth Sciences*, 18(8):1365–1379.
- O’Toole, G., Kaplan, H. B., and Kolter, R. (2000). Biofilm formation as microbial development. *Annual Reviews in Microbiology*, 54(1):49–79.
- Overbeek, J. T. G. (1952). Electrochemistry of the double layer. *Colloid Science*, 1:115–193.
- Paerl, H. W. (1975). Microbial attachment to particles in marine and freshwater ecosystems. *Microbial Ecology*, 2(1):73–83.
- Paerl, H. W. and Huisman, J. (2009). Climate change: a catalyst for global expansion of harmful cyanobacterial blooms. *Environmental Microbiology Reports*, 1(1):27–37.
- Parsons, M. L. and Dortch, Q. (2002). Sedimentological evidence of an increase in *Pseudo-nitzschia* (Bacillariophyceae) abundance in response to coastal eutrophication. *Limnology and Oceanography*, 47(2):551–558.
- Passow, U., Shipe, R., Murray, A., Pak, D., Brzezinski, M., and Alldredge, A. (2001). The origin of transparent exopolymer particles (TEP) and their role in the sedimentation of particulate matter. *Continental Shelf Research*, 21(4):327–346.
- Pavoni, J. L., Tenney, M. W., and Echelberger Jr, W. F. (1972). Bacterial exocellular polymers and biological flocculation. *Journal (Water Pollution Control Federation)*, pages 414–431.
- Pernthaler, J. (2005). Predation on prokaryotes in the water column and its ecological implications. *Nature Reviews Microbiology*, 3(7):537–546.
- Pertuz, S., Puig, D., and Garcia, M. A. (2013). Analysis of focus measure operators for shape-from-focus. *Pattern Recognition*, 46(5):1415–1432.
- Pind, A., Risgaard-Petersen, N., and Revsbech, N. P. (1997). Denitrification and microphytobenthic NO₃⁻ consumption in a danish low land stream: diurnal and seasonal variation. *Aquatic Microbial Ecology*, 12(3):275–284.
- Prokopykin, I., Mooij, W., Janse, J., and Degermendzhy, A. (2010). A general one-dimensional vertical ecosystem model of Lake Shira (Russia, Khakasia): description, parametrization and analysis. *Aquatic Ecology*, 44(3):585–618.
- Ramesh, A., Hasegawa, H., Maki, T., and Ueda, K. (2007). Adsorption of inorganic and organic arsenic from aqueous solutions by polymeric Al/Fe modified montmorillonite. *Separation and Purification Technology*, 56(1):90–100.
- Raven, J. A. (2009). Contributions of anoxygenic and oxygenic phototrophy and chemolithotrophy to carbon and oxygen fluxes in aquatic environments. *Aquatic Microbial Ecology*, 56(2/3):177–192.

- Raymond, R. C. (1950). Communication, entropy, and life. *American Scientist*, 38(2):273–278.
- Reay, D. S., Nedwell, D. B., Priddle, J., and Ellis-Evans, J. C. (1999). Temperature dependence of inorganic nitrogen uptake: reduced affinity for nitrate at suboptimal temperatures in both algae and bacteria. *Applied and Environmental Microbiology*, 65(6):2577–2584.
- Riebesell, U. (1991). Particle aggregation during a diatom bloom. 2. biological aspects. *Marine Ecology Progress Series*, (3).
- Riley, W., Maggi, F., Kleber, M., Torn, M., Tang, J., Dwivedi, D., and Guerry, N. (2014). Long residence times of rapidly decomposable soil organic matter: application of a multi-phase, multi-component, and vertically resolved model (BAMS1) to soil carbon dynamics. *Geosci Model Dev Discussion*, 7:815–870.
- Risgaard-Petersen, N., Nicolaisen, M. H., Revsbech, N. P., and Lomstein, B. A. (2004). Competition between ammonia-oxidizing bacteria and benthic microalgae. *Applied and environmental microbiology*, 70(9):5528–5537.
- Rittmann, B. E. and McCarty, P. L. (2001). *Environmental biotechnology: principles and applications*. New York: McGrawHill.
- Rizzo, W. M. (1990). Nutrient exchanges between the water column and a subtidal benthic microalgal community. *Estuaries*, 13(3):219–226.
- Robens, E., Rouquerol, F., Rouquerol, J., and Sing, K. (1999). Adsorption by powders and porous solids.
- Robson, B. J. (2014). State of the art in modelling of phosphorus in aquatic systems: review, criticisms and commentary. *Environmental Modelling & Software*, 61:339–359.
- Romero, D., Aguilar, C., Losick, R., and Kolter, R. (2010). Amyloid fibers provide structural integrity to bacillus subtilis biofilms. *Proceedings of the National Academy of Sciences*, 107(5):2230–2234.
- Ross, M. A. (1988). *Vertical structure of estuarine fine sediment suspensions*. Coastal and Oceanographic Engineering Department, University of Florida.
- Rubey, W. W. (1933). Settling velocity of gravel, sand, and silt particles. *American Journal of Science*, 148:325–338.
- Saffman, P. and Turner, J. (1956). On the collision of drops in turbulent clouds. *Journal of Fluid Mechanics*, 1(01):16–30.
- Saleh-Lakha, S., Shannon, K. E., Henderson, S. L., Goyer, C., Trevors, J. T., Zebarth, B. J., and Burton, D. L. (2009). Effect of pH and temperature on denitrification gene expression and activity in *Pseudomonas mandelii*. *Applied and Environmental Microbiology*, 75(12):3903–3911.
- Sánchez, N., Alfaro, E. J., and Pérez, E. (2005). The fractal dimension of projected clouds. *The Astrophysical Journal*, 625(2):849.
- Santiago, J. G., Wereley, S. T., Meinhart, C. D., Beebe, D., and Adrian, R. J. (1998). A particle image velocimetry system for microfluidics. *Experiments in Fluids*, 25(4):316–319.
- Schluter, J., Nadell, C. D., Bassler, B. L., and Foster, K. R. (2015). Adhesion as a weapon in microbial competition. *The ISME journal*, 9(1):139–149.
- Schrödinger, E. (1944). *What Is Life? The Physical Aspect of the Living Cell and Mind*. Cambridge University Press, Cambridge.
- Serra, T. and Casamitjana, X. (1998). Structure of the aggregates during the process of aggregation and breakup under a shear flow. *Journal of Colloid and Interface Science*, 206(2):505–511.
- Serra, T. and Logan, B. E. (1999). Collision frequencies of fractal bacterial aggregates with small particles in a sheared fluid. *Environmental Science & Technology*, 33(13):2247–2251.
- Servais, P., Billen, G., and Rego, J. V. (1985). Rate of bacterial mortality in aquatic environments. *Applied and Environmental microbiology*, 49(6):1448–1454.
- Shanks, A. L. and Trent, J. D. (1979). Marine snow: microscale nutrient patches. *Limnology and Oceanography*, 24(5):850–854.
- Shanks, A. L. and Trent, J. D. (1980). Marine snow: sinking rates and potential role in vertical flux. *Deep Sea Research Part A. Oceanographic Research Papers*, 27(2):137–143.
- Shannon, C. E. (1948). A mathematical theory of communication. *The Bell System Technical Journal*, 27:379–423.
- Sheldon, R. W. (1968). Sedimentation in the Estuary of the River Crouch, Essex, England. *Limnology and Oceanography*, 13:72–83.
- Sheng, G.-P., Yu, H.-Q., and Li, X.-Y. (2010). Extracellular polymeric substances (EPS) of microbial aggregates in biological wastewater treatment systems: a review. *Biotechnology Advances*, 28(6):882–894.
- Sheng, G.-P., Yu, H.-Q., Li, X.-Y., et al. (2006). Stability of sludge flocs under shear conditions: roles of extracellular

- polymeric substances (EPS). *Biotechnology and Bioengineering*, 93(6):1095–1102.
- Simon, M., Grossart, H.-P., Schweitzer, B., and Ploug, H. (2002). Microbial ecology of organic aggregates in aquatic ecosystems. *Aquatic Microbial Ecology*, 28(2):175–211.
- Siviglia, A. and Crosato, A. (2016). Numerical modelling of river morphodynamics: Latest developments and remaining challenges. *Advances in Water Resources*.
- Skoglund, U. and Daneholt, B. (1986). Electron microscope tomography. *Trends in Biochemical Sciences*, 11(12):499–503.
- Sobeck, D. C. and Higgins, M. J. (2002). Examination of three theories for mechanisms of cation-induced bioflocculation. *Water Research*, 36(3):527–538.
- Sorooshian, S., Duan, Q., and Gupta, V. K. (1993). Calibration of rainfall-runoff models: application of global optimization to the Sacramento soil moisture accounting model. *Water Resources Research*, 29(4):1185–1194.
- Späth, R., Flemming, H.-C., and Wuertz, S. (1998). Sorption properties of biofilms. *Water Science and Technology*, 37(4-5):207–210.
- Spicer, P. T. and Pratsinis, S. E. (1996). Shear-induced flocculation: the evolution of floc structure and the shape of the size distribution at steady state. *Water Research*, 30(5):1049–1056.
- Stanca, E., Cellamare, M., and Basset, A. (2013). Geometric shape as a trait to study phytoplankton distributions in aquatic ecosystems. *Hydrobiologia*, 701(1):99–116.
- Stanley, H. E. and Meakin, P. (1988). Multifractal phenomena in physics and chemistry. *Nature*, 335(6189):405–409.
- Stokes, G. G. (1851). *On the effect of the internal friction of fluids on the motion of pendulums*, volume 9. Pitt Press.
- Stolzenbach, K. D. (1993). Scavenging of small particles by fast-sinking porous aggregates. *Deep Sea Research Part I: Oceanographic Research Papers*, 40(2):359–369.
- Stolzenbach, K. D. and Elimelech, M. (1994). The effect of particle density on collisions between sinking particles: implications for particle aggregation in the ocean. *Deep Sea Research Part I: Oceanographic Research Papers*, 41(3):469–483.
- Stone, M. and Krishnappan, B. (2003). Floc morphology and size distributions of cohesive sediment in steady-state flow. *Water Research*, 37(11):2739–2747.
- Tan, X.-L., Zhang, G.-P., Hang, Y., Furukawa, Y., et al. (2012). Characterization of particle size and settling velocity of cohesive sediments affected by a neutral exopolymer. *International Journal of Sediment Research*, 27(4):473–485.
- Tang, F. H. M., Alonso-Marroquin, F., and Maggi, F. (2014). Stochastic collision and aggregation analysis of kaolinite in water through experiments and the spheropolygon theory. *Water Research*, 53:180–190.
- Tang, F. H. M. and Maggi, F. (2015a). Anthropogenic nutrient leaching alters the size distribution of suspended particle matter. In *E-proceedings of the 36th IAHR World Congress*, <http://89.31.100.18/iahrpapers/81273.pdf>.
- Tang, F. H. M. and Maggi, F. (2015b). A laboratory facility for flocculation-related experiments. Technical Report Research Report R952, The University of Sydney, Australia.
- Tang, F. H. M. and Maggi, F. (2015c). Reconstructing the fractal dimension of granular aggregates from light intensity spectra. *Soft Matter*, 11(47):9150–9159.
- Tang, F. H. M. and Maggi, F. (2016a). A mesocosm experiment of suspended particulate matter dynamics in nutrient- and biomass-affected waters. *Water Research*, 89:76–86.
- Tang, F. H. M. and Maggi, F. (2016b). Nitrogen-modulated dynamics of microbial colonies living on suspended sediment. *submitted to Ecosystems*.
- Tennekes, H. and Lumley, J. L. (1972). *A first course in turbulence*. MIT press.
- Tezuka, Y. (1990). Bacterial regeneration of ammonium and phosphate as affected by the carbon: nitrogen: phosphorus ratio of organic substrates. *Microbial Ecology*, 19(3):227–238.
- Theng, B. (1974). Complexes of clay minerals with amino acids and peptides. *Chemie der Erde*, 33:125–144.
- Thorn, M. (1981). Physical processes of siltation in tidal channels. *Proceedings of Hydraulic Modelling applied to Maritime Engineering Problems*, pages 47–55.
- Timmerman, C., Fleer, A., Besnier, J., De Graaf, L., Cremers, F., and Verhoef, J. (1991). Characterization of a proteinaceous adhesin of *Staphylococcus epidermidis* which mediates attachment to polystyrene. *Infection and Immunity*, 59(11):4187–4192.
- Toffolon, M. (2002). *Hydrodynamics and morphodynamics of tidal channels*. PhD thesis, University of Padova, Italy, Ph. D. thesis.
- Tonui, N. and Sumner, D. (2011). Flow around impulsively started square prisms. *Journal of Fluids and Structures*,

27(1):62–75.

- Toseland, A., Daines, S. J., Clark, J. R., Kirkham, A., Strauss, J., Uhlig, C., Lenton, T. M., Valentin, K., Pearson, G. A., Moulton, V., et al. (2013). The impact of temperature on marine phytoplankton resource allocation and metabolism. *Nature Climate Change*, 3(11):979–984.
- Tourna, M., Freitag, T. E., Nicol, G. W., and Prosser, J. I. (2008). Growth, activity and temperature responses of ammonia-oxidizing archaea and bacteria in soil microcosms. *Environmental Microbiology*, 10(5):1357–1364.
- Tribus, M. and McIrvine, E. C. (1971). Energy and information. *Scientific American*, 225(3):179–188.
- Tsui, M. T. and Chu, L. (2003). Aquatic toxicity of glyphosate-based formulations: comparison between different organisms and the effects of environmental factors. *Chemosphere*, 52(7):1189–1197.
- Tsuneda, S., Aikawa, H., Hayashi, H., Yuasa, A., and Hirata, A. (2003). Extracellular polymeric substances responsible for bacterial adhesion onto solid surface. *FEMS Microbiology Letters*, 223(2):287–292.
- Tufail, A. (1987). Microbial communities colonising nutrient-enriched marine sediment. *Hydrobiologia*, 148(3):245–255.
- Turley, C. and Mackie, P. (1994). Biogeochemical significance of attached and free-living bacteria and the flux of particles in the ne atlantic ocean. *Marine Ecology-Progress Series*, 115:191–191.
- Vahedi, A. and Gorczyca, B. (2011). Application of fractal dimensions to study the structure of flocs formed in lime softening process. *Water Research*, 45(2):545–556.
- Vainshtein, P., Shapiro, M., and Gutfinger, C. (2004). Mobility of permeable aggregates: effects of shape and porosity. *Journal of aerosol science*, 35(3):383–404.
- Valioulis, I. A. and List, E. J. (1984). Collision efficiencies of diffusing spherical particles: hydrodynamic, van der Waals and electrostatic forces. *Advances in Colloid and Interface Science*, 20(1):1–20.
- Van Kessel, J. (1977). Factors affecting the denitrification rate in two water-sediment systems. *Water Research*, 11(3):259–267.
- Van Leussen, W. (1988). Aggregation of particles, settling velocity of mud flocs a review. In *Physical processes in estuaries*, pages 347–403. Springer.
- Van Leussen, W. (1994). *Estuarine macroflocs*. PhD thesis, University of Utrecht.
- Verhagen, F. J. and Laanbroek, H. J. (1991). Competition for ammonium between nitrifying and heterotrophic bacteria in dual energy-limited chemostats. *Applied and Environmental Microbiology*, 57(11):3255–3263.
- Verschuren, D., Johnson, T. C., Kling, H. J., Edgington, D. N., Leavitt, P. R., Brown, E. T., Talbot, M. R., and Hecky, R. E. (2002). History and timing of human impact on Lake Victoria, East Africa. *Proceedings of the Royal Society of London B: Biological Sciences*, 269(1488):289–294.
- Vicsek, T. (1989). *Fractal growth phenomena*, volume 4. World Scientific.
- Vikash, G. and Prashant, A. (2008). Issues in modeling the stress-strain behavior of Kaolin Clay with dispersed microfabric. In *The 12th International Conference of IACMAG*.
- Villermaux, E., Sixou, B., and Gagne, Y. (1995). Intense vortical structures in grid-generated turbulence. *Physics of Fluids (1994-present)*, 7(8):2008–2013.
- Vitousek, P. M., Aber, J. D., Howarth, R. W., Likens, G. E., Matson, P. A., Schindler, D. W., Schlesinger, W. H., and Tilman, D. G. (1997a). Human alteration of the global nitrogen cycle: sources and consequences. *Ecological Applications*, 7(3):737–750.
- Vitousek, P. M., Mooney, H. A., Lubchenco, J., and Melillo, J. M. (1997b). Human domination of Earth’s ecosystems. *Science*, 277(5325):494–499.
- Von Stockar, U. and Liu, J.-S. (1999). Does microbial life always feed on negative entropy? Thermodynamic analysis of microbial growth. *Biochimica et Biophysica Acta (BBA)-Bioenergetics*, 1412(3):191–211.
- Vymazal, J. (2007). Removal of nutrients in various types of constructed wetlands. *Science of the Total Environment*, 380(1):48–65.
- Wacholder, E. and Sather, N. (1974). The hydrodynamic interaction of two unequal spheres moving under gravity through quiescent viscous fluid. *Journal of Fluid mechanics*, 65(03):417–437.
- Wågberg, L. and Lindström, T. (1987). Kinetics of polymer-induced flocculation of cellulosic fibers in turbulent flow. *Colloids and Surfaces*, 27(4):29–42.
- Wang, X.-C. and Lee, C. (1993). Adsorption and desorption of aliphatic amines, amino acids and acetate by clay minerals and marine sediments. *Marine Chemistry*, 44(1):1–23.
- Wang, Y., Chen, H., Liu, Y.-X., Ren, R.-P., and Lv, Y.-K. (2015). Effect of temperature, salinity, heavy metals, ammonium concentration, pH and dissolved oxygen on ammonium removal by an aerobic nitrifier. *RSC Advances*,

- 5(97):79988–79996.
- Wang, Y. and Mora, P. (2008). Macroscopic elastic properties of regular lattices. *Journal of the Mechanics and Physics of Solids*, 56(12):3459–3474.
- Wendling, L. A., Douglas, G. B., Coleman, S., and Yuan, Z. (2012). Nutrient and dissolved organic carbon removal from water using mining and metallurgical by-products. *Water Research*, 46(8):2705–2717.
- Wheeler, P. A. and Kirchman, D. L. (1986). Utilization of inorganic and organic nitrogen by bacteria in marine systems. *Limnology and Oceanography*, 31(5):998–1009.
- Wilcock, P. R. and Crowe, J. C. (2003). Surface-based transport model for mixed-size sediment. *Journal of Hydraulic Engineering*, 129(2):120–128.
- Williams, H. T. and Lenton, T. M. (2010). Evolutionary regime shifts in simulated ecosystems. *Oikos*, 119(12):1887–1899.
- Willmott, C. J. (1982). Some comments on the evaluation of model performance. *Bulletin of the American Meteorological Society*, 63(11):1309–1313.
- Willmott, C. J., Ackleson, S. G., Davis, R. E., Feddema, J. J., Klink, K. M., Legates, D. R., O’donnell, J., and Rowe, C. M. (1985). *Statistics for the evaluation and comparison of models*. American Geophysical Union.
- Wilson, G. S., Raftos, D. A., Corrigan, S. L., and Nair, S. V. (2010). Diversity and antimicrobial activities of surface-attached marine bacteria from Sydney Harbour, Australia. *Microbiological Research*, 165(4):300–311.
- Wilson, J. (2006). The role of benthic microalgae in the ecology of Lake Illawarra. *Wetlands (Australia)*, 21(2):pp–94.
- Wingender, J., Neu, T. R., and Flemming, H.-C. (1999). *Microbial extracellular polymeric substances: characterization, structure and function*. Springer Science & Business Media.
- Witten Jr, T. A. and Sander, L. M. (1981). Diffusion-limited aggregation, a kinetic critical phenomenon. *Physical Review Letters*, 47(19):1400.
- Wolanski, E., Gibbs, R. J., Mazda, Y., Mehta, A., and King, B. (1992). The role of turbulence in the settling of mud flocs. *Journal of Coastal Research*, pages 35–46.
- Wolery, T. J. (1992). *EQ3/6: A software package for geochemical modeling of aqueous systems: package overview and installation guide (version 7.0)*. Lawrence Livermore National Laboratory Livermore, CA.
- Wu, R. and Lee, D. (2001). Hydrodynamic drag on non-spherical floc and free-settling test. *Water Research*, 35(13):3226–3234.
- Yallop, M., Paterson, D., and Wellsbury, P. (2000). Interrelationships between rates of microbial production, exopolymer production, microbial biomass, and sediment stability in biofilms of intertidal sediments. *Microbial Ecology*, 39(2):116–127.
- Zabawa, C. F. (1978). Microstructure of agglomerated suspended sediments in northern Chesapeake Bay estuary. *Science*, 202(4363):49–51.
- Zamparas, M., Deligiannakis, Y., and Zacharias, I. (2013). Phosphate adsorption from natural waters and evaluation of sediment capping using modified clays. *Desalination and Water Treatment*, 51(13-15):2895–2902.
- Zaranyika, M. F. and Nyandoro, M. G. (1993). Degradation of glyphosate in the aquatic environment: An enzymic kinetic model that takes into account microbial degradation of both free and colloidal (or sediment) particle adsorbed glyphosate. *Journal of Agricultural and Food Chemistry*, 41(5):838–842.
- Zhang, D., Wang, J., and Pan, X. (2006). Cadmium sorption by eps produced by anaerobic sludge under sulfate-reducing conditions. *Journal of Hazardous Materials*, 138(3):589–593.
- Zhang, J.-F. and Zhang, Q.-H. (2011). Lattice Boltzmann simulation of the flocculation process of cohesive sediment due to differential settling. *Continental Shelf Research*, 31(10):S94–S105.
- Zhu, C., Liang, S., and Fan, L. S. (1994). Particle wake effects on the drag force of an interactive particle. *International Journal of Multiphase Flow*, 20(1):117–129.

List of Symbols

α	Coefficient for d_0	[-]	$d_{P,I}$	Perimeter-based fractal dimension spectrum	[-]
$\tilde{\alpha}$	Coefficient for d_0	[-]	$d_{P,\hat{I}}$	Global maximum of $d_{P,I}$	[-]
$\beta_1(\ell)$	Coefficient for $f(\ell)$	[-]	$d_{P,\hat{I}}$	Optimum d_P	[-]
$\beta_2(\ell)$	Coefficient for $f(\ell)$	[-]	e	Electron fraction for anabolism	[-]
$\beta_3(\ell)$	Coefficient for $f(\ell)$	[-]	$f(\ell)$	Empirical expression for $d_{P,\hat{I}}$	[-]
β_g	Coefficient for l	[-]	f_g	Grid frequency	[T ⁻¹]
δ	Primary particle capacity dimension	[-]	$k(\ell)$	Coefficient for d_0	[-]
δ_m	Mortality rate	[T ⁻¹]	k_a^*	Adsorption rate constant	[L ³ M ⁻¹ T ⁻¹]
δ_{o^*}	Precision of measurement	[-]	k_d^*	Desorption rate constant	[T ⁻¹]
δ_s	Relative displacement	[L]	k_s	Coefficient of stiffness	[MT ⁻²]
ℓ	Dimensionless aggregate size	[-]	k_B	Boltzmann constant	[ML ² T ⁻² θ^{-1}]
γ	Characteristic rate of change in d_0	[-]	k_S^*	Shannon constant	[-]
γ_1	Skewness	[-]	l	Integral time scale	[L]
γ_2	Kurtosis	[-]	m_A	Mass of aggregate	[M]
κ	Reciprocal Debye length	[L ⁻¹]	m_s	Spheropolygon mass per unit depth	[ML ⁻¹]
λ	Coefficient of damping	[T ⁻¹]	m_g	Coefficient for u_{rms}	[-]
μ	Dynamic viscosity	[ML ⁻¹ T ⁻¹]	n_a	Number of aggregates analysed	[-]
μ_{s^*}	Maximum specific rate of substrate utilization	[T ⁻¹]	n_o	Number of observations	[-]
$\hat{\mu}_s$	Maximum specific biomass growth rate	[T ⁻¹]	n_{Fr}	Freundlich adsorption coefficient	[-]
ν	Kinetic viscosity	[L ² T ⁻¹]	o^*	Observed values	[-]
ν_p	Poisson ratio	[-]	p	Significance	[-]
ω_0	Normal oscillation frequency	[T ⁻¹]	p_r	Probability	[-]
ϕ	Surface electric potential	[ML ² T ⁻³ I ⁻¹]	q_0	Initial mass of adsorbed ions	[MM ⁻¹]
ρ_f	Fluid density	[ML ⁻³]	q_m	Maximum adsorption capacity	[MM ⁻¹]
ρ_s	Sediment/spheropolygon density	[ML ⁻³]	r	Spheroradius	[L]
σ^*	Standard deviation	[-]	r_{eq}	Equivalent radius	[L]
θ	Angle of orientation	[-]	t_c	Collision time	[T]
ε	Energy dissipation rate	[L ² T ⁻³]	u_{rms}	Root mean square velocity of turbulence	[LT ⁻¹]
ε_0	Permittivity of vacuum	[T ⁴ I ² M ⁻¹ L ⁻³]	v	Aggregate settling velocity	[LT ⁻¹]
ε_{eff}	Effective energy dissipation rate	[L ² T ⁻³]	x, y	Horizontal and vertical position	[L]
ε_r	Dielectric constant of water	[-]	x_n	Stoichiometric number	[-]
$a(\ell)$	Coefficient for d_0	[-]	$z(\ell)$	Coefficient for d_0	[-]
$b(\ell)$	Coefficient for d_0	[-]	A_{agg}	Aggregate area	[L ²]
b_g	Coefficient for ε	[-]	A_s	Spheropolyfloc area	[L ²]
c^*	Calculated values	[-]	C_K	Kaolinite mineral concentration	[ML ⁻³]
c_g	Coefficient for u_{rms}	[-]	D	Aggregate traveled distance	[L]
d	Grid bar size	[L]	D_a	Distance with neutral double layer force	[L]
d_0	Capacity dimension	[-]	D_c	Distance between centers of mass of spheropolyflocs	[L]
d_P	Perimeter-based fractal dimension	[-]			

* Unit changes depending on the definition of other parameters.

D_s	Distance between spheropolyflocs surface	[L]	T	temperature	[θ]
E	Entropy	[-]	V	Error between I_{ref} and I_{SP} in pixels	[-]
F	Focus level	[-]	W	Number of microstates	[-]
F_A	Van der Waals attractive force	[MLT ⁻²]	Y	Young modulus	[ML ⁻¹ T ⁻²]
F_b	Buoyancy force	[MLT ⁻²]	Y_b	Biomass yield	[-]
F_C	Contact force	[MLT ⁻²]	$Z(\ell)$	d_P of a square	[-]
F_d	Drag force	[MLT ⁻²]	Z_g	Orthogonal distance from the grid	[L]
F_E	Elastic force	[MLT ⁻²]	3D	Three-dimensional	
F_g	Gravitational force	[MLT ⁻²]	μ PIV	Micro particle image velocimetry	
F_i	Impact drag	[MLT ⁻²]	ANOVA	Analysis of variance	
F_R	Electrostatic repulsive force	[MLT ⁻²]	B_{DEN}	Denitrifying bacteria	
F_{thres}	Focus level threshold	[-]	B_{DNR}	Dissimilatory nitrate reducing bacteria	
F_V	Viscous force	[MLT ⁻²]	B_{HET}	Heterotrophic bacteria	
F_v	Viscous drag	[MLT ⁻²]	B_{NIT}	Nitrifying bacteria	
G	Turbulence shear rate	[T ⁻¹]	B_{PHOTO}	Phototrophic bacteria	
H	Spacing between grid elements	[L]	B_{TOT}	Total living biomass	
H_A	Hamaker constant	[ML ² T ⁻²]	CCA	Cluster-cluster aggregation	
I	Grayscale image intensity	[-]	CCD	Charge-coupled device	
I_{ref}	Reference pixel image	[-]	DLA	Diffusion-limited aggregation	
I_{SP}	Spheropolygon image	[-]	DNR	Dissimilatory nitrate reduction	
\hat{I}	I value corresponding to $d_{P,\hat{I}}$	[-]	DOF	Depth of field	
\dot{I}	I value corresponding to $d_{P,\dot{I}}$	[-]	EPS	Extracellular polymeric substances	
K_{β^*}	Equilibrium constant in phase β	[-]	FFT	Fast Fourier Transform	
K_{Fr^*}	Freundlich adsorption constant	[L ³ M ⁻¹]	FOV	Field of view	
K_H	Inhibition constant	[ML ⁻³]	IA	Index of agreement	
K_L	Langmuir adsorption constant	[L ³ M ⁻¹]	NABA	Nutrient- and biomass-affected	
K_{linear}	Linear adsorption constant	[L ³ M ⁻¹]	NABF	Nutrient-affected and biomass-free	
K_M	Half-saturation concentration	[ML ⁻³]	NEC	Necromass	
L	Aggregate size	[L]	NFBF	Nutrient- and biomass-free	
L_p	Primary particle size	[L]	NRMSE	Normalized root mean square error	
M	Grid mesh size	[L]	NSE	Nash-Sutcliffe efficiency	
M_{eff}	Effective mass of spheropolyflocs	[ML ⁻¹]	PBIAS	Percent bias	
N	Number of levels of I	[-]	PE	Percent error	
N_b	Number of bins	[-]	R	Correlation coefficient	
N_A	Dimensionless area	[-]	SCA	Self-correlated aggregation	
N_P	Dimensionless perimeter	[-]	SPM	Suspended particulate matter	
N_Q	Number of possible answers to Q	[-]	TEP	Transparent exopolymer particles	
N_v	Number of vertices of a spheropolygon	[-]			
P	Knowledge about Q	[-]			
Q	Question of entropy	[-]			
Q_m	maximum adsorption capacity	[ML ⁻³]			
R_A	Anabolic reaction	[-]			
R_a	Electron acceptor half-reaction	[-]			
R_C	Catabolic reaction	[-]			
R_d	Electron donor half-reaction	[-]			
R_M	Microbial metabolic reaction	[-]			
$R_{NH_4^+}$	Leaching rates of NH ₄ ⁺	[ML ⁻³ T ⁻¹]			
$R_{NO_3^-}$	Leaching rates of NO ₃ ⁻	[ML ⁻³ T ⁻¹]			
R_r	Reaction rate	[ML ⁻³ T ⁻¹]			
R_s	Cell synthesis half-reaction	[-]			
S	Grid stroke	[L]			
S_2	2D image	[-]			
S_3	3D body	[-]			

* Unit changes depending on the definition of other parameters.

Acknowledgements

First and foremost, I would like to thank my supervisor Dr. Federico Maggi. He has been very supportive since the days I started working with him as an undergraduate summer scholar. His enthusiasm and passion for research were contagious and inspiring, and had motivated me to pursue PhD. I truly appreciate his generosity in giving his time and effort to teach and guide me in all aspects of this project, from the design and construction of the facility, to the analyses of data, and to the writing of manuscripts and thesis. His encouragement and emotional support had brought me through difficult times, especially when experiments were not turning out right. I would not have gone this far without his continuous guidance and support.

I would like to thank also my auxiliary supervisor A/prof Abbas El-Zein. He has been continuously giving me feedback on my research and has been always supportive to me. I am also grateful to my annual progress review committee members, Prof. Gianluca Ranzi, Dr. Fernando Alonso-Marroquin, and Dr. Chao Hou for their valuable feedback and suggestions. I would like to address special thanks to Dr. Fernando Alonso-Marroquin for introducing me to the PBM model he developed and letting me to use it to conduct simulations presented in Chapter 6. I would like to thank also Dr. Dorian Hanaor for his help in lithographic fabricating the aggregates used in Chapter 4.

My next word of thanks goes to the technical staff at the School of Civil Engineering, The University of Sydney. I would like to especially thank Mr. Garry Towell for coordinating the construction of the facility, Mr. Theo Gresley-Daines for constructing the settling column, and Mr. Ross Barker for giving me suggestions and advices on the design of the facility. Without technical support from them, progressing through this project would have been even tougher.

My special thanks to my friends and colleagues who generously shared their knowledge and experience with me and always kept me inspired. I would like to especially thank Han Min Thu (electrical engineer) for giving me valuable advices on electronic and electrical circuit design, Young Hong and Hui Ling Tan (current PhD candidates in chemical engineering) for sharing with me their research experience in practical biochemistry, Dr. Youventharan Duraisamy (current lecturer at Universiti Malaysia Pahang) for sharing his experience in dealing with microorganisms, and Tze Hui Goh (architect) for giving me advices on design drawings and constantly giving me encouragement and support. I would like to take this opportunity to thank all my colleagues in Room 101 and my labmates in the Environmental Lab: Dr. Imran Kabir, Dr. Cai Li, Dr. Ahmed Faheem, Danielle Griffani, Daniele la Cecilia, Thu Ha Nguyen, Ali Ghavamnasiri, Scott Manning, Sam Walsh, and many others.

Last but not least, a heartfelt thanks to my amazing family, my parents, my uncles and aunties who I stayed with in Sydney as well as all other close family members. Their unconditional love and support for me have helped me to overcome many difficult and challenging moments of these years of PhD and have made everything possible.